

2018

## BEHAVIOUR OF LAMINATED ROOF UNDER HIGH HORIZONTAL STRESS

Prasoon Garg

Follow this and additional works at: <https://researchrepository.wvu.edu/etd>

---

### Recommended Citation

Garg, Prasoon, "BEHAVIOUR OF LAMINATED ROOF UNDER HIGH HORIZONTAL STRESS" (2018). *Graduate Theses, Dissertations, and Problem Reports*. 7178.

<https://researchrepository.wvu.edu/etd/7178>

This Thesis is protected by copyright and/or related rights. It has been brought to you by the The Research Repository @ WVU with permission from the rights-holder(s). You are free to use this Thesis in any way that is permitted by the copyright and related rights legislation that applies to your use. For other uses you must obtain permission from the rights-holder(s) directly, unless additional rights are indicated by a Creative Commons license in the record and/ or on the work itself. This Thesis has been accepted for inclusion in WVU Graduate Theses, Dissertations, and Problem Reports collection by an authorized administrator of The Research Repository @ WVU. For more information, please contact [researchrepository@mail.wvu.edu](mailto:researchrepository@mail.wvu.edu).

**BEHAVIOUR OF LAMINATED ROOF UNDER  
HIGH HORIZONTAL STRESS**

Prasoon Garg

Thesis submitted to the

Benjamin M. Statler College of Engineering and Mineral Resources

at West Virginia University

in partial fulfillment of the requirement for the degree of

**Master of Science**

**in**

**Mining Engineering**

Brijes Mishra, Ph.D., Chair

Keith A. Heasley, Ph.D., PE.

Bruce S. Kang, Ph.D.

Department of Mining Engineering

Morgantown, West Virginia

July 2018

Keywords: Numerical Modeling, Laminated rock, Beam analysis

Ground Control, Rock Mechanics, Biaxial platens

**Copyright 2018 © Prasoon Garg**

# **ABSTRACT**

## **Behavior of laminated roof under high horizontal stress**

**Prasoon Garg**

Roof falls continue to be one of the greatest hazards in underground coal mines worldwide. The laminated roof contributes to a large number of roof fall incidents, especially in Pittsburgh seam. The presence of high horizontal in-situ stresses is detrimental to the stability of laminated roof and poses challenging ground control problems to the researchers. One of the commonly observed problem is known as “cutter” or “kink” failure. It is a compressional type failure of the roof, commonly observed in Appalachian underground coal mines with laminated roof rock. Historically, laminated rocks are assumed an isotropic material with reduced strength or transversely isotropic material with different deformability properties at directions parallel to lamination. Both these approaches ignore characteristics of the weak planes, which often lead to the formation of thin layers (“Delamination”) as observed in underground coal mines.

The fundamental research presented in this thesis is an attempt to provide a deeper understanding of the behavior of laminated shale roof under high horizontal stress using numerical analysis and laboratory experiments. The numerical analysis involved the plane strain simulation of a laminated roof over a mine entry. The roof was simulated as a combination of isotropic rock (matrix material within the laminates) and discontinuities (representing the weak plane between laminates) using three different models namely; Anisotropic mine model, Elastic beam model, and Plastic beam model to determine its critical behavior. The anisotropic mine model identified three behavioral responses of shale roof namely: stress channeling, multi-beam coupling, and self-stabilizing beams based on lamination thickness. However, the model also showed limited applicability in identifying the underlying mechanism behind failure progression into the shale roof. This limitation was due to the complex layer interaction in the shale roof, which is the result of its interaction with overburden strata. Therefore, beam analysis was used to develop a simplified layer-interaction model and then investigate its influence on the behavior of the laminated roof under the elastic and plastic state. The analysis showed that buckling was the probable failure in a thinly laminated roof, especially under high horizontal stress. The laminar interaction was found to be highly dependent on interface (laminar plane) cohesion as it dictates location and degree of delamination. The laboratory experiments were performed on cubical specimens to replicate the 3-dimensional bending of the laminated roof under high horizontal stress. For this purpose, a biaxial platen was designed with confining device that can apply biaxial and true-triaxial load on cubical specimens. The test design was validated by comparing the failure response of Berea sandstone in poly-axial stress state with other existing devices.

## ACKNOWLEDGEMENTS

The research compiled in this thesis would not have been possible without the continuous support, excellent guidance, motivation, and critical input from my advisor, Dr. Brijes Mishra. I am indebted to him for his contributions towards the successful completion of this thesis and for providing an excellent research atmosphere. I am thankful to the National Institute of Occupational Safety and Health for funding this research project.

I would also like to extend my gratitude to my thesis committee members, Dr. Keith A. Heasley, and Dr. Bruce Kang—for their insightful comments, suggestions, and important inquiries into my work. Their individual perspectives were instrumental in improving the quality of this research.

I would also like to mention the names of my colleagues that have shared and made my academic life in the U.S. become much more wonderful and meaningful: Neel Gupta, Debashis Das, Sameer Mittal, Priyashraba Mishra, Annand Nandula, Yuting Xue, Danqing Gao.

Special thanks to the Howard Mearns for fabricating the biaxial platens used in this work. I will always remember his contributions. I am also thankful to Karla J. Vaughan and Karen Centofanti for their help in administrative matters.

Finally, I dedicate this thesis to my parents and my siblings. Their unconditional love, support, and encouragement have played a pivotal role in shaping my personal and professional life.



# TABLE OF CONTENTS

<b>ABSTRACT</b> .....	ii
<b>ACKNOWLEDGEMENTS</b> .....	iii
<b>TABLE OF CONTENTS</b> .....	iv
<b>LIST OF FIGURES</b> .....	ix
<b>LIST OF TABLES</b> .....	xvii
<b>1. INTRODUCTION</b> .....	1
1.1 Background.....	1
1.2 Research Methodology .....	4
1.3 Thesis Organization: .....	6
<b>2. LITERATURE REVIEW</b> .....	8
2.1 Introduction.....	8
2.2 Influence of layer interaction in failure of laminated roof.....	9
2.2.1 Failure modes of laminated roof .....	11
2.2.1.1 Flexure controlled roof behavior .....	11
2.2.1.2 Deadweight driven shear failure .....	15
2.2.1.3 Shearing of Stiff Bands.....	16
2.2.1.4 Cutter roof or guttering.....	17
2.2.1.5 Factors affecting layer interaction in laminated roof.....	21
2.3 Horizontal Stress Trends in U.S. Coalfields .....	21
2.4 Critical research in failure of laminated roof.....	22

2.4.1 Studies related to implicit anisotropy in laminated rock .....	23
2.4.2 Studies related to explicit anisotropy in laminated rock .....	29
2.4.2.1 Analytical methods.....	29
2.4.2.2 Laboratory experiments.....	34
2.4.2.3 Numerical methods.....	35
2.5 Summary.....	40
<b>3. ANISOTROPIC MINE MODEL .....</b>	<b>42</b>
3.1 Numerical simulation of laminated shale .....	42
3.2. Numerical Modeling Procedures .....	46
3.2.1. The Distinct Element Method .....	46
3.2.2. The Finite Difference Method.....	47
3.2.3. Rock Failure criteria.....	48
3.2.2. Estimation of Rock Mass Strength.....	50
3.2.3. Anisotropic Model.....	51
3.2.4. Selected Constitutive Model .....	53
3.2.5. Lamination properties.....	55
3.2.6. Numerical Simulation of Anisotropic Perfectly Plastic Model.....	57
3.2.6.1 Selection of interface properties for laminar plane.....	67
3.2.7. Limitation of Anisotropic Model .....	68
3.2.7.1 Failure progression within laminated roof.....	69
3.2.7.2 Influence of horizontal stress.....	69
3.2.7.3 Influence of Interface parameters .....	70
3.2.8 Summary .....	71

<b>4. ELASTIC BEAM ANALYSIS.....</b>	<b>74</b>
4.1 Introduction.....	74
4.2 Elastic Solid Beam model.....	74
4.3 Voussoir beam model .....	78
4.4 Solid Beam on Elastic Abutment.....	83
4.5. Parametric Study.....	87
4.5.1. Lamination thickness.....	87
4.5.2. Horizontal Stress .....	94
4.5.2.1. Influence of lamination thickness under high horizontal stress.....	99
4.5.4. Limitation of elastic beam analysis .....	113
4.6 Summary .....	114
<b>5. PLASTIC BEAM ANALYSIS.....</b>	<b>116</b>
5.1 Introduction.....	116
5.2 Load profile on shale roof of beam model.....	116
5.3 Solid beam on elastic abutment under elasto-plastic state.....	119
5.3.1 Lamination properties.....	121
5.3.2 Dimension of lateral boundary .....	122
5.3.3 Comparison with anisotropic mine model.....	125
5.3.4 Failure propagation in solid shale beam on elastic abutment model.....	129
5.4 Parametric Study.....	133
5.4.1 Lamination thickness.....	133
5.4.2 <i>In-situ</i> stress magnitude and ratio.....	141
5.4.3 Interface parameters .....	146

5.4.3.1 Interface strength .....	146
5.4.3.2 Interface stiffness .....	154
5.5 Limitation of Solid beam on elastic abutment model .....	159
5.6 Summary .....	160
<b>6. PLATEN DESIGN</b> .....	<b>162</b>
6.1. Experimental Design and Set-Up .....	162
6.2. The Biaxial Platen .....	163
6.3. Modification of biaxial platens for true triaxial test .....	168
6.4. Uniaxial Compression Testing Machine .....	169
6.5. Friction Effect .....	170
6.6. Laboratory Investigation .....	172
6.6.1. Validation of biaxial device .....	172
6.6.2. Rock types and specimen geometry .....	172
6.6.3. Lithologic description .....	172
6.6.4. Specimen Preparation .....	172
6.6.5. Uniaxial compression test .....	174
6.6.6. Biaxial compression test .....	175
6.6.6.1 Loading path .....	175
6.6.6.2 Test Procedure .....	177
6.6.7 True-triaxial test .....	178
6.7 Test Limitations .....	179
6.8 Test Results .....	179
6.8.1 Uniaxial compressive test .....	179

6.8.1.1 Influence of specimen size on UCS of sandstone.....	182
6.8.1.2 Influence of specimen size on failure mechanism of sandstone.....	184
6.8.2 Biaxial compressive test.....	186
6.8.2.1 Influence of loading path on peak strength of cubic sandstone.....	188
6.8.2.2 Influence of loading path on failure mechanism of cubic sandstone.....	189
6.8.3 True-triaxial test .....	193
6.8.3.1 Influence of confinement on peak strength under triaxial stress state.....	195
6.8.3.2 Influence of confinement on failure mechanism under triaxial stress state.	196
6.8.4 Failure criterion for biaxially loaded intact rocks .....	199
6.8.4.1 Drucker-Prager criterion.....	200
6.8.4.2 Regression curve for biaxial failure points.....	202
6.8.5 True-triaxial failure criterion.....	205
6.8.5.1 Nadai criterion .....	206
6.9 Summary and Conclusion.....	208
<b>7. CONCLUSION AND RECOMMENDATION</b> .....	<b>211</b>
7.1 Conclusion.....	211
7.2 Future recommendation.....	213
<b>REFERENCES</b> .....	<b>215</b>

## LIST OF FIGURES

Figure 1.1 Leading geologic factors contributing to roof falls (Bajpayee et al., 2014).....	1
Figure 1.2 Cutter failure showing delamination in thin beds of shale roof (Esterhuizen and Bajpayee, 2012). .....	2
Figure 1.3 Stages of “cutter-roof” failure development (a) Initial stage of a cutter, (b) Small cutter type roof fall at a corner, and (c) Roof profile after a massive fall initiated by cutters (Gadde and Peng, 2005).....	3
Figure 2.1 Cutter failure in thin beds of shale roof (Esterhuizen and Bajpayee, 2012).....	10
Figure 2.2 Stack rock roof under high horizontal stress (Molinda and Mark 2010) .....	10
Figure 2.3 a) Bending of layered roof under gravity or dead load b) Linear arch formation due to flexural failure (Galvin, 2016). .....	12
Figure 2.4 (a) Bed separation in weak shale (top); (b) Stairstepping tension fractures begin in laminated roof at the rib abutment and extends over the pillar (Molinda and Mark 2010). .....	13
Figure 2.5 (a) Bending of layered roof under the combined load of dead weight and lateral load; (b) Dome shaped failure due to flexural failure under combined load (Galvin, 2016). .....	14
Figure 2.6 Dome-shaped cavity caused by progressive failure of interbedded shale and sandstone roof at a mine located in Illinois (Esterhuizen and Bajpayee, 2012). .....	15
Figure 2.7 (a) Abutment shear under gravity or dead weight; (b) roof fall at intersection due to abutment shear (Galvin, 2016).....	16
Figure 2.8 Compressive failure of stiff beds of stack rock roof under lateral stress along with dilation derived down lower strata (Galvin, 2016). .....	16
Figure 2.9 (a) Failure of bedding laminations in the roof (Esterhuizen and Bajpayee, 2012); (b) vertical zone of small cutter near the entry corners (Peng, 2007) .....	17
Figure 2.10 Result of progressive failure of laminated roof subject to high horizontal stress, the collapse has near vertical sides (Esterhuizen and Bajpayee, 2012). .....	18
Figure 2.11 a-c Conceptual process of cutter roof development (Gadde and Peng, 2005). .....	20

Figure 2.12 Orientation of the maximum horizontal stress measured in eastern US coal mines (Mark, 1991). .....	22
Figure 2.13 Finite element model used by Su and Peng, 1987 for their analysis. ....	24
Figure 2.14 Yielded zones in the immediate roof of the development entry in a longwall gateroad (Morsy and Peng, 2005). ....	26
Figure 2.15 Strain-softening model showing cutter roof failure in the immediate roof in terms of cohesion distribution (Ray, 2009). ....	27
Figure 2.16 Example of a numerical model of an entry supported by 1.8-m grouted bolts in weak bedded shale rocks at the point of collapse. Dark grey shading indicates rock damage (plastic strain). The red shaded roof is collapsing (Esterhuizen et al., 2012). ....	28
Figure 2.17 Deflection profile multi-layered two point (at $x = 0.292L, 0.708L$ ) bolted beam (Panek, 1962). ....	30
Figure 2.18 (a) Jointed rock beams; (b) Voussoir beam analogue (Diederichs and Kaiser, 1999). ....	31
Figure 2.19 Type of roof configuration used in Beam on elastic abutment model (Stephansson, 1971) .....	33
Figure 2.20 Roof failure by slip along bedding planes (top) and low angle shearing (below) for $\theta = 90^\circ$ (Jeremic, 1981). ....	34
Figure 2.21 Micro-crack distributions of the simulation with different layer orientation and for different inter-layer bonding strength (He and Afolagboye, 2018). ....	36
Figure 2.22 (a) Vertical Stress Distribution over the Entry; (b) Horizontal Stress Distribution over the Entry (Zhang et al., 2004). ....	38
Figure 2.23 Numerical model results showing the effect of interface properties on failure in laminated roof rocks (Esterhuizen and Bajpayee, 2012). ....	39

Figure 2.24 Modeled rock failure in a shale roof bed with showing inclined shear surfaces and near vertical tensile fractures (a) 10-cm laminations; (b) 30-cm laminations (Esterhuizen and Bajpayee, 2012).....	39
Figure 3.1 (a-c) Plastic state in immediate roof with lamination thickness of 450 mm in two models at different horizontal stress. ....	44
Figure 3.2 (a-c) Comparison of maximum roof deflections for anisotropic model and equivalent isotropic models of mine entry at ( $k=3, 2.5, 2$ ; $\sigma_h = 15.7, 19.635, 23.55$ MPa).....	45
Figure 3.3 Calculation cycle of FLAC3D program (Itasca, 2012) .....	48
Figure 3.4 Model geometry simulated in FLAC3D of shale roof over a 6 m span mine entry. ....	53
Figure 3.5 (a-c) Failure profile of immediate roof for lamination thickness of 450 mm for various models. ....	57
Figure 3.6 (a-e) Failure profile in shale roof of two anisotropic models at different time step....	60
Figure 3.7 Comparison of modeling methods at various lamination thicknesses using roof deflection. Model results are 6 m span mine entry at 350 m depth and $K=2$ . ....	62
Figure 3.8 (a-d) Failure profile comparison for different models at various lamination thickness .....	65
Figure 3.9 (a-c) Contour of vertical displacement in anisotropic model (interface properties of set1) for various lamination thickness. ....	67
Figure 3.10 Comparison of roof deflection between two different horizontal to vertical stress ratio. ....	70
Figure 3.11 (a-b) Failure profile in anisotropic model for different interface stiffness ratio ( $K_n/K_s$ ) .....	71
Figure 4.1 (a) Vertically-loaded beam; (b) Bending and shearing stresses on section Z-Z'; (c) Distribution of outer-fiber bending stress and middle-surface shearing stress across span; (d) Stress acting on an element at A. Failure in flexure by tension cracks, T.(Panek, 1956).....	75
Figure 4.2 Solid beam geometry with boundary conditions built in UDEC.....	77



Figure 4.3 Half-length solid beam with 1.6 m thickness (a) Horizontal stress contour; (b) Shear stress contour. ....	77
Figure 4.4 Half-length solid beam with 1.6 m thickness (a) Maximum principal stress contour; (b) Principal stress difference contour. ....	78
Figure 4.5 (a) Jointed rock beams; (b) Voussoir beam analogue (Diederichs and Kaiser, 1999).	80
Figure 4.6 Voussoir beam model of half span in UDEC. ....	80
Figure 4.7 Voussoir beam with 2-layers (0.8m lamination thickness) (a) Maximum principal stress contour; (b) Principal stress difference contour. ....	82
Figure 4.8 Type of roof configuration used in Beam with elastic abutment model (Stephansson, 1971) .....	84
Figure 4.9 Solid beam on elastic abutment model in UDEC. ....	84
Figure 4.10 Half-length solid beam on elastic abutment model (a) Maximum principal stress contour; (b) Principal stress difference contour; (c) Horizontal stress contour. ....	86
Figure 4.11 (a-d) Maximum principal Stress contour of half- length solid beam model for different lamination thickness. ....	90
Figure 4.12 (a-d) Maximum principal Stress contour of half- span Voussoir beam model for different lamination thickness. ....	91
Figure 4.13 (a-d) Maximum principal Stress contour of half- length solid beam on elastic abutment model for different lamination thickness .....	94
Figure 4.14 (a-c) Principal Stress tensor plot of half–span 4-layer solid beam at different horizontal stress. ....	96
Figure 4.15 (a-c) Principal Stress tensor plot of half–length 4-layer solid beam on elastic foundation at different horizontal stress, .....	97
Figure 4.16 (a-c) Principal Stress tensor plot of half–length 4-layer Voussoir beam at different horizontal stress. ....	98

Figure 4.17 (a-d) Maximum principal Stress contour of half-span solid beam at -3.6 MPa (k=4) horizontal stress for different lamination thickness. ....	102
Figure 4.18 (a-d) Maximum principal Stress contour of half-span solid beam on elastic abutment at -3.6 MPa (k=4) horizontal stress for different lamination thickness. ....	104
Figure 4.19 (a-d) Maximum principal Stress contour of half-span Voussoir beam at -3.6 MPa (k=4) horizontal stress for different lamination thickness. ....	106
Figure 4.20 (a-c) Maximum principal stress contour of half-length 4-layer solid beam for different interface strength. ....	110
Figure 4.21 (a-c) Maximum principal stress contour of half-length 4-layer solid beam on elastic abutment for different interface strength. ....	111
Figure 4.22 (a-c) Maximum principal stress contour of half-span 4-layer Voussoir beam for different interface strength. ....	112
Figure 5.1 Conformal transformation of a rectangle to a unit circle (Savin, 1961).....	118
Figure 5.2 Methodology for estimating load from approximate analytical solution based on conformal mapping. ....	119
Figure 5.3 Multi-layered solid beam on elastic abutment model in FLAC3D. ....	120
Figure 5.4 Change in horizontal stress for different lateral width of abutment (a) along neutral axis of second layer (N.A.1); (b) along neutral axis of third layer (N.A.2).....	124
Figure 5.5 Lateral width (W) of abutment in terms of entry span (L) when horizontal stress of $\sigma_h = 0.25$ MPa applied at boundary a) $W=1.0 L$ ; b) $W=0.75 L$ ; c) $W=0.5 L$ .....	125
Figure 5.6 Principal stress distribution in shale roof two models.....	126
Figure 5.7 Failure profile comparison in two models.....	129
Figure 5.8 Failure propagation in beam model at different incremental loading stage. ....	132
Figure 5.9 a-c Minimum principal stress distribution at 2% incremental loading stage for different lamination thickness.....	134

Figure 5.10 Failure propagation in shale roof with different lamination thickness.....	137
Figure 5.11 Failure propagation in shale roof with different lamination thickness.....	138
Figure 5.12 Failure propagation in shale roof with different lamination thickness.....	139
Figure 5.13 Failure propagation in shale roof with different lamination thickness.....	140
Figure 5.14 Minimum principal stress distribution in shale roof under different horizontal stress (K=3, 2.5, 2).....	143
Figure 5.15 a-e Failure propagation in shale roof under different horizontal stress (K=3, 2.5, 2) .....	145
Figure 5.16 Minimum principal stress distribution at 2% incremental loading stage for various interface cohesion. ....	149
Figure 5.17 (a-b) Extent of inter-bed slipping along the 1st interface at 2% loading stage for various interface cohesion.....	150
Figure 5.18 (a-d) Failure propagation in shale roof for different interface cohesion .....	152
Figure 5.19 Inter-bed slipping along the 1st interface in case 1 at 47 % loading stage.....	153
Figure 5.20 Final failure profile for different interface tensile strength. ....	154
Figure 5.21 (a-d) Minimum principal stress distribution for different interface stiffness cases. ....	157
Figure 5.22 (a-d) Failure propagation for different interface stiffness cases.....	158
Figure 5.23 Inter-bed slipping at 40 % loading stage for different interface stiffness case .....	159
Figure 6.1 Platen designed by Arora and Mishra 2015. (Unit: inch).....	164
Figure 6.2 (a) Stress acting on the roof of an entry (b) Stress distribution on specimen inside UCS testing machine (Arora and Mishra 2015). ....	164
Figure 6.3 Vertical displacement contours: (a) biaxial device by Arora and Mishra, 2015, (b) modified biaxial design used in this study.....	165
Figure 6.4 (a) Schematic view of experimental set-up of biaxial test with confining device (Units: mm) (top); (b) Test setup with biaxial platens ( $\sigma_1 = \sigma_2$ ).....	166

Figure 6.5 Schematic view of experimental set-up of biaxial test with confining device ( $\sigma_2 =$ constant).	167
Figure 6.6 Schematic view of experimental set-up of true-triaxial test (biaxial frame with confining device) replicating $\sigma_1 = \sigma_2 > \sigma_3$ and $\sigma_3 =$ constant	168
Figure 6.7 MTS servo controlled compression testing machine and its component 1) Machine Load (2) Glass Shield (3) Hydraulic Actuator (4) Manual Control System (5) Strain Gauge Control Panel (6) Computer (7) MTS Data Acquisition System (8) Upper steel platen with circular groves (9) Specimen (10) Lower steel platen with circular groves	169
Figure 6.8 Axial splitting in 50.8 mm cubical sandstone specimen (a) uniaxial stress state; (b)biaxial stress state( $\sigma_1 = \sigma_2$ ); (c) triaxial stress state ( $\sigma_1 = \sigma_2$ and $\sigma_3 = 6.2$ MPa)...	171
Figure 6.9 The geometric shapes of the four groups of Berea sandstone specimens (H, W represent height, width and of the prism specimen, respectively)	173
Figure 6.10 Biaxial test (a) Loading path 1, (b) Loading path 2 ( $n\sigma_c$ represent magnitude of constant intermediate stress in terms of average UCS of cubical sandstone)	176
Figure 6.11 Novel loading path (Ma and Haimson 2017) used in true triaxial testing, $n2\sigma_c$ represent magnitude of constant minor principal stress in terms of average UCS.	178
Figure 6.12 (a) UCS of square shaped cross-section specimens with different slenderness obtained from uniaxial compression test (top); (b) Illustration of end effect in specimens with different slenderness in rock uniaxial compression tests (redraw based on Xu and Cai, 2017).	183
Figure 6.13 (a) Dominant shear failure with spalling at outer surface in cuboidal specimen of 101.16 mm height ( $H/D=2$ ); (b) cross-shear failure of inner-core along with spalling at outer surface in cubical Specimen of 50.8 mm height ( $H/D=1$ ); (c) Hourglass type failure cuboidal specimen of 25.4 mm height Specimen ( $H/D=1/2$ ).	185
Figure 6.14 Experimental results obtained from biaxial tests for different loading paths	189
Figure 6.15 Failure mode of sandstone samples in uniaxial test: (a) $\sigma_1 - \sigma_2$ plane, (b) $\sigma_2 - \sigma_3$ plane.	191

Figure 6.16 Failure mode of sandstone samples in biaxial test with loading path 2, under $\sigma_2$ of 6.89 MPa.....	191
Figure 6.17 Failure mode of sandstone samples in biaxial test with loading path 2, under $\sigma_2$ of 13.79 MPa: (a) $\sigma_2 - \sigma_3$ plane, (b) $\sigma_1 - \sigma_3$ plane.....	192
Figure 6.18 Failure mode of sandstone samples in biaxial test with loading path 2 under $\sigma_2$ of 27.58 MPa: (a) $\sigma_2 - \sigma_3$ plane, (b) $\sigma_1 - \sigma_3$ plane.....	192
Figure 6.19 Failure mode of sandstone samples in biaxial test with loading path 1: (a) Diagonal view, (b) $\sigma_1 - \sigma_3$ plane, (c) $\sigma_2 - \sigma_3$ plane.....	193
Figure 6.20 Variation of $\sigma_1$ (peak strength) with $\sigma_3$ in Berea sandstone for axisymmetric loading conditions ( $\sigma_1 = \sigma_2$ and $\sigma_3 = \text{constant}$ ) .....	195
Figure 6.21 Variation of the octahedral shear at failure ( $\tau_{\text{oct, f}}$ ) with the octahedral normal stress ( $\sigma_{\text{oct, f}}$ ) in Berea sandstones for axisymmetric loading conditions ( $\sigma_1 = \sigma_2$ and $\sigma_3 = \text{constant}$ ).....	196
Figure 6.22 Failure mode of sandstone samples in biaxial test with loading path 1: (a) Diagonal view, (b) $\sigma_1 - \sigma_3$ plane, (c) $\sigma_2 - \sigma_3$ plane.....	197
Figure 6.23 Failure mode of sandstone samples in true triaxial test under $\sigma_3$ of 6.2 MPa: (a) Diagonal view, (b) $\sigma_2 - \sigma_3$ plane, (c) $\sigma_1 - \sigma_3$ .....	198
Figure 6.24 Failure mode of sandstone samples in true triaxial test under $\sigma_3$ of 20.68 MPa: (a) Diagonal view, (b) $\sigma_1 - \sigma_3$ plane, (c) $\sigma_2 - \sigma_3$ plane. ....	199
Figure 6.25 Drucker–Prager yield surface (a) on the principal stress space (Pariseau, 1992); (b) on the deviatoric plane (Desai and Siriwardane, 1984) .....	201
Figure 6.26 Drucker-Prager criteria with experimental data points (EDP) at failure .....	204
Figure 6.27 Polynomial regression curve with experimental data points (EDP) at failure. ....	205
Figure 6.28 Triaxial strength envelop based on Nadai criterion fitted with experimental data points at failure for axisymmetric loading conditions ( $\sigma_1 = \sigma_2$ and $\sigma_3 = \text{constant}$ ).....	208

## LIST OF TABLES

Table 3.1 Mechanical properties of each stratum and bedding planes (Murphy et al., 2014).....	54
Table 3.2 Lamination properties used in this research. ....	56
Table 3.3 Lamination properties used in parametric study.....	71
Table 4.1 Joint strength parameters used in parametric study.....	107
Table 5.1 Mechanical properties of each stratum (Murphy et al., 2014) and laminar planes.....	122
Table 5.2 Interface strength parameters used in parametric study.....	146
Table 5.3 Interface stiffness parameters used in parametric study.....	154
Table 6.1 List of test parameters used in uniaxial test.....	175
Table 6.2 List of test parameters used in biaxial test.....	176
Table 6.3 List of test parameters used in true-triaxial test.....	178
Table 6.4 Results of uniaxial compressive tests for group A. ....	180
Table 6.5 Results of uniaxial compressive tests for group B.....	180
Table 6.6 Results of uniaxial compressive tests for group C.....	181
Table 6.7 Results of uniaxial compressive tests for group D. ....	181
Table 6.8 Results of biaxial tests for loading path 2, constant $\sigma_2$ of 6.89 MPa.....	186
Table 6.9 Results of biaxial tests for loading path 2, constant $\sigma_2$ of 13.79 MPa.....	187
Table 6.10 Results of biaxial tests for loading path 2, constant $\sigma_2$ of 27.58 MPa.....	187
Table 6.11 Results of biaxial tests for loading path 1, $\sigma_1 = \sigma_2$ .....	188
Table 6.12 Results of true triaxial tests for constant $\sigma_3$ of 6.2 MPa.....	194
Table 6.13 Results of true-triaxial tests for constant $\sigma_3$ of 20.68 MPa.....	194

# 1. INTRODUCTION

## 1.1 Background

Roof falls continue to be one of the greatest hazards in underground coal mines worldwide. The development of roof bolting in the late 1940s and other extensive support systems have considerably reduced the number of fatalities from roof falls in recent years. However, each year more than 1,200 such large falls are reported in the active workings of underground coal mines in the United States (Mine Safety and Health Administration, 2011; Esterhuizen and Bajpayee, 2012). The majority of these roofs falls are related to damage in bedded roof rocks. According to the Mine Safety and Health Administration (MSHA), 2010 report, out of 1,428 cases major reportable roof collapses, strongly bedded strata such as “stack rock”, “slate”, “draw rock” and “laminated” rocks were listed as a contributing factor in 43.5% of the cases. Similarly, Bajpayee et al., 2014 investigated the geologic factors contributing to roof falls by analyzing, 825 non-injury roof falls from 1999 through 2008. Their study revealed that a majority of roof falls in US coal mines occur in laminated roofs (consisting of stack rocks, slate, laminated shale, etc.) (Figure 1.1).

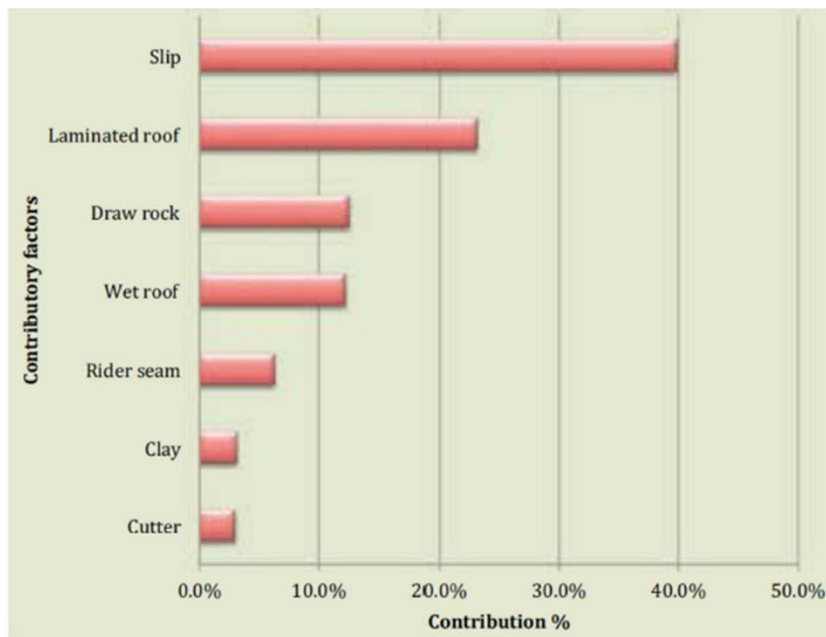


Figure 1.1 Leading geologic factors contributing to roof falls (Bajpayee et al., 2014).

The two main source of these closely spaced bedding rocks are weak lamination within shale or stack rock (Murphy, 2016). These laminas or beds are depositional feature, i.e., inherent to the rock, and structurally reduce the strength of rock along these planes. The presence of high horizontal *in-situ* stresses also damaged the laminated rock along the bedding planes. When an entry is created, high horizontal stresses force the laminated roof to bend towards the opening and inducing failure in the layers. “Delamination” is a common phenomenon under these circumstances (Figure 1.2), in which laminated rock separates into thin beams (Molinda, 2003; Hebblewhite, 2009) which are much weaker than the original combined beam roof. The location and degree of delamination significantly affects the development of failure within the roof (Esterhuizen and Bajpayee, 2012).



Figure 1.2 Cutter failure showing delamination in thin beds of shale roof (Esterhuizen and Bajpayee, 2012).



One of the most commonly observed failure modes in laminated roof rock under horizontal loading is cutter roof, also known as “kink failure,” “gutter,” or “roof gutter,” and “pressure cutting.” It is a compressional type failure of roof (Mark, 1991) observed in Appalachian underground coal mines (Su and Peng, 1987). It is generally a stepwise failure, which initiates when crushing and local buckling of thinly laminated roof beds occurs near the corners of an excavation (Figure 1.2) (Esterhuizen and Bajpayee, 2012). The kink band then grows in size and forms a vertical zone of failed rock. Similarly, the failure propagates through upper strata until it comes across a more competent rock or beyond the bolt horizon. At this stage, the failure then travels across the entry and the entire roof collapses. The entire sequence is shown in Figure 1.3.

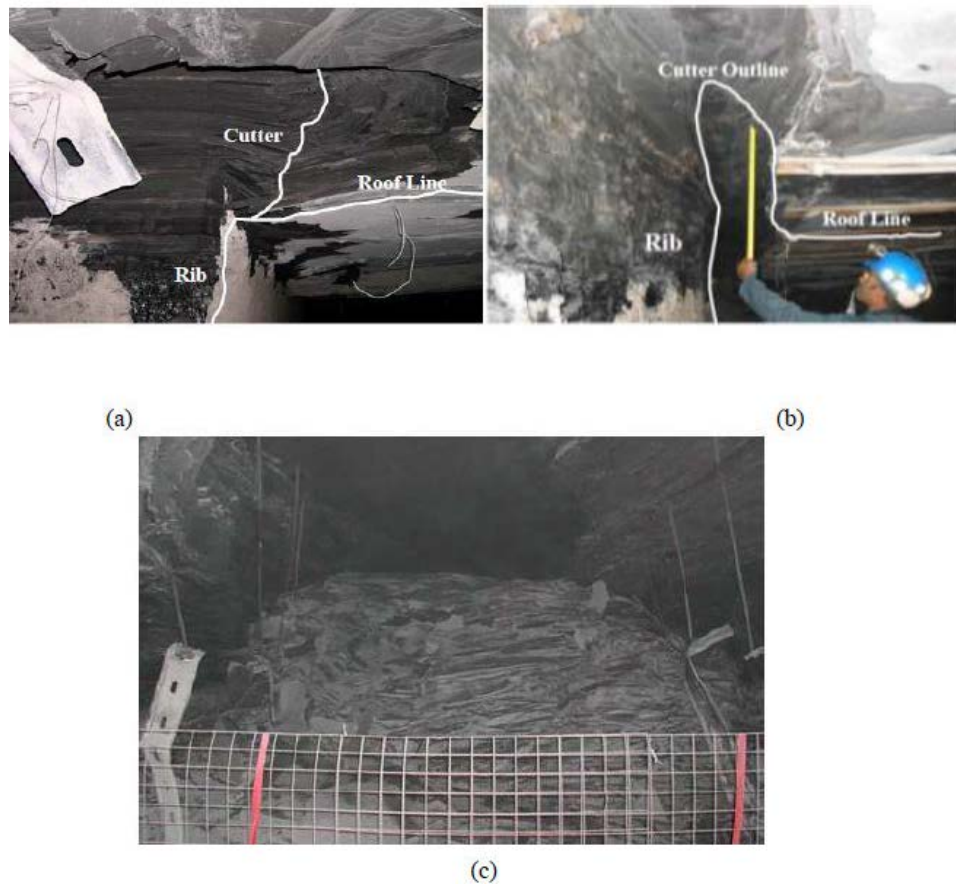


Figure 1.3 Stages of “cutter-roof” failure development (a) Initial stage of a cutter, (b) Small cutter type roof fall at a corner, and (c) Roof profile after a massive fall initiated by cutters (Gadde and Peng, 2005)

Historically, laminated rocks are assumed isotropic material with reduced strength (Ray, 2009; Gadde and Peng, 2005) or transversely isotropic material with different deformability properties at different directions with respect to lamination. The former approach is valid for uniformly jointed or disintegrated rock mass with no persistent parallel discontinuities to control its behavior (Fortsakis et al., 2012). The latter approach involves anisotropic behavior of the rock that exist due to lamination and is generally simulated through ubiquitous joint models (Gale et al., 2004; Sainsbury and Sainsbury, 2017; Esterhuizen et al., 2013). However, behavior of laminated roof strata is primarily controlled by characteristics of the weak planes, which often lead to the formation of thin beams (Fortsakis et al., 2012; Esterhuizen and Bajpayee, 2012) as observed in underground coal mines. In addition, the individual laminas fail primarily in flexure and then accompanied by shear failure in adjacent layers.

Numerical models used in the previous approaches were successful in replicating some of the key aspects of various failure modes in laminated roof such as the location of cutter roof and its causal factors (Su and Peng, 1987; Ahola et al, 1991; Gadde and Peng, 2005). However, the underlying failure mechanism is still poorly understood in these rocks (Arora and Mishra, 2015). In the current research, an attempt was made to understand the influence of laminations on the behavior of shale roof. The bending of shale roof is simulated as an interaction between thin layers to understand the underlying mechanism behind failure initiation and its propagation within the roof.

## **1.2 Research Methodology**

The primary objective of the current research was to study the influence of lamination on the behavior of shale roof under high horizontal stress. The special focus was given on:

1. Influence of explicit lamination in a numerical model on behavior of shale roof.
2. Mechanism behind inter laminar-interaction and its influence on failure progression in laminated roof.
3. Influence of horizontal stress and lamination parameters like its strength and thickness on laminar-interaction within the shale roof under elastic and plastic state.

4. Failure propagation from one lamina to another when layers interact as thin plates using biaxial device that represent 3D bending of shale roof.

A combined approach encompassing numerical simulation and laboratory experiments was used in this research (Figure 1.4). The numerical analysis include the plane strain simulation of laminated roof over mine entry using three models namely: Anisotropic mine model, Elastic beam model, and Plastic beam model. The anisotropic mine model explicitly simulated laminar plane to investigate its influence on behavior of shale roof. However, the model showed limited applicability in identifying the underlying mechanism behind the laminar interaction and its influence on failure progression shale. This limitation was due to the complex layer interaction in the shale roof, which is the result of its interaction with overburden strata. Therefore, beam analysis was used to develop a simplified layer-interaction model and then investigate its influence on the behavior of the laminated roof under the elastic and plastic state. The elastic models were used to understand influence of laminar interaction on stress distribution within shale roof. The plastic beam models were used to investigate the influence of laminar interaction on failure propagation within the shale roof. The model also simulated high *in-situ* stress condition by considering the formation of pressure arch on the vertical load profile on top of shale roof from overburden strata. A parametric study was also performed in both beam models to understand the effect of horizontal stress and lamination parameters on laminar interaction and shale roof behavior.

Layer interaction in the laminated shale roof was not limited to plane strain condition as seen in various cutter roof cases. For better understanding of the underlying mechanism of failure propagation from one lamina to another, experiments are required that involved three-dimensional bending of shale rocks. For this purpose, biaxial platen with confining device that applied biaxial and true-triaxial load on cubical specimens was designed. To validate the design, Berea sandstone was tested to investigate the influence of poly-axial stress state on failure response.

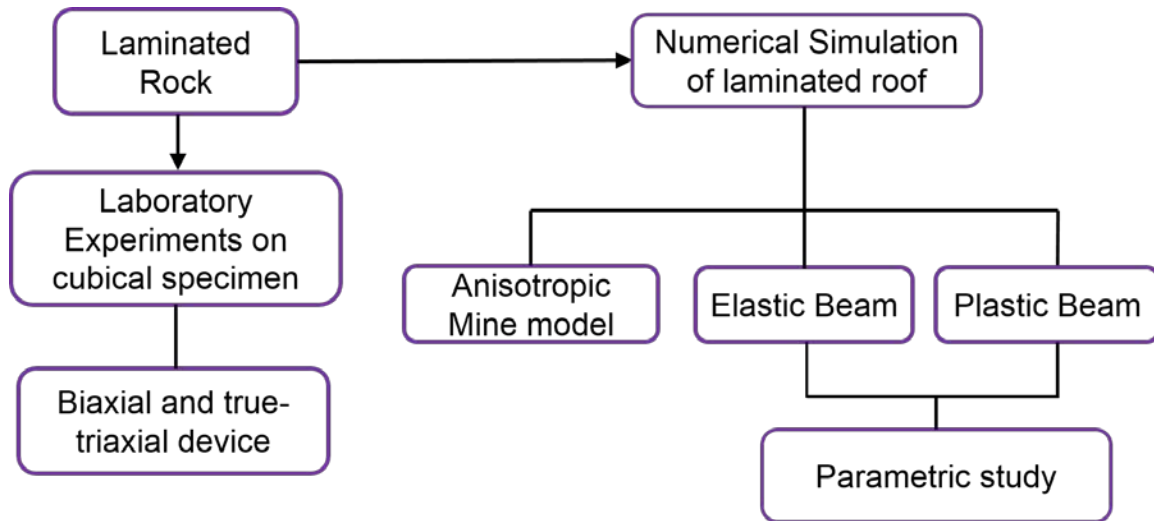


Figure 1.4 Flow sheet of the approach used in the current research.

### 1.3 Thesis Organization:

This thesis is organized into seven chapters with chapter 1 defining background and the scope of present work. Each chapter has an introductory section, which provides the relevant information from literature. It is followed by detailed discussion of the research.

Chapter 2 includes a thorough review of the literature related to failure of laminated rock roof under high horizontal stress and its causal factors. It also include review of research aimed at investigating anisotropic behavior of shale roof due to presence of lamination and related failure modes. Most of studies have ignored that influence of including explicit lamination to simulate the anisotropic behavior of shale roof.

Chapter 3 presents the anisotropic mine model used to investigate the influence of lamination on the behavior of shale roof. It includes the selection of material model, excavation geometry, and effect of the presence of discontinuities (laminar plane) on overall behavior of shale roof. It also describes the effect of high horizontal stress and various lamination properties like stiffness and tensile strength on the failure profile of shale roof. However, the model showed limited applicability in identifying the underlying mechanism behind the laminar interaction and its influence on failure progression shale.

Chapter 4 presents elastic beam analysis aimed to understand the inter-laminar interaction within shale roof under uniform vertical loading. The analysis involve three beam models simulated in UDEC (Distinct Element Method based numerical code) under elastic state. In addition, a parametric study was performed to understand the influence of horizontal stress and lamination parameters on bending profile and stress distribution in the shale roof.

Chapter 5 presents plastic beam analysis in FLAC3D (Finite Difference Method based numerical code) using solid beam on elastic abutment model. It include model formulation along with its validation. In addition, a parametric study was performed to understand the influence of horizontal stress and lamination parameters on layer interaction during failure progression within shale roof.

Chapter 6 describes in detail the experimental set-up used to study the failure response of laminated rock under biaxial and triaxial loading conditions. It also includes the design validation by comparing failure mode and peak strength values of Berea sandstone with other existing devices. The next step would be tests of shale samples. However, accurate sized specimens of shale could not be obtained in the stipulated time and therefore testing on shale specimens can be one area of possible future research. These tests on shale rock can be used to investigate underlying mechanism of failure propagation from one lamina to another when layers interact as thin plates.

Chapter 7 summarizes the important results and conclusions of this research. It also gives an outline of possible areas for future research work.

## 2. LITERATURE REVIEW

### 2.1 Introduction

The roof rocks in the Pittsburgh coal seam are usually constituted of strongly bedded strata such as stack rock, draw rock, laminated rocks, and significantly contributed to majority of roof falls. In the eastern United States, horizontal stress is also often higher than the vertical stress and is pervasive in the mines. The presence of high horizontal stress deeply intensifies the roof fall problem. Records of non-injury roof falls in coal mines (Mine Safety and Health Administration, 2010) showed 43.5% of the total 1,428 cases, bedded strata was the main factor.

These rock types present significant challenges in support design due to localized failure (buckling failure, sagging and roof shear) under high horizontal stress (Molinda and Mark, 2010; Zhang et al., 2010). The common objective of roof support is to build a stable roof beam or to suspend the immediate roof from a competent overlying roof beam between coal pillars (Molinda, 2003). However, under high horizontal stress, the layers delaminate easily into thin beams (Colwell et al., 2008; Hebbelwhite, 2009). These individual beams are much weaker than the original combined beam and influences strength and failure development within the roof. Due to weak bonding between lamination, roof is much weaker in the lateral direction. One of the commonly observed failure modes in laminated roof is “cutter roof”, “kink failure” or “pressure cutting”. It is a compressional type failure with crushing and local buckling of thinly laminated roof beds that occurs at the corners of an excavation (Esterhuizen and Bajpayee, 2012). This type of failure mostly occurs in weak, bedded, and supported roof (Molinda and Mark, 2010). This clearly indicate that inter-layer interaction is imperative to the design of support for strongly bedded strata.

In this chapter, the first influence of layer-interaction on various ground control problems was evaluated through various field case studies. This was followed by review of contributing factors like horizontal stress and their existence in the Appalachian region and Illinois basin. Finally, various reported literatures on layer interaction was extensively reviewed.

## **2.2 Influence of layer interaction in failure of laminated roof**

Coal measure rocks usually contain weak bedding structures that have a significant impact on their stability. In many rocks, the problem becomes acute because of the closely spaced bedding (Esterhuizen et al. 2014). The two main sources of these closely spaced beds in coal measure rocks are a) weak lamination within shale; b) stack rock (Murphy 2016).

The shale rock occurs in laminated formation mainly composed of silt-size and clay-size particles (Terzaghi and Peck, 1996; Murphy, 2016). Most shale display fissility, i.e., tendency to split along relatively smooth and flat surfaces parallel to the bedding (Terzaghi and Peck, 1996; He and Afolagboye, 2018). The laminations are formed due to the variation in the depositional environment that leads to the differences in grain size, clay percentage, organic material content, or mineral content (Boggs, 1987). These laminations mark the differences in shale from other weak rocks such as mudstone. The presence of the laminar planes (weak plane between laminae) have significant effect on the mechanical behavior and strength of shale rock. The bedded shale can be relatively strong perpendicular to bedding, however is often considerably weaker when parallel to the beds (Molinda and Mark, 1996) which makes them highly anisotropic rocks. Therefore, it is imperative to investigate the effect of bedding parameters such as spacing, roughness and weak plane strength on the behavior of shale rock. Figure 2.1 shows the thin beds in shale roof.

Stack rock is a coalfield name representing sequence of interbedded sandstone and shale. The rock is a mixture of sandstone and shale in widely varying proportions. It grades either into a shale with sandstone streaks or vice versa (figure 2.2). The stack rock is formed as result of alternating periods of high-energy water movement (depositing sandstone) with quiet low-energy standing water (depositing shale) (Molinda, 2003).



Figure 2.1 Cutter failure in thin beds of shale roof (Esterhuizen and Bajpayee, 2012)

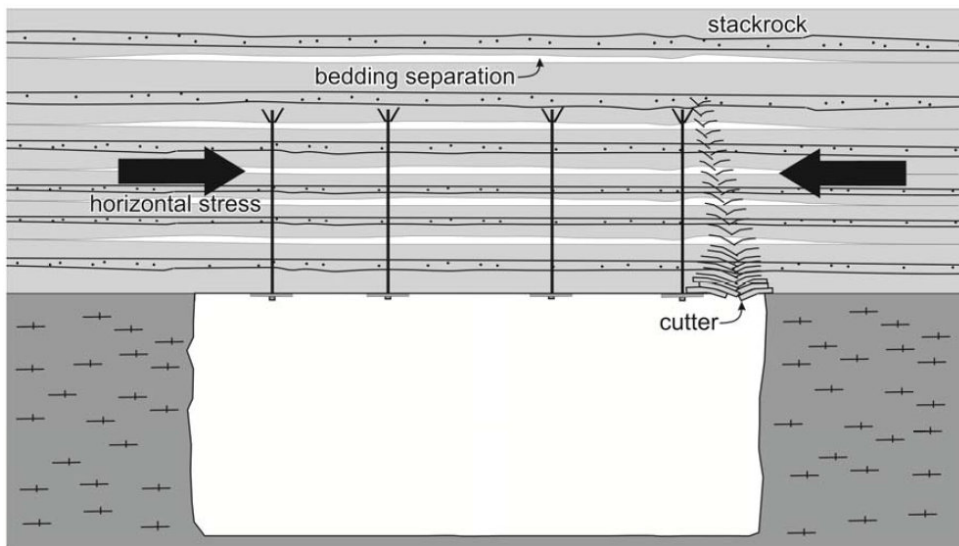


Figure 2.2 Stack rock roof under high horizontal stress (Molinda and Mark 2010)

Both rock types exhibit anisotropic properties, which occur due to the depositional formation of layers inherent to rock fabric (Molinda, 2003; Murphy, 2016). These features are distinguished from structural discontinuities, which are due to erosion, structural faulting/fracturing, and horizontal stress. For instance, joints in coal measures rocks are vertical or near vertical fractures caused by tension (Molinda, 2003; Molinda and Mark, 2010). As mentioned in section 2.1, these



rocks poses serious ground control problems. Therefore, a better understanding of failure of bedded strata will improve the design of supports, which will provide a safe mine environment.

### **2.2.1 Failure modes of laminated roof**

According to Galvin, 2016, there are five basic modes of roof failure in underground coal mining:

1. Gravity driven falls of unrestrained blocks of rock delineated by joints, bedding planes and mining-induced fractures.
2. Compressive (shear) failure of intact rock.
3. Flexural (tensile) failure due to excessive bending stress.
4. Abutment shear.
5. Buckling

Roof failures may include one or a combination of basic modes. For instance, tensile cracking of a roof due to excessive flexural stress may lead to the formation of a linear arch Voussoir beam, which may fail in different modes. The understanding of these basic failure modes are vital to identifying the exact cause of failure modes in mines.. In laminated or stack rock roof, failure modes can be classified into four groups based on the causes and mechanism of the failure (Galvin, 2016):

- a) Flexure controlled roof or buckling
- b) Deadweight driven shear
- c) Shearing of stiff bands
- d) Cutter roof or guttering

#### **2.2.1.1 Flexure controlled roof behavior**

The laminated or stack roof undergoes two failure modes depending on in-situ stress conditions. For low horizontal stress, laminated roof would bending only under its weight. It may lead to formation of linear arch or Voussoir arch (Galvin, 2016) as seen in Figure 2.3a-b. The arch forms due to excessive flexural stress. Tensile cracks appear on the upper surface

of the beam at the abutment-forming arch (Figure 2.3a). Failure progresses through different modes depending on the lamination thickness and stress conditions (Galvin, 2016).

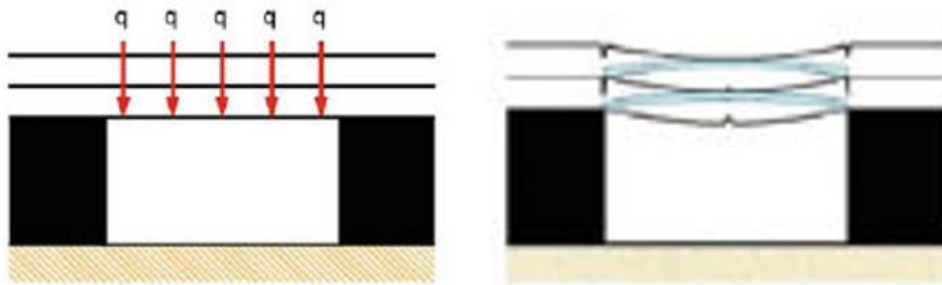


Figure 2.3 a) Bending of layered roof under gravity or dead load b) Linear arch formation due to flexural failure (Galvin, 2016).

Roof sagging occurs due to the separation of roof layers or delamination when roof bends under gravity or dead weight. It occurs in strongly bedded rock such as laminated shale or stack rock with less number of stiff sandstone interbeds (Molinda and Mark, 2010). The sagging occurred when laminar or bedding contacts fail in shear or tension. This would result in delamination of roof into thin beams causing significant bed separation (Figure 2.4a). If the separation occurs above the bolt anchor zone, it may lead to failure of the roof. As the beam deflects, tension cracks can also develop in the entry center (Figure 2.4b). Figure 2.4b shows the roof beam failure under tension along with step-path tension fractures over the rib. To prevent this failure, a stiff primary support is required which reinforces the roof beam and reduces the deflection.

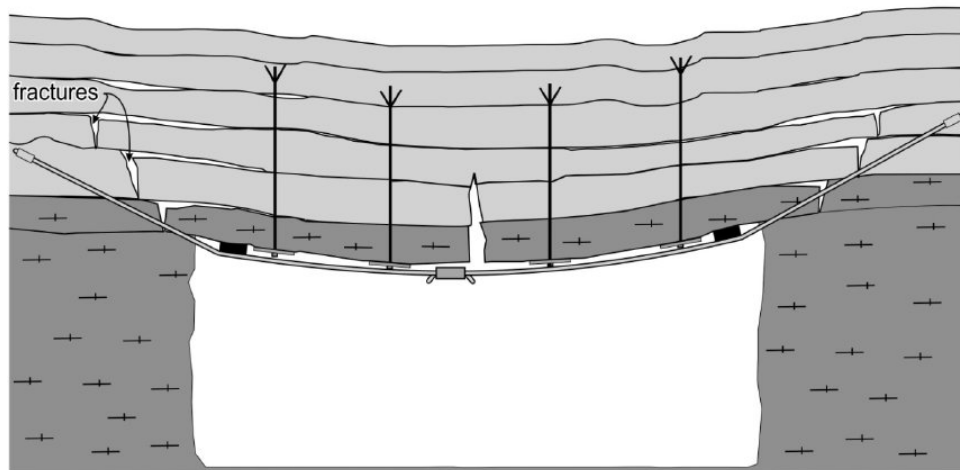


Figure 2.4 (a) Bed separation in weak shale (top); (b) Stairstepping tension fractures begin in laminated roof at the rib abutment and extends over the pillar (Molinda and Mark, 2010).

Under high horizontal stress, laminated or stack rock roof would bend under combined load of dead weight and lateral load (Figure 2.5a). Due to the bending under high lateral load, roof delaminates into thin beam and loses its load bearing capacity. Layers undergo buckling which occurs near the middle of the entry when the immediate roof is highly laminated (Peng, 2005).

This results in dome shaped failure for thinly laminated roof or highly jointed and bedded weak rock roof (Figure 2.5b).

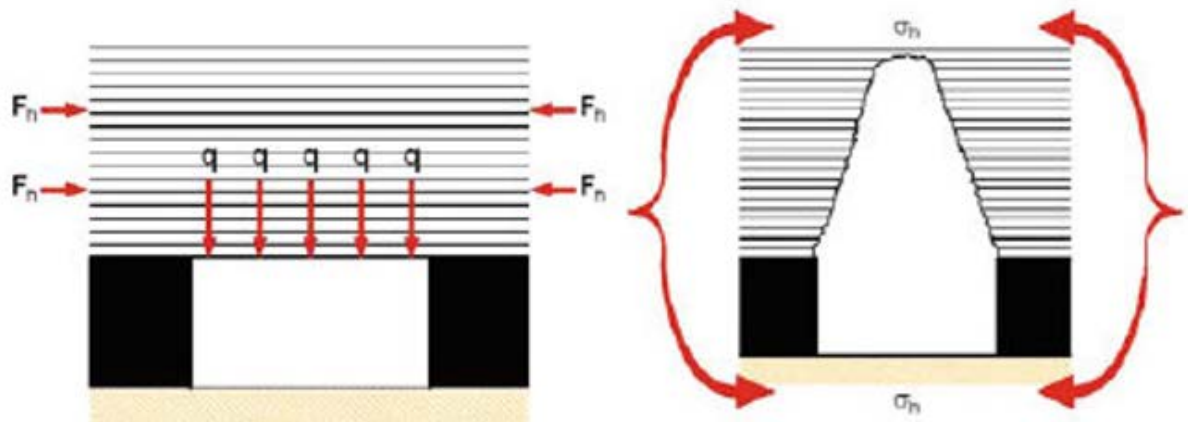


Figure 2.5 (a) Bending of layered roof under the combined load of dead weight and lateral load; (b) Dome shaped failure due to flexural failure under combined load (Galvin, 2016).

Stack rock delamination generally occurs under high horizontal stress when sandstone beds within rock roof acts as stress concentrators. The weak shale bed is crushed resulting in tensional delamination with adjacent sandstone beds. The initial crushing occurs at the center of entry span followed by tensile failure or buckling of individual beds (Molinda, 2003; Esterhuizen and Bajpayee, 2012). The failure progresses until it crosses weak plane above the bolt horizon resulting in dome-shaped failure as shown in figure 2.6 (Peng, 2007). This type of failure occurs in stack rocks with high percentage of sandstone. However, stack roof with mostly shale rock or laminated shale roof gutters easily along the rib-roof interaction due to low stiffness and strength of shale rock (Molinda, 2003).



Figure 2.6 Dome-shaped cavity caused by progressive failure of interbedded shale and sandstone roof at a mine located in Illinois (Esterhuizen and Bajpayee, 2012).

### **2.2.1.2 Deadweight driven shear failure**

This type of failure generally occurred in weaker strata, when it is loaded under gravity (Molinda 2003; Peng 2005). The whole strata sheared off along the abutment and fall down (Figure 2.7a-b). It is often called as abutment shear and not limited to strongly bedded roof. Any weak strata under gravity load can undergo abutment shear.

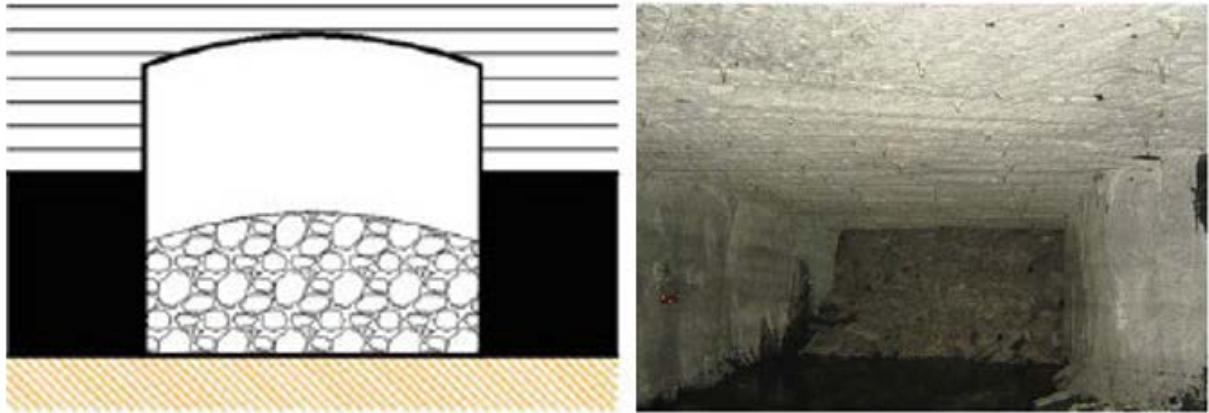


Figure 2.7 (a) Abutment shear under gravity or dead weight; (b) roof fall at intersection due to abutment shear (Galvin, 2016).

### 2.2.1.3 Shearing of Stiff Bands

This type of failure occurs when stack roof with large number of thick stiff beds is subjected to high lateral stress (Figure 2.8a). These stiff sandstone beds would act as stress concentrator and are prone to brittle failure. When the stiff sandstone beds fail, the associated dilation rapidly drives down the immediate roof (Figure 2.8a). This type of failure is highly depended on thickness of stiff and often misinterpreted as buckling failure or delamination (Galvin, 2016). The misinterpretation is due to the similarity in the failure mechanism with stack rock delamination (Section 2.2.1.1).

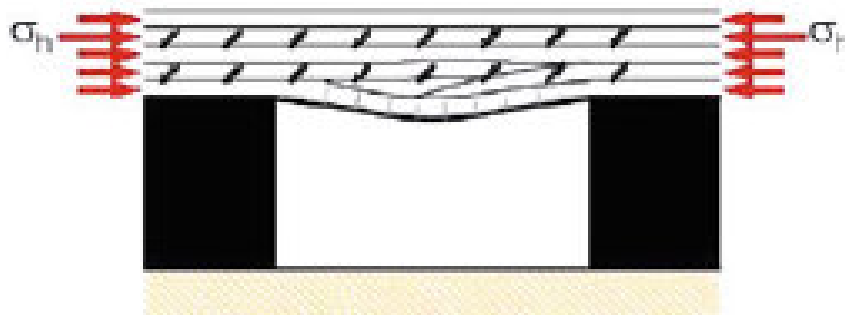


Figure 2.8 Compressive failure of stiff beds of stack rock roof under lateral stress along with dilation derived down lower strata (Galvin, 2016).



#### 2.2.1.4 Cutter roof or guttering

Cutter roof refers to damage of coal mine roof caused by horizontal compression and crushing of roof rock (Molinda and Mark, 2010). It is commonly found in Appalachian coal mines that have laminated roof rock with high horizontal stress (Su and Peng, 1987). In this type of failure, under high horizontal stress, crushing and local buckling of thinly laminated roof beds occurs and forms a near vertical zone of failed rock near the corners of an excavation (Hill, 1986; Esterhuizen and Bajpayee, 2012) (Figure 2.9a-b). The resulting near vertical zone of crushed rock leads to the progressive collapse of the entire roof (Figure 2.10). Although, cutter failure occurs in weak or laminated rocks it is also found to occur in stack rock and even in limestone in near-surface stone mines (Molinda, 2003; Molinda and Mark, 2010).

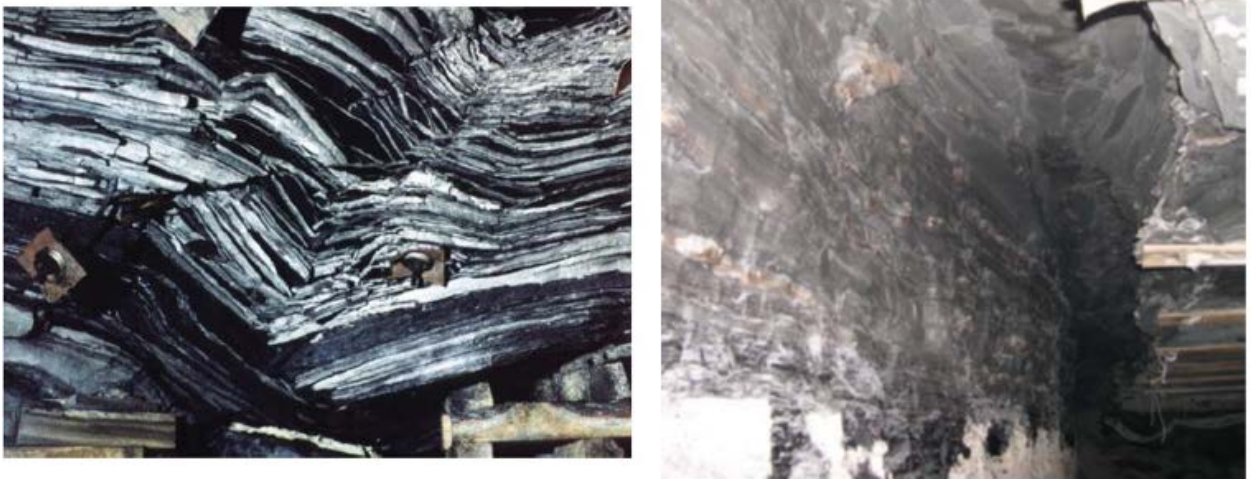


Figure 2.9 (a) Failure of bedding laminations in the roof (Esterhuizen and Bajpayee, 2012);  
(b) vertical zone of small cutter near the entry corners (Peng, 2007)



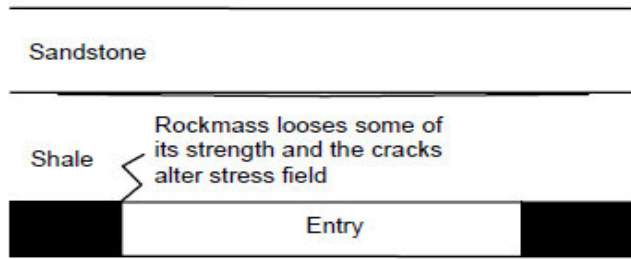
Figure 2.10 Result of progressive failure of laminated roof subject to high horizontal stress, the collapse has near vertical sides (Esterhuizen and Bajpayee, 2012).

Numerous studies indicate factors such as the orientation and magnitude of horizontal *in-situ* stresses control the development of cutters. In addition, mechanical properties (strength and stiffness) of roof rocks and coal (Su and Peng, 1987), presence of geologic anomalies in immediate roof (clay veins, coal cleats) (Hill and Bauer, 1984; Iannacchione et al., 1984; Bauer, 1990), stress inducing activities such as retreating and multi-seam extraction, controls the formation and development of cutters. Among all the numerous factors listed above, most common factors are

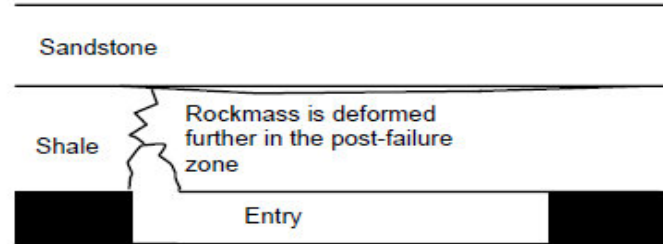


the *in-situ* stresses and laminated roof beds (Mark and Mucho, 1994; Ray, 2009; Esterhuizen and Bajpayee, 2012).

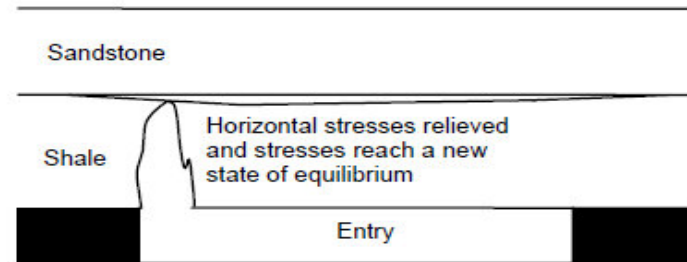
Gadde and Peng, 2005, suggested a conceptual mechanism of cutter roof development based on field observation and the available rock deformation characteristics from laboratory data. They stated that the cutter roof initiates when the shear stress concentration exceeds the rock mass strength at one, or both, corners of an opening causing the failure and fracturing of a rock layer at these locations (Figure 2.11a). As the failed rock enters post failure state, it loses some of its load bearing capacity, which depends on the amount of strain and confinement in the failed region. The shredded load is then transferred to adjacent layers which themselves undergo failure leading to propagation of fracture zone in near vertical direction. With further advancement of the working face and the change in the geometry of workings, the failed rock mass deforms further in the post-failure state and may fall down, further altering the stress state around the fractured region (Figure 2.11b). Subsequently, the failure propagates through the upper strata until it comes across a weak plane or when it is beyond the roof bolt horizon. This progressive process ultimately leads to complete failure of the rock mass leading to roof collapse in a part or across the whole (Figure 2.11c).



(a) Single or multiple cracks at one or both corners of the entry.



(b) With a change in geometry or increasing stand-up time, major cracks extend and cracked zone grows in size; the rockmass that has been deformed most in the post-failure state may fall down or lose its total load bearing capacity.



(c) The caved zone grows in size or if the stresses at the other corner (abutment of cantilever) also exceed strength, then the whole roof may collapse.

Figure 2.11a-c Conceptual process of cutter roof development (Gadde and Peng, 2005).

### **2.2.1.5 Factors affecting layer interaction in laminated roof**

It is clear from section 2.2.1.1-2.2.1.3, that the failure mode in laminated or stack rock roof is highly dependent on *in-situ* stress and lamination parameters such as stiffness and strength. Additionally, exact the failure mechanism of each mode is highly dependent on layer interaction, location and degree of delamination within the roof. For instance, laminated roof under high horizontal loading would undergo dome shaped failure if local crushing initiated at the center of entry (Figure 2.6) while cutter roof occurs if failure initiated at the entry rib corner. Similarly, stack rock roof with stiff beds show shear failure (Figure 2.8) instead of cutter roof or dome shaped failure depending on number and thickness of stiff sandstone layer as discussed in the previous sections. Roof stability of laminated rock is affected by high horizontal stress as it delaminates rock into thin beams that are much weaker than combined beam roof (Esterhuizen and Bajpayee, 2012). Therefore, it is imperative to consider the effect of horizontal stress when designing underground coalmines

## **2.3 Horizontal Stress Trends in U.S. Coalfields**

Horizontal stress is a significant factor contributing to roof instability in bedded coal measures rocks (Aggson and Curran, 1978, Hill, 1986, Iannacchione et al., 1998, Esterhuizen et al., 2007). In coal mines of the United States, horizontal stresses were found to be normally more influential than the vertical stress (Mark and Barczak, 2000). In fact in the eastern United States, the major horizontal stress is generally two to three times of the vertical stress while the minor horizontal stress is approximately equal to the vertical stress

According to Mark, 1991, *in-situ* stress measurements at twenty-five underground coal mine sites in the eastern U.S. indicate E-NE horizontal stress orientation. Sixty-seven percent of the measurements conducted at the Appalachian and Warrior coal basin found the orientation to be between N80E and N50E. In the Illinois basin, seventy-five percent of the measurements found the stress direction had deviated towards E-W by 15° (Figure 2.12).

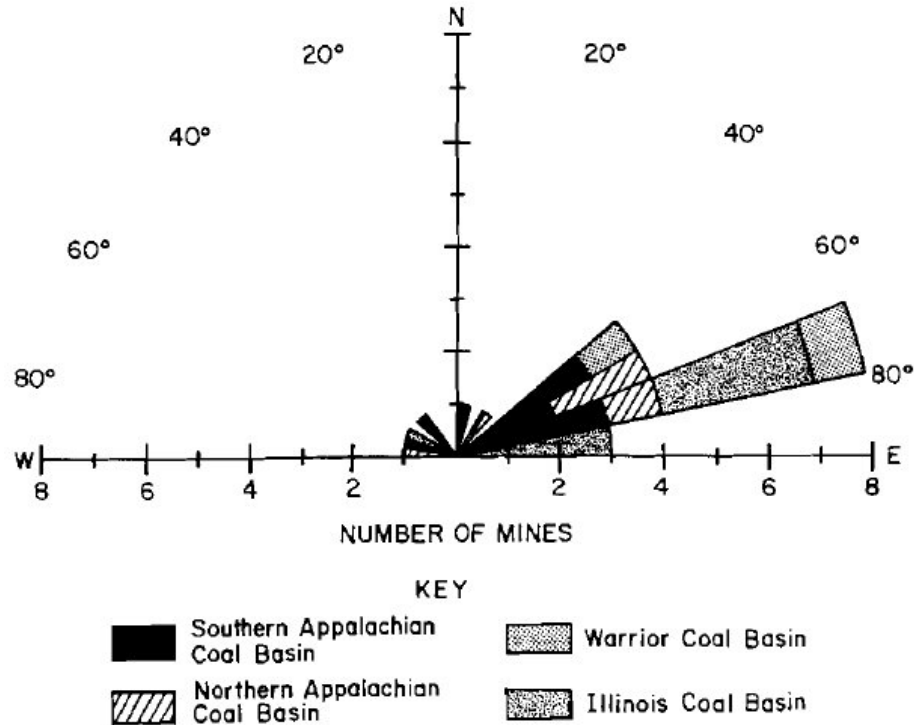


Figure 2.12 Orientation of the maximum horizontal stress measured in eastern US coal mines (Mark, 1991).

Dolinar, 2003 examined the variation of horizontal strain magnitude at 37 sites in the eastern and midwestern United States. The measurements suggest that the eastern U.S consist of two distinct high and low strain zones. The high strain zones comprise the Beckley coal seam and the Central Appalachian region only. The remaining eastern U.S was found to be in the low strain zone, except for the Central Appalachian region, where the distinction remained inconclusive.

#### 2.4 Critical research in failure of laminated roof

As mentioned in previous sections, presence of laminar or bedding plane makes laminated or stack rock weak and highly anisotropic. Attempts have been made in the past to understand this anisotropic behavior and related failure modes in laminated rock especially cutter roof. The use of numerical models (continuum, boundary element, and discontinuum modeling) have been successful in replicating various aspects of behavior of anisotropic rock.

Various methods to incorporate the anisotropy due to lamination have been used and are broadly classified into two types: a) Implicit anisotropy b) Explicit anisotropy. Implicit anisotropy is widely used in design of underground structures especially in coal measure rocks. In this method, material properties are quantified using classification systems (CMMR in coal measure rocks) by considering rockmass as an equivalent “mean isotropic geomaterial”. It reduces the rockmass strength to account for its bedding or lamination (Morsy and Peng, 2001; Badar et al., 2003; Gadde and Peng, 2005; Ndlovu and Stacy, 2007). The assumption of equivalent isotropic rock is generally valid for uniformly jointed or disintegrated rock mass where no family of persistent parallel discontinuities exist to control its behavior (Fortsakis et al., 2012). Alternately, laminated shale roof was also simulated as transversely isotropic material by reducing strength by a factor in direction parallel to bedding (Zhou et al., 2017) or by using ubiquitous joint model that indirectly incorporate effect of laminar or bedding plane (Gale et al. 2003; Esterhuizen et al., 2013).

In explicit anisotropy, rock is treated as an isotropic material with explicit discontinuities that represent weak plane between two laminas (Fortsakis et al., 2012). This approach provides a realistic behavior of anisotropic rock mass. The approach includes either by simulating the whole lamination network using discrete element analysis or by modeling only a representative number of laminations that are sufficient to include the underlying mechanism (Perras and Diederichs, 2009; Fortsakis et al., 2012). The former approach provides a realistic behavior of anisotropic rock mass. However, this approach also requires accurate input parameters such as lamination spacing and its mechanical properties which would require extensive borehole data and detailed laboratory investigation.

#### **2.4.1 Studies related to implicit anisotropy in laminated rock**

Conventional studies have simulated laminated rock as an equivalent isotropic material along with reduced strength to incorporate bedding. This simplification provided an insight into complex failure modes such as cutter failure. Su and Peng (1987) used finite element modelling to determine the “intrinsic” mechanism of cutter roof failure (Figure 2.13). They conducted an exhaustive parametric study to identify varied factors affecting the cutter roof failures such as effect of *in-situ* stress, relative stiffness between coal and its immediate roof, large topographic relief, bed separation, and geologic anomalies (clastic dikes). The results of their numerical

modeling showed that the direction and magnitude of horizontal stress affected the nature and location of cutter roof failure. On the other hand, vertical stress controlled the behavior of the immediate roof at the entry corner.

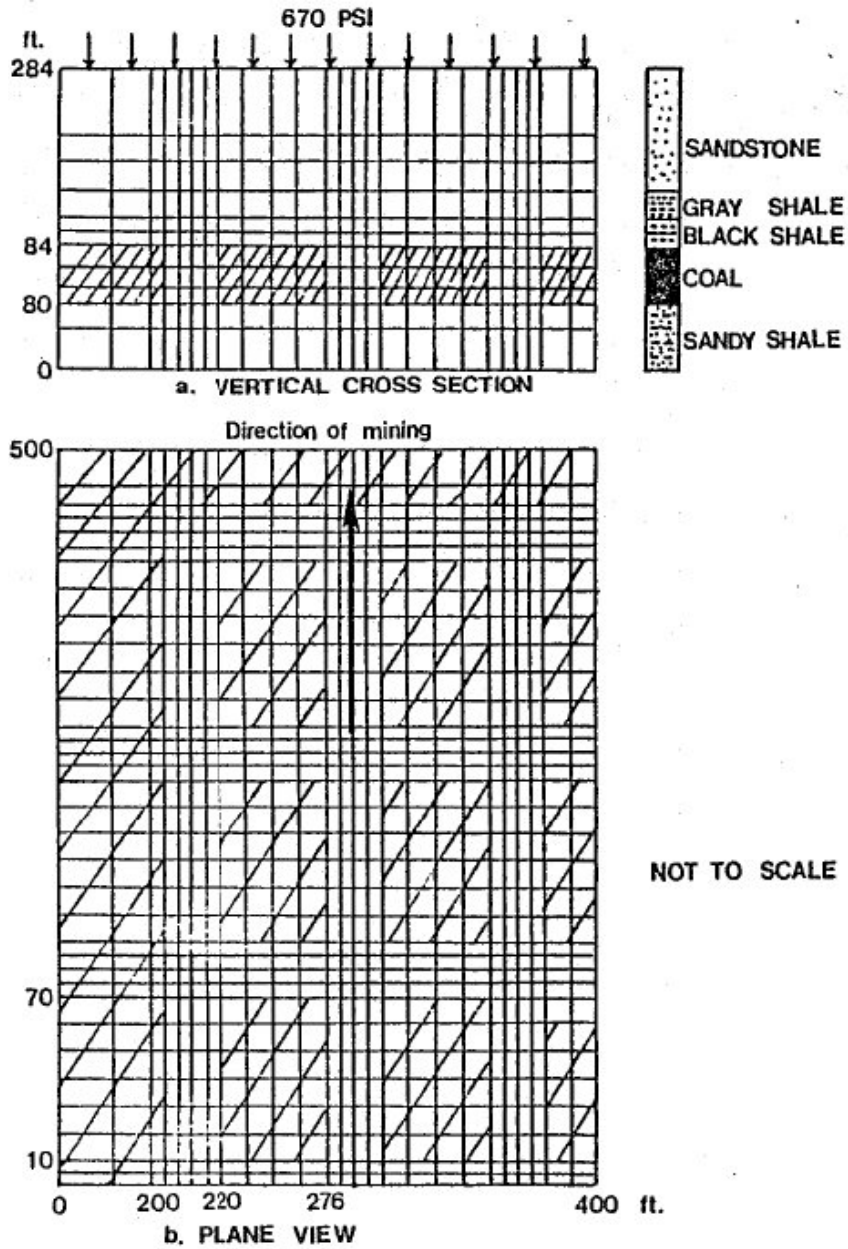


Figure 2.13 Finite element model used by Su and Peng, 1987 for their analysis.

Although this study was comprehensive, it suffered from drawbacks that are mentioned below:

- Elastic material was explicitly used in the Finite Element Analysis and the failure was predicted Ducker-Prager rock failure criteria. Elastic analysis prevented prediction of progressive failure in the roof.
- Strata separation and interface sliding which significantly influence roof stability were excluded in the analysis

Subsequently, other studies like Meyer et al., 1999, and Morsy and Peng, 2005 used elastic perfectly plastic constitutive behavior for immediate roof. Meyer et al., 1999 extended the work of Gale and Blackwood, 1987 using the three-dimensional finite difference software, FLAC<sup>3D</sup>. They used roadway convergence data to verify the modeling results, which were obtained from the British coal mines (Kent et al., 1999). Morsy and Peng, 2005 investigated the effect of the horizontal stress angle on the stability of the face using (ABAQUS), a commercial finite element software package. They used three-dimensional failure criterion (Drucker-Prager) to evaluate the stability of the gate-road system. Figure 2.14 shows the variation of the predicted yielded zones (black cell) in the immediate roof of the headgate for different entry orientations ( $\theta = 0^\circ, 30^\circ, 60^\circ$  and  $90^\circ$ ). Unfortunately, the plastic modeling was not comprehensive enough to gain a more detailed understanding of cutter failures, particularly in the case of weak immediate roof.

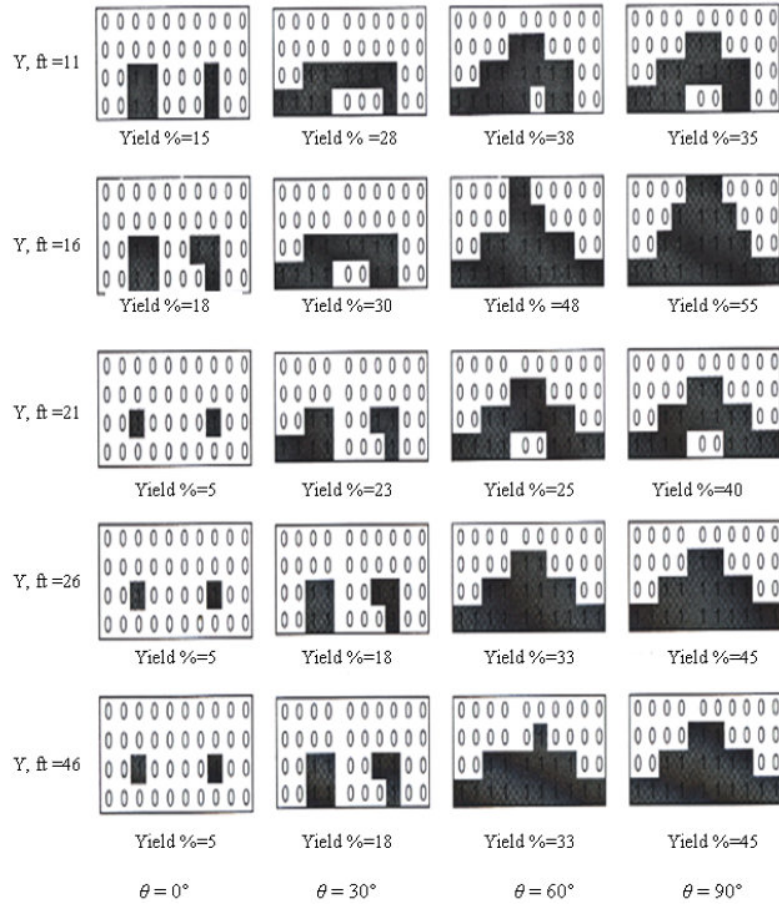


Figure 2.14 Yielded zones in the immediate roof of the development entry in a longwall gateroad (Morsy and Peng, 2005)

Gadde and Peng, 2005; Ray, 2009 modeled cutter roof failure using three-dimensional finite difference numerical model with strain softening constitutive behavior to simulate load-shedding mechanism observed at cutter locations. They compared different material behavior models and showed that strain-softening material model accurately predicts failure progression in immediate roof during cutter failure (Figure 2.15). Additionally, they showed the considerable influence of cutting sequence and entry-crosscut development sequence on cutter failure patterns.



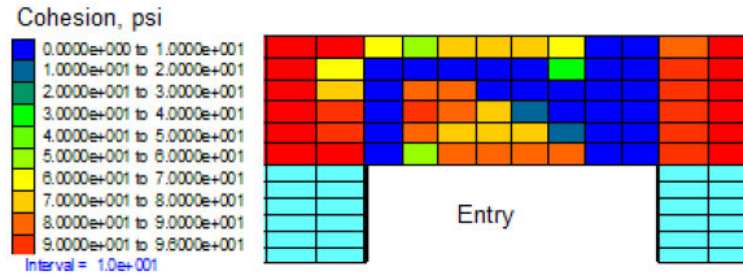


Figure 2.15 Strain-softening model showing cutter roof failure in the immediate roof in terms of cohesion distribution (Ray, 2009).

Although, strain-softening behavior was able to capture realistic cutter patterns, the model's accuracy was significantly affected by strain-softening approach. This approach governs the variation of the rock mass strength parameters (cohesion, friction angle and tensile strength) with plastic shear strain. It is extremely difficult to determine rock mass softening properties especially for coal measure rocks and no recommendations from the scientific community have been adopted for consistent use. The strain softening model also has high mesh and boundary condition sensitivity due to strain localization (Maleki et al., 2009; Perras and Diederichs, 2009; Lorig and Varona, 2013). Additionally, the study assumed laminated shale roof to be isotropic and suggested that laminations would only arrest the cutter roof propagation. However, this differs from field observations where highly laminated shale is more susceptible to cutter failure (Esterhuizen and Bajpayee, 2012; Molinda, 2003). This model completely ignores the layer interaction and subsequent delamination process involved in failure of the laminated roof as observed in the field (section 2.2.1)

Current studies (Sainsbury and Sainsbury, 2017; Esterhuizen et al., 2012; Esterhuizen et al., 2013) are simulating shale roof as transversely isotropic material by using strain-softening ubiquitous joint constitutive model in finite difference code FLAC3D. The material model simulates the rock matrix strength and the effect of weak plane (laminar or bedding plane) using individual plastic yielding approach. In this model, a ubiquitous weak plane exists within every element and the failure is checked for both rock matrix and weak plane. Additionally, rock matrix was simulated as anisotropic softening material with lower strength of roof when loaded parallel

to the bedding planes (Esterhuizen et al., 2012; Esterhuizen et al., 2013). In this approach, the numerical models capture both rock matrix failure and bedding-related slip in the sedimentary coal measure rocks. The analysis included a strength reduction method (SRM) that calculates the stability of the mine entry by gradually reducing the rock mass strength until complete failure. The collapse is indicated by inability of the model to reach a state of equilibrium. The method allows the model to simulate roof failure (Esterhuizen et al., 2012) as shown in Figure 2.16.

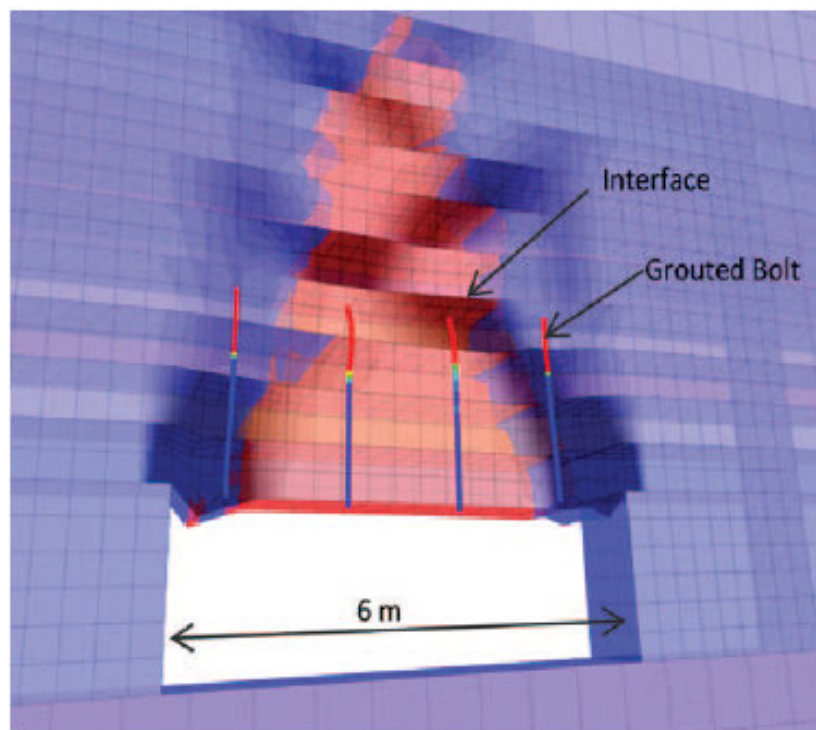


Figure 2.16 Example of a numerical model of an entry supported by 1.8-m grouted bolts in weak bedded shale rocks at the point of collapse. Dark grey shading indicates rock damage (plastic strain). The red shaded roof is collapsing (Esterhuizen et al., 2012).

Although this approach gave a realistic inter-bed slip and failure of coal measure rocks. It ignores beam rigidity of the individual layers or laminas within strongly bedded rocks (Sainsbury and Sainsbury, 2017; Adhikary, 2010). The beam bending of the individual layer significantly affects failure of the rock mass when bedding slip is large, and the direction of loading is not aligned with direction of layering (Adhikary, 2010). This characteristic is essential for laminated

or stack rock where layer interaction along with location and degree of delamination decides its dominant failure mode as discussed in previous section 2.2.1.5. Additionally, the model also includes demerits of softening material model, which includes high mesh sensitivity and no softening rule for coal measure rocks. For instance, Esterhuizen et al., 2013 assumed linear rate of 90% cohesion loss after 0.5% of strain at laboratory scale. The rate was not adjusted for field conditions and maintained same for all mesh sizes.

## **2.4.2 Studies related to explicit anisotropy in laminated rock**

Various studies have used explicit beds to understand anisotropic behavior of laminated or stack rocks. Initial studies from 1950 to 1980 used analytical models to understand the deformation and stress distribution in the roof after excavation of an entry (Evans, 1941; Panek, 1956; Stephansson, 1971; Sheorey, 1976; Sterling, 1980). These studies mostly relied on plane strain condition and mathematical solutions based on theory of elasticity.

With increase in computational efficiency, numerical models were frequently used to simulate the bedded or layered rock at both laboratory and field scales (Ahola et al., 1991; Zhang et al., 2004; Peng, 2005; Shabanimashcool and Li, 2015; He and Afolagboye, 2018). This section provides a review of research on influence of layer interaction on failure of laminated or stack rock

### **2.4.2.1 Analytical methods**

Panek, 1962 developed analytical solutions for multi-layered beam based on classical Euler-Bernoulli beam theory. The roof was clamped at both ends and subjected to uniform distributed load. The roof consists of stack of layer that would interact with one another through frictional sliding. The solutions for stress distribution and roof deflection was determined for both multi-layered bolted and unbolted beam based on theory of elasticity. The study provided a detailed insight on influence of the layer interaction on stress distribution and bending profile of laminated roof. Figure 2.17 showed deflection profile of multi-layered bolted beam.

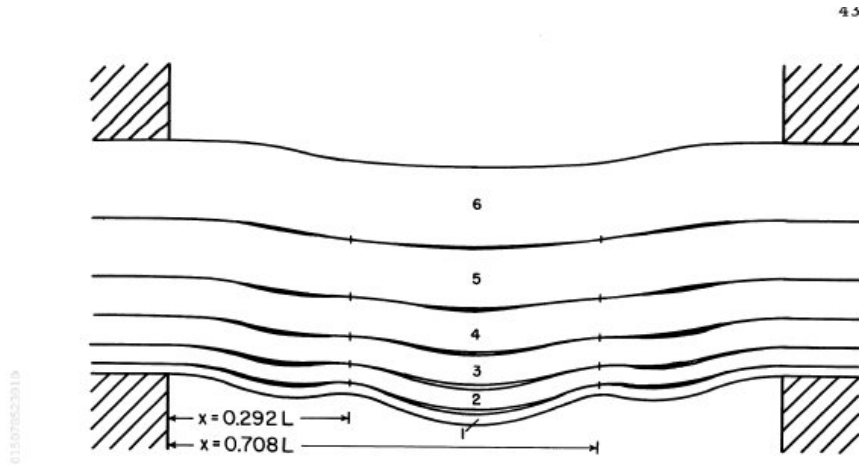


Figure 2.17 Deflection profile multi-layered two point (at  $x = 0.292L$ ,  $0.708L$ ) bolted beam (Panek, 1962).

Although this study was helpful in estimating the initial indication of failure mode and condition for stable configuration in laminated roof rocks, it excluded excavation induced stress and inter-bed cohesion. Additionally, the analytical model ignored curvature in roof beds caused by gravity loading and elastic rebound of the rock mass into the excavation resulting in underestimating buckling limits (Esterhuizen and Bajpayee, 2012). Similar limitations exist in other studies that used classical beam analytical solutions (Frith, 2000; Colwell (2004, 2012)) to analyze laminated rock roof. Therefore, classic roof beam equations are only useful in understanding the overall response of bedded roof rocks, however, their practical application in excavation design is limited and thus should be used with caution (Frith, 2000; Galvin, 2017).

Various studies (Beer and Meek 1982, Brady and Brown, 2004, Diederichs and Kaiser, 1999) also used “Voussoir beam” analogy by assuming roof to be dominated by horizontal laminations along with uniformly spaced vertical joints bending under its own weight. As roof bends, vertical joints open up at abutment resulting in roof to separate into thin beams. With further bending of thin beam, it’s joint at mid-span opens up that lead to formation of compression arch (Figure 2.18). Evan (1941) established the initial analytical solution of this concept by treating the beam as a statically indeterminate beam. Later, based on physical model and laboratory testing, solution was reformulated by various researchers (Sterling, 1980; Beer and Meek 1982; Stimpson and Ahmed,

1992) to provide failure modes such as buckling, crushing at the mid-span and abutments or slippage at the abutments. This approach was found to be better than the classical beam in predicting stability of stratified roof in large excavation (Diederichs and Kaiser, 1999). Additionally, number of studies used numerical models to simulate Voussoir beams that provided detailed insight into bending profile and stress distribution in cracked beams.

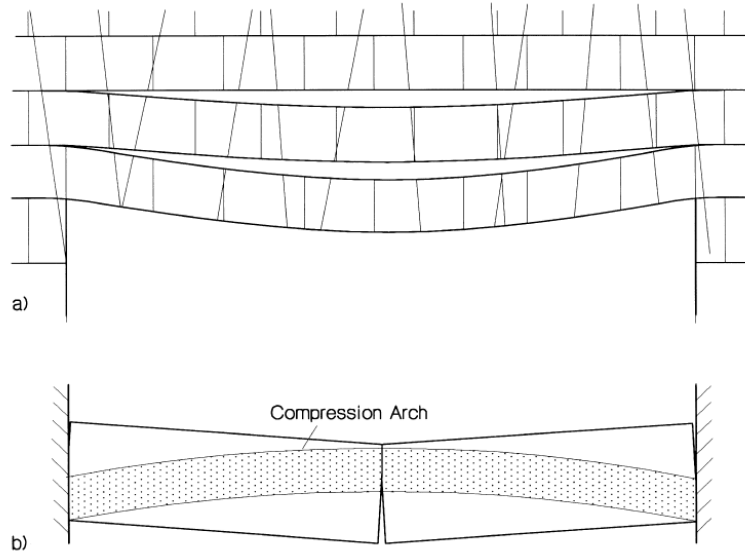


Figure 2.18 (a) Jointed rock beams; (b) Voussoir beam analogue (Diederichs and Kaiser, 1999).

Voussoir approach was rarely used for modeling excavations in coal measures rocks, especially for entry over laminated or stack roof rock (Esterhuizen and Bajpayee, 2012). The Voussoir beam, approach is based on bending of jointed roof especially when near vertical joints are present in the immediate roof. However, vertical joints are not often found in laminated shale roof. Additionally, most studies related to Voussoir beam do not consider end loading, which is key to laminated roof instability.

The analytical model that has most practical application in mining is elastic beam on elastic abutment model. Stephansson, 1971 derived analytical solutions for deflection and bending

stresses for seven different configurations of single and multi-layered roof in horizontally bedded rock (figure 2.19a). The model included excavation stress with realistic boundary conditions, which was not provided with other beam models. Jeremic, 1981 also used similar models to analyze the effect of the orientation of high horizontal stress ( $\theta$ ) on the opening stability. The model showed the effect of maximum horizontal stress direction on cutter locations on laminated shale roof to massive roof like sandstone at some Canadian mines. From this analysis, roadways perpendicular to the lateral stress were reported to experience maximum instability and about 80% of roof falls were recorded in roadways in this condition. Two types of roof failures were postulated to take place when  $\theta = 90^\circ$  as shown in Figure 2.20. For roadways parallel to the maximum lateral tectonic stress, it was assumed that lateral extension would develop along its width.

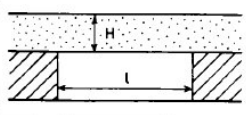
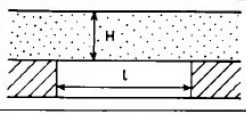
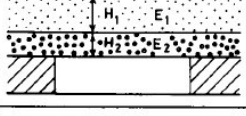
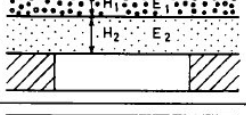
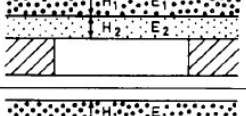
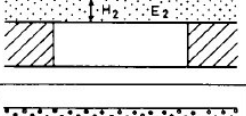
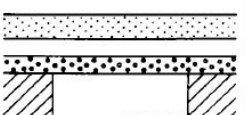
SINGLE-LAYER ROOF	I		$H < \frac{l}{5}$
	II		$\frac{l}{2} > H > \frac{l}{5}$ Including shear stress in the layer
DOUBLE-LAYER ROOF	III		$E_1 I_1 > E_2 I_2$ Free slip along the contacts Detaching
	IV		$E_1 I_1 < E_2 I_2$ Free slip along the contacts No detaching
	V		$E_1 < E_2$ Welded contact
	VI		$E_1 > E_2$ Welded contact
MULTI-LAYER ROOF	VII		Welded contacts

Figure 2.19 Type of roof configuration used in Beam on elastic abutment model  
(Stephansson, 1971)

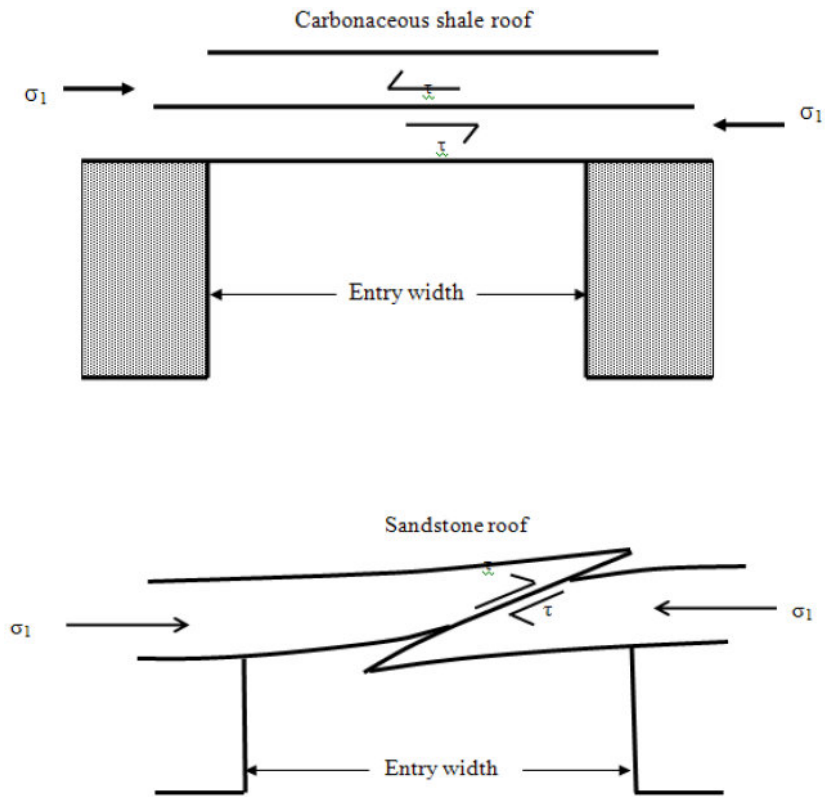


Figure 2.20 Roof failure by slip along bedding planes (top) and low angle shearing (below) for  $\theta = 90^\circ$  (Jeremic, 1981).

Although bending profile and stress distribution was similar to field conditions, the beam model provided limited information on failure progression in the roof. Additionally, the beam model cannot be used to simulate high *in-situ* stresses as roof is assumed to bend under its own weight or uniform load on its top. In mines, the uniform vertical load profile on immediate roof would only be valid when pressure arch is within the roof, which represent low *in-situ* stresses. These limitations are valid for all type of analytical beam models.

#### 2.4.2.2 Laboratory experiments

Various studies (Niandou et al., 1997; Cho et al, 2012; Ambrose, 2014; He and Afolagboye, 2018) have conducted different laboratory tests to understand the anisotropic behavior of shale due



to laminations. These studies included triaxial and Brazilian tests at different lamination orientation with respect to loading direction to study influence of weak plane (laminar plane) on anisotropic response of laminated shale. The anisotropy was observed in terms of failure mode and peak strength (Niandou et al., 1997; Ambrose, 2014). Although these studies identify the lamination as a source of anisotropy, the mechanism is not clear behind layer interaction during failure propagation within laminated layers. Limited studies (Arora and Mishra, 2015; He and Afolagboye, 2018) have attempted to study the inter-laminar interaction.

### **2.4.2.3 Numerical methods**

Numerical models have been successful in analyzing the effect of lamination on behavior of shale rock especially at laboratory scale. Various studies have used discrete element based numerical code such as PFC (Park and Min, 2015; Duan and Kwok, 2015; Chong et al., 2017; He and Afolagboye, 2018) to analyze the influence of layer orientation (with respect to loading direction) on progressive failure of various laminated rocks in uniaxial compression and Brazilian tests. These models represent inherently anisotropic rocks by including weak planes within rock matrix.

The rock matrix is simulated using bonded particle model (BPM) that assume material to be assembly of circular or sphere shaped particles that are bonded together. These bonds break and then particles are detached completely resulting in creation of fractures within the rock matrix. The laminar plane or bonds between laminas are simulated with smooth-joint model that introduce lower bond strength between specified particles as compared to particles with rock matrix. This method represents both the stiffness and strength anisotropy of laminated rock. The method simulates inter-laminar slip and bending stiffness of individual layer. This approach can provide detail insight into layer-interaction and its influence on failure propagate in laminated rock. For instance, He and Afolagboye, 2018 simulated the Brazilian tests at lamination orientation of shale specimen in PFC2D. The lamination was modeled with 1.0 mm thickness in a 50 mm diameter disc to understand the effects of the weak lamination planes and interlayer bonding force on the failure strength and fracture patterns. The results showed that the fracture pattern was highly dependent on layer orientation angle. The failure through rock matrix at orientation angle of  $0^\circ$  is replaced by failure along laminar planes at  $90^\circ$  orientation angle (Figure 2.21). Additionally,

anisotropic of behavior of the laminated shale is highly dependent on inter-layer bonding strength (laminar plane strength), which includes decrease in rock anisotropy with higher bonding strength (Figure 2.21). Similar observation was reported by other researchers (Park and Min 2015; Duan and Kwok, 2015). All these studies indicated that both shear and tensile strength of the weak planes are significantly higher than joints or fractures based on laboratory scale numerical model. For instance, tensile strength of as 0.9-3 MPa and shear strength of 3-10 MPa was used to represent laminar plane properties (Park and Min, 2015; Chong et al., 2017; He and Afolagboye, 2018) in a lab scale numerical model.

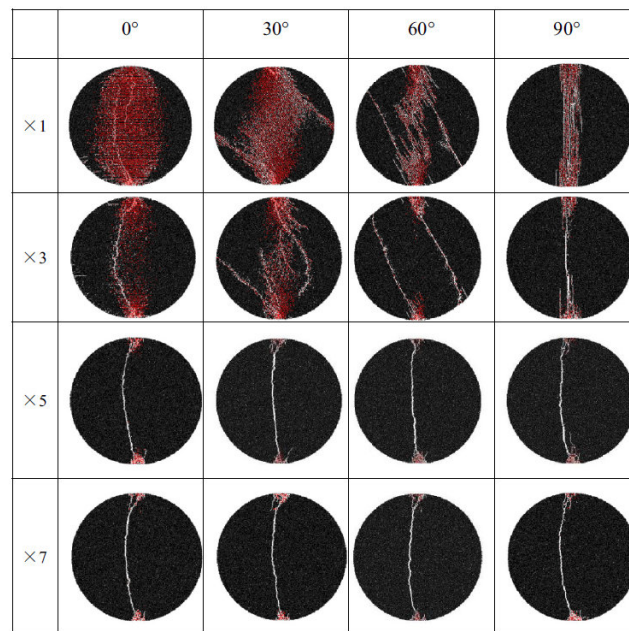


Figure 2.21 Micro-crack distributions of the simulation with different layer orientation and for different inter-layer bonding strength (He and Afolagboye, 2018).

This approach has been successful in accurately simulating the mechanical response of laminated shale because of following reasons:

- The ease of availability of laboratory scale data for calibration and validation the numerical model.

- Lab scale numerical simulation facilitate model to be more detailed and realistic in terms of actual lamination number and its thickness in a shale specimen.

When mine-scale models are simulated, rockmass parameters estimated are on 1-m to 10-m scale. It is difficult to simulate entire lamination network, as their thickness is around 1-10mm. Therefore, researchers have used numerical models with only a representative number of lamination that would sufficiently replicate the anisotropic behavior of laminated shale.

Chen, 1999 conducted a finite element analysis on the influence of bedding or lamination and high horizontal stress on shale roof over gate road entry. Interface elements were used to simulate roof layers slip and separations under frictional sliding. The analysis showed that sliding along the interface allowed layer separation resulting in higher displacement and stress concentration as compared to the roof with no interface elements. Additionally, layer separation changes stress distribution resulting in higher shear stress concentration at entry corner and tensile stress concentration at mid-span of lowest layer. Zhang et al., 2004 showed higher bending of laminated roof caused by higher horizontal stress concentration and release of vertical confinement allowing roof to undergo delamination (Figure 2.22).

These studies although involved detailed analysis of layer interaction in laminated roof, still have following drawbacks:

- Although it is seen that laminar plane have high cohesion and tension (Park and Min, 2015; He and Afolagboye, 2018) as compared to joints, these studies ignore this aspect and only simulated frictional sliding of the interface.
- The shale roof was assumed elastic and thus failure initiation was estimated while ignoring influence of lamination on failure propagation.

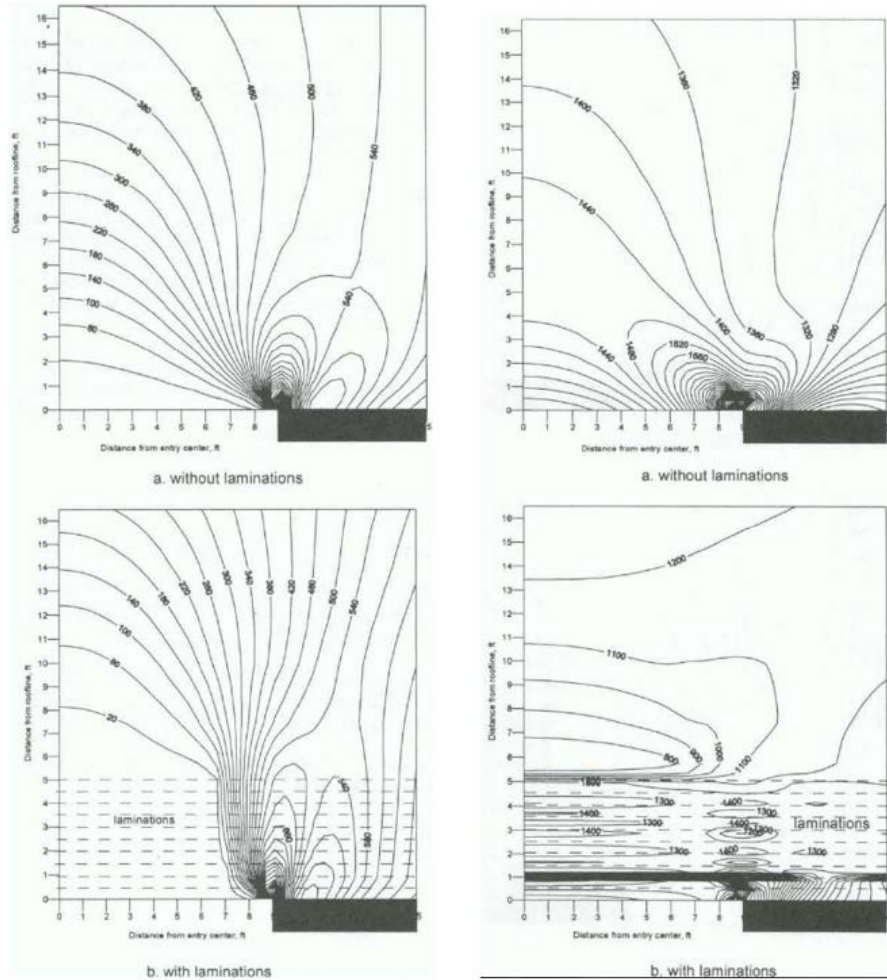


Figure 2.22 (a) Vertical Stress Distribution over the Entry; (b) Horizontal Stress Distribution over the Entry (Zhang et al., 2004).

Recently studies have considered higher interface cohesion and simulated the effect of lamination on failure propagation in shale roof. For instance, Esterhuizen and Bajpayee, 2012 used detailed numerical models to obtain a better understanding of the failure mechanisms observed in layered rocks. The models were set up to simulate multiple beds under strain-softening behavior in the roof of a 6-m-wide entry. Various loading scenarios were used to identify the mechanisms behind failure propagation into the laminated roof. The results showed that location of failure initiation and its development is highly dependent on interface (laminar plane) stiffness and strength. For low strength or low stiffness interface, the failure occurs at the excavation corners, progressing vertically (Figure 2.23). For high strength and stiffness interface, failure occurs at the

center of the roof span (Figure 2.23). Additionally, failure development was found to be independent of lamination thickness (Figure 2.24a-b). This was due to the high excavation stress that reduced the effects of layer stiffness at failure.

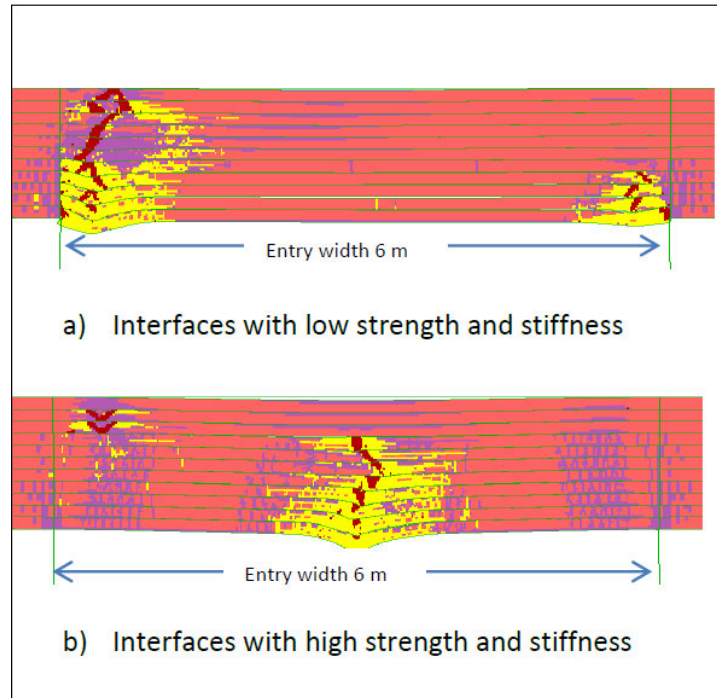


Figure 2.23 Numerical model results showing the effect of interface properties on failure in laminated roof rocks (Esterhuizen and Bajpayee, 2012).

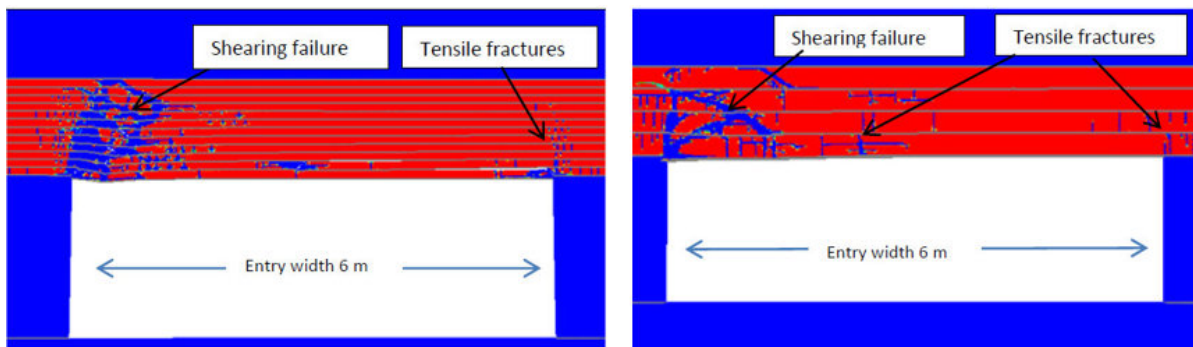


Figure 2.24 Modeled rock failure in a shale roof bed with showing inclined shear surfaces and near vertical tensile fractures (a) 10-cm laminations; (b) 30-cm laminations (Esterhuizen and Bajpayee, 2012).

This study involved detailed analysis of layer interaction and its influence of failure propagation in laminated roof, however some of the shortcomings are as follows:

- The model includes shortcomings of softening material model such as high mesh sensitivity and no accurate methodology for calibrating for coal measures rocks.
- In strain-softening model failure, progression is highly dependent on the stress path. The study increased horizontal stress in stages of 5.0 MPa, which may differ from field, conditions where induced stresses developed immediate roof after entry is created.
- Although influence of the interface parameters on mode of failure in the laminated roof was studied, clear mechanism behind difference in roof failure was not clearly reported.
- The study assumed interface properties similar to infilled joints with zero tensile strength, which may not be the case for laminar plane as shown by Park and Min, 2015; He and Afolagboye, 2018.
- Mechanism behind failure initiation at the upper surface of the bed (Figure 2.24b) was not clearly explained.
- Influence of layer stiffness was not studied in detail as no influence of layer thickness on failure profile was suggested only the basis of two case of lamination thickness.

## **2.5 Summary**

On careful review of the past research on failure of laminated or stack rock roof, the conclusions are:

- 1) Eastern United States coalfields experience horizontal stress, which is generally higher than the vertical stress. This relatively high horizontal stress coupled with a laminated roof pose safety hazards to miners.
- 2) From field observation it is clear that failure modes in the laminated roof are dependent on layer interaction such as location and degree of delamination determine whether the failure is dome-shaped, shear of stiff beds or cutter roof.

- 3) Most of studies related to field scale numerical simulation have assume shale roof to be “equivalent isotropic” and completely ignored layer-interaction due to lamination rock.
- 4) Studies involving the laboratory scale simulation of laminated rock suggested laminar plane have significantly higher shear and tensile strength as compared to infilled joints.
- 5) However, majority of the studies that simulated layer-interaction on field scale have assumed laminar plane similar to joint or fracture, i.e., very low cohesion and tensile strength.
- 6) Influence of lamination parameters such as its stiffness and strength on failure progression have not been investigated in detail.
- 7) Mechanism behind failure progression in a laminated roof under high horizontal stress is not clearly understood.

### 3. ANISOTROPIC MINE MODEL

#### 3.1 Numerical simulation of laminated shale

As mentioned in chapter 2, the failure mechanism in a bedded or laminated rock is controlled by layer or inter-laminar interaction, which also induces anisotropy in these rocks. Therefore, any numerical model should include explicit laminations to capture the realistic behavior of anisotropic shale rock. For the better understanding of its failure mechanism, the model should include the whole lamination network, which can be done by using discrete elements codes like PFC (Itasca, 2012). However, this simulation will be computationally expensive, especially for field scale problem. The model will require a detailed geological mapping and extensive borehole data and absence of the data will include the high degree of uncertainty (Fortsakis et al., 2012).

Alternatively, only a limited number of laminations can be incorporated that are sufficient to include the underlying mechanism (Perras and Diederichs, 2009). In the current study, an anisotropic mine model was used to simulate shale rock as the isotropic rock along with (representing the matrix material within the laminates) along with discontinuities (representing the weak plane between laminates). A study was conducted in section 3.2.6 to understand the influence of laminations thickness on the behavior of shale roof. The study also determined when lamination thickness develops into an important factor in the stability of the shale roof.

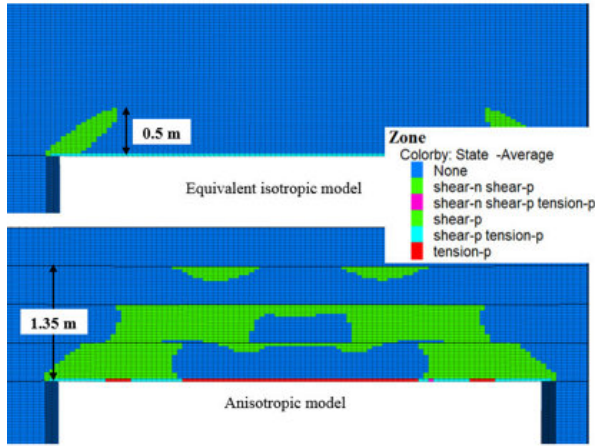
Before quantifying the number of discontinuities needed to represent the anisotropic behavior of laminated shale, it is imperative to have a basic understanding of the difference in behavior of shale rock in the anisotropic model and equivalent isotropic model. Very few studies such as Perras and Diederichs, 2007; Perras and Diederichs, 2009a-c have included this behavior in their analysis. However, most of them are related to hard rock excavations. The two models with a series of lamination thicknesses were compared based on indicators of model performance, which included vertical roof deflection, failure profile.

The anisotropic model simulated anisotropic shale rock as the rock matrix with the laminar plane, while equivalent isotropic model reduced rock modulus to account for laminations. The models represent a coal mine entry (6m wide by 2m high) with laminated shale roof under the

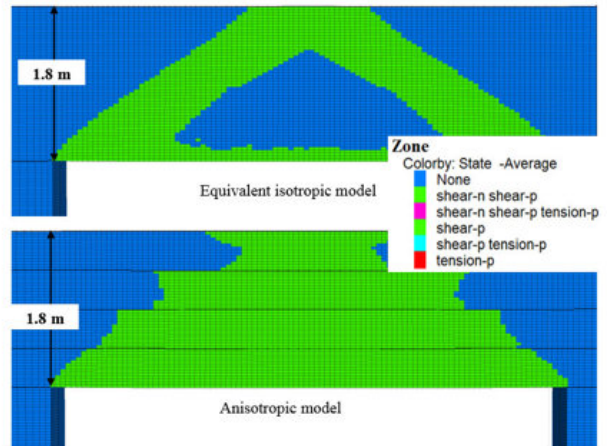


350m depth of cover at the K ratio of 2, 2.5 and 3. More detailed model setup and procedure are discussed in Section 3.2.3.

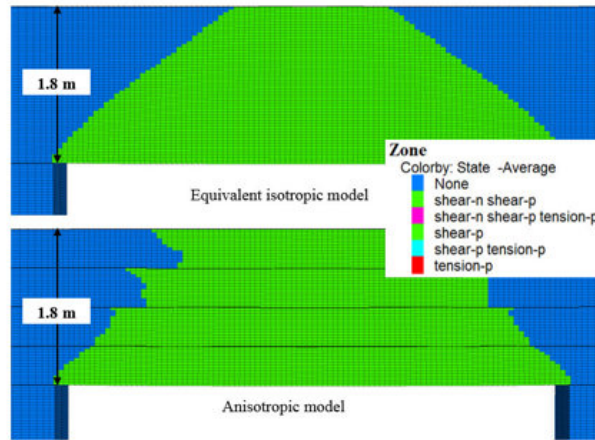
The failure profile in shale roof with lamination of 450 mm of anisotropic and equivalent isotropic model is compared (Figure 3.1a-c) for K ratio (horizontal to vertical stress ratio) of 2, 2.5 and 3. The failure extent was larger in the anisotropic model as compared to the equivalent isotropic model for all K ratios (Figure 3.1a-c). In case of K=2, failure propagated to 1.34 m in the anisotropic model as compared to 0.528 m in the equivalent isotropic model (Figure 3.1a). As K increased to 2.5, failure propagated to the entire thickness of the immediate roof in both models (Figure 3.1b). However, failure propagation is different in the anisotropic model from the isotropic model as the extent of failure around center span is higher in the former model. In the case of K=3, the entire roof has failed in both anisotropic and isotropic model due to high horizontal stress ( $\sigma_h=23.55$  MPa). In this case, although failure extent is same, there is a significant difference in roof deflection (Figure 3.2c), which can be attributed to decrease in overall roof bending stiffness caused by beam formation in the anisotropic model. Figure 3.2a-c shows roof deflection for series of lamination thickness in anisotropic and equivalent isotropic model for K= 2, 2.5 and 3. The difference in roof deflection between two models increases as layer thickness decreases for K= 2, 2.5. As individual layer thickness decreases, overall roof bending increases causing higher bending stress and consequently larger extent of failure. However, for K= 3, as discussed above, the decrease in lamination thickness only decreases the elastic stiffness of the shale roof. Therefore, roof deflection, in this case, would be governed by lamination stiffness and their interaction along the interface, which often led to complex bending of shale roof at low thickness. It could result in an abrupt change in roof deflection with lamination thickness as seen in Figure 3.2c (below 180 mm lamination thickness).



a) -15.7 MPa (K=2) horizontal stress



b) -19.625 MPa (K=2.5) horizontal



c) -23.55 MPa (K=3) horizontal stress

Figure 3.1 (a-c) Plastic state in immediate roof with lamination thickness of 450 mm in two models at different horizontal stress.

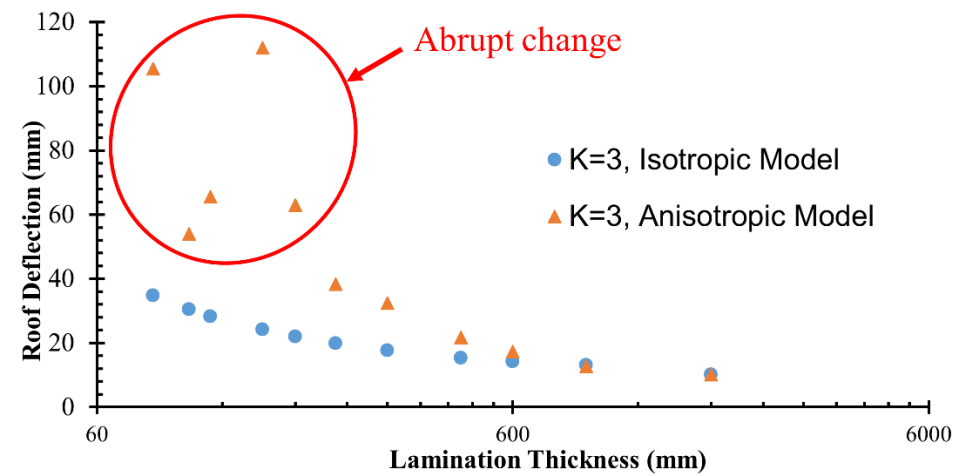
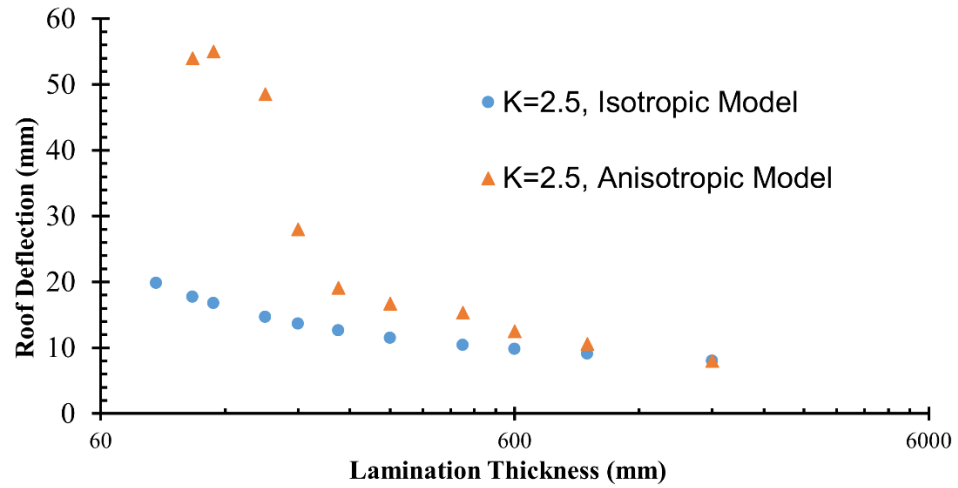
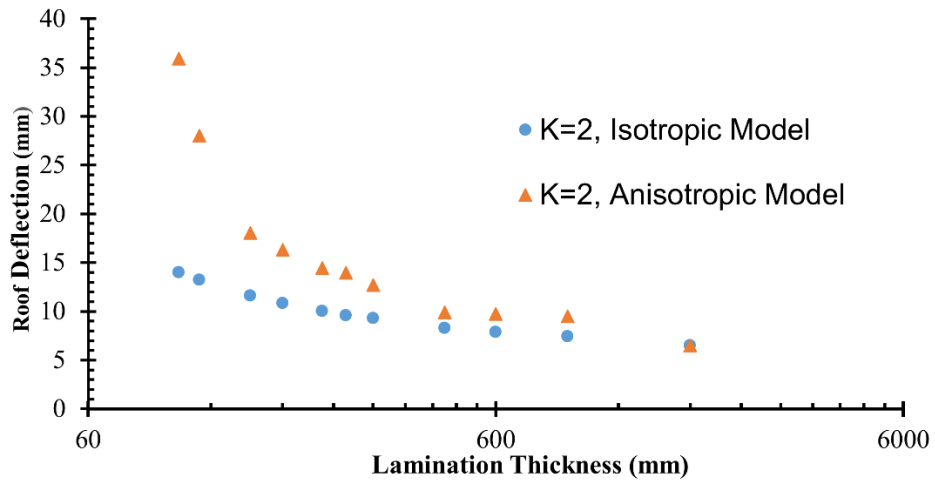


Figure 3.2 (a-c) Comparison of maximum roof deflections for anisotropic model and equivalent isotropic models of mine entry at ( $k=3, 2.5, 2$ ;  $\sigma_h = 15.7, 19.635, 23.55$  MPa).

### **3.2. Numerical Modeling Procedures**

Two popular geotechnical codes UDEC and FLAC3D were used in this research. Both codes are based on explicit solution techniques, which allow them to simulate non-linear problems accurately. However, they differ in treating the rock-mass as continuum and discontinuum material. The sections that follow briefly describe both the methods.

#### **3.2.1. The Distinct Element Method**

In Distinct Element Method, the rock mass is treated as a series of blocks bonded together with joints. A block represents a finite area of intact rock in a similar manner to finite difference codes. The joints between blocks represent pre-existing discontinuities. The constitutive criteria for the joints and intact rock are specified separately. The blocks forming the model are free to move and rotate, and completely detach from the rock mass body when failure occurs. The governing laws of motion are based on Newtonian mechanics and when one block contacts its neighbor, it creates a chain reaction of movements throughout the model. The solution is based on contact and impact between multiple bodies (Pande et al., 1990) and time steps, are used to cycle through to equilibrium.

UDEC, (a DEM based program), was used to represent the laminations as discrete elements. The rock matrix within the laminates were represented by the deformable blocks which are separated by discontinuities modeled using joint elements, which can be defined as contact point with friction and cohesion. These discontinuities act as weak planes along which layers or beams of roof rock interact. This also allowed for flexural bending of the laminations and plastic yielding of both the discontinuities and the rock beams.

The primary use of the UDEC software in current research was to simulate elastic beam models. These beam models were used to understand the influence of high horizontal stress and lamination parameters on bending profile and stress distribution within the shale roof.

### 3.2.2. The Finite Difference Method

The finite difference method uses partial differential equation to solve any mathematical problem with approximate solutions. The problem domain is broken into small zones, called elements, which have nodes at the intersection of zone edges. The nodes connect each element together to form a continuum and the nodes are the central location where data is stored and updated as the stresses or forces are applied to the problem. The assembly of elements is called a mesh. As the mesh density increases, a better approximation of the mechanical equations across the problem is achieved. However, as the mesh density increases, the calculation time increases and a balance between the results and the processing time must be optimized.

For the present study, an explicit finite-difference based three-dimensional numerical modeling code; FLAC3D 5.0 (Itasca, 2012) was used to simulate a horizontally laminated shale roof over a mine entry. FLAC3D is based on an explicit solution technique, in which the evolution of a system is computed by means of a time-stepping numerical integration of Newton's equations of motion for grid points or blocks within the model. Nonlinear effects arising from material yield in shear or tension can be treated using Mohr-Coulomb and other elasto-plastic constitutive models. Interface elements can be placed between regions of a rock mass, to simulate slip and separation on a major fault or other discontinuity.

The basic solution scheme employed in FLAC<sup>3D</sup> is shown on Figure 3.3. FLAC invokes the equation of motion and constitutive relations to describe the deformation of a given problem. The estimation of velocities and displacements from forces and stresses are estimated using the dynamic equation of motion. Velocities and displacements are then used to derive strain rates from which new stresses are generated.

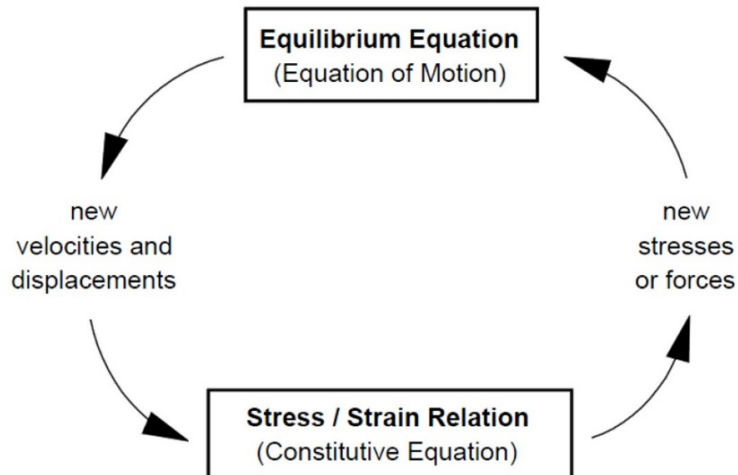


Figure 3.3 Calculation cycle of FLAC3D program (Itasca, 2012)

The grid defines the geometry of the problem. The constitutive behavior and associated material properties dictate the type of response the model will display upon disturbance (e.g., deformational response due to excavation). FLAC3D can accommodate various types of constitutive behavior of the material. The boundary and initial conditions define the *in-situ* state (i.e., the condition before a change or disturbance in the problem state is introduced).

The primary use of the FLAC3D in current research was to simulate mine models and plastic beam models of a laminated roof.

### 3.2.3. Rock Failure criteria

Among the many failure criteria, the Mohr-Coulomb and Hoek-Brown rock are most popular for coal measures rocks. Both of these criteria assume rock as an isotropic material. Gadde et al. (2007) has compared these two criteria and found Hoek-Brown criteria to perform better than Mohr-coulomb criteria in the tensile zone. However, Mohr-Coulomb criterion with tensile cut-off, has been used in this research as the Hoek-brown is an empirically based criterion requiring extensive calibration

The Mohr-Coulomb failure criteria is a linear failure surface that corresponds to shear strength of material. The failure envelop for shear is represented in Equation 3.1 (Itasca 2012):

$$f^s = \sigma_1 - \sigma_3 N_\phi + 2c\sqrt{N_\phi} \quad \text{Equation 3.1}$$

Where

$$N_\phi = (1 + \sin \phi)/(1 - \sin \phi)$$

$\sigma_1$  = major principal stress

$\sigma_3$  = minor principal stress

$\phi$  = friction angle

c = cohesion

Shear yield is detected if  $f^s < 0$ . The two strength constant,  $\phi$  and c are estimated from the laboratory triaxial tests. In tensile region, FLAC3D employs a failure envelop with tension cut off as represented by

$$f_t = \sigma_3 - \sigma^t \quad \text{Equation 3.2}$$

Where,  $\sigma^t$  is tension cut off value, generally obtained from Brazilian tests. Depending on the scale of simulation, rock properties are reduced based on certain rule to represent the rock mass. The estimation of rock mass strength is discussed in detail in section 3.2.2.

Traditional plasticity in rocks is generally of two type; a) perfectly plastic, b) strain softening. Perfectly plastic means that rock mass behaves plastically without a drop in peak strength once the stress exceeds the failure envelope. Before its failure, the rock behaves elastically following the prescribed stress-strain slope defined by the modulus. After the strength is exceeded, flow rule is applied to bring back stress level on the failure envelope. In the FLAC3D and UDEC, the failure envelopes for shear and tensile failure are shown in Equation 3.1 and 3.2.

Strain softening means the rock mass strength will decrease with an increase in plastic strain after failure. After the stress exceeded failure envelope, rockmass behaves plastically with reduced strength. The strength drop can be instantaneous or gradual depending on brittleness of rock. It is generally expressed in terms of variation in the cohesion and friction of the material with the value of plastic strain. Few studies have been done to estimate the strength drop of rock mass such as Hajiabdolmajid's CWFS model for the brittle failure in hard rocks (Hajiabdolmajid et al., 2002) and Cai's system based on a residual GSI value (Cai et al., 2004).

Similarly, for coal measure rocks, Zapf, 2005 and Esterhuizen, et al., 2013 suggested a drop of 90 % in cohesion over 0.5 % of post-failure strain in laboratory scale. The rate was not calibrated with field measurements. A strength drop rate was assumed irrespective of rock type due to insufficient laboratory data for coal measures rocks. Additionally, it is difficult to estimate the residual rock mass strength values. In fact there no recommendations for its usage from the scientific community. The strain softening model along with the scaling problem also has high mesh and boundary condition sensitivity due to strain localization (Perras and Diederichs, 2009; Lorig and Varona, 2013).

The elastic-perfectly plastic method is the simplest plasticity model with no requirement to determine the residual rockmass strength values. Therefore, for this research it was adopted for both the isotropic plastic models and the anisotropic plastic models to minimize the number of variables.

### **3.2.2. Estimation of Rock Mass Strength**

The coal measures rocks most of the time comprises several discontinuities cannot be represented intact rock tested in the laboratory. The rock mass strength can be estimated through either field scale testing or back analysis of observed failures. The former option is neither practical nor economically feasible. The latter option can provide representative values for large-scale rock mass strength, but obviously cannot be used for designing the underground structures.

Majority researchers use a scaling factor, which may vary from 0.2 to 0.6 to match their parameters and simulate the known rock mass behavior. For example, Gale et al. (2004) used a strength reduction multiplying factor of 0.58 for the rock matrix to simulate the rock as ubiquitous joint type material. Approach that is more systematic was given by Gadde et al. (2007) to estimate the strength reduction factor when the UCS tests are not available for different size of the specimen. The reduction factor, RF is given by-



$$RF = \left[ \frac{T}{d} \right]^{-0.5} \text{ if } T < 48 \text{ inches}$$

Equation 3.3

$$RF = \left[ \frac{48}{d} \right]^{-0.5} \text{ if } T > 48 \text{ inches}$$

Where T is the thickness of the stratum between any two adjacent bedding planes, and d is the diameter, or the edge length of the sample tested in the laboratory for UCS. T and d should have the same units. For rock mass strength estimation the procedure described by Gadde et al., 2007 has been used.

In case of stack type rock like laminated shale, even intact specimen contains a good number of discontinuities or weak plane. As a result, failure modes of these rocks at laboratory scale differ significantly from other layered rocks. Therefore, the strength reduction factor of 0.58 should be used for rock matrix between two weak planes (Gadde et al., 2007).

### 3.2.3. Anisotropic Model

An anisotropic model was used to study the influence of lamination on behavior of shale roof and to determine when lamination thickness become an important consideration in its stability. The horizontal laminations were modeled using interface or joint elements.

By including lamination using interface elements, the mechanical behavior of shale roof is controlled by both the interface properties and the intact rock properties between them. The interface elements reduce the roof modulus in the vertical direction. The elements also allowed greater layers displacements parallel to interface resulting in higher roof deflection. In addition, stress distribution within the roof will differ significantly as compared to the equivalent isotropic roof. This behavior is vital to understand exact failure mechanism in a laminated rock mass.

In this study, the geometry of the entry was kept fixed for developing a clear understanding of the influence of lamination thickness on the immediate roof behavior. A coal mine entry with laminated shale rock as the immediate roof (based on the study by Murphy et al., 2014) was modeled in FLAC3D (Figure 3.4). The model simulated a 6m wide by 2m high coal mine entry

with 1.8 m high immediate roof. The remainder of the roof consists of main roof and overburden strata. The main roof and floor were made of strong sandstone rock. The depth of cover was 350m, i.e., 7.85 MPa vertical stress along with 15.7 MPa major horizontal stress. The model runs were also tested at major horizontal to vertical stress ratio ( $K$ ) of 1.5, 2, 2.5 and 3. The major to minor horizontal stress ratio ( $I$ ) was kept 1.3 in all cases. The model simulated plane strain condition with the width of 0.4 m in Y-direction (out of plane direction). The boundaries in X- direction were located at distance of '3L' from entry edges for a span of 'L' m to remove the influence of boundary conditions.

The stiffness of individual rock layers is influenced by element size and the number of nodes in it, especially in case of small lamination thickness (Perras and Diederichs, 2009; Esterhuizen and Bajpayee, 2012). A minimum 3-5 row of elements along the thickness (z-direction) should be used to eliminate the influence of element size (Itasca, 2012; Murphy et al., 2014). In this study, for small lamination thickness, minimum five row of elements were kept in Z-direction in each layer of shale roof. The zone size is kept same for larger lamination thickness. The zone size in X-direction near the entry is 0.06 m and was increased up to about 1.25 m at the excavation's remote locations where rock failure was not expected to occur

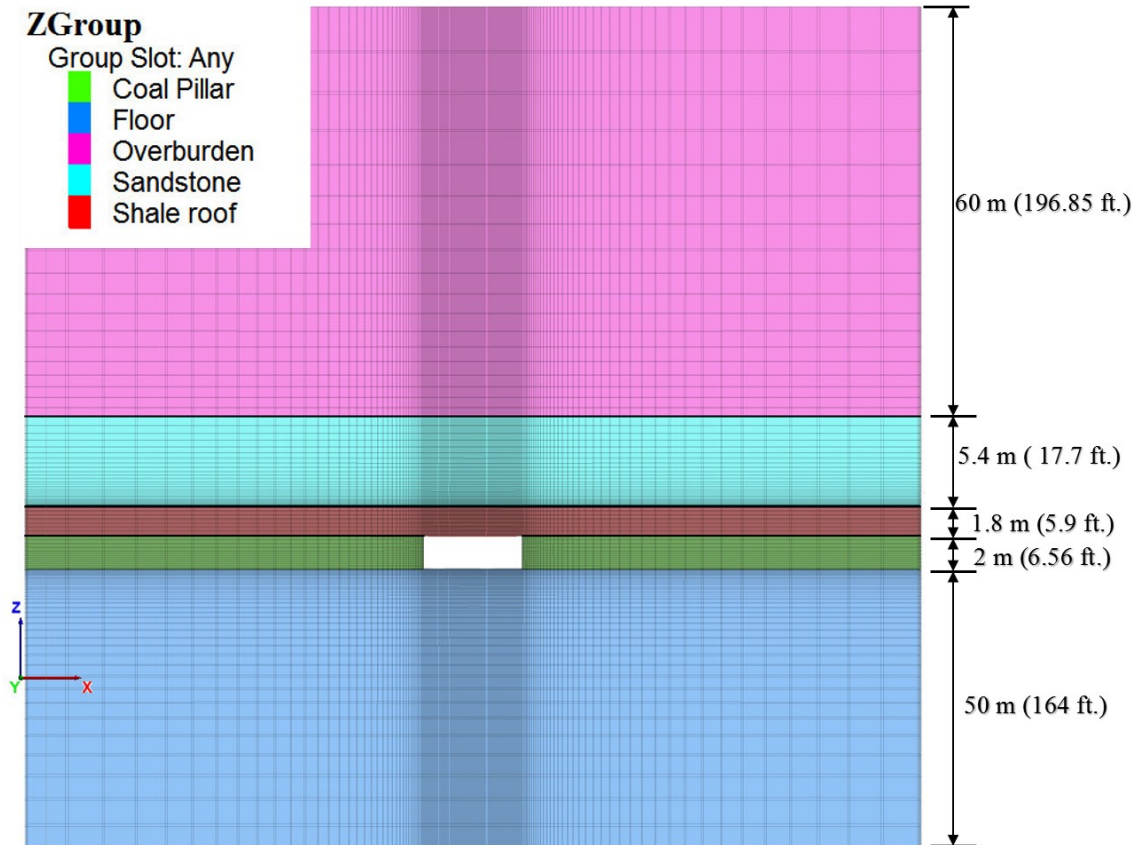


Figure 3.4 Model geometry simulated in FLAC3D of shale roof over a 6 m span mine entry.

### 3.2.4. Selected Constitutive Model

The shale roof stratum was simulated as an isotropic rock matrix (within the laminates) along with interface elements representing weak plane between two laminas. The bedding planes between different strata were also modeled using interface elements. The rock matrix within shale roof was an elastic-perfectly plastic material that fails under Mohr-Coulomb criteria. All other strata including coal seam were considered elastic. The detailed explanation of failure criteria and plastic behavior is given in section 3.2.1. The uniaxial compressive strength (UCS) of intact shale rock was assumed 30 MPa (Murphy et al., 2014). The strength of rock beams in shale roof was reduced to 17 MPa (0.58 times UCS) to represent the field scale strength of rock matrix for stack rocks like laminated shale (Gadde et al., 2005). The scaling criterion is discussed in detail in section 3.2.2. The mechanical properties of each stratum and bedding planes used in the base

model were based on the study by Murphy et al., 2014 and summarized in Table 3.1. Various input properties of the interface representing laminar plane are given in Table 3.2.

Table 3.1 Mechanical properties of each stratum and bedding planes (Murphy et al., 2014)

<b>Property</b>	<b>Shale</b>	<b>Sandstone</b>	<b>Coal</b>	<b>Overburden</b>
Elastic Modulus (GPa)	12	20	3	14
Poisson ratio	0.2	0.2	0.25	0.25
UCS (MPa)	17	-	-	-
Tensile Strength (MPa)	1.7	-	-	-
Dilation angle (deg.)	5	-	-	-
Interface normal stiffness (GPa/m)	10	10	10	10
Interface shear stiffness (GPa/m)	5	5	5	5
Interface friction (deg.)	30	30	30	30
Interface cohesion (MPa)	0.1	0.1	0.1	0.1

### 3.2.5. Lamination properties

The interface properties are not readily available for laminations or bedding planes for coal measures rocks. Most of the initial studies are related to the constitutive behavior of infilled or open joints. Barton et al., 1974 provide some estimates for peak and residual strength parameters for filled discontinuities and filling material. Bandis et al., (1983, 1980) provide stiffness parameters values through repeated load cycling test on a wide variety of fresh and weathered joints in different rock types. While there are numerous studies related to estimation and scaling of input properties for discontinuities in a jointed rock mass (Mitani et al., 2004; Lendel, 2004), very few studies involve bedding planes. Gale et al. 2004 estimated strength of intact bedding surface through the triaxial test on samples obtained from drill core oriented at 30 degrees to the bedding surfaces. The strength parameters were then reduced by half to account for field applications based on Hoek and Brown (1980) criteria. Similarly, Esterhuizen et al., 2013 suggested an empirical method to estimate bedding strength parameters from field techniques. The method involved the application of discontinuity cohesion rating (DCR) (included in the CMRR) in Barton and Choubey's (1977) method used for estimating joint strength.

Most of the above studies assumed low tensile strength, i.e., from 0-50 KPa, which may not represent the weak plane in stack rocks like laminated shale. Studies involving Brazilian test on shale rocks at different lamination orientation (Cho et al., 2012; He and Afolagboye, 2018) indicated the decrease in tensile strength by 40-50 % when laminations are parallel to the load than when lamination is perpendicular to loading direction. Based on these results, some researchers like Park and Min 2015; He and Afolagboye 2018; Chong et al., 2017 have simulated lamination in DEM based numerical software with the tensile strength of 0.9-3 MPa at laboratory scale. However, limited studies involved field scale application (Esterhuizen and Bajpayee, 2012; Perras and Diederichs, 2009).

In the current research, two different sets of lamination properties were used (Table 3.2). The first set was based on work by Esterhuizen and Bajpayee, 2012 that assumed zero tensile strength and stiffer weak plane by taking  $K_n/K_s = 2$ . The second set assumes the tensile strength of lamination to be higher than its cohesion and  $K_n/K_s = 10$  based on the study by Perras and Diederichs, 2009a-c. It is noted that Perras and Diederichs, 2009a-c considered lamination stiffness equal to rock matrix and thereby representing “intact” planes of weakness. It may not precisely represent stiffness of weak plane in field scale especially in case of stack rock. Therefore, the magnitude of  $K_n$  is kept same in both sets of properties.

Table 3.2 Lamination properties used in this research.

Researcher	Normal Stiffness (GPa/m)	Shear Stiffness (GPa/m)	Cohesion (MPa)	Tension (MPa)	Friction (degree)
Set 1: Esterhuizen and Bajpayee, 2012	10	5	0.13	0	30
Set 2: Perras and Diederichs, 2009	10	1	0.13	0.3	25

To ensure compatibility between the anisotropic models and isotropic model, the equivalent elastic modulus ( $E_{rm}$ ) for isotropic model based on equivalent continuum model was determined whose equation (Amadei, 1982) is given by:

$$\frac{1}{E_{rm}} = \frac{1}{E_{beam}} + \frac{1}{T K_n} \quad \text{Equation 3.4}$$

Where  $E_{beam}$  is beam/layer modulus;  $K_n$  is the normal stiffness of weak planes;  $T$  is lamination thickness. Then  $E_{rm}$  is harmonically average with beam modulus to ensure that at larger thicknesses, the equivalent properties were similar to the individual beam properties.

### 3.2.6. Numerical Simulation of Anisotropic Perfectly Plastic Model

To quantify the number of laminas needed to represent the anisotropic behavior of shale rock, a series of anisotropic and equivalent isotropic models were computed and compared in terms of plastic yielding. Figure 3.5a-c compares failure profile of anisotropic model of two different set of interface properties as well as the equivalent isotropic model for lamination thickness of 450 mm.

In the isotropic model, shear failure propagated upwards at a steep angle from entry corners up to 0.5 m height (Figure 3.5a). While in the anisotropic models (in both cases set 1 and set 2), failure has reached approximately 1.35 m into the roof (Figure 3.5b-c). However, failure profile differs significantly between the anisotropic models. For instance, in the anisotropic model with interface properties of set 1 (case 1), failure is mostly concentrated around mid-span with the complete failure of the first lamination (Figure 3.5b). While in the anisotropic model with interface properties of set 2 (case 2), failure is symmetric about the mid-span leaving region around the entry center intact (Figure 3.5c). A similar trend was seen when three models were compared for various lamination thickness (Figure 3.8a-c).

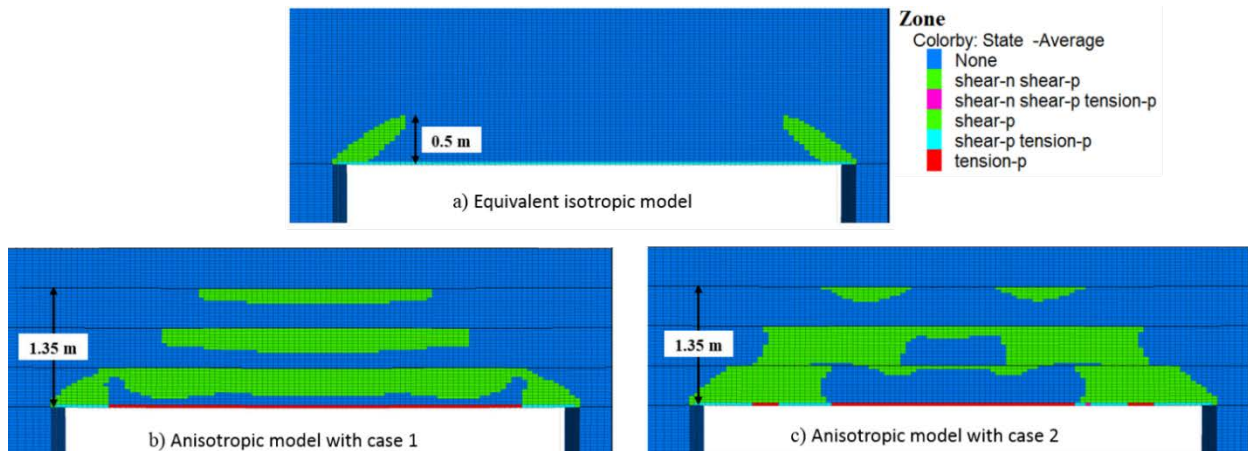


Figure 3.5 (a-c) Failure profile of immediate roof for lamination thickness of 450 mm for various models.

To understand the difference in failure mechanism between two cases of anisotropic models shown in Figure 3.5b-c, failure propagation in these models was analyzed at different time steps (Figure 3.6a-g). At 1200 time step, failure extent is nearly same in both case 1 and 2 with shear failure initiation at entry corners and tension failure at the bottom zone of the entry roof (Figure 3.6a). As time steps reached to 2100, failure propagated upwards in both cases and reached to the upper surface of the bottom layer in case 2 (Figure 3.6b). At time step 3000, failure in the bottom layer of the shale roof propagated downward from upper surface in both cases (Figure 3.6c). The downward propagation can be attributed to the interface, which acts as a weak plane preventing failure to propagate into the second layer. Therefore, with further bending, failure propagates downward from the upper surface. In addition, failure has also initiated at the upper surface of the second layer in both cases. This mechanism is entirely different from the failure propagation that occurs in an isotropic model where roof acts as the massive rock without any weak plane as seen in Figure 3.6a.

During subsequent time steps, roof bends further causing failure to propagate towards the lower surface of each layer in both cases but with different rate. For instance, at 3900 time step, failure profile is same in both cases (Figure 3.6d), however, its extent is higher in case 2 due to a less stiff interface that allows a larger amount of roof bending. At this point, delamination occurred around mid-span in case 1 (location highlighted by a red circle) due to the low tensile strength of the interface thereby allowing nearby layer (first layer) to form an individual beam. It resulted in failure propagation toward the mid-span in case 1 as observed at time step 7200 (Figure 3.6e). In case 1, failure propagated to mid-span at the upper surface of the first layer, whereas, mid-span is mostly intact in case 2. With further stepping, in case 1, every layer of shale roof separated from each other and started bending as individual beams. The behavior of these beams can be explained by classical beam theory, which suggested the formation of the compression and tension zone at the upper surface and lower surface around entry center respectively. In addition, the zone of maximum stress concentration lies inside the compression zone, and thus the failure is most likely around mid-span as was seen at time step 9000 (Figure 3.6f). In case 2, the high tensile strength of interfaces will prevent any layer separation. The laminations will bend together leaving intact region around mid-span as seen at time step 9000 (Figure 3.6f). The final failure profile of both cases is shown in (Figure 3.6g). The difference in maximum roof deflection was around 2.1 mm



between cases 1 and 2, with a higher deflection in case 1 (12.86 mm) due to layer separation. Although, in case 1, each beam got separated and bend under self-weight, roof deflection only increased by 20 % as compared to case 2. The small difference in roof deflection is due to the combined effect of high horizontal stress and stiffness of individual beams, which prevented significant bending of layers. However, when lamination thickness decreases, high horizontal stress may cause the individual beam to buckle due to the small bending stiffness of layers. Therefore, roof deflection can be used to compare the above two cases and identify the possible mechanism in the same stress regime.

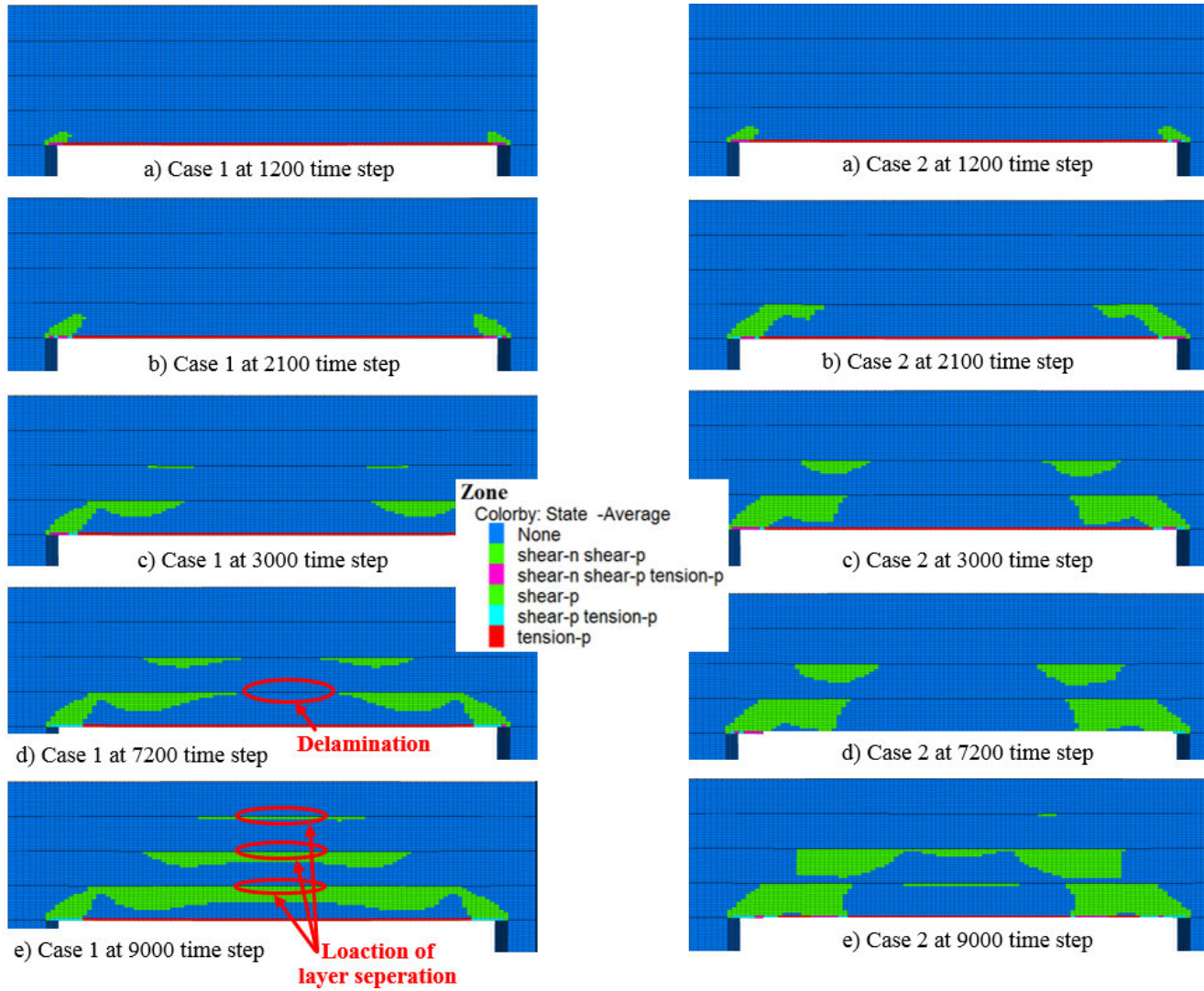


Figure 3.6 (a-e) Failure profile in shale roof of two anisotropic models at different time step.

Using maximum roof deflection for comparison, the influence of lamination thickness is ascertained as shown in Figure 3.7. For various material models used earlier such as; the anisotropic model with interface properties set1, the anisotropic model with interface properties set2, and equivalent isotropic model, the validity of these models can be quantified from figure 3.7. The anisotropic plastic model runs indicate that there is a unique behavior of an anisotropic material, which is not predicted by the isotropic model as shown by the difference in roof deflection trend with lamination thickness (Figure 3.7). This behavior is the result of the ability of rock mass to slip laterally and deflect due to the presence of the lamination, which leads to higher roof deflection and plastic yield. Based on lamination thickness, three different behavior types similar to the study by Perras and Diederichs, 2009 were found in the current study.

For lamination thickness around 600-1800 mm, i.e., T/L (thickness to Span ratio) 0.1-0.3, maximum roof deflection was around 7.4 mm in the isotropic model and 8.6-9.5 mm in two anisotropic models (Figure 3.7). In the isotropic model, the roof failed under shear and the failure extended from the entry corner at step angle to a height of 0.63 m (Figure 3.8a). The plastic yield in both anisotropic models is about 0.9 m height, i.e., failure in first layer only (Figure 3.8a). As failure is limited to the first layer, coupled with inter-bed slipping, stress begins to channel through this layer resulting in higher yield and slightly higher roof deflection (Figure 3.7). As lamination thickness decreases, a second lamination above the bottom layer began to slip, causing the stress flow to be concentrated across two layers of the shale roof. This load shedding to the second layer would result in its failure and increase in yield height within the shale roof. This transition of stress release into multiple layers and increased the yield height according to a study by Perras and Diederichs, 2009 marks the end of stress challenging zone (Figure 3.7). Above this thickness, rock support should target specific laminations to prevent lateral slip (Pells 2002).

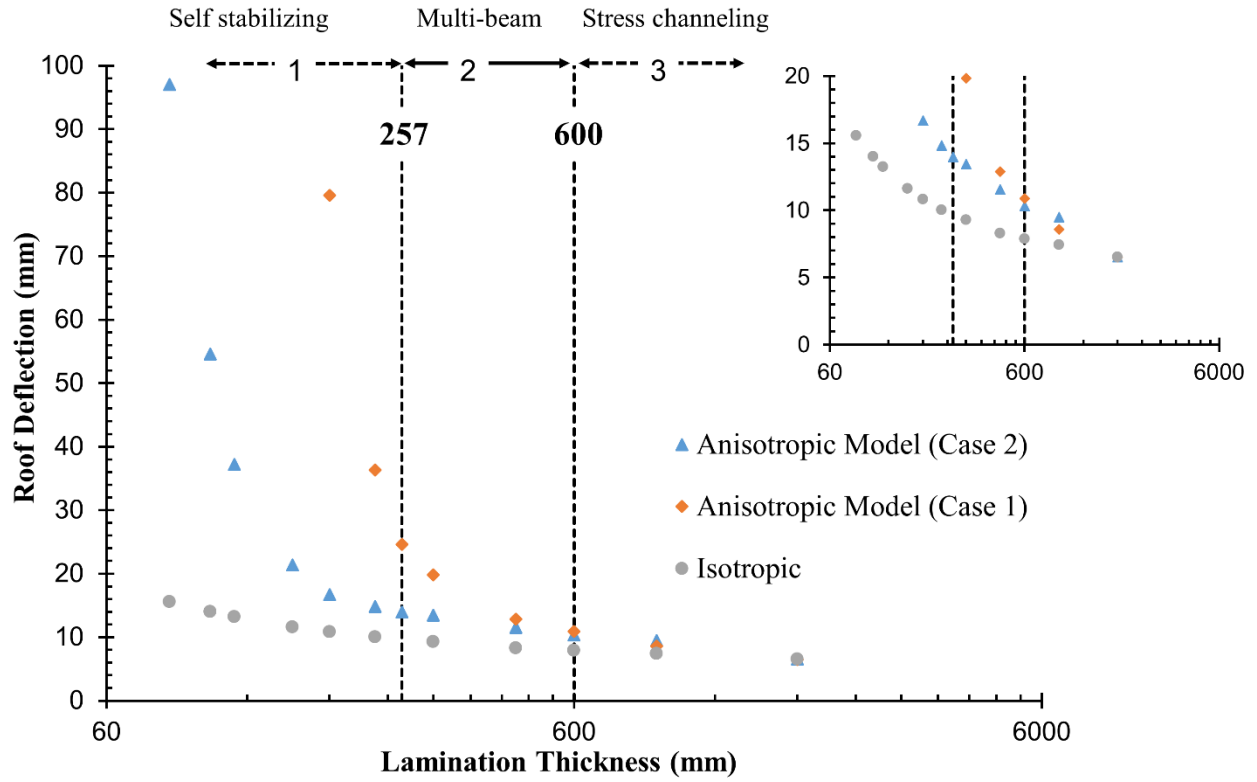
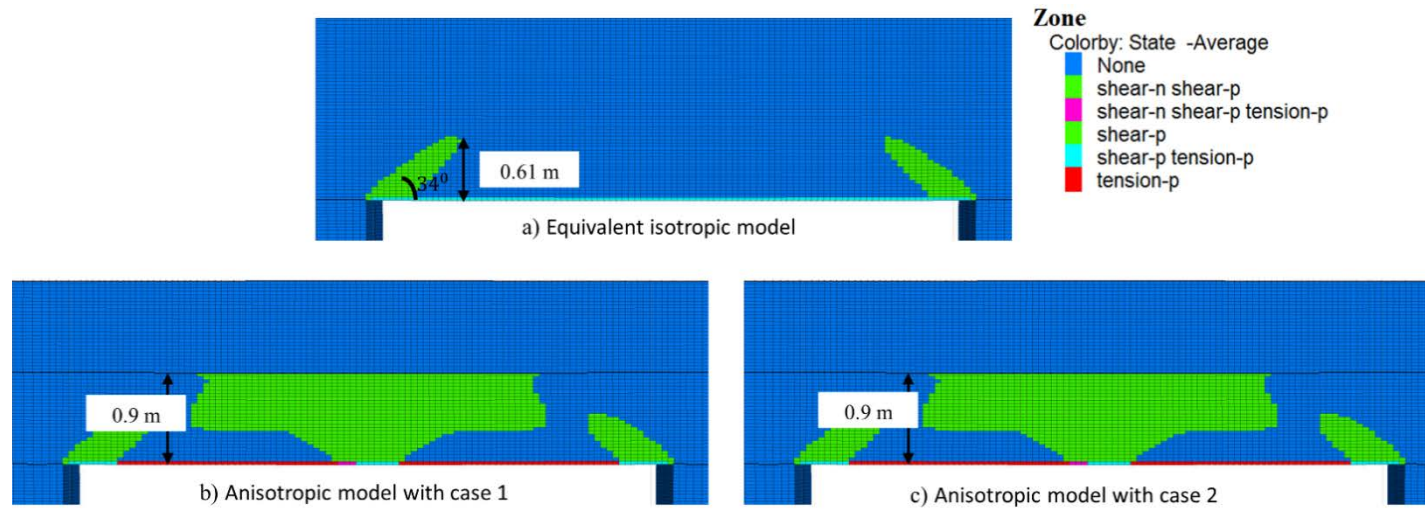


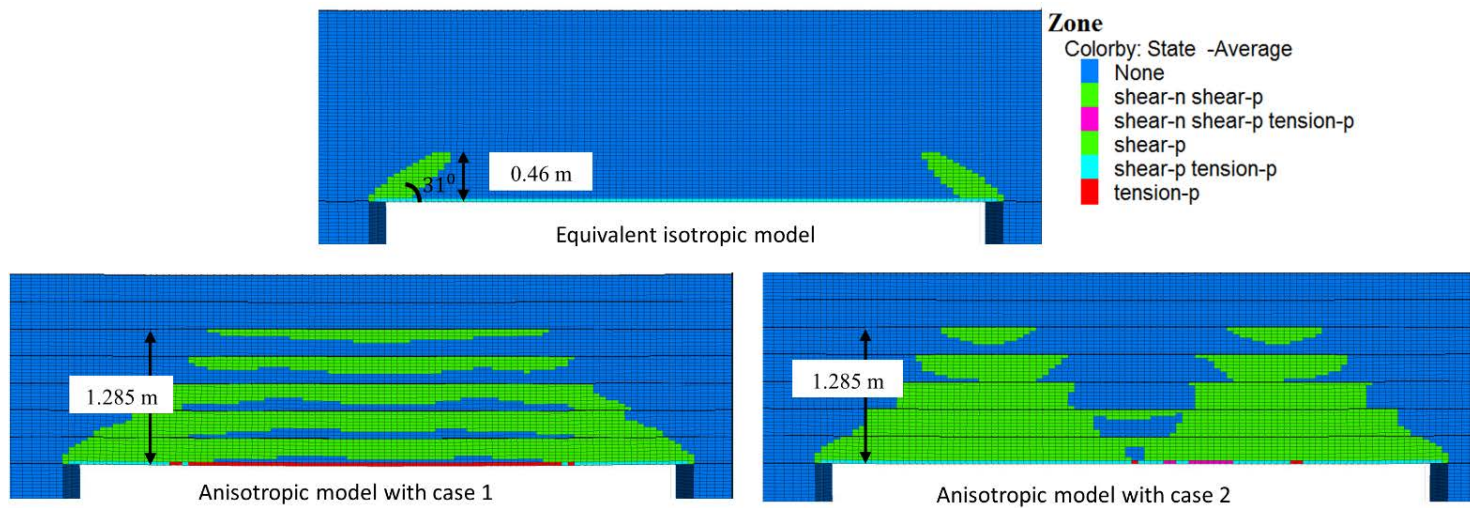
Figure 3.7 Comparison of modeling methods at various lamination thicknesses using roof deflection. Model results are 6 m span mine entry at 350 m depth and  $K=2$ .

When lamination thickness decreased from 600-257 mm, multiple layers started sharing the induced stresses due to excavation thereby, inducing failure into these layers. The increase in yield height and along with lamination or inter-bed slipping play a dominant role, as seen by significantly larger deflection in models with weak planes as compared to isotropic models. For instance, as lamination thickness decreased from 600 mm to 300 mm, roof deflection only increased by 2-2.5 mm (9.5 mm in 0.3m thickness) in isotropic models. While in anisotropic models, deflection increased by 4.5 mm (50% increase) in case 2 and 25.46 mm in case 1. Further, yield height reached to 1.285 m into shale roof with lamination thickness of 257 mm in both anisotropic models as compared to 0.56 m in isotropic model (Figure 3.8b). Here, plastic yielding and lamination slip extended into several layers and are not truncated by the presence of the laminations, as in the stress channeling section. The increase in the plastic height and roof deflection can be considered as multi-beam coupling as suggested by Perras and Diederichs, 2009. The primary roof support provides beam-building effect that stabilize the roof by creating a composite beam.

Although, yield height was in same in two cases of the anisotropic model, significant difference in failure profile was found between them as shown in Figure 3.5b-c and figure 3.8b for lamination thickness 450 mm and 257 mm respectively. The difference in failure profile is due to interface properties such as zero low tensile strength in case1, which allowed laminas to separate and form individual beams. However, the difference in roof deflection was less than 10.56 mm for lamination thickness higher than 257 mm (figure 3.7) which indicates no significant difference in roof stability between two cases. Higher stiffness of the individual beams and presence of high horizontal stress resulted in the small deflection of the roof in spite of formation of individual layers.

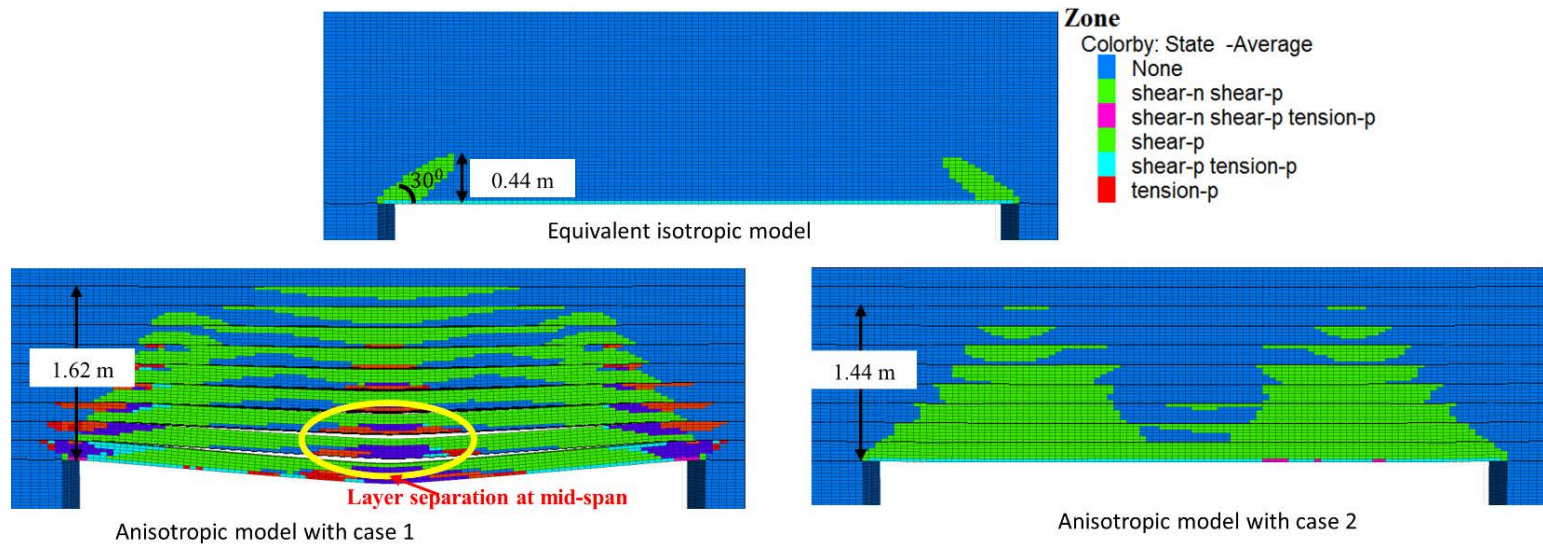


a) 900 mm Lamination thickness

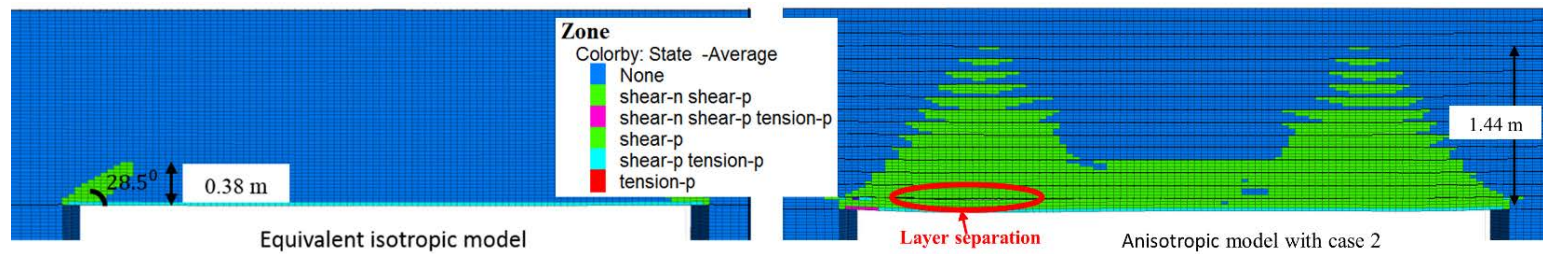


b) 257 mm Lamination thickness





c) 180 mm Lamination thickness



d) 112.5 mm Lamination thickness

Figure 3.8 (a-d) Failure profile comparison for different models at various lamination thickness

With further decrease in lamination thickness, interface/weak plane properties played a dominant role in roof yielding and deflection. As seen in Figure 3.7 when lamination decreased from 257 mm to 150 mm, the slope of the anisotropic model with interface properties set1 (case1) quite steep as compared to the anisotropic model with interface properties set2 (case2). At lamination thickness of 150 mm, case1 show roof deflection of about 295 mm as compared to 21.38 mm deflection in case 2. In a similar manner for 112.5 mm lamination thickness, buckling occurred in the case 1, while in case 2, roof deflection was only around 37.184 mm. The difference in failure mode was due to zero tensile strength of interface in case1, which allow layers to separate (mostly initiated at mid-span) and form individual beams bending under self-weight and horizontal stress. The bending and yielding of these individual layers can be predicted by Voussoir model (Diederichs & Kaiser, 1999). For instance, Shabanimashcool and Li, 2015 suggested buckling as most likely failure under high horizontal stress ( $\sigma_h > 5\text{MPa}$ ) for beam thickness to span ratio is less than 0.025 that was similar to the current study where it occurred for thickness below 150 mm ( $T/L < 0.025$ ).

In case 2, the high tensile strength of interface (0.3 MPa) prevent layer separation especially at higher lamination thickness, i.e., 900 mm to 225 mm. For lamination thickness, less than 225 mm, separation of layers occurs at locations other than at mid-span of the roof. This behavior is due to the complex bending of shale roof under high horizontal stress (Figure 3.8c-d). The complex bending of shale roof can also be confirmed by the change in location of maximum roof deflection in case 2 as lamination thickness decrease from 150 mm to 81.8 mm (Figure 3.9a-c). In addition, the plastic yielding has stabilized as seen by approximately same yield height (1.44 m) as lamination thickness decreased from 225 to 81mm (Figure 3.8c). Therefore, reducing lamination thickness only has an elastic effect on the roof deflection and thereby forming self-stabilizing thin beams (Figure 3.7). Perras and Diederichs, 2009 also reported similar observation, i.e., for T/L (thickness to span ratio) ratio less than 0.03 (around 180 mm lamination thickness in the current study), the extent of plastic yield begins to stabilize forming self-stabilizing beams. At the lamination thickness of 81.8 mm, roof deflection was around 97 mm, which would require some support to sustain the roof. Due to a high computational requirement, smaller lamination thickness ( $< 81.8\text{ mm}$ ) was not analyzed in the current study.



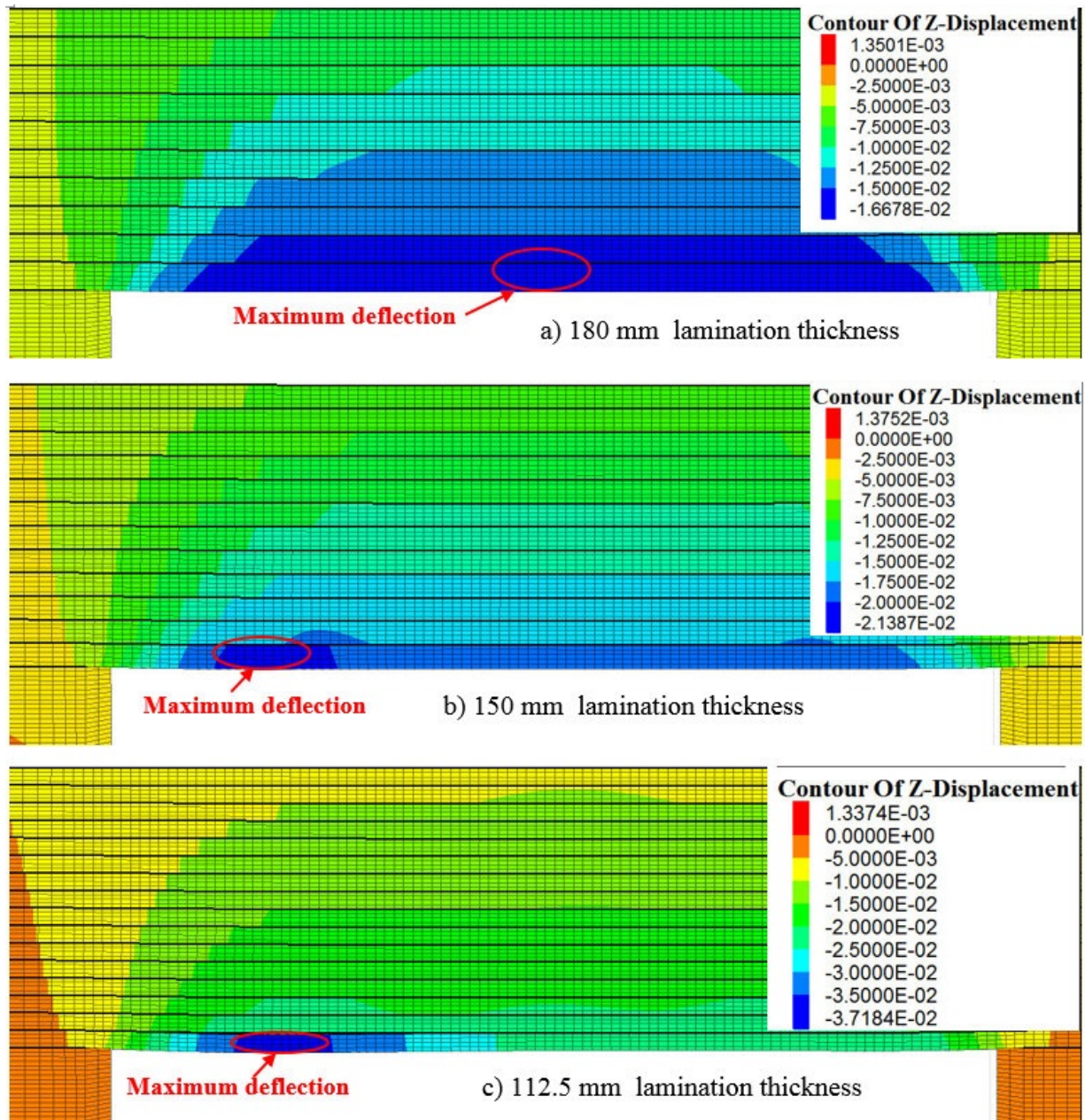


Figure 3.9 (a-c) Contour of vertical displacement in anisotropic model (interface properties of set1) for various lamination thickness.

### 3.2.6.1 Selection of interface properties for laminar plane

The anisotropic behavior, as discussed above is highly dependent on weak plane/interface properties. Therefore, all three types of behavior zones namely: stress channeling, multi-beam

coupling, and self-stabilizing beams may not exist in the roof with different interface properties as seen in case 1 (Figure 3.7). In this case, due to zero tensile strength of interface, layers separated (which initiate at mid-span) to form individual beams. The bending of these individual layers can be analyzed using Voussoir beam concept, especially for thinly laminated roof. In case 2, layer interaction in shale roof becomes complex especially at the small lamination thickness, where layer separation does not initiate at mid-span. The delamination and failure are more concentrated towards entry corner (figure 3.8c-d). Therefore, lamination properties have a significant influence on layer interaction and failure progression within the shale roof. The models run for case 2 shows a constant yield height at the low thickness, which can provide a very general mechanism called self-stabilizing beams. However, failure propagation and subsequent layer interaction do not appear to follow any trend. Hence, a more detailed analysis perhaps using simple beam models is required.

As two cases of interface properties were considered and assessed above, it is clear case 2 shows a significant amount of layers interaction for small thickness ( $< 150$  mm) which makes it a realistic representation of the behavior of thinly laminated shale roof. As discussed in section 2.2.1.5 of chapter 2, exact failure mechanism of shale roof is highly dependent on layer interaction, location and degree of delamination within the roof. Additionally, laminar planes have significantly higher tensile strength than infilled joint or fractures as discussed in section 2.5 of chapter two. Many studies in the past (Wright, 1978) have simulated bolting by increasing the strength of joints/interfaces present in the roof. If case 2, can be considered to be an equivalent bolted roof, then delamination may not necessarily occur at mid-span. Therefore, interface properties presented in case 2 (Table 3.2) were used as base properties for laminated rock in the remainder of the study.

### **3.2.7. Limitation of Anisotropic Model**

Even though the anisotropic model provided a detailed insight into the influence of lamination on behavior of shale roof. There are some limitations in using this model which are discussed in sections that follow.

### **3.2.7.1 Failure progression within laminated roof**

In the anisotropic model runs, failure in second or above laminations was found to propagate from their upper surface towards lower surface. For instance, as discussed in Figure 3.5b-c in section 3.2.6, failure in the second layer of both the anisotropic models initiates at the upper surface and then propagates towards the lower surface. This behavior is independent of weak plane properties and occurs only due to the presence of weak plane. Further, the bending profile of the roof affects the overall roof behavior. Additionally, as discussed in section 2.2.1.5 of chapter 2, inter-laminar interaction plays vital role in failure initiation and propagation into shale roof. For example, in cutter roof combination of delamination and buckling occurs at entry corners. Therefore, it is imperative to perform detailed analysis using a simplified model for understanding the exact failure mechanism within laminated rock strata.

### **3.2.7.2 Influence of horizontal stress**

The anisotropic behavior, as mentioned in earlier sections, can be classified into three types based on the failure extent into shale roof, layer interaction and lamination thickness. However, these behavior types are found to be highly dependent on the magnitude of horizontal stress. For instance, higher horizontal stress would cause failure in the roof, which would precede roof bending, causing the roof “self-stabilize” irrespective of the lamination thickness as seen in Figure 3.1a-b in section 3.1. Two lamination thickness, 1.8 and 0.45 m were simulated with each representing massive and laminated roof and subjected to 23.55 MPa horizontal stress with K-ratio = 3 (i.e., 7.85 MPa vertical stress). In both cases (Figure 3.1c), the entire roof failed which showed that reduction in laminations thickness produced an elastic effect on roof deflection. In addition, with low layer thickness and high horizontal stress was abrupt with no regular trend in roof deflection with lamination thickness (Figure 3.10). Figure 3.10 compares the roof deflection variation with laminations thickness for K=2 and 3. For lamination thickness varying from 900 to 150 mm, roof deflection is larger for K=3 than for the stress ratio K=2. This occurs due to the failure of the entire roof when K=3, whereas in case of K = 2, the yield height increased from 0.53 to 1.1 m as lamination was decreased to 150 mm. However, when lamination thickness decreased below 150mm, maximum roof deflection changed abruptly (highlighted by red circle) for K=3

(Figure 3.10). Therefore, a basic understanding of failure propagation in laminated roof under high horizontal especially at low layer thickness is required.

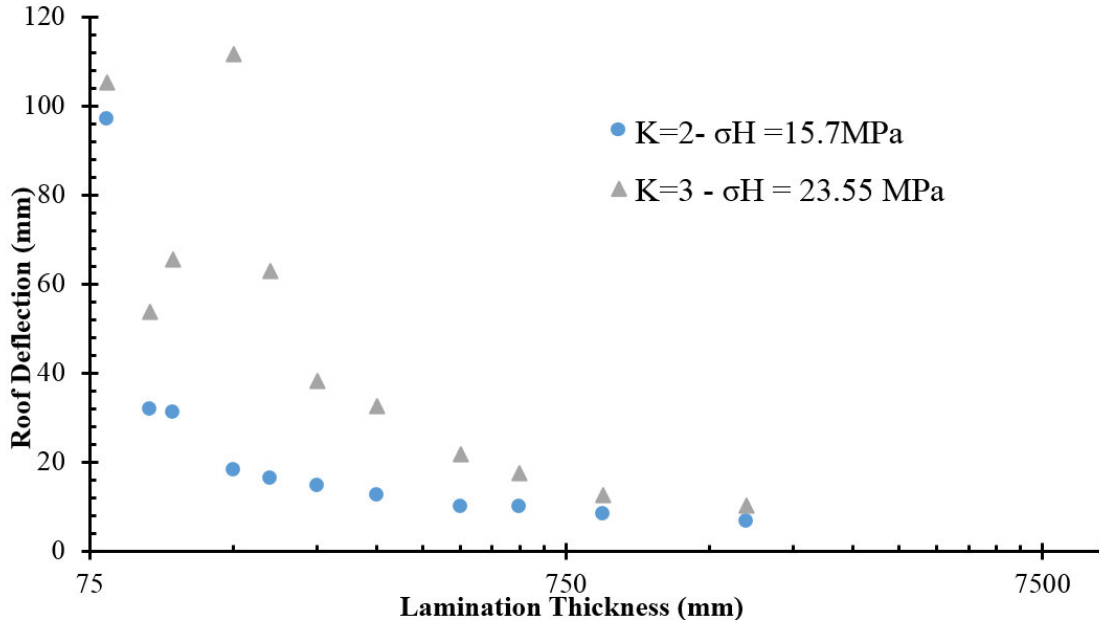


Figure 3.10 Comparison of roof deflection between two different horizontal to vertical stress ratio.

### 3.2.7.3 Influence of Interface parameters

As discussed in section 3.2.6, interface properties play a vital role in simulating the behavior of laminated shale roof. The influence of interface strength parameters controls the layer interaction and overall bending profile of shale roof (Figure 3.7 in section 3.2.6). However, the influence of interface stiffness can only be explained in terms of bending stiffness. With stiffer interface, the roof bending is restricted, which reduces the yield height and roof deflection. For instance, in figure 3.11 a-b, failure profile is compared between the two different normal to shear stiffness ratio of interface as shown in Table 3.3 at lamination thickness of 100 mm. The yield height in case of stiffness ratio ( $K_n/K_s$ ) of 10 (about 1.4 m) is higher as compared to when stiffness ratio is 2 (about 1.17 m) which is due to stiffer interface in former case restricting bending of shale roof. However, the difference in failure propagation cannot be explained clearly, especially in case  $K_n/K_s = 2$  where failure extent from entry corners at a sharp angle to 0.68 m and

then it expand in the horizontal direction towards at the mid-span. The complex bending profile of shale roof makes layer interaction difficult to analyze.

Table 3.3 Lamination properties used in parametric study

Normal Stiffness (GPa/m)	Shear Stiffness (GPa/m)	Cohesion (MPa)	Tension (MPa)	Friction (degree)
10	5	0.13	0.3	25
10	1	0.13	0.3	25

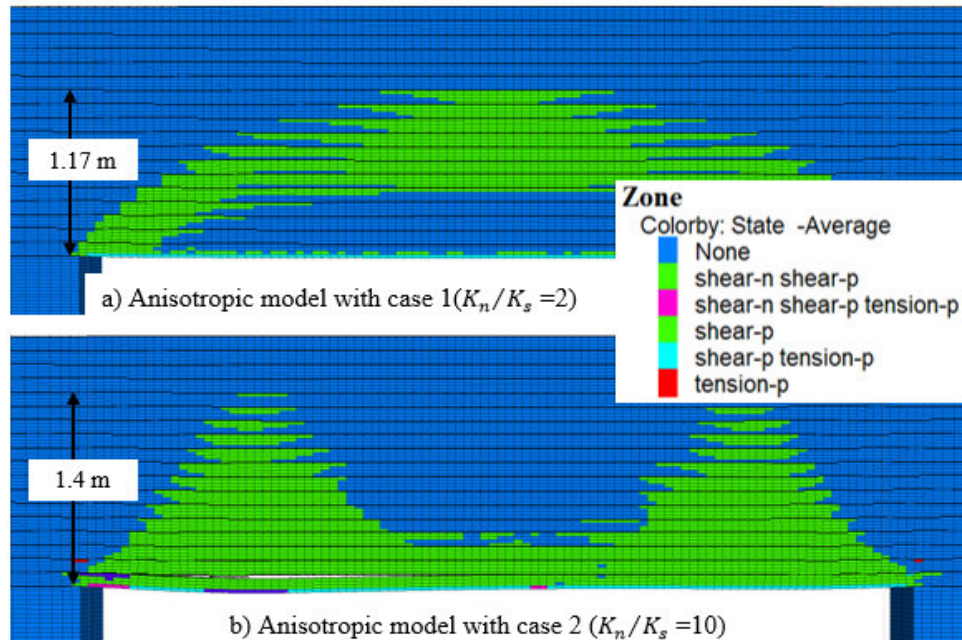


Figure 3.11 (a-b) Failure profile in anisotropic model for different interface stiffness ratio ( $K_n/K_s$ )

### 3.2.8 Summary

In this chapter anisotropic mine model was used to investigate the influence of lamination on the behavior of shale roof. In addition, the model was compared with the equivalent isotropic model to develop a basic understanding of difference in their behavior.



Based on the numerical analysis the following findings were observed:

- The anisotropic model identified three behavioral responses of shale roof namely: stress channeling, multi-beam coupling, and self-stabilizing beams based on lamination thickness that are not present in isotropic model.
- These behavior types were also found to be highly dependent on lamination properties. For instance, the laminar plane's tensile strength dictates the behavior of thinly laminated roof.
- In case of interfaces with zero tensile strength, layers separated to form individual beams and undergo buckling at mid-span for small lamination thickness ( $< 150$  mm).
- While in high tensile strength (0.3 MPa), failure is more concentrated towards the entry corner and delamination also occurred near to entry corner indicating complex layer interaction similar to bolted shale roof in field condition.
- Therefore, inter-laminar interaction and failure propagation is directly dependent on lamination properties as seen in the case of interface tensile strength.
- These behavior types were also found to be highly dependent on the magnitude of horizontal stress. For instance, if horizontal stress is very high and rock fracture/failed would precede roof bending, that shale roof only show "self-stabilizing beam" behavior irrespective of lamination thickness.
- Although the anisotropic mine model provided a detail insight into behavior of laminated roof, underlying mechanism behind the failure propagation was not clearly understood. For instance, failure initiation at upper surface and its downward propagation in the overlying layer (second and above layer) cannot be explained.
- Similarly, the influence of interface stiffness on failure profile of shale roof cannot be clearly explained. The only possible explanation was high stiffness increased the overall system stiffness resulting in reduction of roof bending. The decrease in bending stresses has reduced the yield extent in the roof in the case of higher interface stiffness.
- The failure propagation in the laminated roof is directly depended on inter-layer interaction. In the anisotropic model, due to complex layer interaction, the analysis of failure propagation from one lamina to another becomes a difficult task.

- The complex layer interaction is due to bending profile of immediate shale roof which in anisotropic mine model depend on various factors like its interaction with overburden strata and *in-situ* stresses. For instance, the vertical load of the immediate roof is dependent on bending profile of overburden strata for given stress conditions.
- Therefore, overburden strata and its interaction with immediate shale roof increase the complexity of mine model. Due to this limitation, beam models were used in chapter four and five where shale roof is constant load is applied to shale roof and thereby creating a simplified layer interaction.

## 4. ELASTIC BEAM ANALYSIS

### 4.1 Introduction

In the previous chapter, an anisotropic mine model was used to understand the influence of laminations thickness on the behavior of shale roof. Although the model provided a detailed insight into the behavior of laminated roof, it showed limited applicability in identifying the underlying mechanism behind the layer interaction in a shale roof, which can be attributed to complex bending of the roof in the mine model. In addition, the influence of high horizontal stress and lamination parameters like laminar plane stiffness on the behavior of lamination roof is poorly understood.

In this chapter, three beam models namely: Solid beam model, Voussoir beam model, Solid Beam on Elastic Abutment were analyzed to better understand layer interaction in multi-layer roof like laminated shale under uniform loading. The uniform loading provides a simplified bending profile of the shale roof as compared to anisotropic mine model in chapter 3. The models were simulated in UDEC (Itasca, 2011a) under elastic state. The UDEC is a Distinct Element Method based numerical code by Itasca, 2011a that simulate the material as 2-dimensional discrete blocks, which interact along the joints. The joint elements are used to simulate laminar planes or discontinuities. It is described in detail in section 3.2.1 of chapter 3. Additionally, a parametric study was performed to understand the influence of horizontal stress and lamination parameters on the bending profile and stress distribution in the shale roof presented in section 4.5.

### 4.2 Elastic Solid Beam model

The model is based on the classical Euler-Bernoulli beam approach (Panek, 1956) which treats mine roof as a solid elastic beam with fixed ends and rectangular cross section. The beam will bend either under its own weight or under a uniform vertical load, which is approximated as force ‘ $W$ ’ acting at the center of the beam. The stresses that act on any section of beam (Figure 4.1a) are bending stress  $\sigma_{xx}$  and shear stress  $\tau_{xy}$ , their distribution along the beam thickness is shown in figure 4.1b. At any cross section, the bending stress is maximum on upper (compressive stress) or lower surface (tensile stress) of the beam and the shear stress is maximum on the middle surface,



Figure 4.1c. The maximum values of both bending stress and shear stress both occur at supports are given by

$$(\sigma_x)_{\max} = wL^2/2t \quad (4.1)$$

$$(\tau_{xy})_{\max} = 3wL/4 \quad (4.2)$$

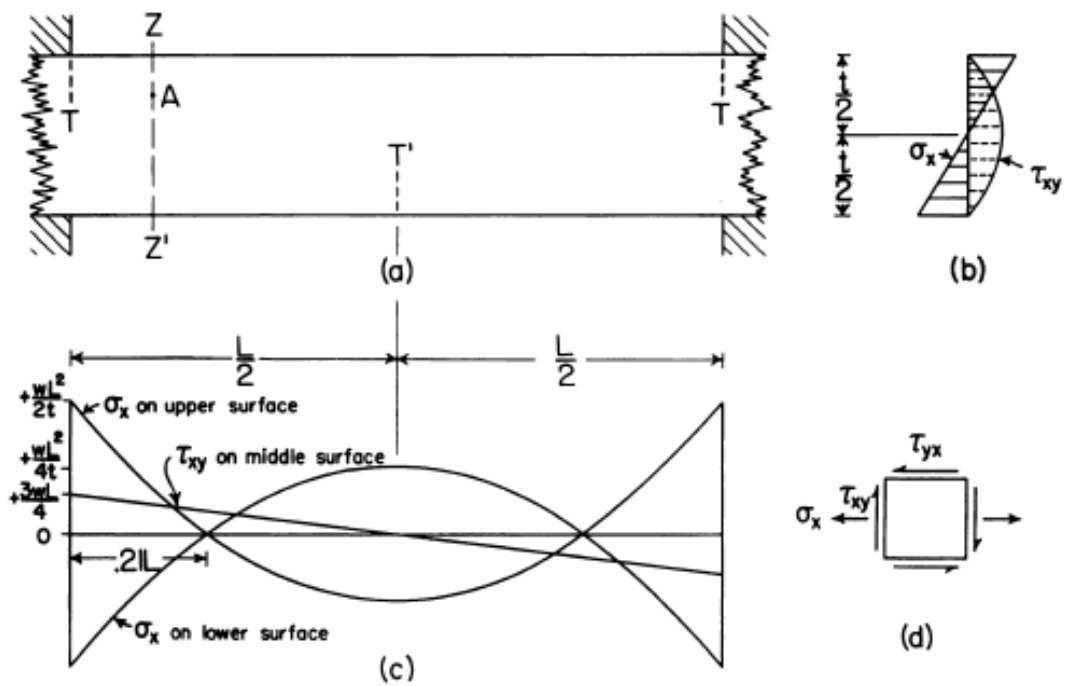


Figure 4.1 (a) Vertically-loaded beam; (b) Bending and shearing stresses on section Z-Z'; (c) Distribution of outer-fiber bending stress and middle-surface shearing stress across span; (d) Stress acting on an element at A. Failure in flexure by tension cracks, T.(Panek, 1956)

The model was simulated under the elastic state in UDEC. It consists of 6 m long beam representing shale stratum with a thickness of 1.6 m. A uniform vertical load of 0.03 MPa was applied to the top of the beam to simulate the interaction between the overlying strata and the immediate roof. The load of 0.03 MPa is equivalent to 0.9 MPa of in-situ vertical stress on top of immediate roof. The boundary condition includes fixing the left and right side of the beam which constraints both horizontal and vertical deformation (Figure 4.2). Figure 4.3a shows the horizontal stress distribution in the half-span solid beam model. The horizontal stress profile at the lower and upper surface of the beam is similar to the distribution obtained from the analytical solution (Figure 4.1c), i.e., maximum compression (around 2-4 MPa) and tension (around 4-6 MPa) at the corner of the lower surface and upper surface of beam respectively. Further, the shear stress distribution, shown in Figure 4.3b, also confirms the trend of shear stress in the beam with a zero value at the center and maximum in magnitude at the ends of the beam.

The principal stress distribution (Figure 4.4a) shows an arch-shaped compressive stress zone extending from the left lower corner at the support to the top corner at the mid-span. The remaining region around the top corner of the support and lower corner of the mid-span represents tensile zone with the maximum stress value lower than the compression zone. The principal stress value at the left top corners was low due to the influence of boundary conditions, which caused the tensile stress to develop in this region as shown in Figure 4.3. The right bottom corner is under tension as it lies below the neutral axis formed due to beam bending.

Failure of the beam will occur at the location of highest stress concentration, which is at the lower left corner of the beam (lower abutment corner) under compression and top abutment corner (Figure 4.3a) under tension. As rocks have low tensile strength, failure is most likely to initiate under tension at the top abutment corner.

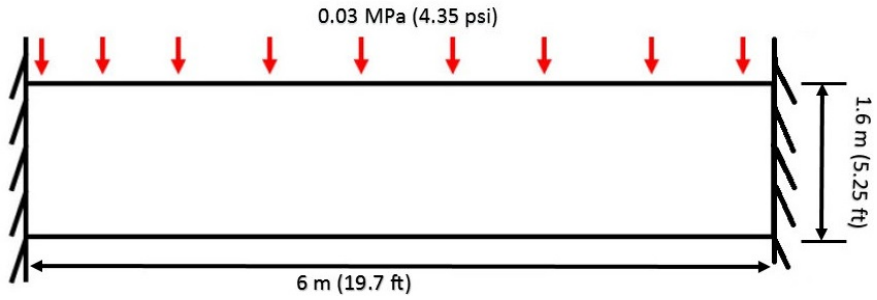


Figure 4.2 Solid beam geometry with boundary conditions built in UDEC.

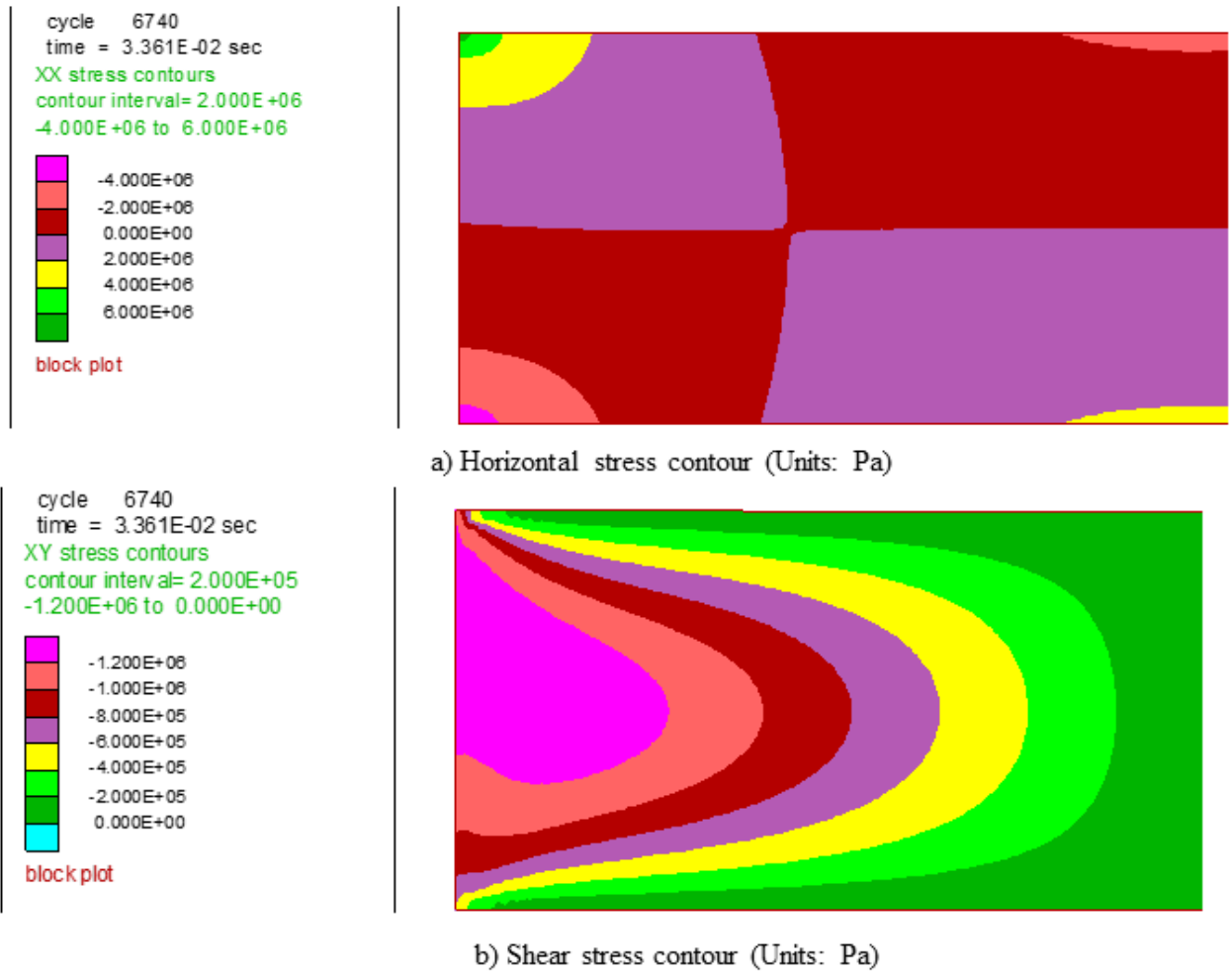
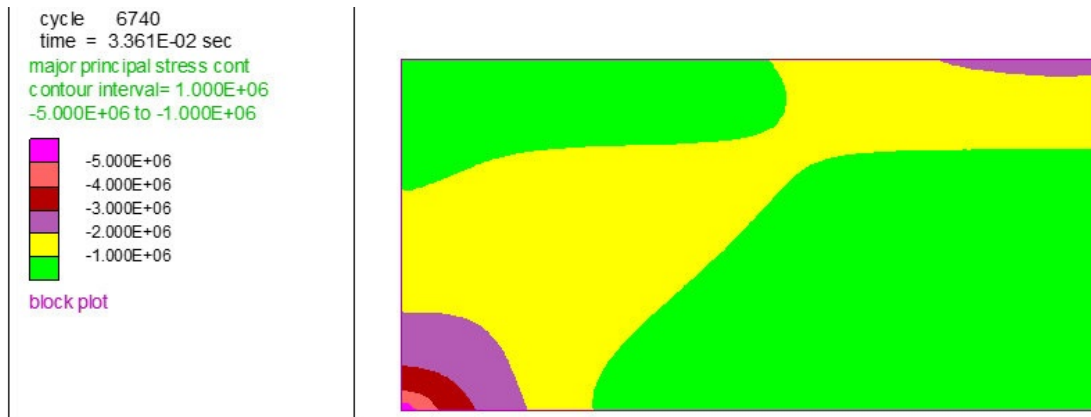
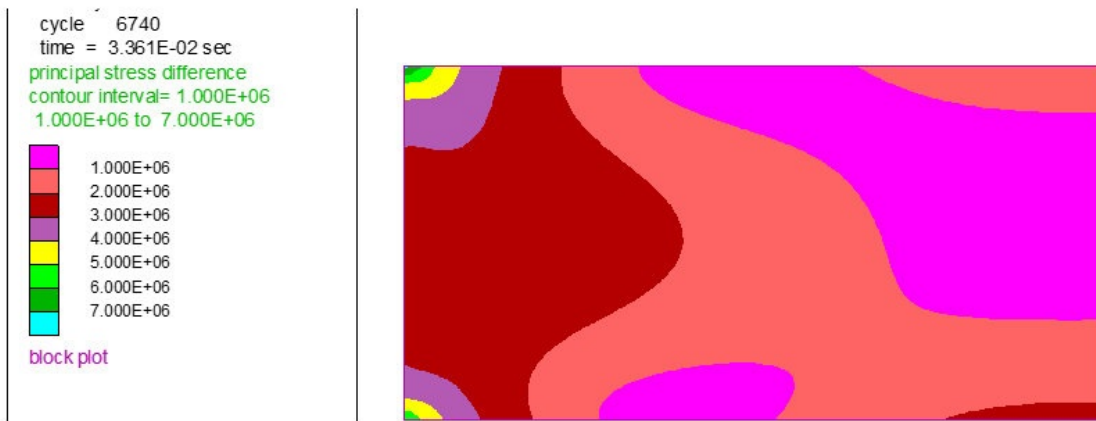


Figure 4.3 Half-length solid beam with 1.6 m thickness (a) Horizontal stress contour; (b) Shear stress contour.



a) Maximum principal stress contour (Units: Pa)



b) Principal stress difference contour (twice of maximum shear stress) (Units: Pa)

Figure 4.4 Half-length solid beam with 1.6 m thickness (a) Maximum principal stress contour; (b) Principal stress difference contour.

### 4.3 Voussoir beam model

The concept of the Voussoir beam was proposed by Evans, 1941 especially to explain the stability of a jointed or cracked beam. He proposed an analytical solution to estimate the vertical deflection and overall stability of the cracked beam. The Voussoir beam concept consists of the following assumption:

- Rockmass is assumed to be dominated by parallel laminations along with vertical joints.
- Vertical joints reduce the ability of the rockmass to sustain tensile stresses parallel to the boundary resulting in opening of these joint at the ends of excavation around the upper part.

- c) The joint opening allows the lowest layer to separate from the roof and bend under its own weight.
- d) As the layer bends further, the joint at the mid-span opens up around the bottom part.
- e) At this point stability is achieved through a compression arch formed from the abutment to the center (Figure 4.5a-b).

After the initial analytical solution, numerous studies such as Sterling, 1980; Stimpson and Ahmed, 1992, suggested improved analytical solutions through numerical modeling and laboratory experiments. These studies (Beer and Meek, 1982; Sofianos, 1996) also suggested various failure modes such as buckling, crushing (i.e., Compressive failure) at the mid-span and abutments or slippage at the abutments depending on the span to thickness ratio. However, these studies included only a single layer model with no consideration of horizontal loading. Very few studies such as Shabanimashcool and Li, 2015; Wright, 1974 have considered the effect of horizontal stress along with multi-layer beams. Both of these studies although analytical have used numerical model.

For this research, a half-span Voussoir model based on the study by Sofianos et al., 2000 was used. Sofianos et al., 2000 simulated this model in UDEC to investigate the influence of vertical joint spacing on the stability of the Voussoir beam when loaded under self-weight. The model consists of two rigid blocks on the side with a deformable block in the center. The deformable block represents a 3m half-length shale stratum with a thickness of 1.6m. It includes two layers (i.e., 0.8 m lamination thickness) interacting with each other through the joint element. The left rigid block represents the abutment whereas the right rigid block imposed the appropriate boundary conditions of the mid-span (Figure 4.7). The right-hand vertical discontinuity or joint (between deformable and rigid block) represents the mid-span of the beam where both vertical slip and lateral separation are permitted. This condition is achieved by imposing zero value of the friction angle  $f$  and cohesion  $c$ . The left-hand vertical discontinuity or joint (between deformable and rigid block) represented the beam abutment where only separation is permitted. This boundary condition is achieved by imposing very large values for the friction angle and for the cohesion (i.e.,  $f=890$ ,  $c=10$  GPa), to prevent shear slip. The uniform vertical load of 0.03 MPa at the top of the beam was applied. It is to be noted that the model in the initial study by Sofianos et al., 2000 considered

beam under self-weight which differs from the current study that includes the vertical load on the beam. When the single beam was simulated under vertical load, the model did not converge. Therefore, beam with two layers was simulated for model calibration.

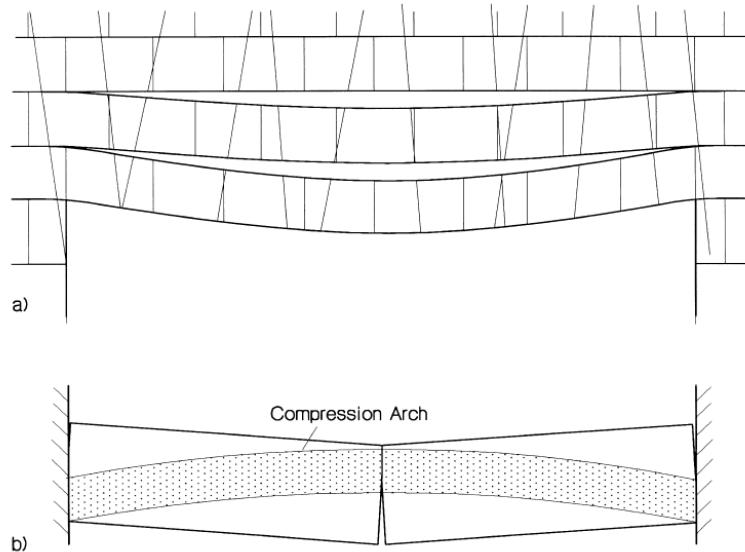


Figure 4.5 (a) Jointed rock beams; (b) Voussoir beam analogue (Diederichs and Kaiser, 1999).

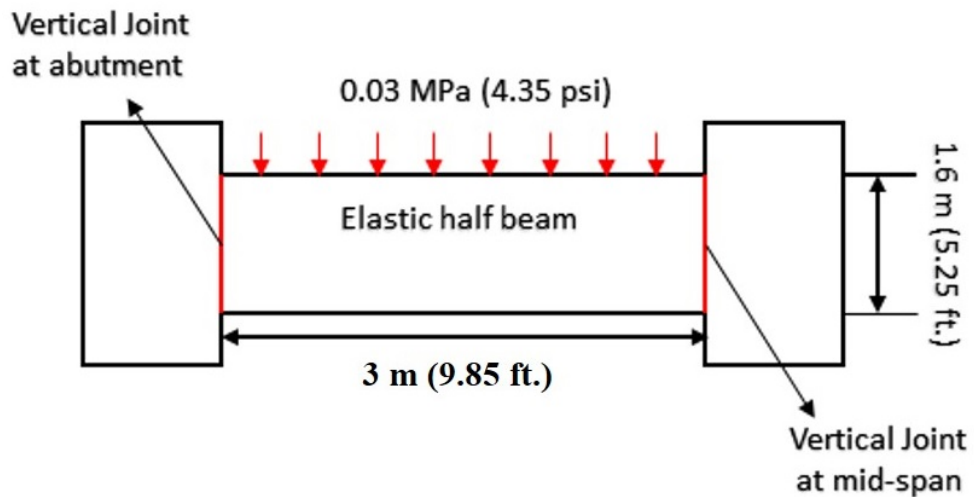


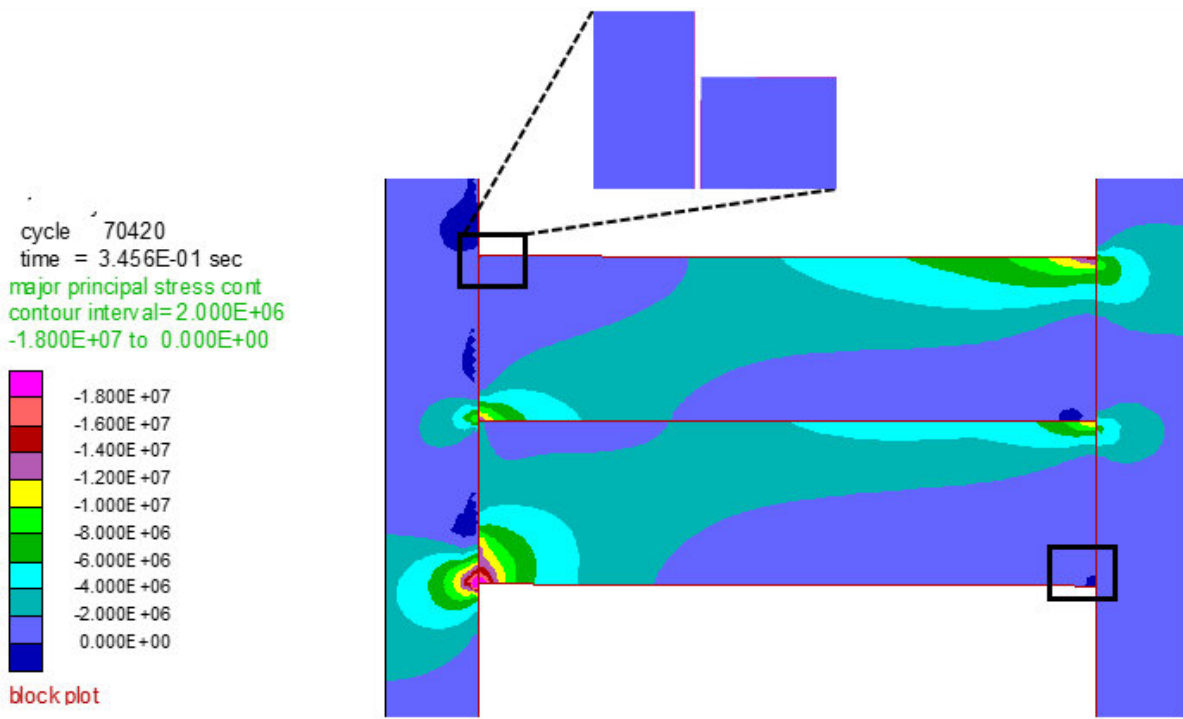
Figure 4.6 Voussoir beam model of half span in UDEC.

The arch-shaped compressive zone similar to conceptual model (Figure 4.5b) was formed in each layer extending from the lower corner at the left side to the top in the right side of half beam (i.e., mid-span of the full beam) (figure 4.7a-b). This compression arch formation can be attributed to the opening at the upper corner of left side vertical joint and lower corner of right side vertical joint (highlighted by a black rectangle).

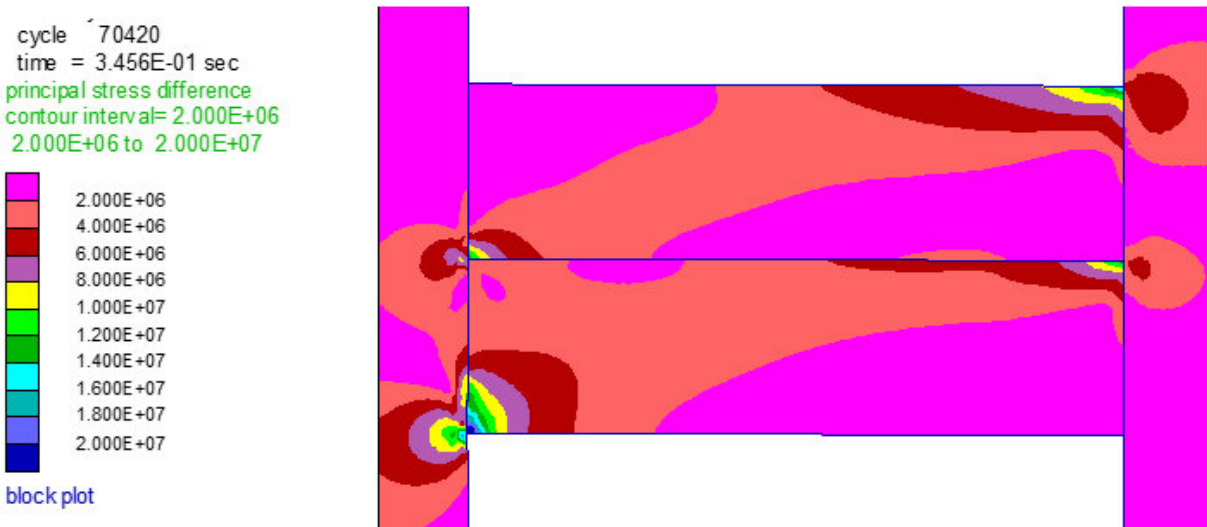
The principal stress control plot (Figure 4.7a) showed that the stress concentration was highest at the lower left corner in the bottom layer (around 12-18 MPa) and at right upper corner of the top layer around (10-14 MPa). It is significantly lower in the right upper corner of the bottom layer and left lower corner of the top layer (around 7-11 MPa) than the other two corners. The result shows that majority of the beam load is on the abutment of the lowest beam corner and at the topmost right corner of mid-span.

A similar trend was observed in the maximum shear stress distribution with the highest concentration around 7-10 MPa (Figure 4.7b). As mentioned earlier, the opening of vertical joint at abutments and mid-span produces compression arch during bending of the beam. The crack length or amount of joint opening can be used to qualitatively compare the overall bending of the Voussoir beam (Shabanimashcool and Li, 2015). The crack length, in this case, is around 0.7 m (87.5% of vertical joint length). The overall bending stress was found to vary from 2 to 2.5 times higher than the equivalent solid beam model (Figure 4.11b). Therefore, the effective bending of multi-layered beam increased by introducing vertical joint at the abutment and the center of the beam.

The opening of vertical joints at top abutment corner and bottom mid-span corner (highlighted by a black rectangle) indicate the tensile failure initiation at these locations (Figure 4.7a). The final failure mode as suggested by Shabanimashcool and Li, 2015; Wright, 1974 could be buckling, crushing or slippage at the abutments depending on layer thickness and other parameters. In this case, no buckling or slipping at the abutment was observed. In addition, the highest shear stress concentration occurs at the lower left corner in the bottom layer and right upper corner of the top layer (Figure 4.7b) and thus shear failure is most likely at these locations. It can be concluded that final failure will most likely be crushing due to shear failure at abutment and mid-span in this case.



a) Maximum principal stress contour (Units: Pa)



b) Principal stress difference contour (twice of maximum shear stress) (Units: Pa)

Figure 4.7 Voussoir beam with 2-layers (0.8m lamination thickness) (a) Maximum principal stress contour; (b) Principal stress difference contour.



#### 4.4 Solid Beam on Elastic Abutment

This beam is a modified version of the solid beam model as it considers elastic abutments instead of rigid support to account for deformation of coal pillar on the stability of a mine entry. Stephansson (1971) introduced this model for deriving analytical solutions for deflection and bending stresses in seven different configurations of a single and multi-layered roof in horizontally bedded rock (figure 4.8a). Various other researchers had used this model (Sheorey, 1976; Garrad, 1981) for calculating the stress on abutments, chain pillars, and the immediate roof adjacent to the longwall face and in gate roads. The model is based on following assumptions:

- a) Entire model is elastic with interface/joint that simulate inter-layer interaction in the roof.
- b) Ratio of individual layer thickness and entry span should be less than  $\frac{1}{2}$ .
- c) Length of roof over abutment can vary however, it should not be very large otherwise, boundary force cannot be used to apply horizontal load.

The beam model was built in UDEC to simulate the 6 m working span of immediate roof with elastic coal pillars (Figure 4.9). A uniform vertical load of 0.03 MPa on top of the beam, which was equivalent to 0.9 MPa of in-situ vertical stress. The length of the elastic abutments (L in Figure 4.9) which represents the size of a coal pillar was around 12 m on each side of the working span of the beam. The boundary condition included fixing the left and right side of the beam, which constrained the horizontal deformation. Murphy et al. 2014 recommended a minimum five element along the layer thickness in each individual layer to calibrate the numerical beam model with analytical solution.

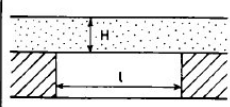
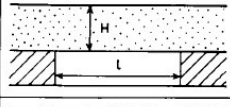
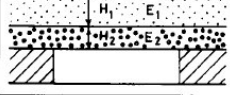
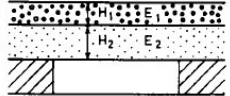
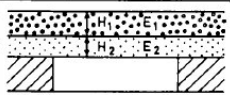
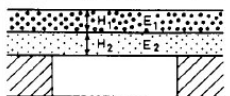
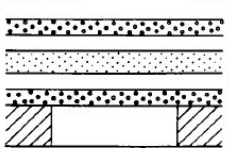
SINGLE-LAYER ROOF	I		$H < \frac{L}{5}$
	II		$\frac{L}{2} > H > \frac{L}{5}$ Including shear stress in the layer
DOUBLE-LAYER ROOF	III		$E_1 I_1 > E_2 I_2$ Free slip along the contacts Detaching
	IV		$E_1 I_1 < E_2 I_2$ Free slip along the contacts No detaching
	V		$E_1 < E_2$ Welded contact
	VI		$E_1 > E_2$ Welded contact
MULTI-LAYER ROOF	VII		Welded contacts

Figure 4.8 Type of roof configuration used in Beam with elastic abutment model (Stephansson, 1971)

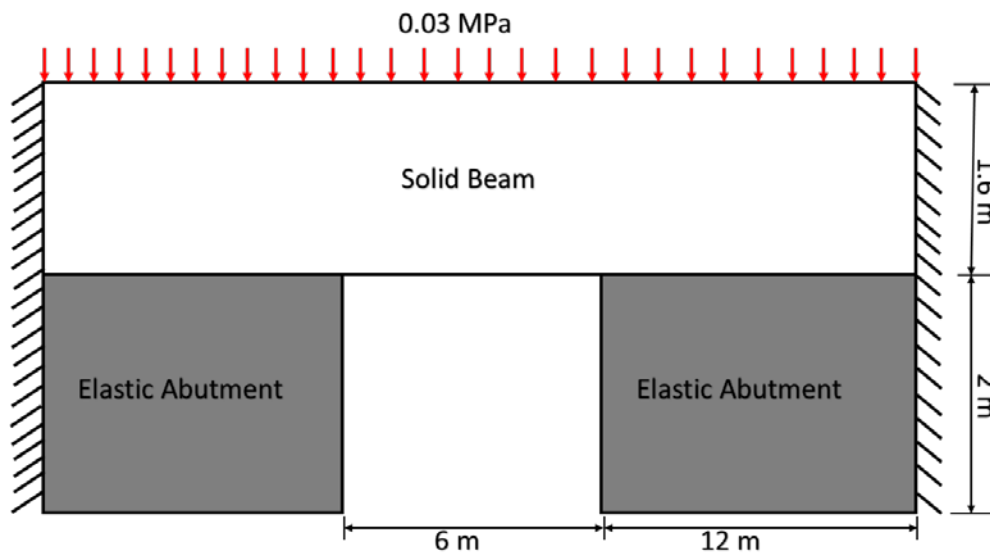
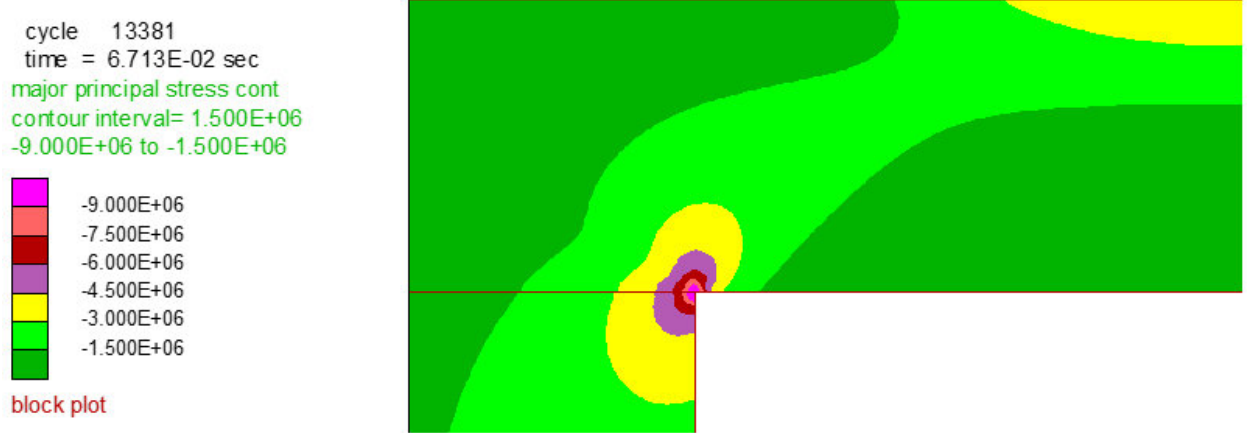


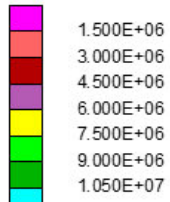
Figure 4.9 Solid beam on elastic abutment model in UDEC.

Figure 4.10a shows the compression arch in a half-span beam, which is similar to the other two beam models (Solid beam and Voussoir beam models), and extends from left lower corner at abutment to right top corner at mid-span. The remaining region of the beam is under tension as seen in Figure 4.10c and thus classified as tensile zone similar to solid beam model. The highest stress concentration occurred at the entry corner (Figure 4.10a-b) which is nearly 1.5 to 2.2 times higher than the solid beam model. The lower stress concentration in solid beam model is due to the rigid support that reduces bending of the roof. Due to the same reason, the horizontal stress near the left top corner at abutment (tensile stress) is lower as compared to the solid beam model (Figure 4.3a, Figure 4.10b). From this analysis, it can be concluded that the failure in this model most likely to initiates at the lower abutment corner under shear whereas in solid beam model tensile failure occurs at the top abutment corner.

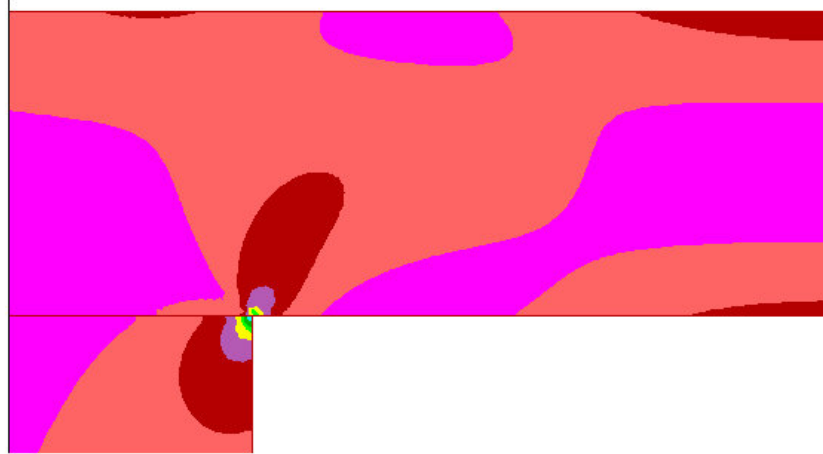


a) Maximum principal stress contour (Units: Pa)

cycle 13381  
time = 6.713E-02 sec  
principal stress difference  
contour interval= 1.500E+06  
1.500E+06 to 1.050E+07

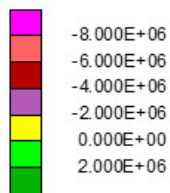


block plot

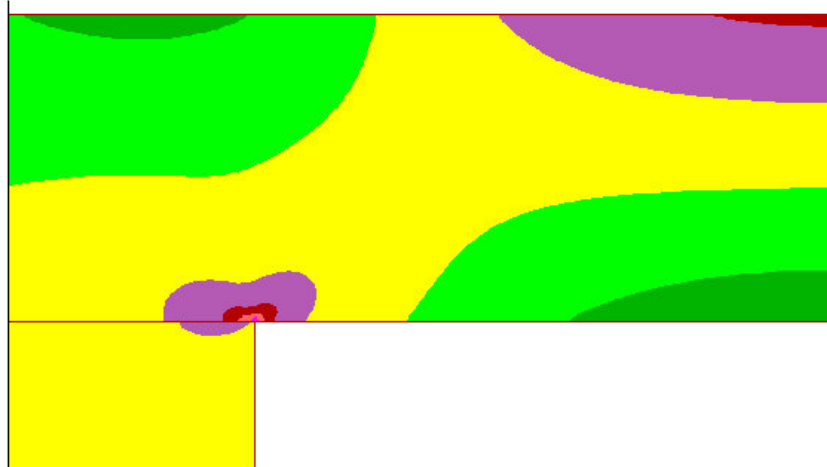


b) Principal stress difference contour (twice of maximum shear stress) (Units: Pa)

cycle 13381  
time = 6.713E-02 sec  
XX stress contours  
contour interval= 2.000E+06  
-8.000E+06 to 2.000E+06



block plot



c) Horizontal stress contour (Units: Pa)

Figure 4.10 Half-length solid beam on elastic abutment model (a) Maximum principal stress contour; (b) Principal stress difference contour; (c) Horizontal stress contour.

## 4.5. Parametric Study

A parametric study was conducted on three beam models mentioned in earlier sections to understand the influence of horizontal stress and other parameters on bending profile and stress distribution in laminated shale roof. The following parameters were considered:

- a) Lamination thickness
- b) High horizontal stress
- c) Joint parameters ( joint stiffness and strength)

For this analysis, model formulation of each beam type was same as mention in section 4.2-4.4. Here, beam comprises of multiple horizontal layers with joint elements to simulate interlayer interaction. The properties of joint elements or weak plane between layers of base model were same as used in Chapter 3 and shown in Table 3.2.

### 4.5.1. Lamination thickness

The lamination thickness was evaluated by using span ( $L$ ) to thickness ( $t$ ) ratio ( $L/t$ ). In this analysis, the beam comprises of multiple horizontal layers with joint elements to simulate interlayer interaction. The total thickness of beam is constant (1.6m) with variation in only number and thickness of individual layers.

Figure 4.11a-d compared maximum principal stress distribution for different lamination thickness in solid beam model. In the laminated or multi-layered beam (Figure 4.11b-d), compression arch was formed in each individual layer, but stress distribution was same as in single layer beam (Figure 4.11a), i.e., maximum stress concentration around left abutment corner at the lower surface and right mid-span corner at the upper surface of each layer. This trend indicates minimal layer-interaction as layers are acting as individual beams. As the lamination thickness decrease, the bending stiffness of the individual layer would also decrease thereby reducing the overall bending stiffness of the roof resulting in higher bending.

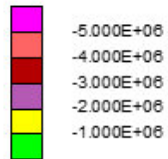
The maximum stress concentration increased from 4 to 6 MPa in 1-layer and then from 18-24 MPa in 8-layer beam model at lower abutment corner (Figure 4.11a-d). However, the extent of compression arch decreased with reduction in lamination thickness. No compression arch

developed for 8-layer case (0.2 m layer thickness) as seen in Figure 4.11a-d. As layers are acting as individual beams, tensile stress concentration at top abutment corners also increased proportionally and reached to 20 MPa in 8-layer beam case. From this analysis, it is concluded that with the decrease in lamination thickness, overall bending of the beam increases resulting in tensile failure at the top abutment corners of each layer.

In Voussoir beam model, the influence of lamination thickness was similar to solid beam model. The compression arch is formed in each layer and the overall beam bending increased with the decrease in the lamination thickness. Figure 4.12a-d presents maximum principal stress distribution with varying lamination thickness. The results indicate that the stress distribution is same; however, stress concentration in the compressive zone increased with the decrease in the lamination thickness. The bending stress (defined as average stress in compression arch) increased from 4 MPa in the two-layer beam to 9 MPa in eight layer beam (Figure 4.12a-c) models. Furthermore, the crack length increased from 0.59m (73.75 % of joint length) to 0.19 m (95 % of joint length) as lamination thickness decreased from 0.8 to 0.2 m (i.e.,  $L/t$  ratio 7.5 to 30) respectively. However, when lamination thickness was decreased to 0.1m ( $L/t = 60$ ), stress distribution in the beam changed completely as shown in Figure 4.12d. This occurred due to the low bending stiffness of the individual layer that resulted in almost complete of vertical joints as crack length increased to 99.5 % of the joint length and thus contact of the layers with the rigid block is reduced to a point (Figure 4.12d). Therefore, all the layers are only in point contact with the rigid blocks at the abutment and mid-span causing low bending stress. When lamination thickness was decreased to 0.02 m thickness, buckling of the roof was observed.

From this analysis, it is concluded that decrease in lamination thickness would increase overall bending, resulting in increase in joint opening and stress concentration in compressive zone for span to thickness ratio ( $L/t$ ) greater than 30. The failure mode will most likely be crushing at the lower abutment and upper mid-span corner due high shear stress concentration. However, for roof with span to thickness ratio ( $L/t$ ) is less than 60, buckling is the most likely failure that will occur in the roof.

major principal stress cont  
 contour interval= 1.000E+06  
 -5.000E+06 to -1.000E+06



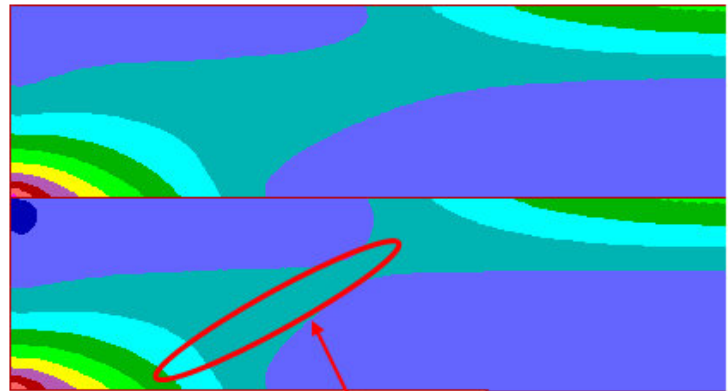
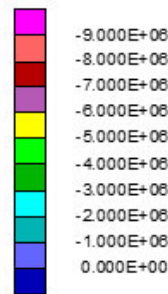
block plot



a) 1.6m layer thickness ( $L/t=3.75$ ).

Extent of compression arch

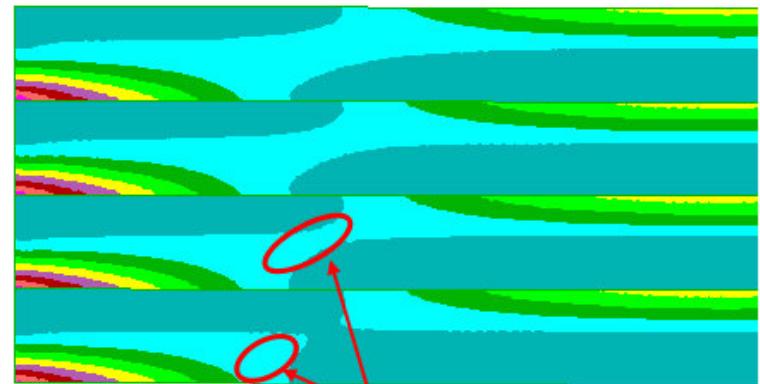
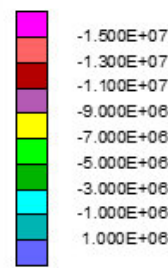
major principal stress cont  
 contour interval= 1.000E+06  
 -9.000E+06 to 0.000E+00



b) 0.8 m layer thickness ( $L/t=7.5$ ).

Extent of compression arch

major principal stress cont  
 contour interval= 1.000E+06  
 number of contour/color= 2  
 -1.600E+07 to 0.000E+00



c) 0.4 m layer thickness ( $L/t=15$ ).

Extent of compression arch

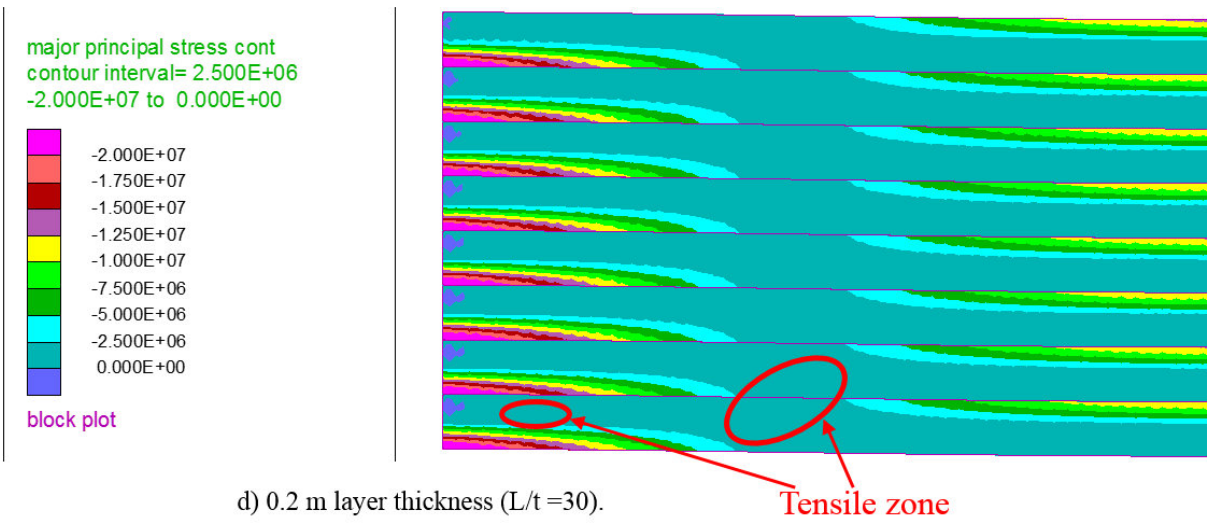
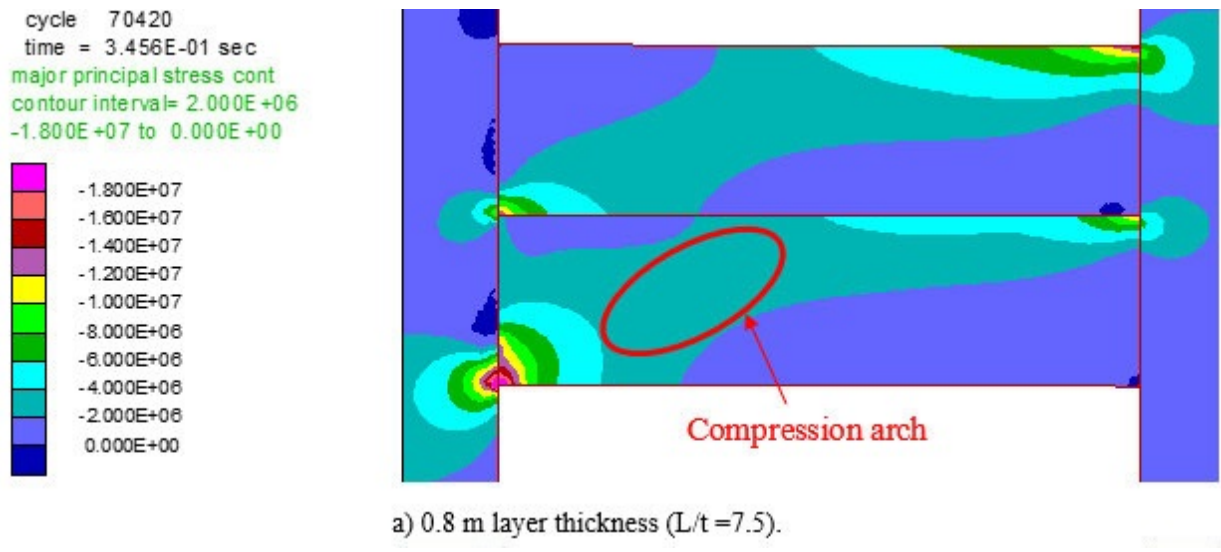


Figure 4.11 (a-d) Maximum principal Stress contour of half- length solid beam model for different lamination thickness





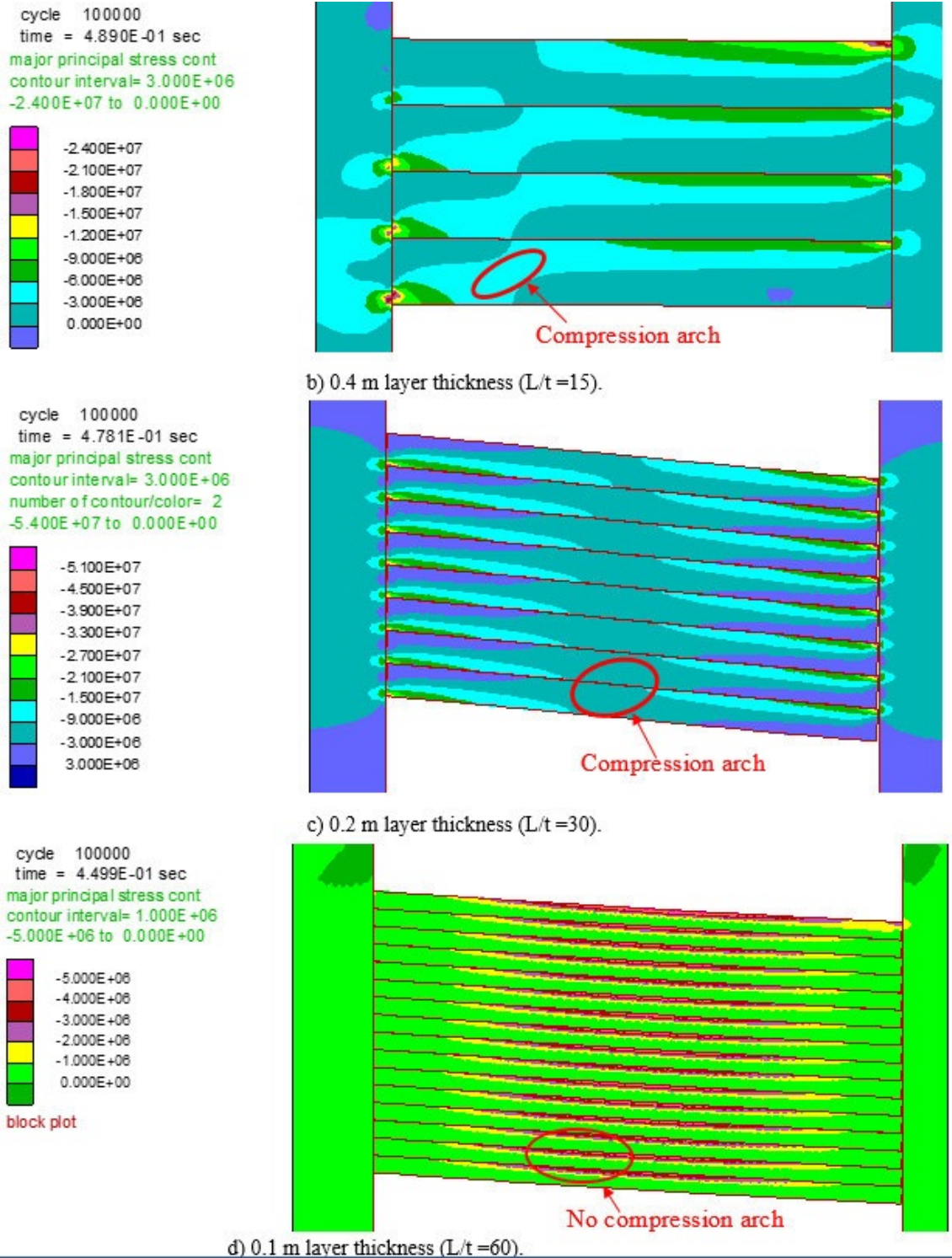


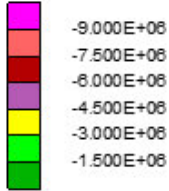
Figure 4.12 (a-d) Maximum principal Stress contour of half- span Voussoir beam model for different lamination thickness

Figure 4.13a-d shows the maximum principal stress distribution in the solid beam model on elastic abutment with varying lamination. In the multi-layered beam, compression arch was formed in each layer with maximum stress concentration at their upper surface around mid-span and at their lower surface around abutment. This trend clearly indicate that failure in each layer except bottom one can also initiate at their upper surface.

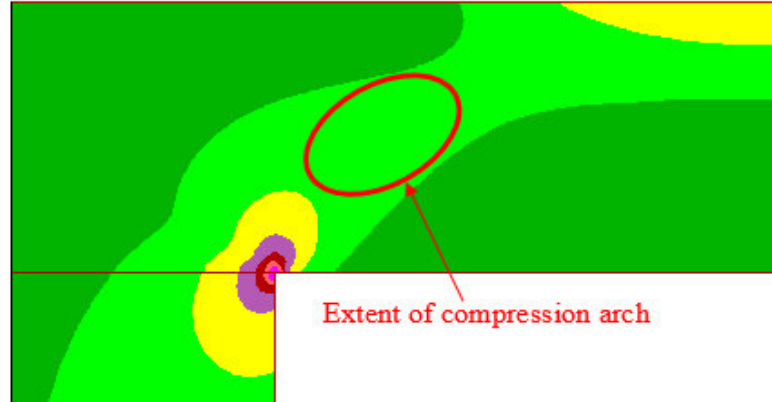
The maximum stress magnitude varied from 7 MPa in 1-layer to 18 MPa in 8 layer beam and was concentrated near the left corner at the abutment. Similarly, the maximum shear stress distribution trend matched earlier observation. The results also indicate that shear failure would initiate at this abutment corners in bottom layer especially in case of thinly laminated beams. Additionally, extent of the compression arch (highlighted by red circle) has decreased with decreased in lamination thickness with no compression in 8 layer laminations case (Figure 4.13d). The decrease in extent of compression arch is due to large bending of individual layers, which reduced their ability to sustain vertical load. This trend is also confirmed by increased in roof deflection from 0.2 mm in 1-layer lamination to 33 mm in 8 layer laminations case. The roof large deflection in 8-layer case clearly indicates the beam tendency to buckling with further decrease in lamination thickness. Uncontrolled buckling did not occur in this model as beam was simulated under elastic state.

It is concluded from the analysis that in the multi-layered beam, each layer would act as a separate beam reducing the stiffness of entire system that would lead to higher bending of entire beam and stress concentration at abutment corners. The failure initiate is most likely shear at entry corners in all thickness. Further, thinly laminated beam is most likely to undergo buckling.

cycle 13381  
 time = 6.713E-02 sec  
 major principal stress cont  
 contour interval= 1.500E+06  
 -9.000E+06 to -1.500E+06

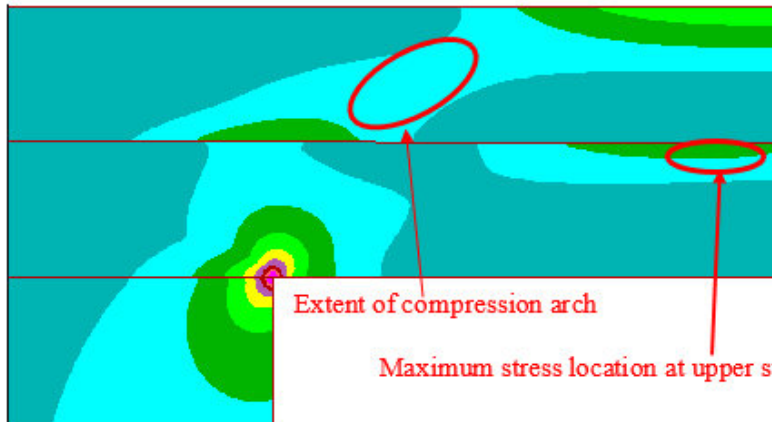
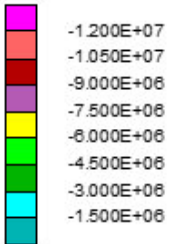


block plot



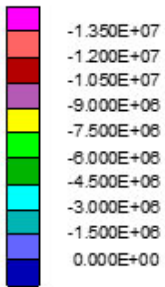
a) 1.6 m layer thickness ( $L/t=3.75$ ).

cycle 37450  
 time = 1.874E-01 sec  
 major principal stress cont  
 contour interval= 1.500E+06  
 -1.200E+07 to -1.500E+06

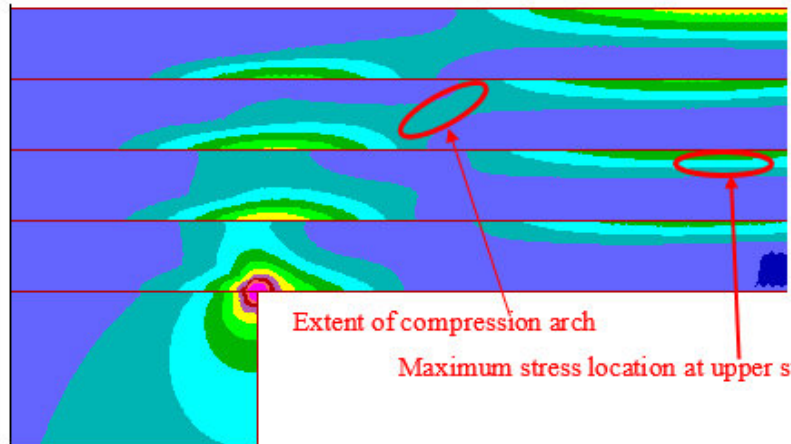


b) 0.8 m layer thickness ( $L/t=7.5$ ).

time = 4.081E-01 sec  
 major principal stress cont  
 contour interval= 1.500E+06  
 -1.350E+07 to 0.000E+00



block plot



c) 0.4 m layer thickness ( $L/t=15$ ).

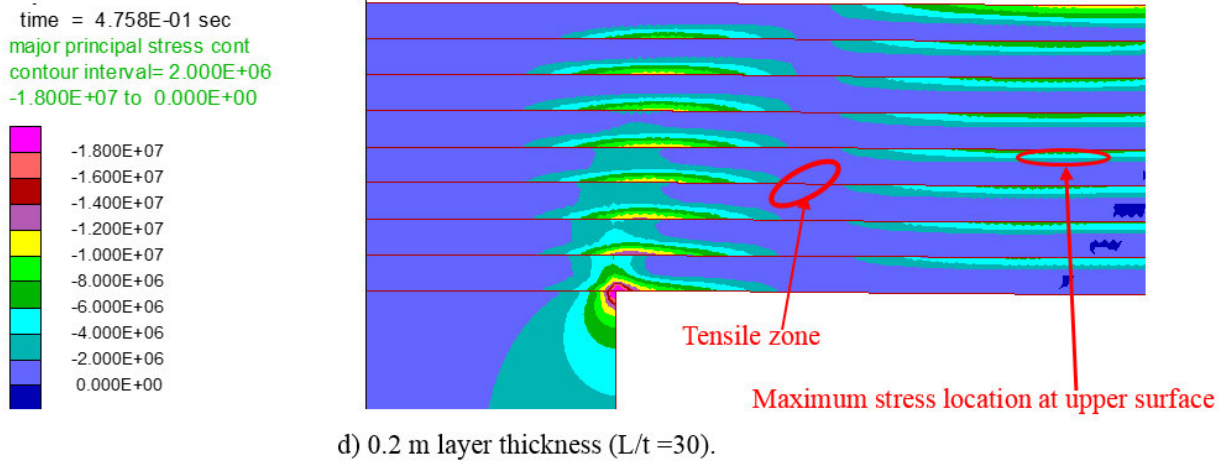


Figure 4.13 (a-d) Maximum principal Stress contour of half- length solid beam on elastic abutment model for different lamination thickness

#### 4.5.2. Horizontal Stress

The horizontal stress was varied by changing the stress ratio from  $K = 0$  to 4. The base models for each beam type including interface properties are same as used in section 4.4.2. Figure 4.14a-c, shows the maximum principal stress tensor in the 4-layer (0.4 m lamination thickness) solid beam model at different horizontal stress, i.e.,  $K$  ratio 0, 2 and 4. The extent of tensile zone (shown in red color) decreased while the extent of compression zone (shown in green color) increased with increase in horizontal stress. It can be attributed to increase in the compressive stress in each element of beam thereby reducing overall beam bending. It can be concluded that horizontal stress would compress each layer of the beam reducing to its overall bending.

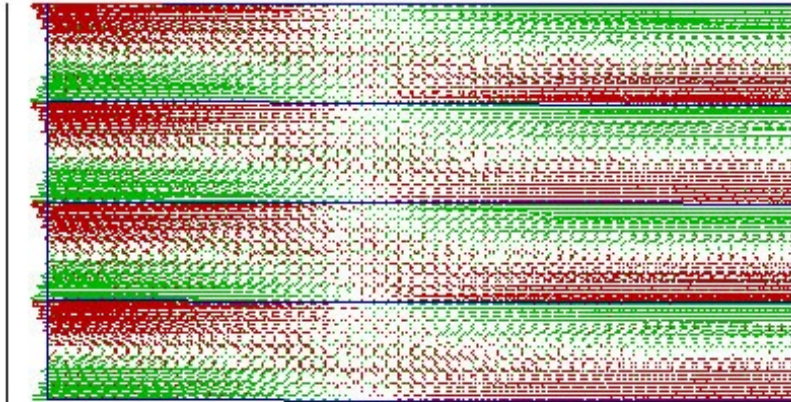
Similar trend was found for solid beam on elastic abutment (Figure 4.15a-c), which showed that the extent of tensile zone decreased with increase in compressive zone. This also showed reduction in effective beam bending with increase in horizontal stress. This trend can attributed to horizontal stress compressing each zone in the beam as suggested decreased in maximum tensile stress by 3.9 MPa from  $K=0$  to 4.

In Voussoir beam model, influence of horizontal stress was similar to other two beam models with effective bending of beam decrease with increase in the horizontal stress. Figure 4.16a-c

shows maximum principal stress tensor in the 4-layer (0.4 m lamination thickness) Voussoir beam model at different horizontal stress. The maximum tensile stress concentration decreased from 14.6MPa at 0 MPa (K=0) to 7.56 MPa at -3.6 MPa (K=4) horizontal stress (Figure 4.16a-c). Additionally, the crack length decreased from 0.35 (85 % of joint length) to 0.28m (70% of joint length) at K=4. From these results, it is concluded that decrease in overall bending of Voussoir beam occurred with increase in the horizontal stress. The horizontal stress compresses each element in the beam thereby reducing effective bending of the beam along with stress increase in compressive zone. However, the maximum compressive stress decreased by small amount (6.98 MPa) from k=0 to k=4. This trend indicates that increased stress in the compression zone due to increase in horizontal stress was compensated by reduction in overall bending. Therefore, analysis of maximum principal stress contours showed an increase in area of compression zone with constant average stress in the compression.

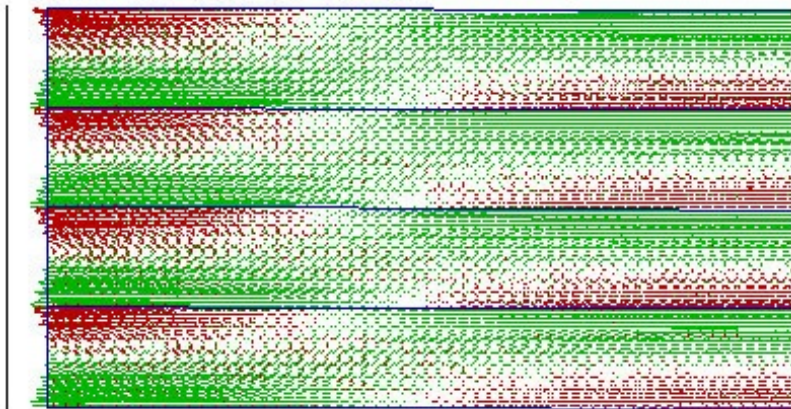


time = 8.482E-02 sec  
principal stresses  
minimum = -1.798E+07  
maximum = 1.875E+07  
magnified block deformation  
magnification = 1.200E+00



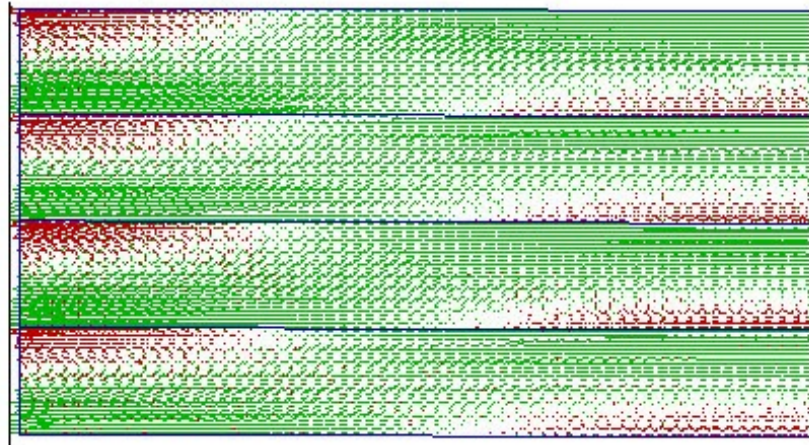
a) 0 MPa (K=0) horizontal stress.

time = 8.429E-02 sec  
principal stresses  
minimum = -1.990E+07  
maximum = 1.708E+07  
magnified block deformation  
magnification = 1.200E+00



b) -1.8 MPa (K=2) horizontal stress

time = 8.314E-02 sec  
principal stresses  
minimum = -2.181E+07  
maximum = 1.541E+07  
magnified block deformation  
magnification = 1.200E+00

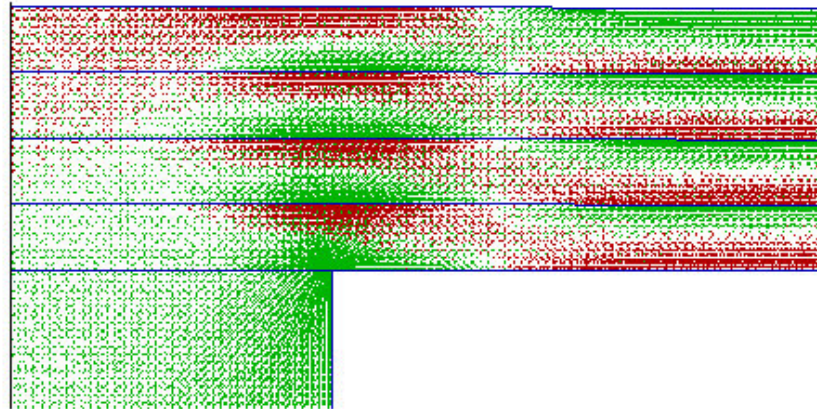


c) -3.6 MPa (K=4) horizontal stress

Figure 4.14 (a-c) Principal Stress tensor plot of half-span 4-layer solid beam at different horizontal stress.

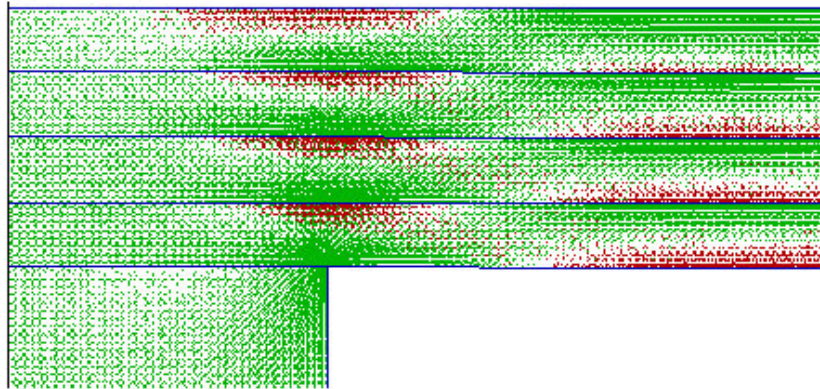


cycle 82011  
time = 4.081E-01 sec  
principal stresses  
minimum = -2.549E+07  
maximum = 9.659E+06  
magnified block deformation  
magnification = 1.200E+00



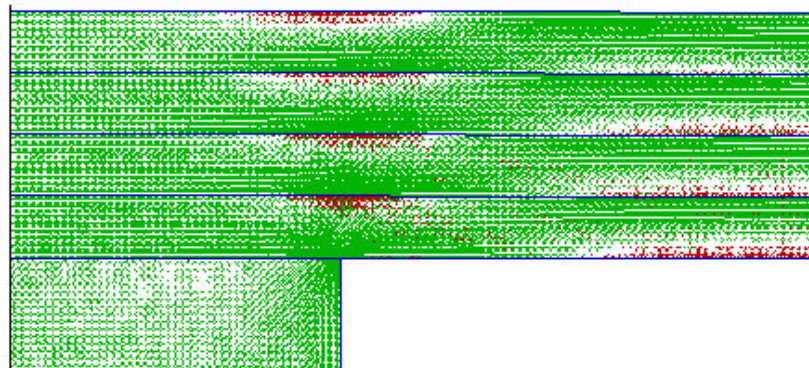
a) 0 MPa (K=0) horizontal stress.

cycle 77660  
time = 3.865E-01 sec  
principal stresses  
minimum = -2.755E+07  
maximum = 7.605E+06  
magnified block deformation  
magnification = 1.200E+00



b) -1.8 MPa (K=2) horizontal stress

cycle 70741  
time = 3.521E-01 sec  
principal stresses  
minimum = -2.899E+07  
maximum = 5.753E+06  
magnified block deformation  
magnification = 1.200E+00



c) -3.6 MPa (K=4) horizontal stress

Figure 4.15 (a-c) Principal Stress tensor plot of half-length 4-layer solid beam on elastic foundation at different horizontal stress,



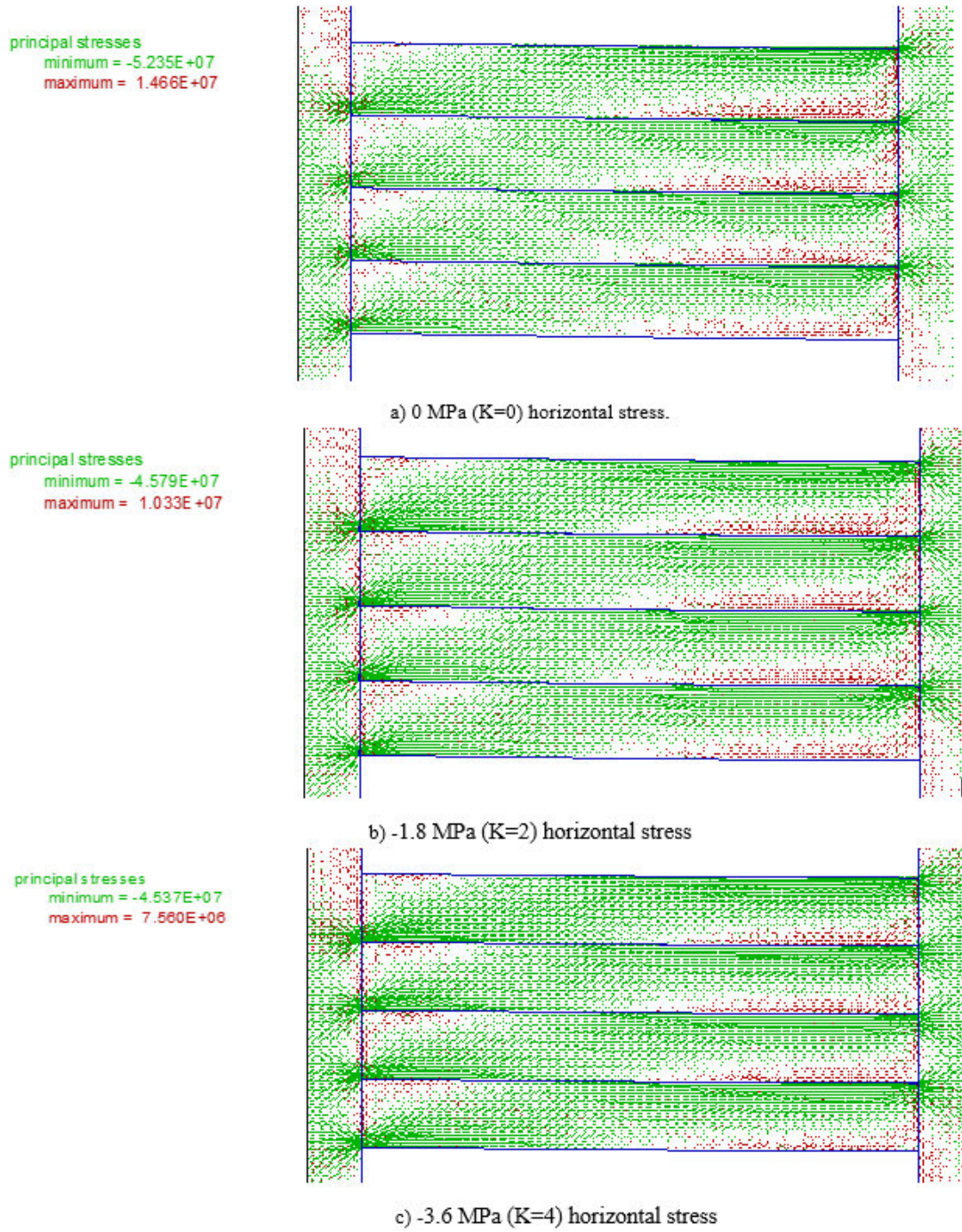


Figure 4.16 (a-c) Principal Stress tensor plot of half-length 4-layer Vousoir beam at different horizontal stress.



#### 4.5.2.1. Influence of lamination thickness under high horizontal stress

The influence of lamination thickness was evaluated under the horizontal stress of -3.6 MPa ( $K=4$ ) to layer interaction at the low thickness and high horizontal stress. The lamination thickness was varied from 1.6 to 0.1 m.

Figure 4.17a-d shows the maximum principal stress for lamination thickness of 1.6 to 0.2 m under -3.6 MPa ( $K=4$ ) horizontal stress. The stress concentration trend is similar to the results from lamination thickness analysis with no horizontal stress (Figure 4.11a-d in section 4.5.1). However, the stress concentration in compression arch was higher for all lamination thickness cases indicating lower bending than the models with stress ratio  $K=0$ . In addition, the extent of compression arch is higher beam models with  $K=0$  as seen in 8 layer case (Figure 4.11d and 4.17d). This trend is due to increase in compression with the increase in horizontal stress for all lamination thickness.

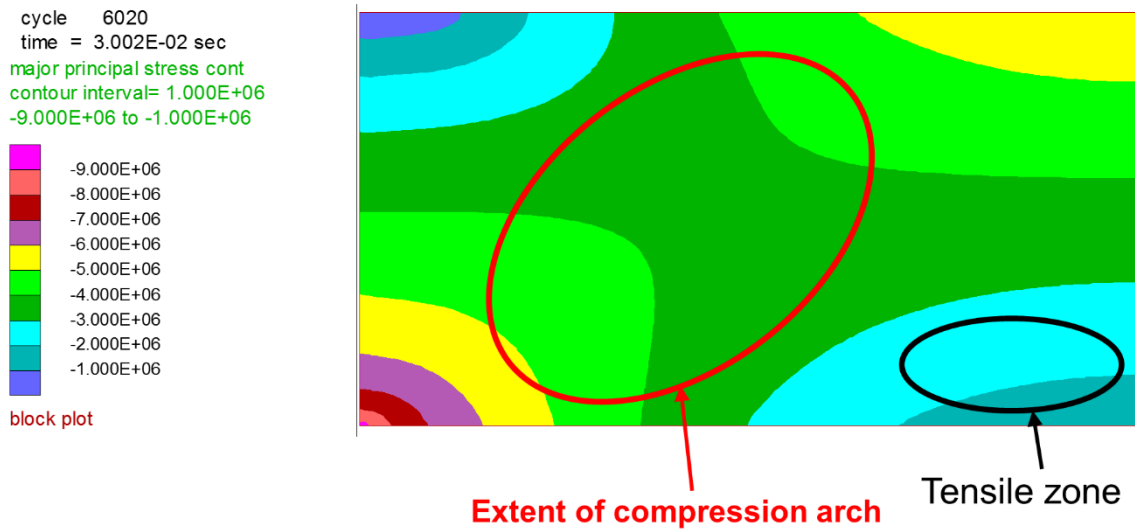
Under high horizontal stress, the entire span of beam especially with large lamination thickness is most likely to be under compression as seen in case of 1.6 m lamination thickness (Figure 4.17a) where the extent of the tensile zone is small (highlighted by a black circle). As lamination thickness is decreased, higher bending creates the larger magnitude of tensile stresses, which negates the compressive stress resulting in the contraction of the compression zone (Figure 4.17b-d). Therefore, in thick beams under high horizontal stress shear failure will initiate at the lower abutment corner. Whereas in thinly laminated beams, failure is most likely to initiate under tension at upper abutment corners similar to the beams with low horizontal stress. In addition, the thinly laminated solid beam is also most likely to buckle under high horizontal stress due to layers behaving as slender columns bending under axial load. It is difficult to simulate actual buckling in solid elastic beam model, however, in case of 0.1 m lamination thickness roof deflection increased by 10% as  $K$  was varied from 0 to 4 which suggested that horizontal stress caused higher beam bending instead of compressing it.

A similar trend was found for the solid beam on elastic abutment model (Figure 4.18a-d), which showed same stress distribution along with a decrease in the extent of compression arch (highlighted by the red circle) with the decrease in lamination thickness. The decrease in the extent of compression arch is again due to higher bending which negates the compressive stress resulting in the contraction of the compression zone. The maximum stress concentration occurred at lower abutment corner in the bottom layer and at the upper surface around mid-span of remaining layers. However, maximum stress concentration in bottom layer increased from 14 MPa in 1-layer beam to 24 MPa in the 8-layer beam. Thus, failure initiation is most likely shear at abutment corners in bottom layer especially in case of thinly laminated beams. Additionally, roof deflection similar to the case of beams with  $K=0$  increased by 175 times which suggest the beam is most likely to undergo buckling with further decrease in lamination thickness. Uncontrolled buckling did not occur in this model as the beam was simulated under the elastic state.

It is concluded from the analysis that under high horizontal stress, failure initiation will be at the lower abutment of the bottom layer for all lamination thickness. In thick beams, shear failure can also occur around the mid-span of overlying layers. While buckling is most likely failure in the thinly laminated beam.

In the Voussoir beam, behavior similar to other two models was observed as effective bending increased with the decrease in lamination thickness, which was lower than the model with low horizontal stress for the same layer thickness. Figure 4.18a-c showed maximum principal stress distribution for lamination thickness of 0.8 to 0.2 m under -3.6 MPa horizontal stress. The results indicate that as the thickness decreases the effective bending increases, which leads to higher stress concentration in the compressive arch zone. Furthermore, the crack length of vertical joints increased from 0.38 m (47.5 % of joint length) in the 2-layer beam to 0.39 m (97.5 % of joint length) in the 8-layer beam. The failure initiates with the opening of the vertical joint followed by either localized shear or crushing at abutments.

However, when lamination thickness was less than 0.1m (Figure 4.18d), crack length of the vertical joint was about 98 % of total length (shown by a black rectangle). Therefore, each layer of the beam is under small contact with the rigid block at left and right side (at abutment and mid-span of the beam). The beam with low bending stiffness (horizontal stress acting as an axial force in the slender column) would buckle when bending stiffness is decreased further. This observation is similar to model under zero horizontal stress ( $K=0$ ) however, at larger lamination thickness (0.05 m) as compared to former case (0.02 m thickness under  $K=0$ ) as seen in section 4.5.1.



a) 1.6 m layer thickness ( $L/t = 3.75$ ).

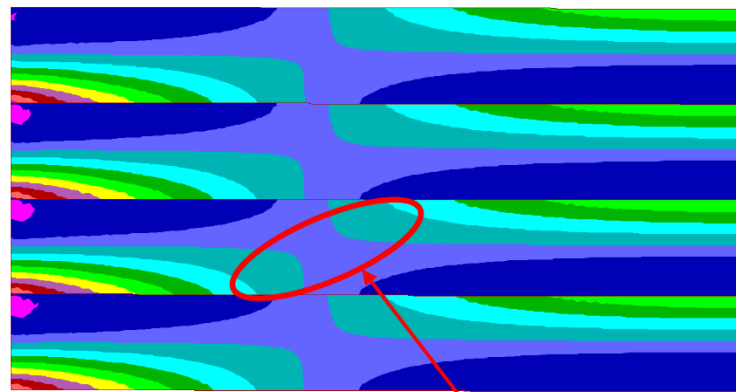
cycle 6970  
 time = 3.384E-02 sec  
 major principal stress cont  
 contour interval= 2.000E+06  
 -1.200E+07 to 0.000E+00  
 -1.200E+07  
 -1.000E+07  
 -8.000E+06  
 -6.000E+06  
 -4.000E+06  
 -2.000E+06  
 0.000E+00  
 block plot



b) 0.8 m layer thickness ( $L/t = 7.5$ ).

**Extent of compression arch**

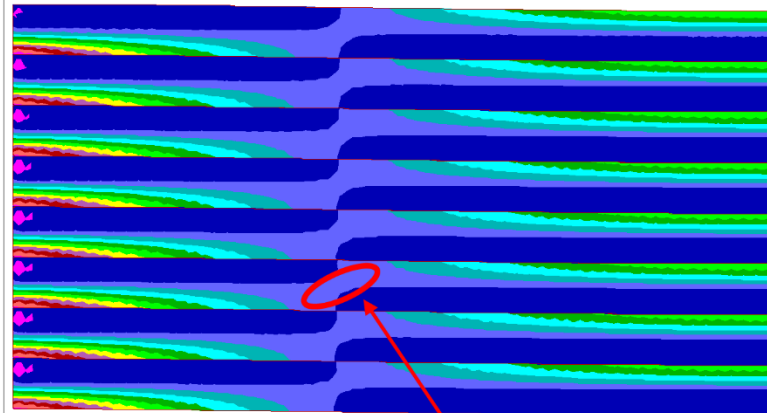
time = 8.314E-02 sec  
 major principal stress cont  
 contour interval= 2.000E+06  
 -2.000E+07 to 0.000E+00  
 -2.000E+07  
 -1.800E+07  
 -1.600E+07  
 -1.400E+07  
 -1.200E+07  
 -1.000E+07  
 -8.000E+06  
 -6.000E+06  
 -4.000E+06  
 -2.000E+06  
 0.000E+00



c) 0.4 m layer thickness ( $L/t = 15$ ).

**Extent of compression arch**

cycle 27250  
 time = 1.303E-01 sec  
 major principal stress cont  
 contour interval= 3.000E+06  
 -3.000E+07 to 0.000E+00  
 -3.000E+07  
 -2.700E+07  
 -2.400E+07  
 -2.100E+07  
 -1.800E+07  
 -1.500E+07  
 -1.200E+07  
 -9.000E+06  
 -6.000E+06  
 -3.000E+06  
 0.000E+00

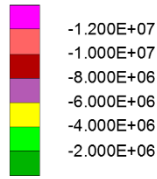


d) 0.2 m layer thickness ( $L/t = 30$ ).

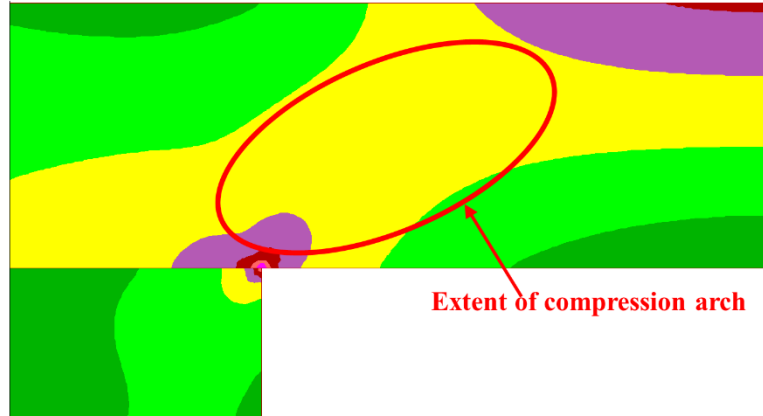
**Extent of compression arch**

Figure 4.17 (a-d) Maximum principal Stress contour of half-span solid beam at -3.6 MPa ( $k=4$ ) horizontal stress for different lamination thickness.

cycle 26840  
 time = 1.346E-01 sec  
 major principal stress cont  
 contour interval= 2.000E+06  
 -1.200E+07 to -2.000E+06

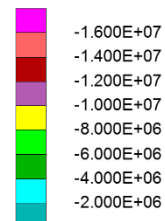


block plot

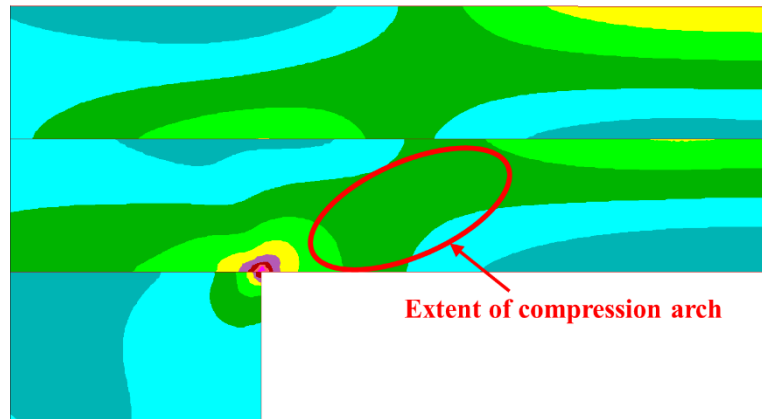


a) 1.6 m layer thickness ( $L/t=3.75$ ).

cycle 35090  
 time = 1.756E-01 sec  
 major principal stress cont  
 contour interval= 2.000E+06  
 -1.600E+07 to -2.000E+06

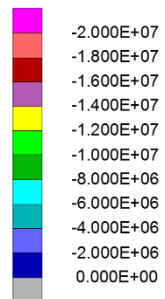


block plot

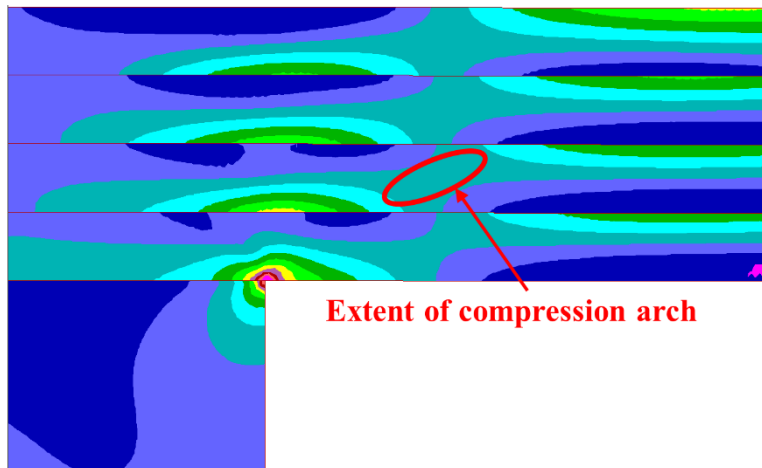


b) 0.8 m layer thickness ( $L/t=7.5$ ).

cycle 70741  
 time = 3.521E-01 sec  
 major principal stress cont  
 contour interval= 2.000E+06  
 -2.000E+07 to 0.000E+00

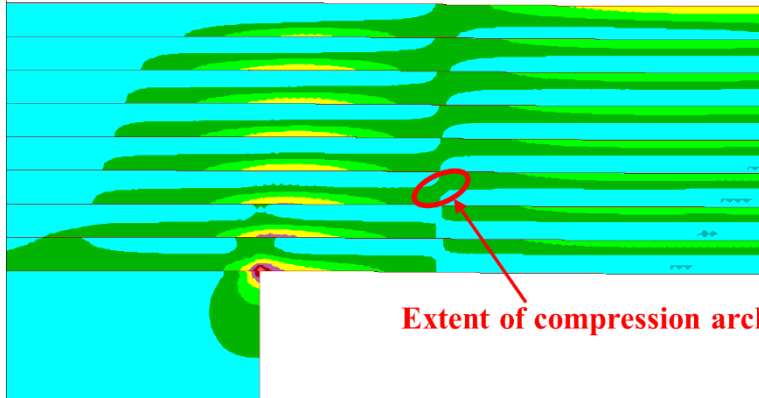
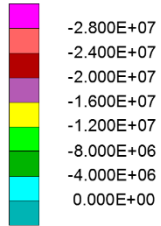


block plot



c) 0.4 m layer thickness ( $L/t=15$ ).

cycle 100000  
time = 4.758E-01 sec  
major principal stress cont  
contour interval= 4.000E+06  
-2.800E+07 to 0.000E+00

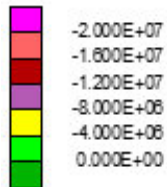


**Extent of compression arch**

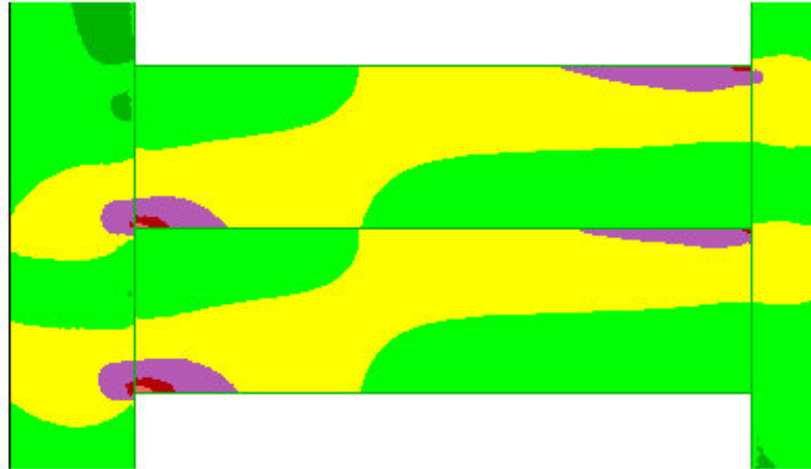
d) 0.2 m layer thickness ( $L/t = 30$ ).

Figure 4.18 (a-d) Maximum principal Stress contour of half-span solid beam on elastic abutment at -3.6 MPa ( $k=4$ ) horizontal stress for different lamination thickness.

cycle 21510  
 time = 1.056E-01 sec  
 major principal stress cont  
 contour interval= 4.000E+06  
 -2.000E+07 to 0.000E+00

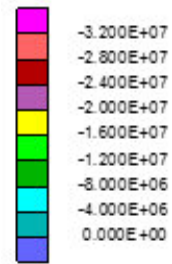


block plot

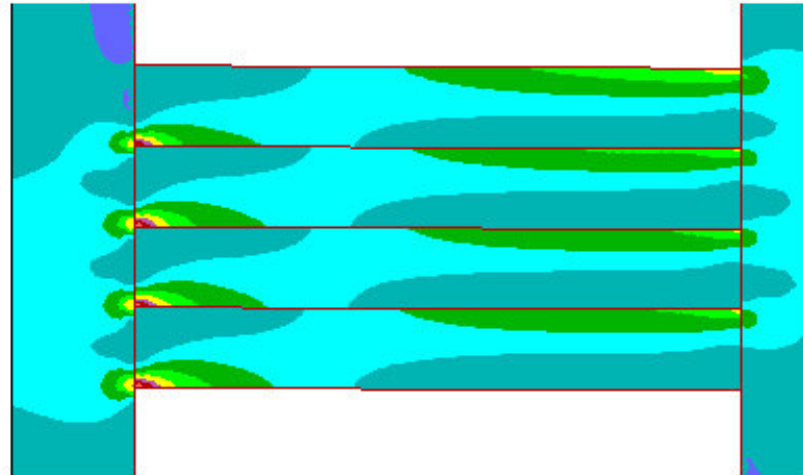


a) 0.8 m layer thickness ( $L/t=7.5$ ).

cycle 53160  
 time = 2.602E-01 sec  
 major principal stress cont  
 contour interval= 4.000E+06  
 -3.200E+07 to 0.000E+00

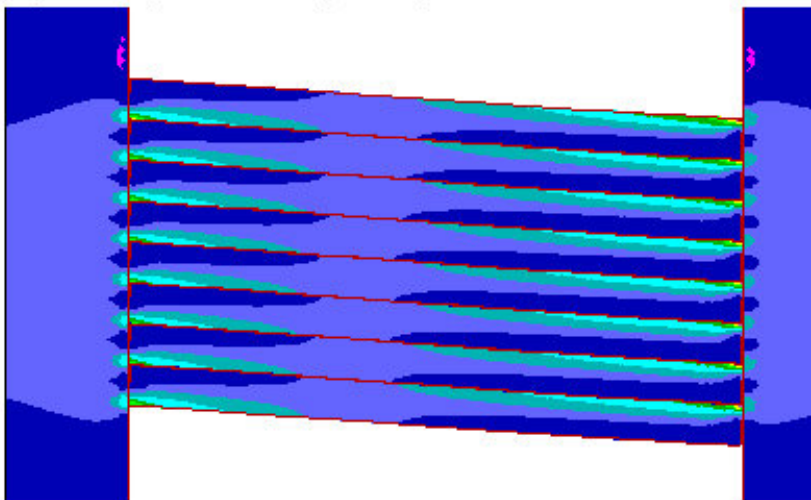
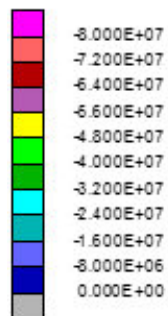


block plot



b) 0.4 m layer thickness ( $L/t=15$ ).

cycle 100000  
 time = 4.781E-01 sec  
 major principal stress cont  
 contour interval= 4.000E+06  
 number of contour/color= 2  
 -8.400E+07 to 0.000E+00



c) 0.2 m layer thickness ( $L/t=30$ ).

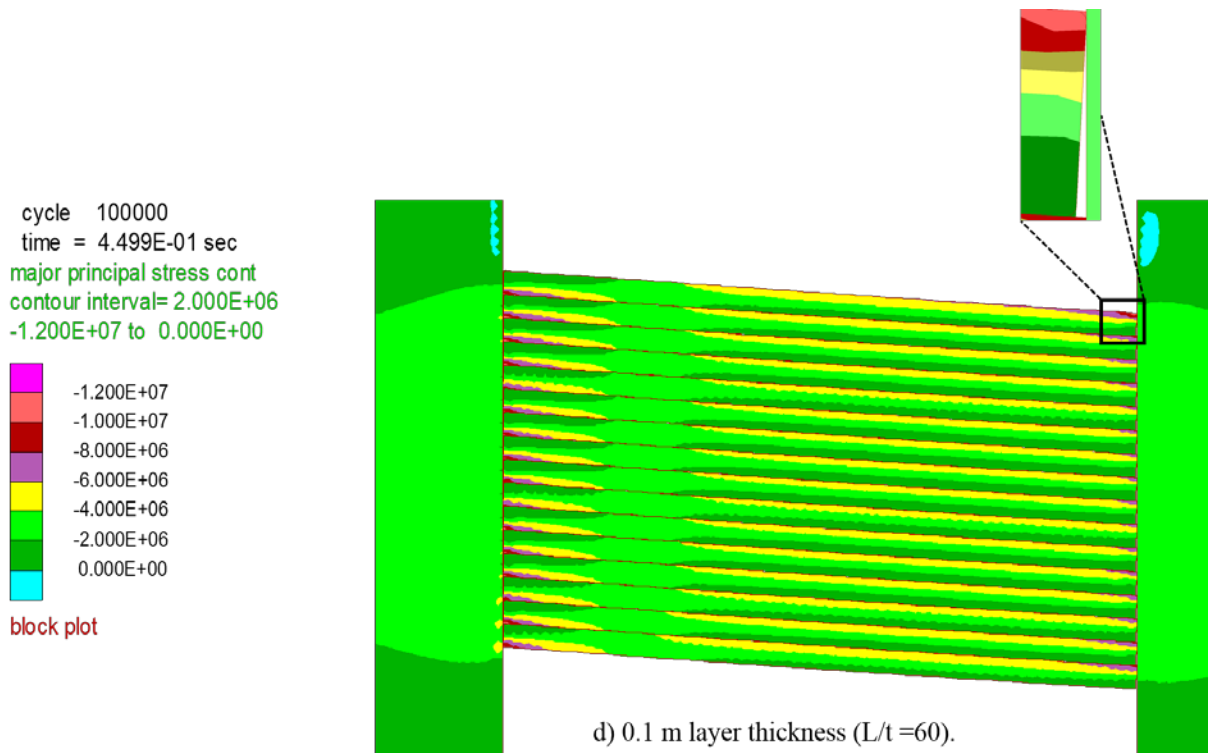


Figure 4.19 (a-d) Maximum principal Stress contour of half-span Voussoir beam at -3.6 MPa ( $k=4$ ) horizontal stress for different lamination thickness.

### 4.5.3. Influence of Joint Strength and Stiffness

The influence of weak plane or laminar plane was simulated using joint elements. The joint element in UDEC is a contact surface formed between two block edges. The elements represent elastic springs that resist normal and shear deformation based on their stiffness and strength parameters. The input properties mentioned in section 4.5.1 are used in this section with constant horizontal stress of -3.6 MPa ( $K=4$ ) magnitude applied to the model. The influence of joint parameters on the bending profile and stress distribution on the roof was studied using three beam models mentioned in the earlier section.

The influence of joint stiffness was evaluated in terms of normal stiffness and  $K_n / K_s$  ratio. In addition, there is a limit to the maximum value of stiffness that can be used in the UDEC model (Itasca, 2001a). The limit is sensitive to the adjacent zone size and rock modulus and therefore



was used as a “reference” for this parametric analysis. The results of this analysis show that joint stiffness does not affect the stress distribution in beams. It was also found that if the normal stiffness of joint is greater than half of the rock modulus, the extent of the joint opening (between two layers of the beam) increases with increase in its normal stiffness.

The influence of joint (laminar plane) strength was evaluated in terms of its cohesion and tensile strength. As discussed in section 3.2.5 of chapter 3, laminar planes have significantly higher shear and tensile strength as compared to infilled joints or bed based on laboratory scale studies. However, on the field scale, most studies assume lamination with zero or negligible tensile strength and low shear strength. Therefore, it is vital to understand the influence of joint properties on layer interaction and stress distribution within the shale roof. Three cases were simulated to investigate the influence of interface strength. Case 1 and case 2 studied the influence of interface cohesion on layer interaction. While case 2 and case 3 were used to study the influence of interface tensile strength.

Table 4.1 Joint strength parameters used in parametric study

	<b>Shear Strength</b>		<b>Tensile Strength (MPa)</b>
	Cohesion (MPa)	Friction Angle (degrees)	
Case 1	0.13	25 <sup>0</sup>	0
Case 2	0.13	25 <sup>0</sup>	0.3
Case 3	1.3	25 <sup>0</sup>	0.3

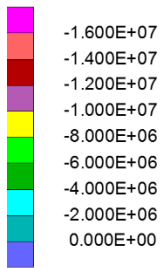
Figure 4.20a-c show the maximum principal stress for three cases of interface strength parameters (Table 4.1). The stress distribution as well magnitude is the same in cases 1 and 2. Additionally, no layer separation was observed in any cases, which suggested that the interface tensile strength does not affect the bending profile of the solid beam model. However, when interface cohesion was increased to 1.3MPa in case 3, stress distribution changed completely as compared to cases with low cohesion (Figure 4.20b-c).

In case 3, compression arch initiates from the lower corner in the bottom layer to top right corner in the top beam with 4-layers acting as a single beam (Figure 4.20c). Therefore, shear failure will initiate at the lowest left abutment corners. Additionally, the extent of the tensile zone at abutment is only limited to the top layer which reduces the chances of tensile failure at the top abutment corners in individual layers. In the other two cases, the compression arch is formed in each layer (Figure 4.20a-b) along with the formation of the tensile zone at the top right corner of each layer. Further, inter-layer slipping was observed along the entire joint length that allowed layers to act as separate beams and thus no or minimal layer interaction in these two cases. Thus, failure initiation in case 1 and 3 is most likely tension failure at top left corners of each layer. While in case 2, no inter-layer slipping was observed. This showed that high interface cohesion (1.3MPa in this study) prevented slip in layers and thereby layers act as a composite beam. It is concluded that failure initiation and layer interaction in laminated roof only depends on the interface shear strength and is independent of its tensile strength. A similar trend was observed in the solid beam on elastic abutment model where with high interface cohesion in case 3, multi-layer beam acts as single composite beam (Figure 4.21c). While in case 1, layers act as individual beams with no or minimal layer interaction (Figure 4.21a-b). However, the bending stress in the beam with elastic abutment was higher than the solid beam model. In addition, failure initiates at the lowest left corner of abutment under shear irrespective of interface strength. Whereas, in solid beam model, interface strength especially shear strength will decide the failure initiation and its location.

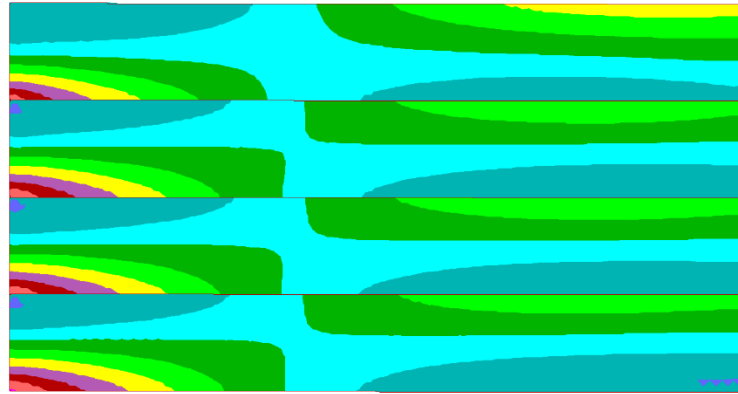
Figure 4.22a-c show maximum principal stress distribution in the Voussoir beam model for different joint strength parameters. Similar to other two models, stress distribution is identical between case 1 and case 2 which suggest no significant influence of interface tensile strength. In addition, vertical joint opening (0.28 m; 70% of total joint length) was the same in both cases 1 and 2. While in case 3, the joint opening decreased to 0.11 (12.5% of total joint length) which indicate a significant reduction of overall beam bending in this case as compared to the other two cases.

In case 3, compression arch initiates from the lower corner in the bottom layer to top right corner in the top beam with 4-layers acting as a single beam (Figure 4.22c). Additionally, vertical joint has only opened up in left abutment corner of top layer suggesting that only top will undergo tensile failure initiation. While in the other two cases, compression arch is formed in individual layers (Figure 4.22a-b). This difference in stress distribution between case 3 and 2 was due to high joint cohesion in case 3 which prevented any slip along the horizontal joints thereby increasing overall bending stiffness of beam. The increase in bending stiffness also resulted in the decrease in bending stresses as seen in Figure 4.22b-c. The maximum stress concentration was around 20-24 MPa in case 2 which decreased to 12-14 MPa in case 3. From this analysis, it is concluded that in Voussoir beam, layer interaction is highly depended on joint cohesion and is independent of joint tension. In addition, failure initiation is most likely tensile, and only its location would depend on joint shear strength. For high cohesion joint, tensile failure would initiate only in top layer as opposed to in each layer in the case of low cohesion joint. The final failure mode will most likely be crushing whose location would again depend on joint cohesion.

time = 3.575E-01 sec  
 major principal stress cont  
 contour interval= 2.000E+06  
 -1.600E+07 to 0.000E+00

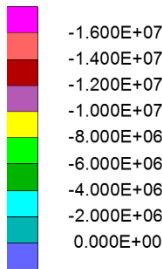


block plot

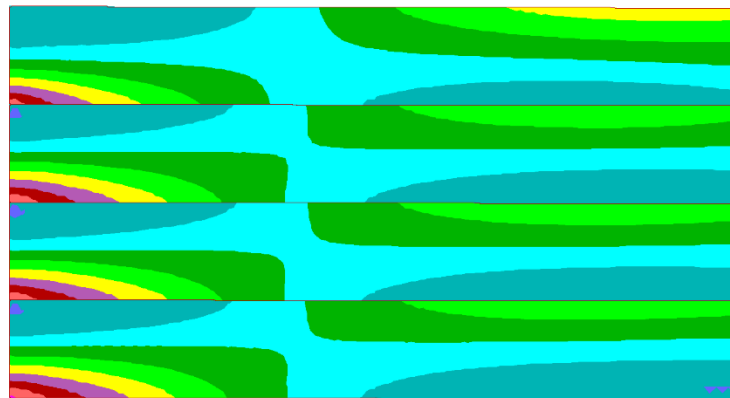


a) Case1

time = 3.491E-01 sec  
 major principal stress cont  
 contour interval= 2.000E+06  
 -1.600E+07 to 0.000E+00

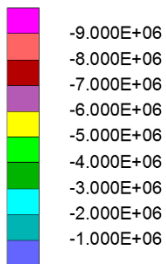


block plot

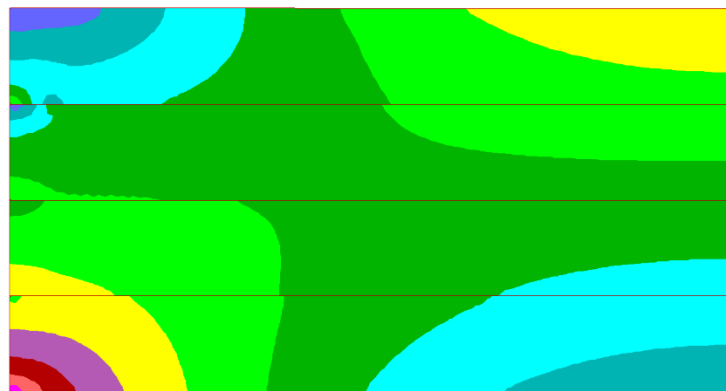


b) Case2

time = 2.449E-02 sec  
 major principal stress cont  
 contour interval= 1.000E+06  
 -9.000E+06 to -1.000E+06



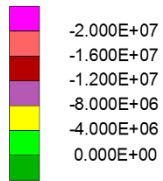
block plot



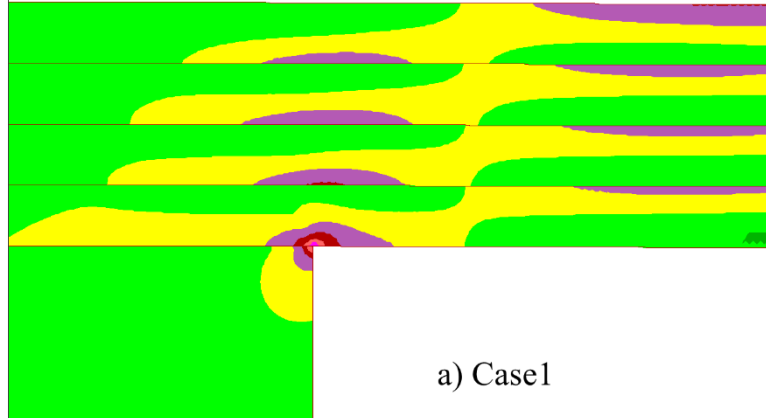
c) Case3

Figure 4.20 (a-c) Maximum principal stress contour of half-length 4-layer solid beam for different interface strength.

cycle 70741  
time = 3.521E-01 sec  
major principal stress cont  
contour interval= 4.000E+06  
-2.000E+07 to 0.000E+00

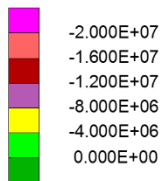


block plot

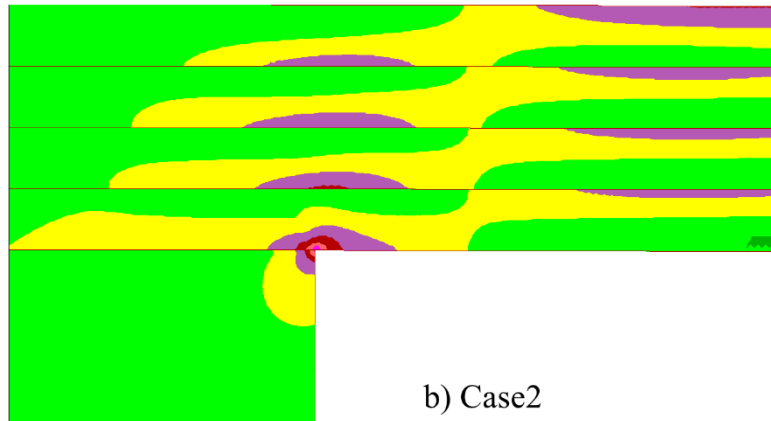


a) Case1

cycle 70330  
time = 3.500E-01 sec  
major principal stress cont  
contour interval= 4.000E+06  
-2.000E+07 to 0.000E+00

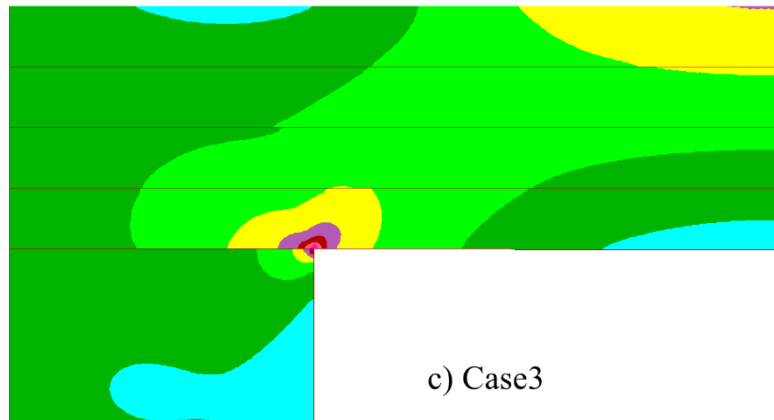
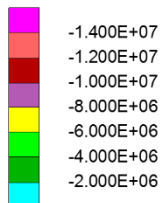


block plot



b) Case2

cycle 33790  
time = 1.682E-01 sec  
major principal stress cont  
contour interval= 2.000E+06  
-1.400E+07 to -2.000E+06



c) Case3

Figure 4.21 (a-c) Maximum principal stress contour of half-length 4-layer solid beam on elastic abutment for different interface strength.

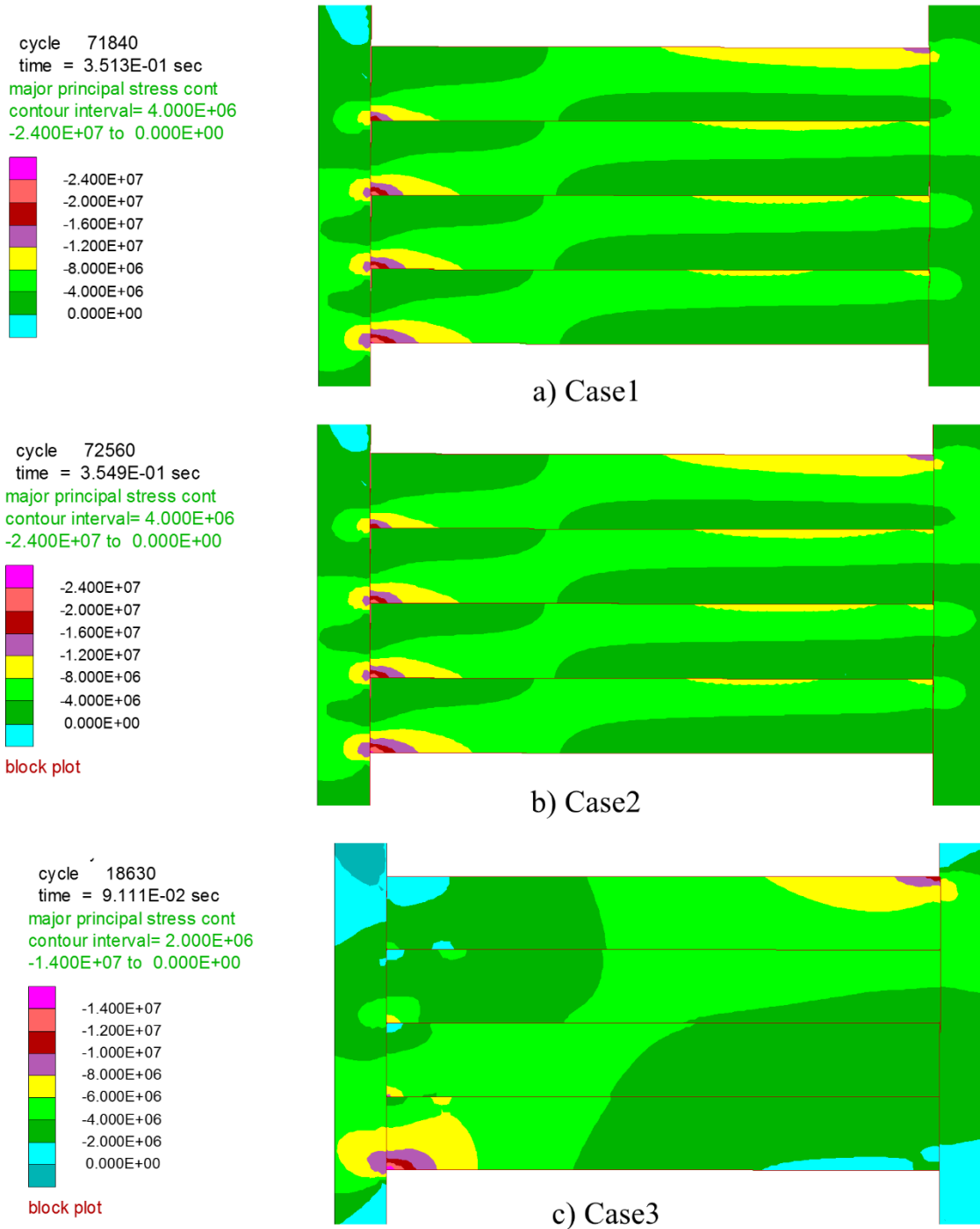


Figure 4.22 (a-c) Maximum principal stress contour of half-span 4-layer Voussoir beam for different interface strength.

#### 4.5.4. Limitation of elastic beam analysis

In this chapter the elastic beam analysis was performed to understand layer (laminar) interaction and stress distribution in a laminated shale roof under high-horizontal stress. However, this analysis has some limitation, which are as follows

- Analysis is limited to elastic conditions and thus only failure initiation can be estimated.
- Layer interaction under plastic state could not be investigated.
- High in-situ stress conditions cannot be simulated
- Bending profile of bolted shale roof was not studied.

As beam models were simulated under elastic condition, only location failure initiation can be estimated based on stress distribution. Therefore, layer interaction within a shale roof will be based on lamination stiffness and initial stress conditions. Therefore, layer interaction within a laminated roof will be based on stiffness and initial stress conditions. The influence of rock strength and roof bending under plastic deformation on layer interaction would be ignored. As discussed in section 3.7.2 of chapter 3, the extent of failure in shale roof changed its bending profile and thereby affecting the layer interaction.

The beam models analyzed in this chapter were loaded under uniform load. In field conditions, the uniform load profile on immediate roof would only be valid when the pressure arch is within the roof, which represent low in-situ stresses. Therefore, the load profile on the beam should be based on the pressure arch on the immediate roof to simulate high in-situ stress conditions. Additionally, for low lamination thicknesses all beam models suggested buckling as most likely failure. However, in the field, the roof is typically bolted or some other supports and therefore roof buckling rarely occurred in the field.

## 4.6 Summary

In this chapter, elastic beam analysis was performed to understand layer interaction in a laminated shale roof under uniform loading. Three beam models namely: Solid beam model, Voussoir beam model, Solid Beam on Elastic Abutment beam were simulated in UDEC. The advantage this approach is simplified bending profile of immediate roof as compared to the anisotropic mine model in chapter 3. This analysis provided a detailed understanding of the stress distribution and layer-interaction within the laminated roof. The three beam models provided detailed insight into the influence of horizontal stress and lamination parameters on layer interaction and bending profile of shale roof but within elastic limit. The important findings are as follows:

- In the solid beam model, rigid support created high tensile stress concentration zone at top abutment corner of roof that would result in tensile failure.
- In the multi-layered solid beam model, under low horizontal stress, the bending stiffness of roof decreased with decrease in layer thickness causing high bending stress. The increase in overall bending of the beam results in tensile failure at the top abutment corners of each layer. In addition, the model showed unrealistic bending of the roof for lamination thicknesses below 0.1m.
- In the Voussoir beam model, opening of vertical joints at abutment with roof bending clearly indicated tensile failure initiation at these locations. Final failure mode of roof can be buckling, crushing or slippage at the abutments depending on layer thickness and loading conditions.
- In the multi-layered Voussoir beam model, under low horizontal stress, overall roof bending increased with the decrease in layer thickness resulting in higher joint opening and stress concentration in compressive zone. The failure mode will most likely be crushing at the lower abutment and upper mid-span corner due high shear stress concentration for span to thickness ratio ( $L/t$ ) greater than 30.
- However, for thinly laminated Voussoir beam, i.e., span to thickness ratio ( $L/t$ ) less than 60, buckling is most likely failure due to complete opening of vertical joints.



- In the solid beam on elastic abutment model, shear failure initiates at the lower abutment corner in the absence of rigid support, which reduces high tensile stress concentration zone at top abutment corner.
- In the multi-layered solid beam on elastic abutment model, under low horizontal stress, the influence of lamination was similar to other model with increase in overall beam bending.
- High horizontal stress reduced overall roof bending in all three-beam models as it compressed each element of the beam.
- Under high horizontal stress, only solid beam on elastic abutment model suggests shear failure initiation at entry corners, which makes it most appropriate model to simulate the laminated roof. The other two-beam models solid beam and Voussoir beam model suggested tensile failure initiation at the top abutment corners.
- For thinly laminated roof, the three models suggested buckling as most likely failure especially under high horizontal stress.
- Laminar interaction in all the three models was found to be highly depended on the joint (laminar plane) cohesion. The multi-layered roof function as a composite beam under high joint cohesion.

## 5. PLASTIC BEAM ANALYSIS

### 5.1 Introduction

In previous chapter elastic beam analysis was performed to understand the layer interaction in a laminated shale roof with high-horizontal stress. As mentioned in section 4.8, a solid beam on elastic abutment was the most appropriate model to simulate the laminated roof under high horizontal stress as it showed shear failure initiation at entry corners. However, elastic analysis suffers from drawbacks, which are discussed in section 4.5.4. One significant limitation is the role of layer interaction on failure propagation in shale roof, which is beyond the scope of elastic analysis. In addition, the influence of high in-situ stress condition was ignored by applying uniform load on the roof beams over an entry. Finally, for in-situ conditions, the uniform load is applied only when low in-situ stresses are present, and pressure arch is formed within the shale roof. Based on these limitations, elastic beam models are not suitable for understanding the progressive failure in the laminated roof.

In this chapter, plastic beam analysis was performed using a solid beam on elastic abutment model. The analysis was performed in FLAC3D. High in-situ stress condition was simulated using the methodology presented in section 5.2. The model formulation and its comparison with anisotropic mine model is presented in section 5.3. The influence of horizontal stress and lamination parameters on layer interaction during failure propagation was investigated through parametric plastic analysis.

### 5.2 Load profile on shale roof of beam model

As seen in section 4.3-4.5 of chapter 4, analysis using beam models involved bending either under their own weight or under a uniform vertical load. The majority of the beams models (Evans, 1941; Panek, 1956; Stephansson, 1971; Sheorey, 1976; Sterling, 1980;) were developed between 1950 and 1970 which included analytical techniques for deriving deformation and stress distribution in the roof after excavation of an entry or a longwall face. Therefore, uniform load was assumed to simplify the calculation as computational efficiency was quite low at that time. Additionally, there was another type of approach, which assumed formation of pressure arch after entry is created and roof within the dome is loaded under its own weight (Dinsdale, 1935; Duvall,

1948). The analytical solutions were derived based on the theory of elasticity to determine the stress distribution around an opening. This approach accounts for the high *in-situ* stresses by assuming non-uniform load on roof over entry. However, stress distribution was found to be independent of roof stiffness. For instance, the Kirsch solution for stresses around circular opening under plane stress condition and Panek's solution under plane strain condition are independent of the elastic moduli of the surrounding rock. However, deformations observed in mines indicate that stiffness significantly affects roof stability/instability. In fact, it may be concluded that both approaches individually will produce unrealistic stress conditions around the roof.

In the current study, these two approaches were combined together and deformation in an immediate roof after excavation of the entry was approximated as a two-step process. In the first step, stress distribution after excavation of the entry is calculated. The resulting induced stresses around the opening considers the pressure arch formed over the roof. In the second step, the immediate roof is assumed as a multi-layered beam, which bends under the induced stress thereby changing the stress distribution in the roof. This approach considers the roof rock type, its properties, *in-situ* stress state, and size and shape of the opening; and therefore, will produce more realistic roof behavior. However, the stress distribution produced using this approach will be less accurate as compared to an anisotropic model used in chapter 3. A major advantage in using this approach is that it reduces the model complexity. The load profile over the immediate roof will be fixed which eliminates the role of overburden stiffness and its interaction with immediate roof. As discussed in section 3.2.7 of chapter 3, the limitation of the anisotropic model will be eliminated by this simplified approach.

As mentioned above, vertical load profile on the immediate roof just after the formation of pressure arch was estimated in the first step. This was followed by the second step, which included implementing the vertical load profile on the solid beam on the elastic abutment model. Stress in the roof was estimated using analytical solution based on the theory of elasticity. Mindlin in 1939 first developed the analytical solution for stress distribution around opening using theory of elasticity. He solved the problem of stresses around a horizontal cylindrical hole of circular cross-section in a semi-infinite elastic solid stressed by gravity under plane strain condition. Using a polar coordinate system (Mindlin, 1939), an exact solution of classical elasticity was

obtained. Afterward, Panek, 1951, compared his solution of the same problem under plane stress condition with Mindlin's results. He found that for the ratio of depth to diameter of the hole is more than 2.5 both solutions are approximately same. Further, Panek, 1951 reduced the stress distribution around the opening to the classical problem of a thin plate with a small hole at the center. In this research, the opening is rectangular and analytical solutions are not available to provide stress distribution for rectangular openings. As elliptical opening is the closest shape for which analytical solution is available, stress distribution around it in a thin plate was compared with the results of the rectangular opening using a numerical model. The analysis indicated that there was a significant difference in the stress magnitudes for points, which were located from the opening with distances, less than the span of rectangular opening. Therefore, approximated solution based on conformal mapping was used (Savin, 1961). In this method, using special shape function (Figure 5.2a), a cross-section of the rectangular opening was transformed to a circle of unit radius (Figure 5.1). The analytical solution for stress around this transformed circular opening was derived using Airy stress function under plane stress condition in the curvilinear coordinate system (Timoshenko, 1959). The vertical load at discrete points on the immediate roof was determined by transforming stress in horizontal and vertical direction. The estimated vertical load profile was derived for same base model as used in section 3.2.3 which included immediate roof of 1.8 m thickness over 6 m span rectangular entry. Figure 5.2b, shows the variation of vertical load over immediate roof along the horizontal direction and  $x=0$  represents the center of the opening in horizontal direction. This load was then applied on the top immediate roof in the beam with elastic abutment model.

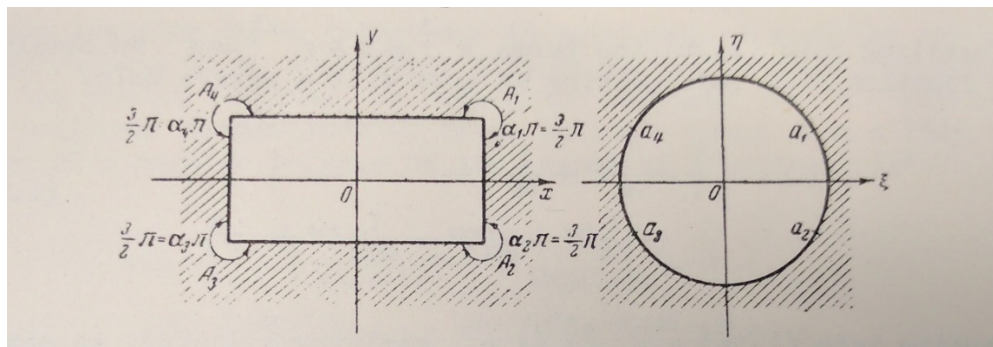
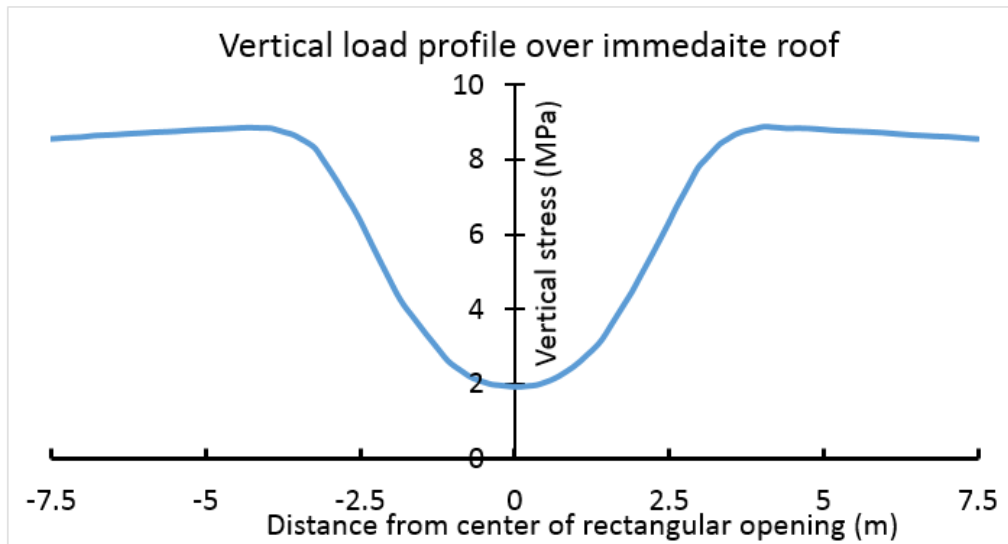


Figure 5.1 Conformal transformation of a rectangle to a unit circle (Savin, 1961)

$$z = \omega(\zeta) = c \left\{ \frac{1}{\zeta} + \frac{a + \bar{a}}{2} \zeta + \frac{(a - \bar{a})^2}{24} \zeta^3 + \right. \\ \left. + \frac{(a^2 - \bar{a}^2)(a - \bar{a})}{80} \zeta^5 + \frac{5(a^4 + \bar{a}^4) - 4(a^2 + \bar{a}^2) - 2}{896} \zeta^7 + \right. \\ \left. + \frac{7(a^5 + \bar{a}^5) - 5(a^3 + \bar{a}^3) - 2(a + \bar{a})}{2304} \zeta^9 + \right. \\ \left. + \frac{21(a^6 + \bar{a}^6) - 14(a^4 + \bar{a}^4) - 5(a^2 + \bar{a}^2) - 4}{11264} \zeta^{11} + \dots \right\},$$

where  $a = e^{2k\pi i}$ ;  $\bar{a} = e^{-2k\pi i}$ .

a) Shape function used to transform rectangular opening to a unit circle (Savin, 1961)



b) Vertical load profile on the immediate roof

Figure 5.2 Methodology for estimating load from approximate analytical solution based on conformal mapping.

### 5.3 Solid beam on elastic abutment under elasto-plastic state

The solid beam on an elastic abutment model was simulated in FLAC3D. The case study in section 3.2.3, of chapter 3 was used in this analysis. A coal mine entry (6m wide by 2m high) with laminated shale rock as the immediate roof of 1.8 m thickness (based on the study by Murphy et al., 2014) was built in FLAC3D. The model simulated a multi-layered shale beam on elastic coal pillars (Figure 5.3). The shale beam consisted of 4-layers (i.e., 0.45 m individual layer or lamination thickness) that interact with each other along interface elements. The beam was

considered as elastic-perfectly plastic that fails under Mohr-Coulomb criteria while coal pillars were considered elastic. The mechanical properties of both strata in the base model are same as mentioned in section 3.2.4, shown in Table 5.1.

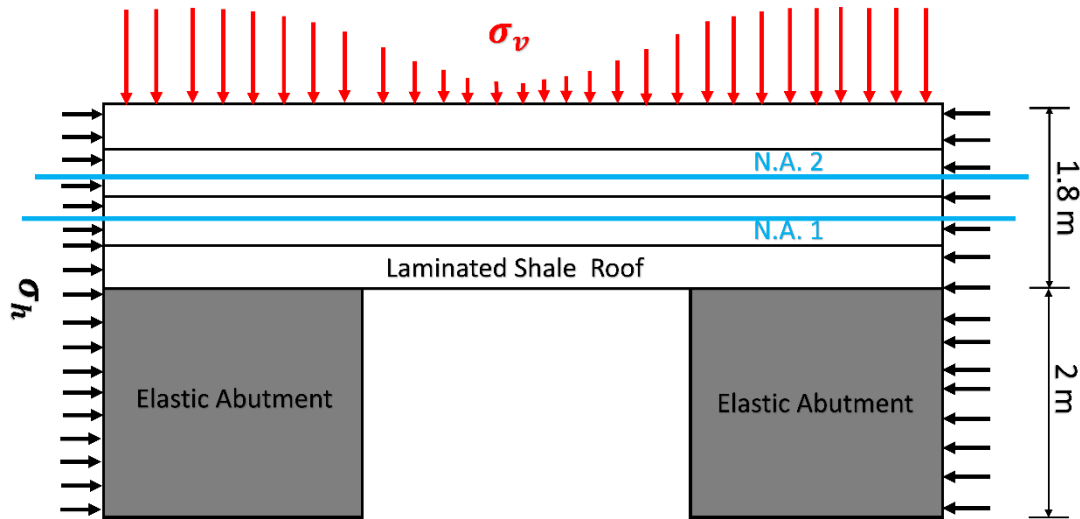


Figure 5.3 Multi-layered solid beam on elastic abutment model in FLAC3D.

The vertical load profile as shown in Figure 5.2 was applied on top of the shale beam. The load profile was obtained based on the approach mentioned in section 5.2. The pressure arch is formed after excavation of 6 m span entry under 7.85 MPa and 15.7 MPa of vertical and horizontal in-situ stresses respectively. The vertical load was applied in the increment of 1% of the original magnitude while maintaining the same vertical profile at each incremental stage. The incremental loading stages eliminated any shock and unrealistic bending of shale beam due to high amplitude non-uniform vertical load profile. A uniform horizontal load of 15.7 MPa was also applied in same increments to the lateral boundaries to keep vertical to horizontal stress ratio ( $K$ ) constant at each incremental loading stage.

The model was solved to equilibrium at each incremental loading. It must be noted here that the horizontal stress was applied at the lateral boundary and not initialized as used with earlier models in chapter 3 and 4. This approach was adopted to maintain the same horizontal stress distribution at each incremental loading stage. Initialization of the stress was excluded to prevent

any abrupt stress distribution in each element of model at each loading stage. The model simulated plane strain condition with the width of 0.4 m in Y-direction (out of plane direction). The minor horizontal stress was applied in Y-direction and its magnitude was selected to maintain the major to minor horizontal stress ratio ( $\lambda$ ) of 1.3 in all loading stages. For lamination thickness of 0.225m, the elements size along the layer thickness (Z-direction) consisted of five row of elements along the thickness in each individual layer. The zone size was same for larger lamination thickness. The uniform zone size of 0.06 m kept in X-direction.

### **5.3.1 Lamination properties**

The interface elements were used to simulate weak plane between two layers or laminas. The properties mentioned in section 3.2.5 and shown in Table 5.1 was used in this analysis. For mine model simulated in chapter 3, interface cohesion of 0.13 MPa was used based on the reported studies (Esterhuizen and Bajpayee, 2012; Perras and Diederichs, 2009). However, the elastic beam analysis (section 4.5.3 in chapter 4) showed negligible layer interaction with 0.13 MPa interface cohesion as inter-bed slipping was observed along the entire entry span. Additionally, elastic beam analysis did not consider high *in-situ* stress as discussed in section 5.1. Therefore, interface cohesion of 1.3 MPa was used for this analysis, which reduced the inter-bed slip as observed in section 4.5.3 of chapter 4 especially for high *in-situ* stress condition. This assumption also includes the beam building effect by roof bolting (Wright, 1978). Furthermore, various laboratory scale studies (Park and Min, 2015; He and Afolagboye, 2018) suggested that the laminar plane will have significantly higher shear strength (3-5 MPa) as compared to the infilled joints.

Table 5.1 Mechanical properties of each stratum (Murphy et al., 2014) and laminar planes

<b>Property</b>	<b>Shale</b>	<b>Coal</b>
Elastic Modulus (GPa)	12	3
Poisson's ratio	0.2	0.25
UCS (MPa)	17	-
Tensile Strength (MPa)	1.7	-
Dilation angle (deg.)	5	-
Interface normal stiffness (GPa/m)	10	-
Interface shear stiffness (GPa/m)	1	-
Interface friction (deg.)	25	-
Interface cohesion(MPa)	1.3	-

### 5.3.2 Dimension of lateral boundary

As mentioned earlier, the horizontal stress was applied to the lateral boundary. Therefore, the model length along the lateral direction was kept small. Stephansson in 1971 suggested boundary force should not be applied as horizontal load for models with longer length of over abutment. However, if the length of the model dimension was too small then the stress distribution in the beam over entry would be affected by stress reflection from the boundaries. Hence, an optimal length is required such that the horizontal stress developed around the entry would be equal to the value applied at the lateral boundary. To find this optimal length, base model mentioned in section 5.3 was simulated with three cases of different lateral width, i.e., 1L, 0.75L and 0.5L (L is entry span).

The width was varied in ratio of entry span and change in the horizontal stress along the neutral axis (from here is referred to as N.A) of two layers (N.A.1 and N.A.2 in figure 5.3) was analyzed. The change was plotted in terms of percentage of the magnitude applied at lateral boundary. Figure



5.4a-b compared percentage change in horizontal stress along neutral axis (N.A.1 and N.A.2) from entry corner ( $x=0$  in the plot) to lateral boundary at right side of the model at 5% of incremental loading stage.

As seen in Figure 5.4a, within 1m from the entry corners along N.A.1, the percentage change is large (12% to 32%) for all three cases, which is due to the large roof bending and its close proximity to the beam over the entry. For distances more than 1m from entry corner, the percentage change is small (2 to 7%) in cases 2 and 3 with the lateral width of 0.75 and 0.5 times the entry span. Whereas in case 1, the change is still significant (around 20%). Similar trend was found along the neutral axis N.A.2, where percentage change was higher in case 1 as compared to cases 2 and 3 (Figure 5.4a). Therefore, lateral width can be either 0.75 times and 0.5 times the entry span.

Figure 5.5a-c showed horizontal stress distribution over half-span beam on elastic abutment model for three cases of lateral width at 5% of incremental loading. The magnitude of the horizontal load applied at the boundary was 0.25 MPa (5% incremental loading stage). The results indicate that for case 3(Figure 5.5c), horizontal stress applied to the boundary of the coal pillar was directly affecting the entry corner. This would result in higher confinement to entry corners in case 3. Thus, stresses in the beam are significantly affected by boundary conditions in case 3. As lateral width is increased from case 3 to 1 (Figure 5.5a-c), the confinement at the entry corner reduces significantly with minimal value in case 1. However, as discussed above, the percentage horizontal change is significantly high in case 1(Figure 5.4a-b) which is due to significant reduction in the magnitude of horizontal stress near the entry as compared to the lateral boundary. The load at the lateral boundary of the beam reduces in magnitude as it reaches over the entry, which changes the initial stress ratio ( $K$ )  $t$ . Therefore, the lateral width of 0.75 times the entry span ( $T=4.5$  m) was used for the remainder of the study.

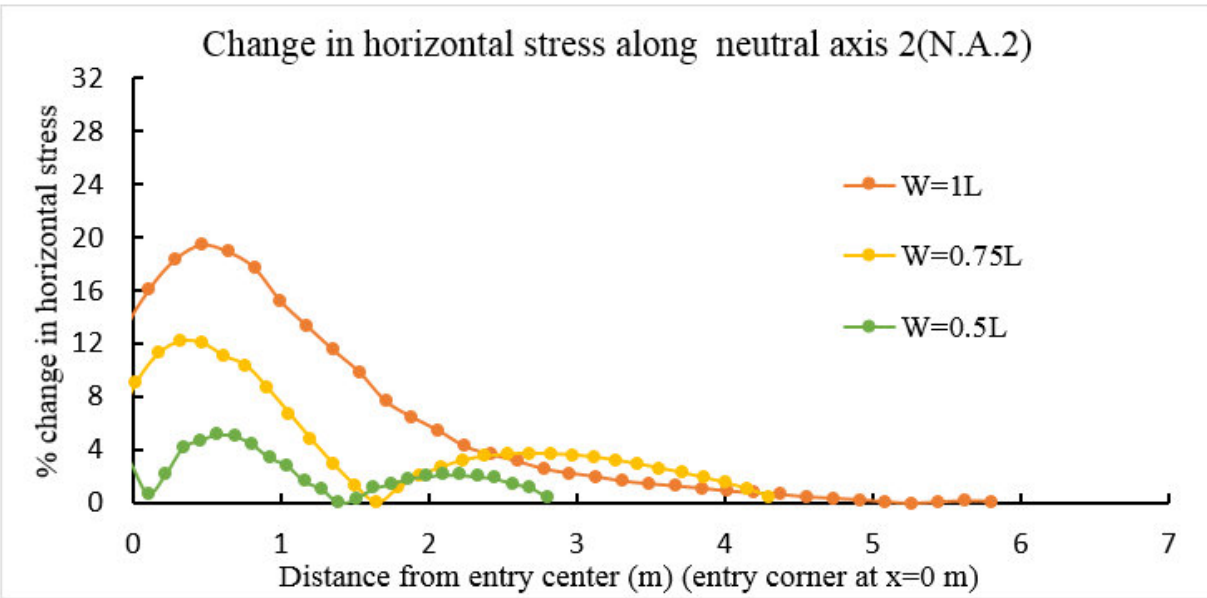
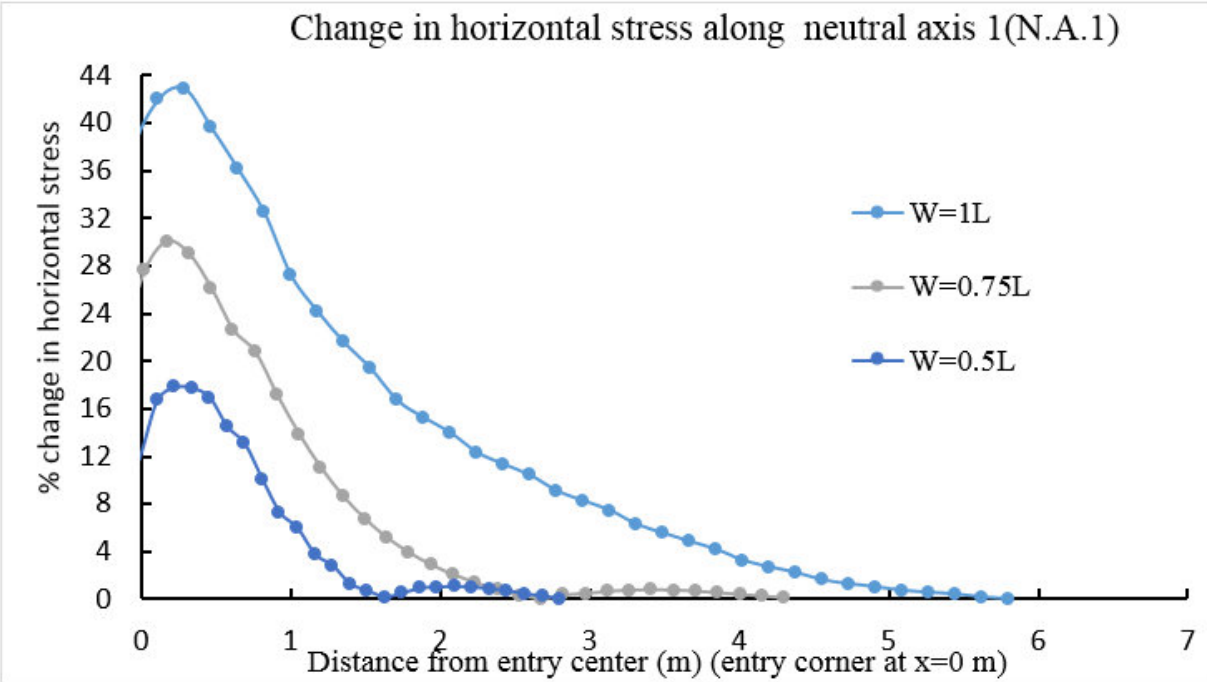


Figure 5.4 Change in horizontal stress for different lateral width of abutment (a) along neutral axis of second layer (N.A.1); (b) along neutral axis of third layer (N.A.2)

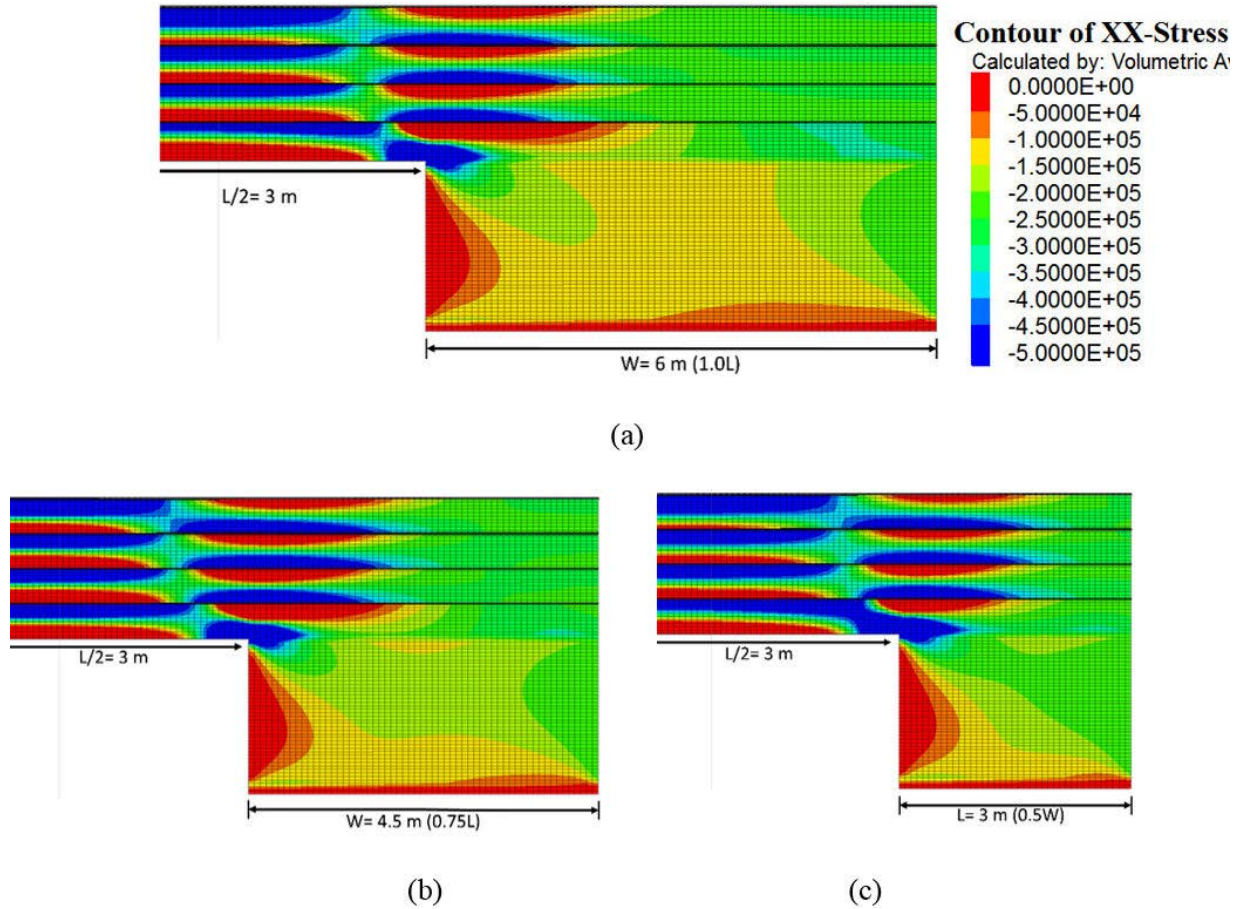


Figure 5.5 Lateral width (W) of abutment in terms of entry span (L) when horizontal stress of  $\sigma_h = 0.25 \text{ MPa}$  applied at boundary a)  $W = 1.0 L$ ; b)  $W = 0.75 L$ ; c)  $W = 0.5 L$

### 5.3.3 Comparison with anisotropic mine model

As mentioned earlier, the solid beam on elastic abutment model under elasto-plastic state was developed to understand the layer interaction and its influence on failure progression in the shale roof. The beam model was compared with anisotropic mine model used in chapter 3 to see the difference bending mechanism between two model. This would help in determining the condition in which this model can replace a mine model with detailed lithology. Additionally, complexity of the mine model could be quantified to have better understanding of layer interaction.

First, both models were compared under elastic state (Figure 5.6a-b). The base model for beam on elastic abutment was same as i mentioned above (section 5.3) with the exception that the model was solved under elastic state. The anisotropic mine model was also solved elastically for the same

stress conditions and lamination thickness as similar to the beam model. The formulation of anisotropic mine model was same as used in section 3.2.3 of chapter 3. Additionally, mesh size was kept same in both the models. Figure 5.6a-b presents the maximum principal stress distribution in 4-layer shale roof for both beam model and anisotropic mine model.

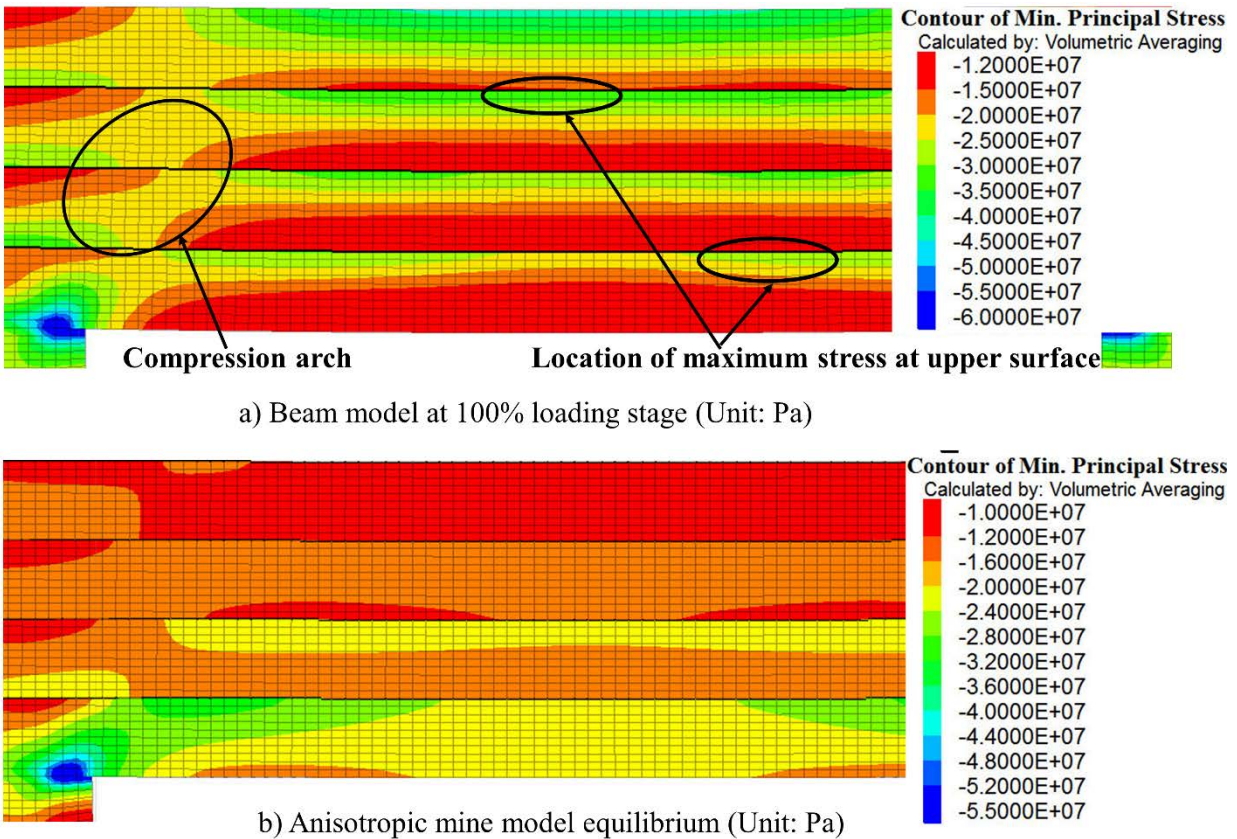


Figure 5.6 Principal stress distribution in shale roof two models

In beam model (Figure 5.6a), maximum stress was concentrated at entry corner (around 55-60 MPa) and at the upper surface of top layer (around 40-48 MPa). Whereas, in the mine model, maximum stress was only concentrated at the entry corner (around 50-55 MPa). Additionally, compression arch (similar to elastic beam analysis in chapter 4) is developed in each layer of beam model with highest stress concentration at the upper surfaces (however at different location along the entry span) except in the lowest layer. In the mine model, the compression arch develops only in the second layer. The failure initiation in both models occurs at entry corners in the lowest layer. In the remaining layers (second and third layers) stress concentration is highest at the upper surface and therefore failure initiation in this layer occurs at these locations in both models. Additionally, inter-bedding sliding was observed in the all three interfaces between four layers in both models. The extent of sliding was different in individual interfaces. It was found to be dependent on interface shear strength and bending profile of shale roof in beam model. The inter-bed sliding and its influence on layer interaction is discussed in detailed section 5.3.3 and 5.4.3.1.

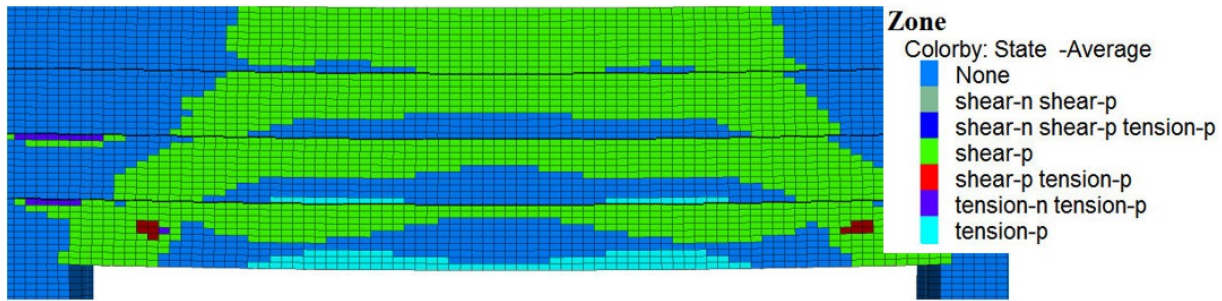
The high stress concentration in the top layer of the beam model is due to high stress boundary condition. The vertical load applied on its upper surface is maintained until equilibrium is attained in each loading stage. The vertical load, as mentioned above was based on analytical solution. The analytical solution excluded the effect of overburden strata's elastic stiffness resulting in higher load on shale roof as compared to the mine model. In mine model, vertical load on shale roof will depend on its interaction with overburden strata. As the model reached to equilibrium, this interaction will change depending on bending stiffness of the overburden strata that would result in complex bending profile of immediate roof in mine model (Figure 5.6b).

In the beam model, as load profile was fixed, the bending mechanism is easier to understand as seen from Figure 5.6a, compression arch formed in each layer. The bending stresses of each layer (except lowest layer) of beam model was higher than the mine model (Figure 5.6a-b). This is due to the higher magnitude of vertical load in beam model as it was obtained from analytical solution. It can be concluded that due to the difference in the bending profile of shale roof, stress distribution differed significantly in these models. However, the maximum stress concentration and its location is nearly same in both the models. Furthermore, bending in the beam model is more simplified and better suited to understand the layer interaction of laminated shale roof.

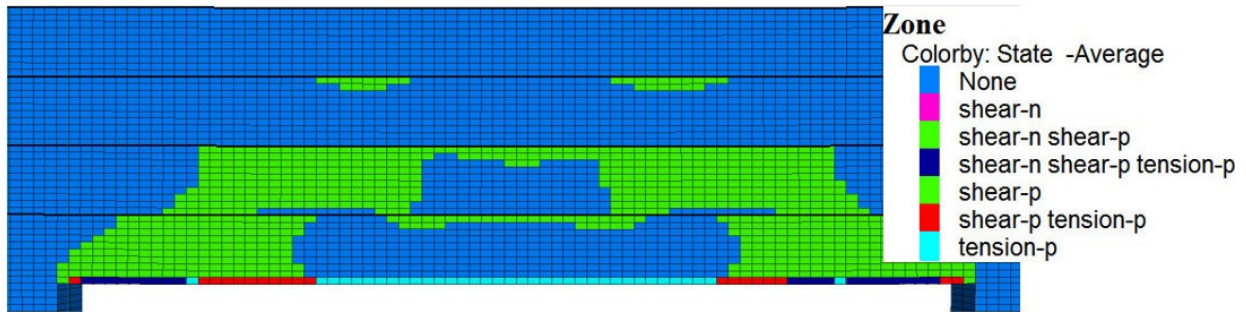
Figure 5.7a-b presents failure profile of beam model and anisotropic mine model when analyzed under elasto-plastic state. In both models, failure profile in bottom layer was similar, i.e., failure extend from entry corners to its upper surface along with tensile failure around mid-span. Additionally, failure seems to propagate from upper surface to lower surface in both models. In beam model (Figure 5.7a), top layer has failed which can be attributed to load boundary that creates at region of high stress concentration as seen in elastic analysis (Figure 5.6a). Whereas in mine model no failure occurred in top layer. The failure profile of shale roof in two models differ significantly which can be attributed to difference in bending profile as discussed above in elastic analysis.

In mine model, the initial virgin conditions were simulated first and then entry was created. Whereas, in the beam model, the load was applied to the top of the model, which undergo displacement and induces stresses in the beam. Additionally, the beam model was solved in 100 incremental loading stage to avoid unrealistic bending of the top layer. This caused layers to bend more in each incremental stage and thus higher stress concentration at the top layer as compared to the top layer of mine model. It is inferred from the analysis that although overall failure profile is different in both the models, failure pattern in lowest layers are same. Additionally, failure propagates downward from the upper surface of layers. Therefore, using the simplified model, accurate insight into the layer interaction can be obtained if the mechanism behind layer interaction during plastic state is clearly understood in the beam model.





a) Final failure profile in beam model



b) Final failure profile in anisotropic mine model

Figure 5.7 Failure profile comparison in two models

### 5.3.4 Failure propagation in solid shale beam on elastic abutment model

The failure propagation in shale roof of solid beam on elastic abutment was analyzed to understand the mechanism behind the layer interaction in plastic state. Figure 5.8a-g presents failure profile of the shale roof with lamination thickness of 0.45 m at various loading stages. The base model as discussed in section 5.3.2 was simulated in plastic state. The shear failure initiated at entry corners at 47% incremental loading stage (Figure 5.8a) which is due to the high stress concentration at these location as seen in elastic analysis (Figure 5.6a).

Additionally, inter-bed sliding was observed in the first interface (between the bottom layer and second layer) at distance of  $0.11L$  distance form entry corner (shown by red circle). The exact location and its extent depend on the interface cohesion and bending profile of the shale roof. The influence of interface shear strength on inter-bed slipping is discussed in detail in parametric study section 5.4.3.2. The stress release at the location of sliding increased the shear stress concentration

in nearby interface nodes. Therefore, with further roof bending, these nearby interface nodes would also undergo sliding. During subsequent loading stages, the extent of inter-bed slipping would increase along with initiation in other interfaces. For instance, sliding also initiated in second interface as shown by red circle (Figure 5.8b) at 57% incremental loading stage. Additionally, shear failure started to propagate upward at step angle along with failure initiated in upper surface of fourth layer (top layer) which can be attributed to high stress concentration due to boundary effect as discussed in elastic analysis in section 5.3.3.

With further loading, failure at the top layer started to propagate downward as seen at 60% incremental loading stage (Figure 5.8c). At this loading stage, shear failure also initiated at the upper surface of the bottom layer which was the location of high-stress concentration in compression arch (shown by the black circle in the elastic analysis; Figure 5.6a). The exact location of failure in the upper surface as seen in the elastic model depends on the bending profile of the shale roof along with the interface cohesion value. For instance, in this model, interface cohesion of 1.3 MPa was used which led to failure initiation near the entry corner than at the entry center. The influence of interface cohesion is further analyzed in detail in section 5.4.3.1.

With further loading, shear failure in the upper surface started propagating in the lateral direction as seen in 63% incremental loading stage (Figure 5.8d). The failure propagation in the lateral direction is due to high-stress concentration in nearby zones at the upper surface similar to elastic analysis (Figure 5.6a). After failure initiation at the upper surface, load shedding of already failed zones increases stress concentration in the adjacent zones. At this loading stage, shear failure also initiated in the upper surface of the second and third layer (Figure 5.8d). As loading increased further, failure in the upper surface of all layers propagated laterally, however, with varying rate as seen at 67 % incremental stage (Figure 5.8e). This rate depends on the bending profile of the individual layer. At this loading stage, failure at the upper surface reached mid-span and also propagated in the downward direction in the second and third layer. Additionally, tensile failure initiated at the lower surface of the bottom layer around mid-span. In subsequent loading stages, failure propagated in similar manner in all layers as seen at 82 % incremental stage (Figure 5.8f). The downward failure propagation is due to the load shedding by failed zones at upper surfaces causing high stress concentration in remaining zones of compression arch. At this loading stage,



tensile failure is also initiated at the lower surface of the second layer with large inter-bedding slippage in the first interface (approximately  $0.45L$ ;  $L$ = entry span). The large inter-bed slippage in the first interface has caused higher bending of adjacent layers and thereby initiating tensile failure in the second layer. In the subsequent loading stages, failure has propagated the entire compression arch (shown in figure 5.6a) in every layer (as seen in at 100 % incremental stage (Figure 5.8g). At this loading stage, failure in top layer has also reached to its lower surface. The failure at this stage looks like step-path failure that propagated from the entry corner to top layer.

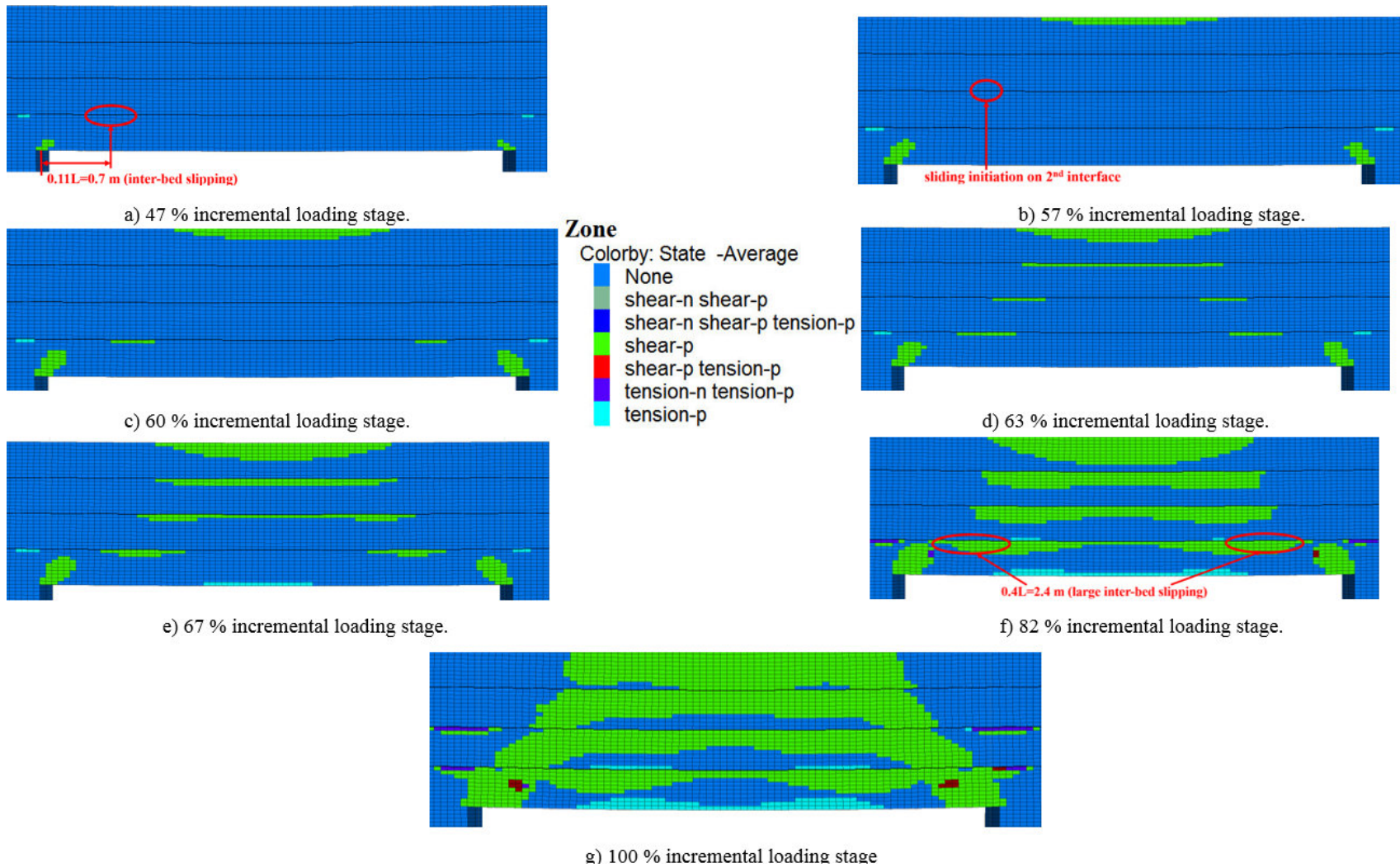


Figure 5.8 Failure propagation in beam model at different incremental loading stage.

## **5.4 Parametric Study**

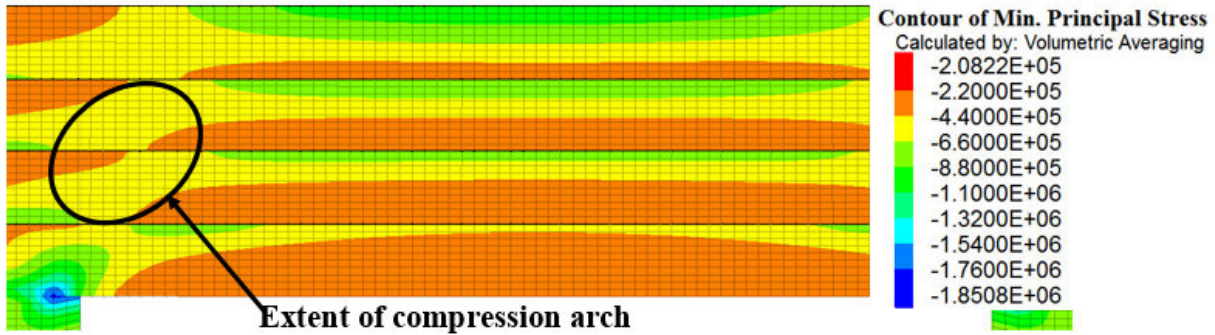
A parametric study was conducted on solid beam on elastic abutment model under plastic state to understand the influence of horizontal stress and other parameters on failure propagation and layer interaction in laminated shale roof. For this analysis, base model was kept same as used in previous sections. The following parameters were considered:

- a) Lamination thickness
- b) High horizontal stress
- c) Interface/laminar plane parameters (interface stiffness and strength)

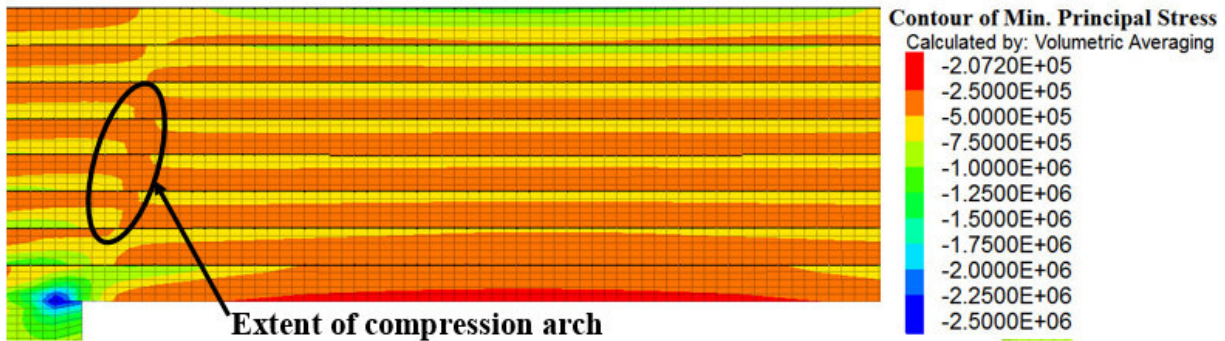
### **5.4.1 Lamination thickness**

The lamination thickness was evaluated by using span (L) to thickness (t) ratio (L/t). The total thickness of beam was constant (1.8 m) with variation in only number and thickness of the individual layers. Three lamination thicknesses of 450 225 and 150 mm were analyzed using numerical models.

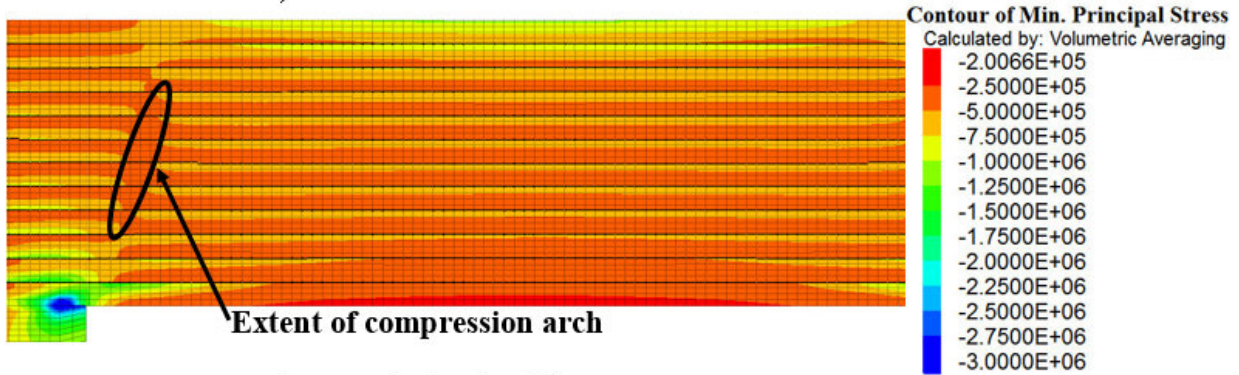
For all lamination thicknesses, stress distribution was similar at initial loading stages (seen in figure 5.9a-c) however, the extent of compression arch in individual layers decreased with decrease in layer thickness. This trend was due to large bending of individual layers, which reduced their ability to sustain vertical load (discussed in detail in section 4.5.1 of chapter 4). For the three cases, the maximum stress was concentrated at entry corners. However, due to decrease in bending stiffness of individual layer, the stress concentration increased with decrease in layer thickness.



a) 450 mm lamination thickness



b) 225 mm lamination thickness



c) 150 mm lamination thickness

Figure 5.9 a-c Minimum principal stress distribution at 2% incremental loading stage for different lamination thickness.

The stress distribution in the individual layer is similar for all lamination thickness and the only difference is the stress concentration, .i.e., stress concentration increases with decrease in lamination thickness. In addition, the failure initiation although similar occurred at different loading stages. For instance, failure initiation occurred at the entry corners at incremental loading stages of 23, 35 and 47% in lamination thicknesses of 150 mm, 225 and 450 mm respectively (figure 5.10a-c). The tensile failure was also observed near the top abutment corners (highlighted by red circle) in the bottom layer in all three cases due to the tensile stress concentration caused by large bending of the layer. Additionally, tensile failure also occurred in various overlying layers (second and above layers; highlighted by red circle) and number of layers under such failure increased with decrease in lamination thickness. This was due to increase in layer bending caused by decrease in the bending stiffness.

As load on the beam increased, the failure propagation was found similar to the base model (section 5.3.3). In all the three cases, shear failure initiated at upper surface and propagates laterally in overlying layers (second and above layers) however at different loading stages. Figure 5.11a-c show similar failure profile at 53, 58 and 63% loading stage for 150 mm, 225 mm and 450 mm lamination thickness. Additionally, inter-bed slipping (sliding along the first interface) was also observed with different extents (highlighted by red circle) for all three cases. The difference in slipping can be again attributed to bending stiffness of individual layers. The large sliding along the interface caused higher bending of adjacent layers resulting in tensile failure at the lower surface of these layers (Figure 5.11a-b). Furthermore, the extent of tensile failure in overlying layers (second and above layers) increased as lamination thickness decreased from 225 mm to 150 mm.

When load in the model was increased further, shear failure in overlying layer propagated downwards at different rates along with tensile failure at lower surface of more overlying layers as seen in figure 5.12a-c. Additionally, it was observed that the failure is mostly concentrated at the mid-span for lamination of 450 mm thickness and moved towards the entry corner as lamination thickness is decreased to 150 mm (highlighted by red circle). The decrease in the bending stiffness along with increase in the inter-bed slipping allowed layers to work as individual beams. The extent and exact location of inter-bed slipping depends on the interface strength and

bending profile of the shale roof (explained in detail in section 5.4.3.1). Similarly, the extent of tensile failure at layers lower surface increased with decrease in the lamination thickness (figure 5.13a-b).

In subsequent loading stage, large inter-bed slipping caused layer separation (delamination) in both 225 mm and 150 mm lamination thickness (figure 5.13a-b). Additionally, failure propagated along the entire thickness of overlying layers in both cases. In 450 mm lamination thickness case and at 82% loading stage, failure is limited to upper surface and concentrated around the mid-span (figure 5.13c). With further loading, more layers in both 225 mm and 150 mm lamination thickness cases separated resulting into thin beams. The thin beams are weaker than the intact beam roof and therefore failed in both cases. However, no layer separation occurred in 450 mm lamination thickness as the extent of inter-bed slipping was limited to approximately  $0.4L$  ( $L$ = entry span). The failure at 100 % incremental stage in 450 mm lamination thickness case is limited to compression arch in every layer (similar to base model as seen in Figure 5.8g).

From the above analysis, it is concluded that with the decrease in lamination thickness, the overall bending of roof increases, which will result in the greater extent of failure in individual layers. In additions, if the roof is allowed to bend significantly, layers can delaminate easily even with high interface cohesion as layer separation is seen in both 225 mm and 150 mm lamination thickness cases. After delamination into thin beams, the roof layers can rupture very quickly as seen by the increase in failure propagation rate along layer thickness with the decrease in lamination thickness.



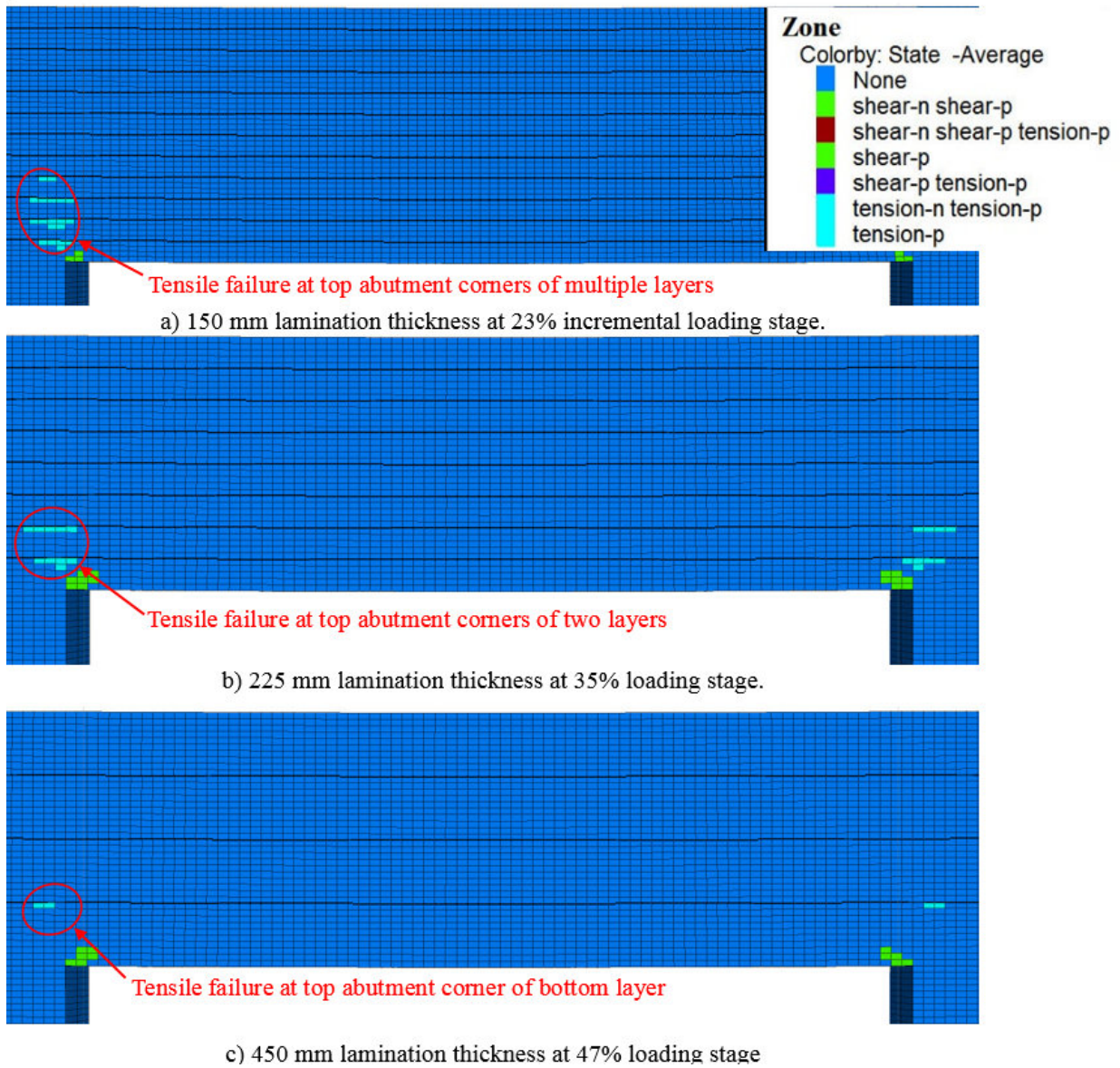


Figure 5.10 Failure propagation in shale roof with different lamination thickness

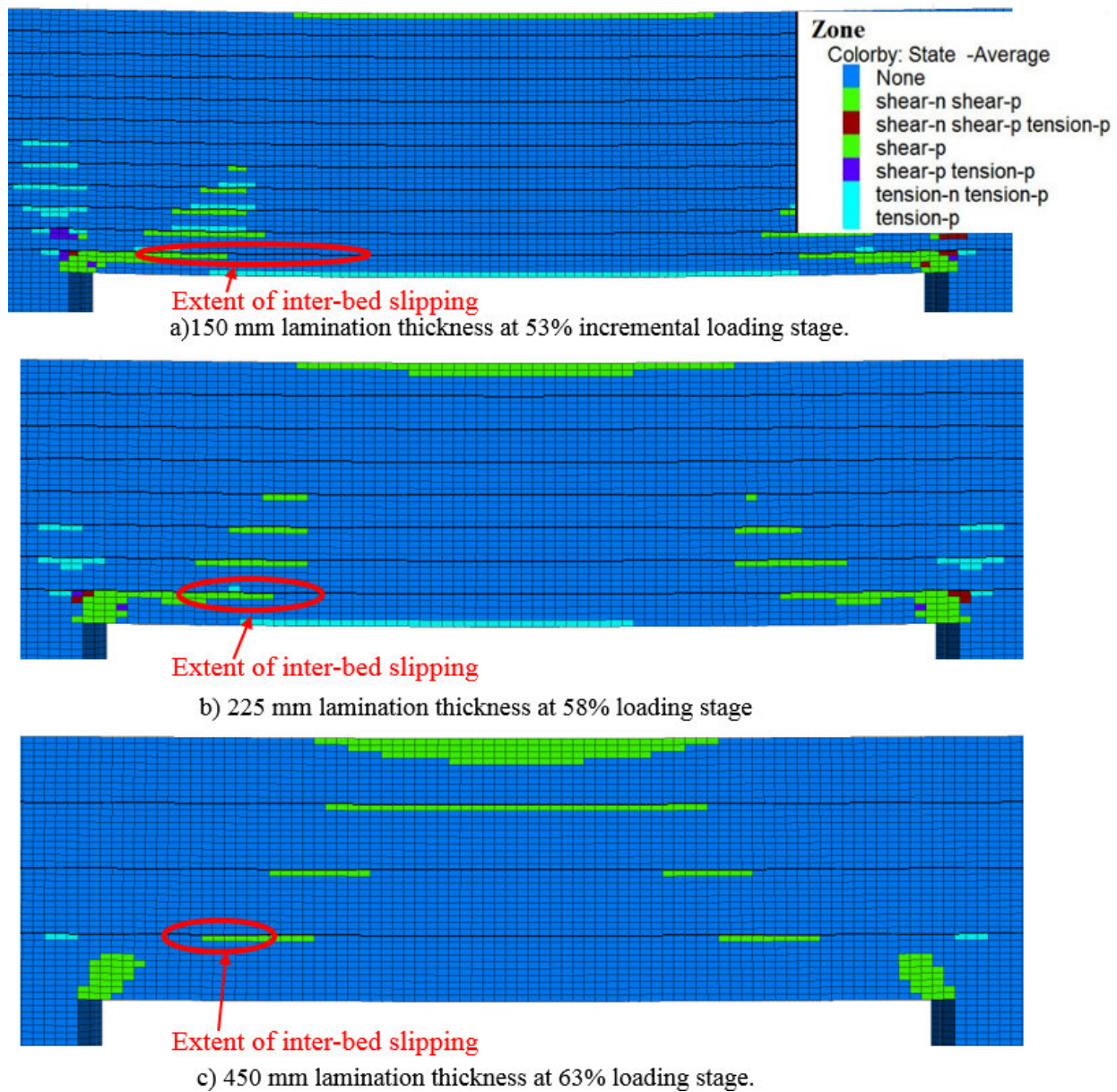
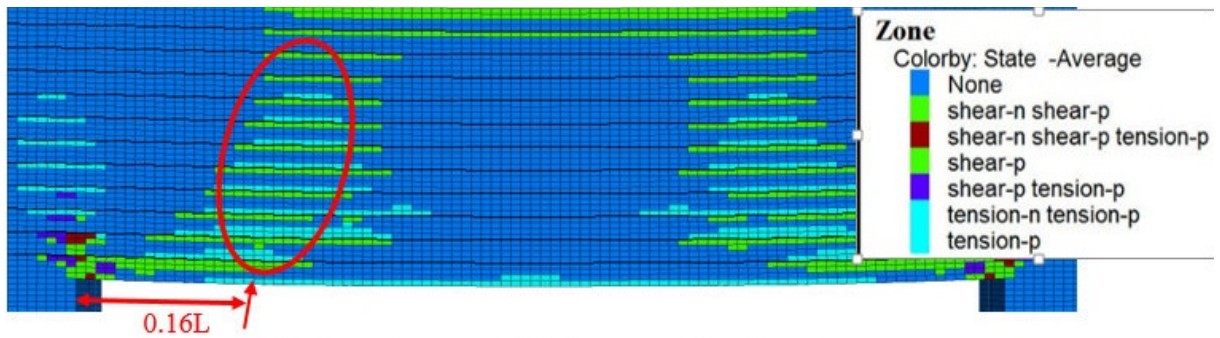
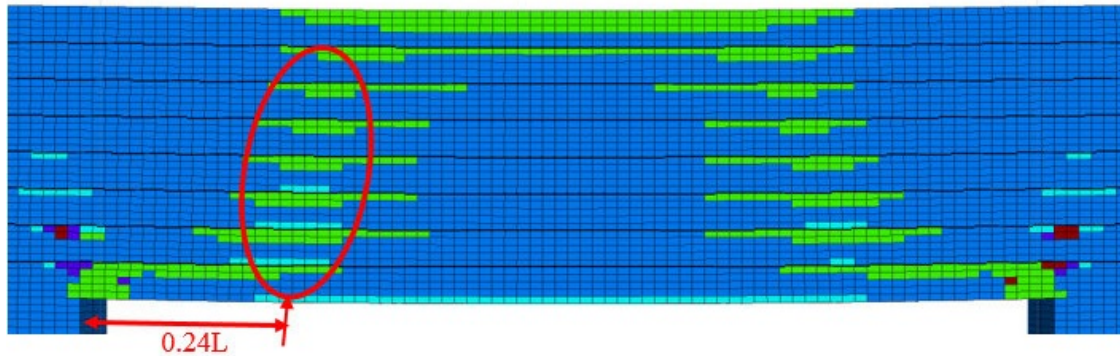


Figure 5.11 Failure propagation in shale roof with different lamination thickness

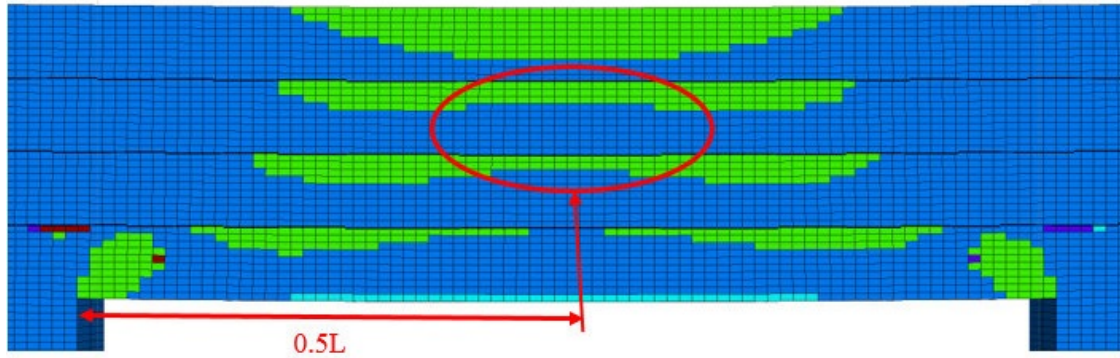




a) 150 mm lamination thickness at 58% incremental loading stage.

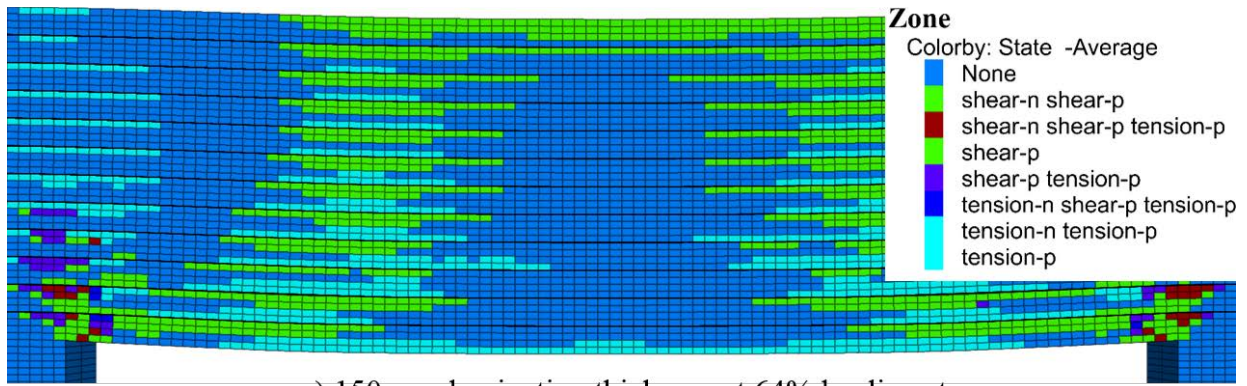


b) 225 mm lamination thickness at 67% loading stage

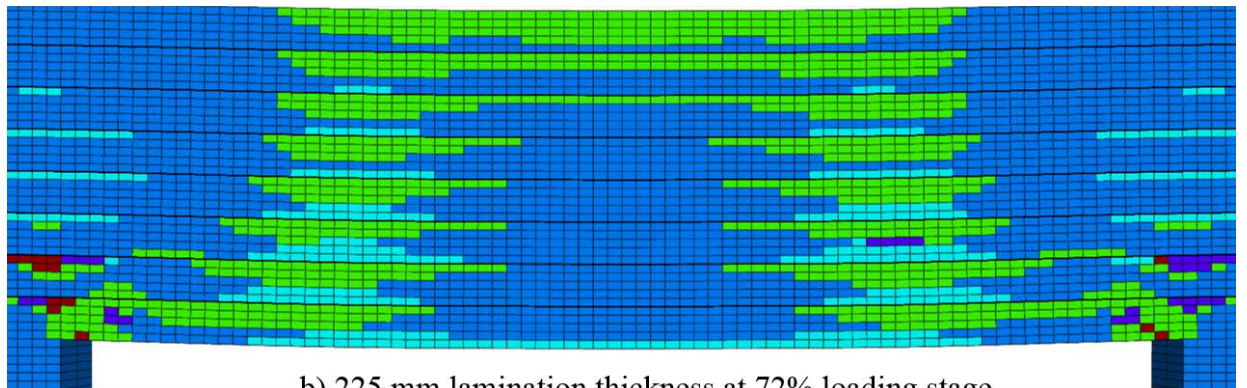


c) 450 mm lamination thickness at 77% loading stage.

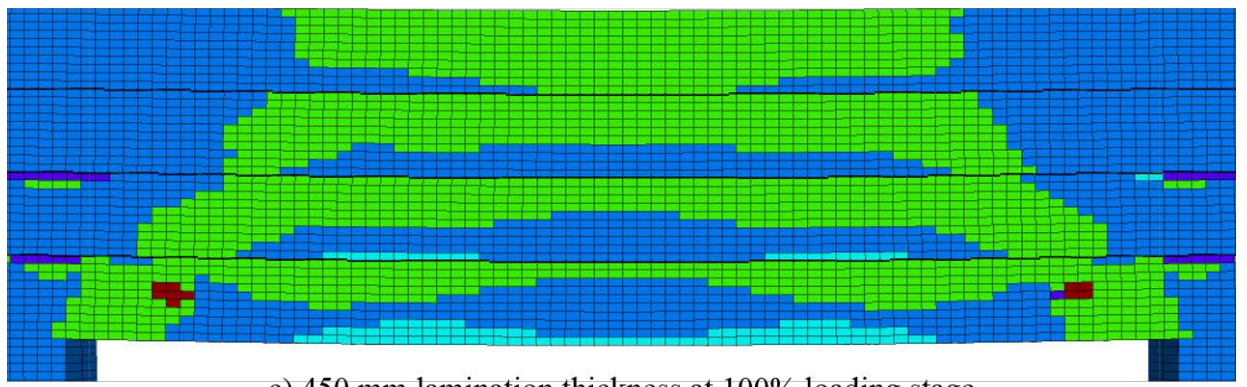
Figure 5.12 Failure propagation in shale roof with different lamination thickness



a) 150 mm lamination thickness at 64% loading stage



b) 225 mm lamination thickness at 72% loading stage



c) 450 mm lamination thickness at 100% loading stage

Figure 5.13 Failure propagation in shale roof with different lamination thickness



#### 5.4.2 *In-situ* stress magnitude and ratio

The horizontal stress was varied by changing the stress ratio  $K=2$  to 3. Figure 5.14 compared the maximum principal stress distribution in the 4-layer (0.4 m lamination thickness) beam under different horizontal stress (i.e.,  $K$  ratio 3, 2.5 and 2) with 25 % incremental loading stage. For all  $K$  values, stress distribution was same with compression arch in each layer and with the maximum stress concentration occurring at entry corners. However, the extent of compression arch increased with increased in the horizontal stress as seen in Figure 5.14. Similar observation was found in elastic analysis, (section 4.3.1) where extend of tensile zone decreased and compression zone increased with increase in the horizontal stress. The maximum stress concentration increased from 16.67 MPa when  $K=2$  to 19 MPa when  $K=3$ . Further, average stress in compression arch increased with increased in horizontal stress ( $K=2$  to  $K=3$ ). This suggested that failure initiation with further loading stages would be at entry corners.

Figure 5.15a-e shows failure profile with different horizontal stress ratios (i.e.,  $K$  ratio 2, 2.5 and 3) at various loading stage. As seen at 25% incremental loading stage, stress distribution is same for all  $K$  values. Thus, shear failure would initiate at entry corners for all three cases with different loading stages. For instance, shear failure initiated at 38, 42 and 47% of incremental loading stage for varying ratios of  $K$  (Figure 5.15a). With additional load, shear failure propagated upwards from entry corners along with its initiation at upper surface of overlying layers (second and above layer) for all ratios of  $K$ . Figure 5.15b presented failure initiation at upper surface of the fourth layer (top layer) at 47, 54 and 63% of incremental loading stage for  $K$  ratios of 3, 2.5 and 2 respectively. The failure initiation at upper surfaces was similar to the failure in the base model.

With further loading, shear failure at the upper surface of second and third layer propagated laterally toward mid-span and in the downward direction for all  $K$ -ratio however at different loading stages (Figure 5.15c). Additionally, tensile failure occurred in the lower surface of the fourth layer around mid-span in cases of  $K=2$  at 67% of the incremental stage. Similarly, tensile failure was observed for all  $K$ -ratios of 3, 2.5 and at 67% of incremental loading stage. The tensile failure initiation at same loading stage is different from shear failure trend, which was similar however at different loads for all  $K$  values. It indicates that although the shear failure at the given

loading stage was different, tensile stress concentration remained the same in the layers. This trend also indicated that increased compression due to high horizontal stress was compensated by larger failure extent thereby resulting in similar bending of the beam in all three cases.

With further loading, failure was propagated to the entire compression arch as seen at 68%, 79%, and 95% incremental stage for K ratios of 3, 2.5 and 2 respectively (Figure 5.15d). Additionally, tensile failure propagated vertically upward in the lowest layer for all K ratios. Therefore, the trend of failure profile remained the same for all K ratios; however, they occurred at different loading stages, which suggested similar failure propagation mechanism in all cases. The only difference was in the magnitude of stress at any loading stage. For instance, Figure 5.15e compared final failure profile for all K ratio. The results showed an increase in the extent of failure with the increase in K. In addition, complete roof failed when K was equal to 3.

It is concluded that the horizontal stress has no significant influence on layer interaction and failure propagation in the shale roof. It only affects the extent of failure in the roof. The trend differs from the results of anisotropic models as observed in figure 3.12 in section 3.2.7.2 of chapter 3. In the anisotropic mine model, high horizontal stress affected the behavior of laminated roof with the abrupt change in roof deflection with lamination thickness. It can only be explained by the difference in failure progression within the roof. The results showed that the incremental loading stages did not influence the failure propagation in the beam model. In mine model, the roof bending is preceded by the entire roof failure under high horizontal stress.

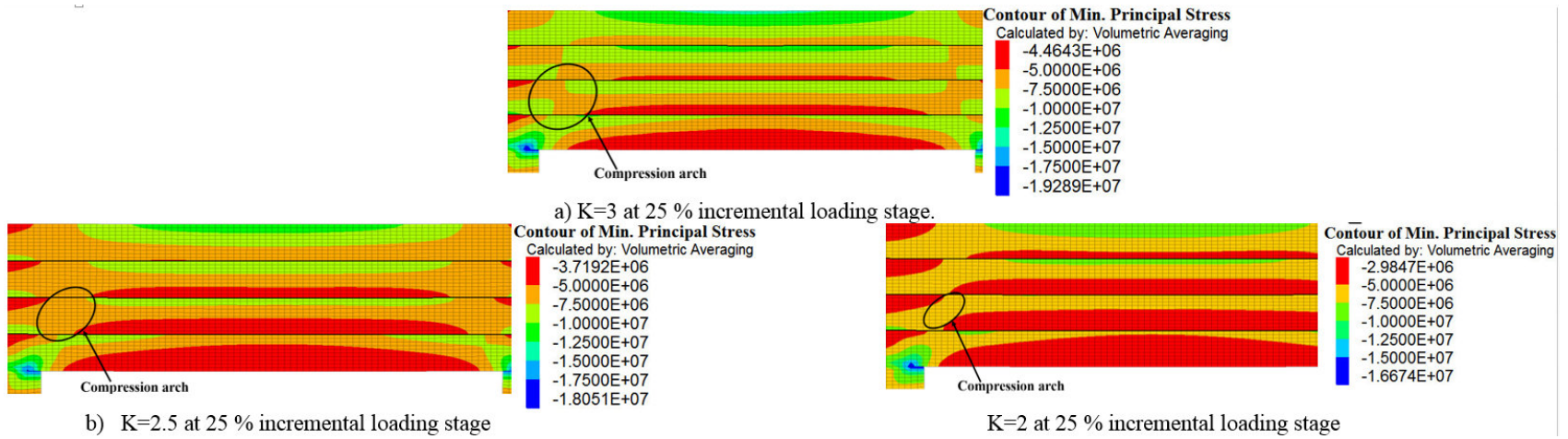
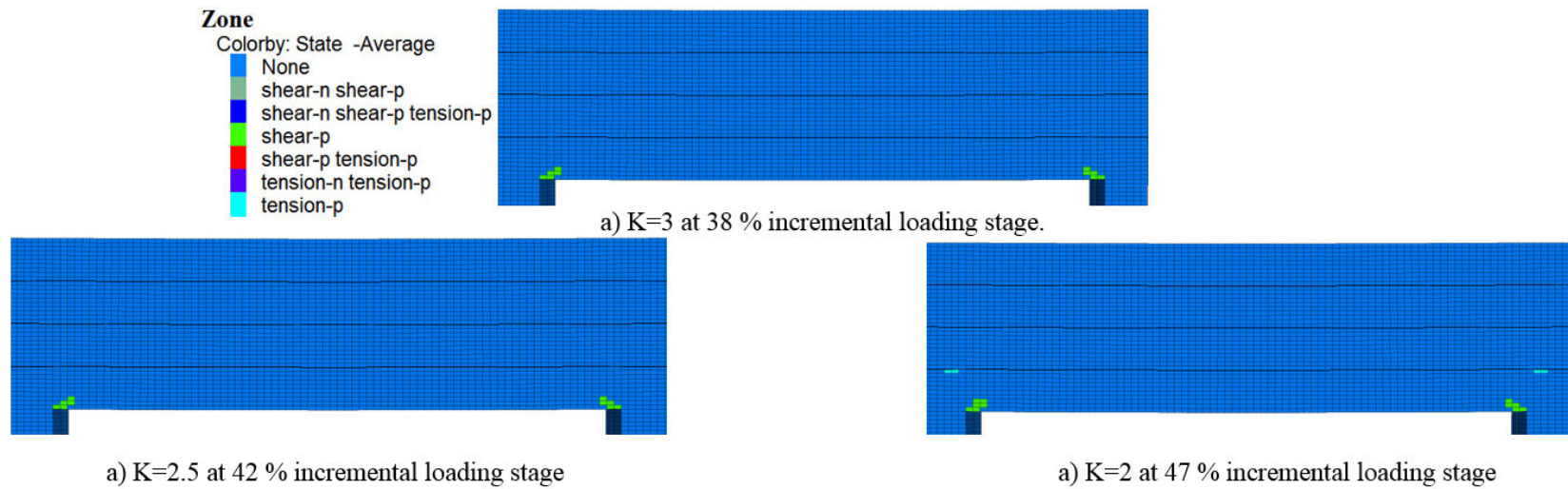
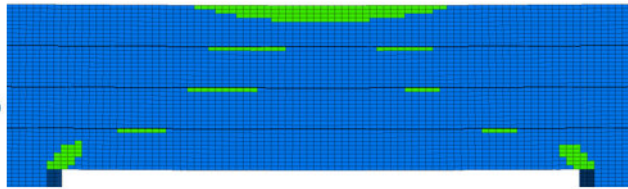


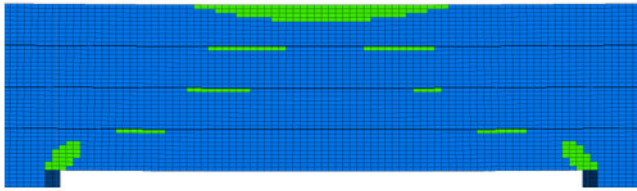
Figure 5.14 Minimum principal stress distribution in shale roof under different horizontal stress (K=3, 2.5, 2)



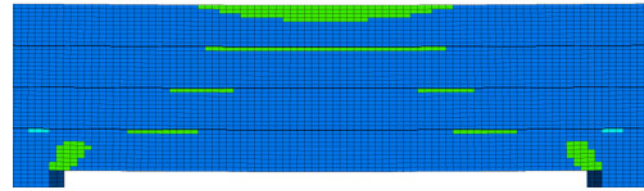
**Zone**  
 Colorby: State -Average  
 None  
 shear-n shear-p  
 shear-n shear-p tension-p  
 shear-p  
 shear-p tension-p  
 tension-n tension-p  
 tension-p



b) K=3 at 47 % incremental loading stage.

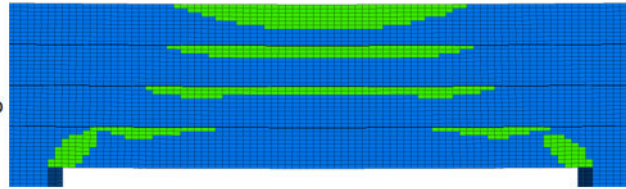


b) K= 2.5 at 54 % incremental loading stage

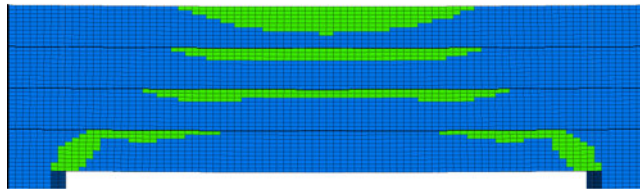


b) K=2 at 63 % incremental loading stage

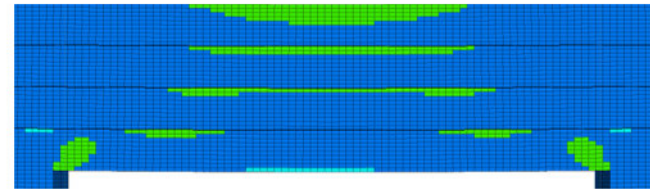
**Zone**  
 Colorby: State -Average  
 None  
 shear-n shear-p  
 shear-n shear-p tension-p  
 shear-p  
 shear-p tension-p  
 tension-n tension-p  
 tension-p



c) K=3 at 53 % incremental loading stage.

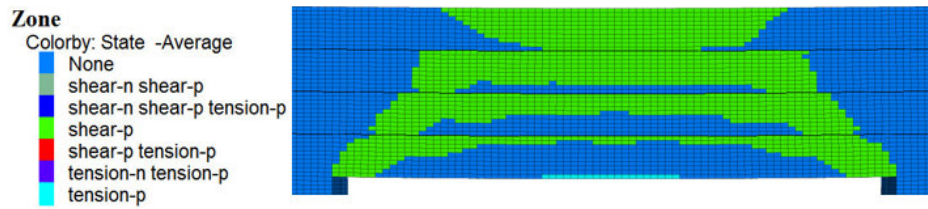


c) K= 2.5 at 62 % incremental loading stage

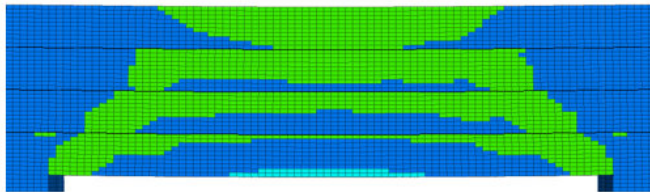


c) K=2 at 67% incremental loading stage

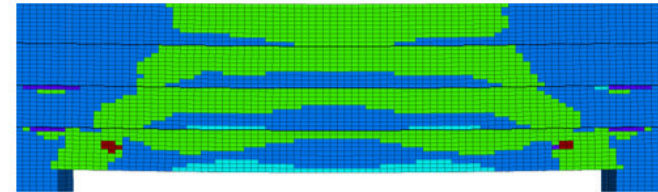




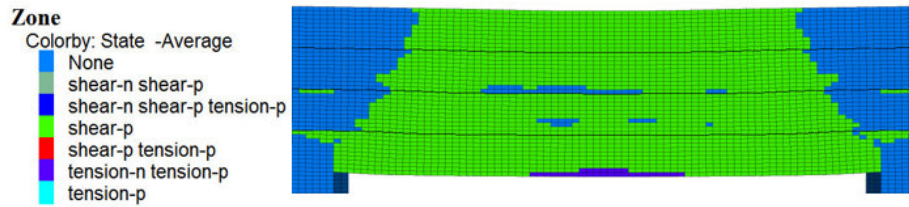
d) K=3 at 68 % incremental loading stage.



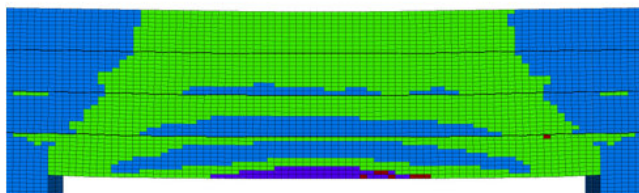
d) K=2.5 at 79 % incremental loading stage.



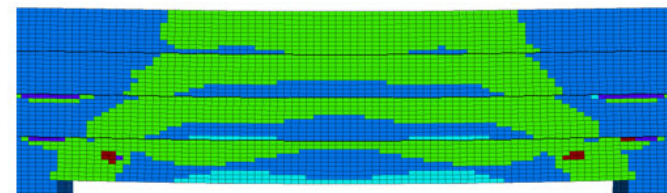
d) K=2 at 95% incremental loading stage.



e) K=3 at 100 % incremental loading stage



e) K=2.5 at 100 % incremental loading stage.



e) K=2 at 100 % incremental loading stage.

Figure 5.15 a-e Failure propagation in shale roof under different horizontal stress (K=3, 2.5, 2)

### 5.4.3 Interface parameters

The interface elements were used to simulate weak planes between two layers or laminas. These elements represent elastic springs that resist normal and shear deformation based on their stiffness and strength parameters. The influence of joint parameters on the layer interaction during failure propagation in shale roof was studied in this section. For this analysis, the base model was kept the same as used in section 3.2.5. A 4-layer solid beam on elastic abutment was simulated with 7.85 and 15.7 MPa of vertical and horizontal *in-situ* stresses.

#### 5.4.3.1 Interface strength

The influence of interface (laminar plane) strength was evaluated for three cases (Table 5.2) for analyzing the influence on failure propagation in laminated shale beam. Cases 1 and 2 were simulated to investigate the influence of interface cohesion on layer interaction. Cases 2 and 3 was used to study the influence of interface tensile strength.

Table 5.2 Interface strength parameters used in parametric study

	Shear Strength		Tensile Strength (MPa)
	Cohesion (MPa)	Friction Angle (degrees)	
Case 1	1.3	25 <sup>0</sup>	0.3
Case 2	0.013	25 <sup>0</sup>	0.3
Case 3	0.013	25 <sup>0</sup>	0.0

The interface elements in FLAC<sup>3D</sup> is characterized by Coulomb sliding where maximum shear force is limited by Coulomb shear-strength criterion (Itasca, 2012) given by:

$$F_{smax} = cA + F_n \tan \varphi \quad \text{Equation 5.1}$$

Where  $c$  is the cohesion (stress) along the interface;  $\varphi$  is the friction angle (degrees) of the interface surface. The sliding along the interface will only occur if  $|F_s| \geq F_{smax}$  ( $F_s$  is maximum



shear force along the interface) and then,  $F_s = F_{smax}$ , with the direction of shear force preserved. Thus shear stress required for sliding (Brady and Brown 1993) can be described as:

$$\tau \geq c + \sigma_n \tan \varphi \quad \text{Equation 5.2}$$

Where  $\tau$  and  $\sigma_n$  are normal and shear stress along the interfaces or on contact faces of nearby zones. As these contact faces are part of nearby zones, stresses along the faces can also be described in terms of principal stress components of these nearby zones using the Mohr circle:

$$\tau = \frac{\sigma_1 - \sigma_3}{2} \sin 2\theta \quad \text{Equation 5.3}$$

$$\sigma_n = \frac{\sigma_1 + \sigma_3}{2} \cos 2\theta \quad \text{Equation 5.4}$$

Where  $\sigma_1$  and  $\sigma_3$  are major and minor principal stresses in nearby zones and  $\theta$  is angle between the interface and major principal axis in the nearby zone. Now using value of  $\sigma_1$  and  $\sigma_3$  are in equation 5.2 will give condition of sliding in terms of principal stresses of nearby zones:

$$\frac{\sigma_1 - \sigma_3}{2} (\sin 2\theta - \tan \varphi \cos 2\theta) \geq c \quad \text{Equation 5.5}$$

In the current study, the interface friction angle of  $25^\circ$  is kept constant in all cases (Table 5.3) thus

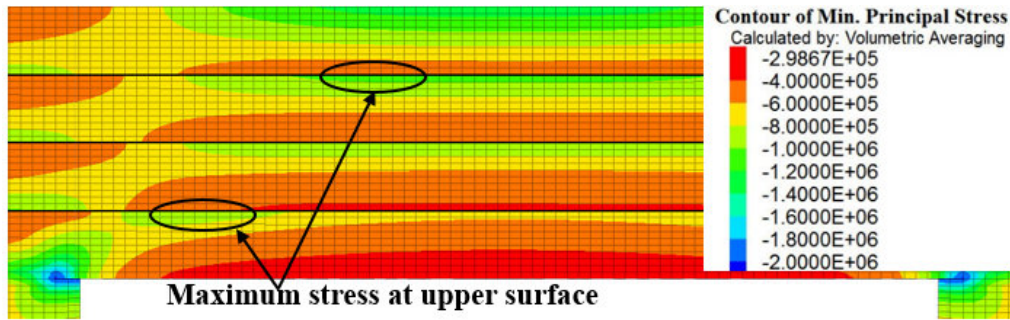
$$\frac{\sigma_1 - \sigma_3}{2} (\sin 2\theta - 0.46 \cos 2\theta) \geq c \quad \text{Equation 5.6}$$

If interface cohesion,  $c=0$  then equation 5.6 will reduce to

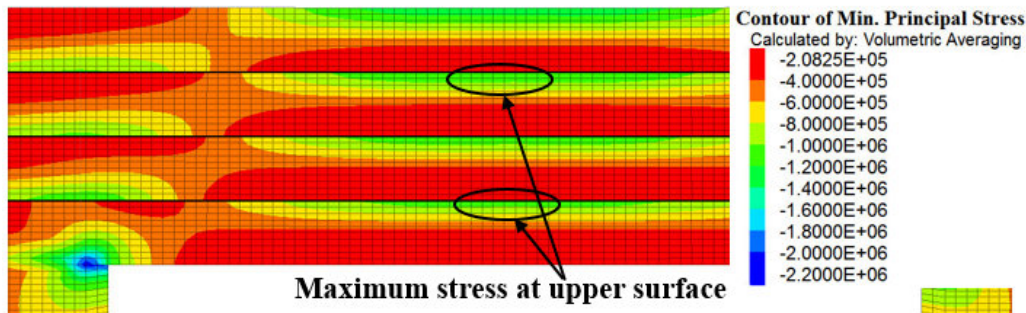
$$\sin 2\theta \geq 0.46 \cos 2\theta \quad \text{Equation 5.7}$$

Sliding will occur in the interface nodes where  $\theta > 12.5$ . Additionally, the interface sliding is independent of bending stress magnitude and only depends on the angle between the major principal stress angle and interface ( $\theta$ ). However, if cohesion is high, principal stresses in nearby zones would have overcome the interface cohesion to initiate sliding as seen by equation 5.5. Thus, in the case of high cohesion, principal stresses and their angle from interface ( $\theta$ ) would dictate the location and extent of interface sliding.

Figure 5.16a-b compares the stress distribution at 2 % of incremental loading stage between case 1 and 2. For case 2, the compression arch is formed in each layer of the beam with equal extent and same stress distribution, i.e., maximum stress concentration around mid-span at upper surface of each layer (highlighted by the black circles in Figure 5.16b). On the other hand, the extent of compression is highest in top layer and lowest in bottom layer for case 1 as seen from different location of maximum stress concentration at the upper surface of these two layers (highlighted by the black circles in Figure 5.16a). Additionally, inter-bed slippage occurred along the entire entry span (Figure 5.17a) for case 2, while no slippage occurred in case 1 (Figure 5.17b). Figure 5.17a-b shows extent of slippage along the first interface of the beam for two cases 1 and 2 at 2% incremental loading stage. For case 2, due to low interface cohesion, the total shear strength is nearly equal to its frictional strength, indicating that inter-bed slippage can be determined using Equation 5.7. The equation indicates that the interface sliding is independent of bending or principal stresses and would occur even in initial loading stages. The large frictional sliding allowed layers to act as individual beams which decreased the layer interaction within beam. In case 1, high interface cohesion increased its shear strength, which prevented any slipping and allowed greater layer interaction. This resulted in smaller extent of compression arch as compared to case 2 (Figure 5.16a-b). The high inter-bed slipping also increased the overall bending of the beam as deflection increased from 0.8 mm in case 1 to 3 mm in case 2.



a) Case 1



b) Case 2

Figure 5.16 Minimum principal stress distribution at 2% incremental loading stage for various interface cohesion.

The difference in overall bending increased in subsequent loading stages, which caused early failure initiation in case 2 as compared to case 1. For instance, the failure initiated at 18% incremental loading stage in case 2 while at 47% incremental loading stage in case 1 (figure 5.18a). In case 2, failure initiated under tension in bottom layer around mid-span, while shear failure occurred at the entry corner in case 1. The tension failure at early loading stage in case 2 is due to the layers bending as individual beams with high inter-bed slippage. For case 1, at 47% loading stage, small inter-bed slippage occurred in the first interface near the entry corner (figure 5.19).

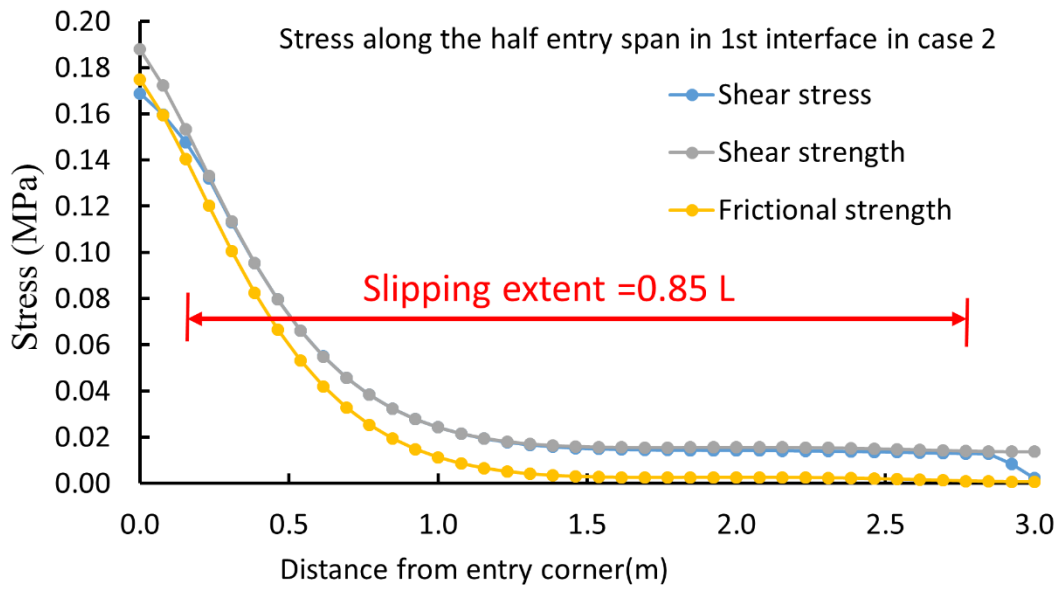
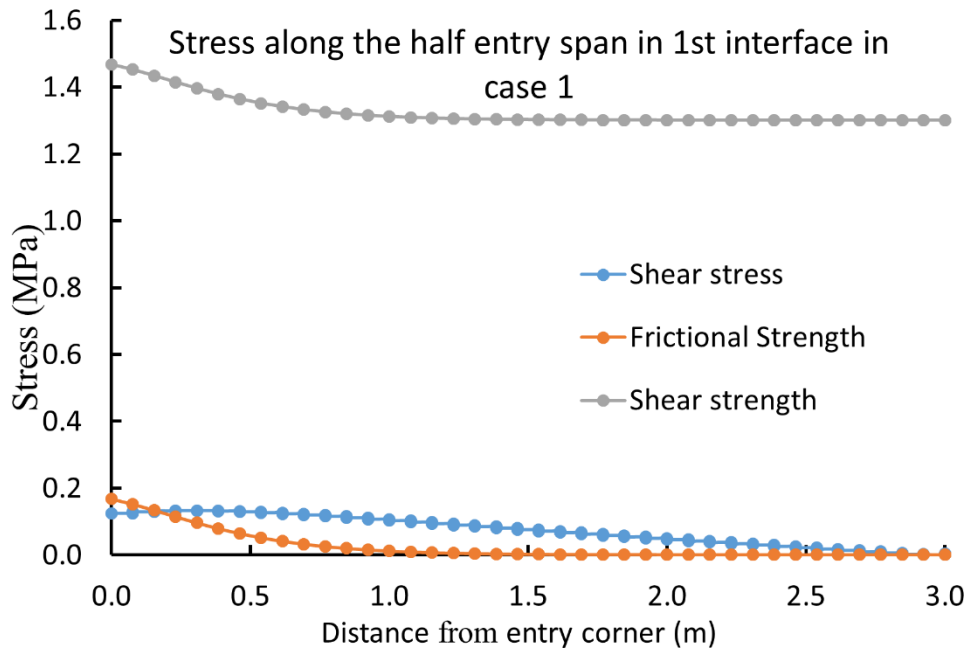


Figure 5.17 (a-b) Extent of inter-bed slipping along the 1st interface at 2% loading stage for various interface cohesion

At subsequent loading stages, tensile failure occurs in the lower surface of overlying layers (second and above layers) of case 2 as seen at 45 % incremental loading stage (figure 5.18b). Additionally, shear failure was also observed at the entry corner and the upper surface of each layer around mid-span. The shear failure at the upper surface around the mid-span was again due to the bending of laminae as individual beams, which resulted in maximum stress concentration at this location in each layer as seen at initial loading stages (Figure 5.16b). Similarly, due to bending as individual beams in case 2, failure was limited to zones around mid-span as seen at 55 % incremental loading stage (Figure 5.18c). In each layer, both shear failure (from the upper surface) and tensile failure (from the lower surface) propagated vertically into the beam. In a similar manner, failure propagated along the entire thickness of each layer as seen at 67 % loading stage (Figure 5.18d). At this loading stage, failure has propagated to the entire thickness of all the layers. This will reduce the load bearing capacity of the entire beam causing complete failure, which was observed at 68% incremental loading stage.

In case 1, failure propagation is similar to the base model described in section 5.3.2 where shear failure propagated upwards into the beam from the entry corners. Failure also initiated at the upper surface of overlying layers at 63% incremental loading stage (Figure 5.18b). The exact location of this failure as discussed for the base model is directly depended on beam bending profile and interface cohesion. The high interface cohesion allowed significant layer interaction within the beam by preventing the formation of individual beams. The significant amount of layer interaction in case 1 resulted in the different location of maximum stress concentration in each layer as seen in the initial loading stage (Figure 5.16a). Therefore, the location of failure initiation is different in each layer (Figure 5.18b). In subsequent loading stages, failure at the upper surface of various overlying layers propagated in both lateral and downward direction as seen at 82 % incremental loading stage (Figure 5.18c). Figure 5.18d shows final failure profile at 100 % loading stage. The failure propagated in step-path fashion from entry corner to the top of the layer along with failure around the upper surface of each layer. Additionally, failure profile is also similar to the compression arch in individual layer seen in the initial loading stage (Figure 5.16a) which indicated the clear influence of bending profile of shale roof on its failure.

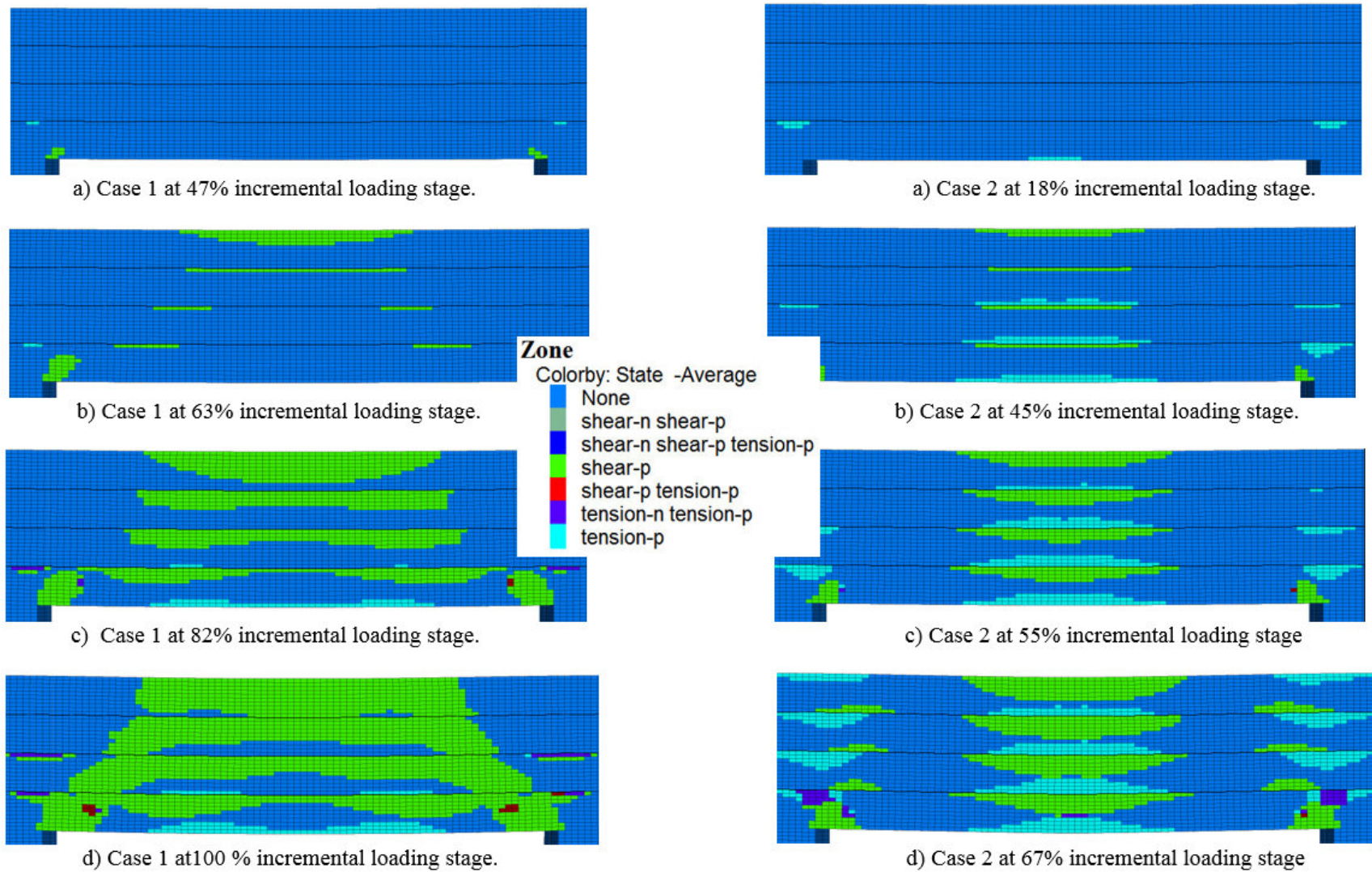


Figure 5.18 (a-d) Failure propagation in shale roof for different interface cohesion



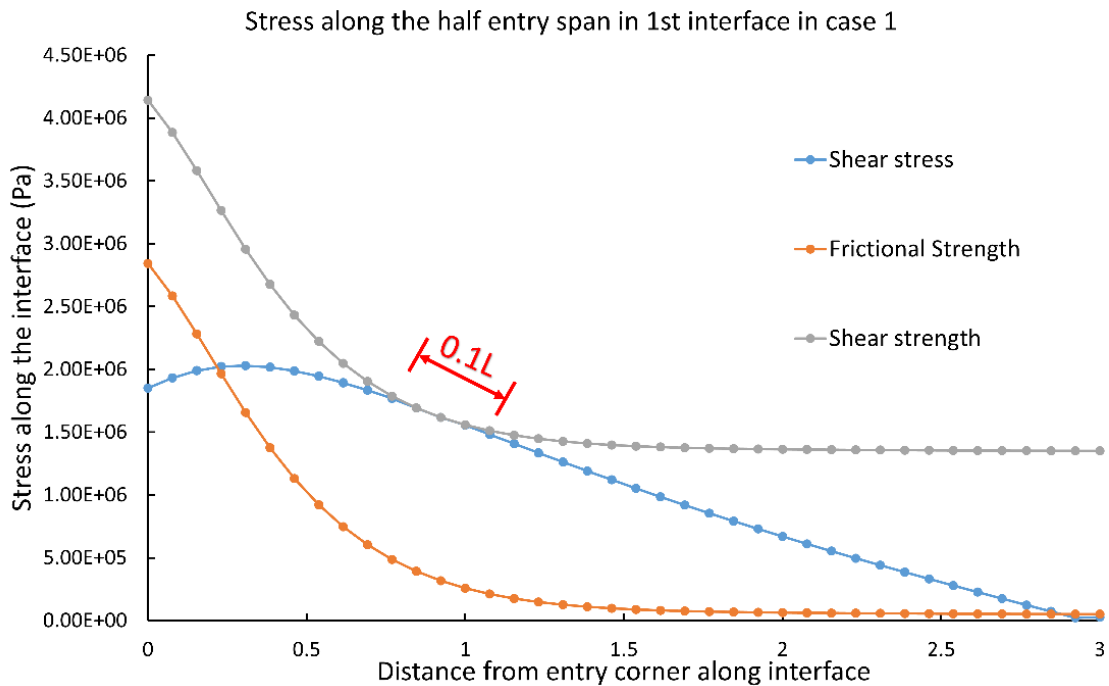


Figure 5.19 Inter-bed slipping along the 1st interface in case 1 at 47 % loading stage

Figure 5.20a-b shows the final failure profile at 67 % loading stage for cases 2 and 3. At 68 % incremental loading stage, complete roof failure occurs in both case 1 and 2. In both cases, failure profile is nearly same indicating no influence of interface tensile strength for this beam model. The trend differs from the anisotropic models results as observed in Figure 3.9 in section 3.2.6 of chapter 3. In anisotropic mine models, it was found that interface tensile strength has significant influence on the failure mode and roof deflection of shale roof especially for small lamination thickness.

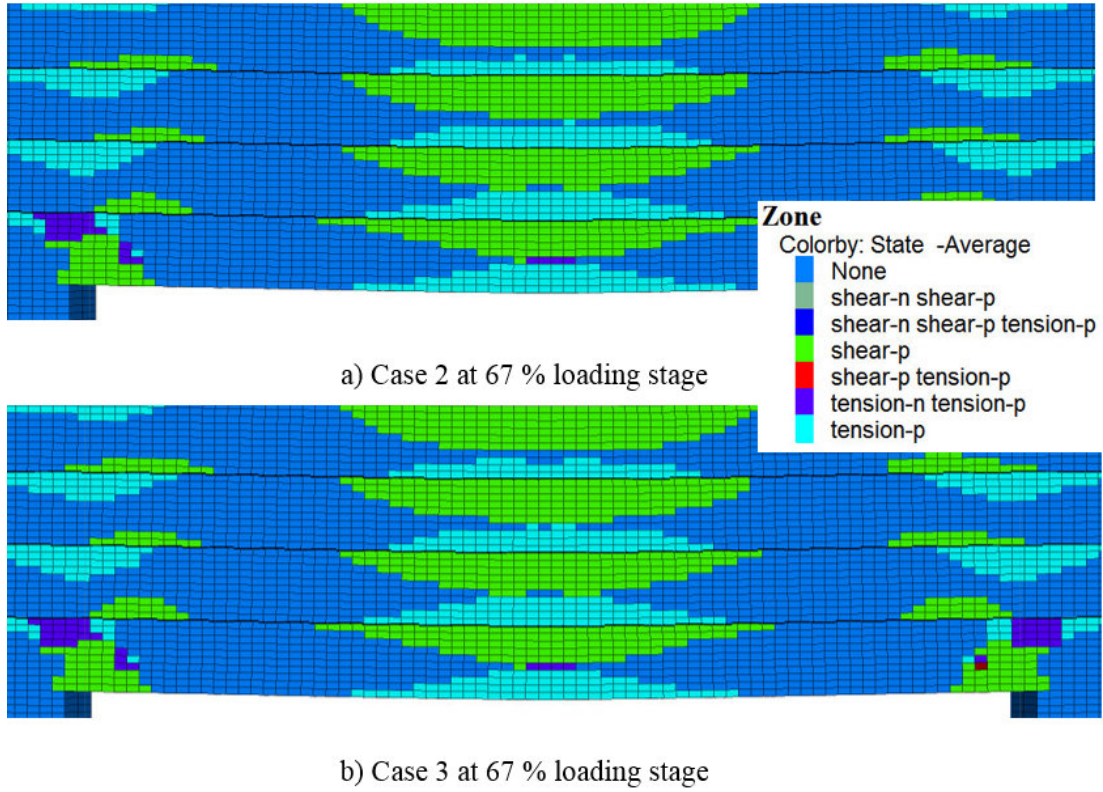


Figure 5.20 Final failure profile for different interface tensile strength.

#### 5.4.3.2 Interface stiffness

The influence of interface stiffness was evaluated in terms of normal to shear stiffness ( $K_n/K_s$ ). Two cases (Table 5.3) were simulated to understand the influence of joint stiffness on failure propagation in laminated shale beam.

Table 5.3 Interface stiffness parameters used in parametric study

	Normal stiffness (GPa/m) ( $K_n$ )	Shear stiffness (GPa/m) ( $K_s$ )	$K_n/K_s$ ratio
Case 1	10	1	10
Case 2	10	10	1



Figure 5.21a-d shows principal stress distribution at different incremental loading stages for case 1 and 2. At the initial stage, comparison arch is formed in each layer of shale roof for case 1 with maximum stress concentrated at the upper surface (Figure 5.21a), except for the bottom layer where entry corner has the highest stress concentration. For case 2, the compression arch is formed from the entry corner to the top layer indicating the multi-layered shale roof represented a single layer composite beam (Figure 5.21a). The composite behavior is due to low  $K_n/K_s$  ratio that made the entire roof stiff (Perras and Diederichs, 2009). It also reduced the overall bending of the shale roof seen from the decrease in roof deflection from 1.18 mm for case 1 to 0.74 mm from case 2.

On further increase in load, the difference in overall roof bending increased as seen at 40 % incremental loading stage (Figure 5.21b). Additionally, large inter-bed slippage (Figure 5.22) was observed for case 2, which did not occur in case 1. The early inter-bed slippage in case 2 occurs due to higher interface shear stiffness that produces large shear stress even for smaller shear displacement. Therefore, at the same loading stage, shear stress along the interface for case 2 was significantly higher than case 1, resulting in larger extent of inter-bed slippage in case 2.

The difference in overall roof bending between the two cases caused failure initiation at earlier loading stage in case 1 as compared to case 2. For instance, the failure initiated at 47 % incremental loading stage in case 1 while at 60% incremental loading stage in case 2 (figure5.23a). The failure initiated at the entry corner and the upper surface of top layer for both the cases (figure5.23a). In subsequent loading stages, failure propagation is similar to the base model in case 1 with upward shear failure propagation in lowest layer along with failure initiation and its lateral propagation at upper surface of overlying layers. However, in case 2, the failure propagated in only the top and bottom layers as seen at 70 % loading stage (figure5.23b). At this loading stage, failure is mostly concentrated around upper surface of overlying layers (second and above layers) in case 1(figure5.23b). While for case 2, failure occurred only in the top and bottom layers along with its initiation at the upper surface of the third layer (figure5.23b). The failure initiation at the third layer occurred due to the load shedded by the top layer as it has failed along the entire thickness. The loading shedding on the remaining layers along with large inter-bed slippage (approximately  $0.85L$ ;  $L$ = entry span) decreased layer interaction and resulted in the formation of compression arch in each layer in subsequent loading stages (figure5.21c-d). Therefore, at successive loading

stages failure propagation in case 2 was similar to case 1 which included failure initiation at the upper layers and its lateral progression as seen at 82 % incremental stage (figure5.23c). Although failure propagation is similar, failure extent is significantly lower in case 2 is due to lesser roof bending caused by the stiffer interface. The final failure profile of both cases is shown in figure 5.22d.

It is concluded that interface stiffness affects layer interaction of laminated shale roof. A multi-layer roof with stiffer laminar planes will create a composite beam. Although the interface stiffness did not significantly affected final failure profile of shale roof, it changed the failure propagation within the shale roof. This observation varies when the roof is loaded in a single stage. For instance, in anisotropic mine model interface stiffness affected the final failure profile as seen in Figure 3.14a-b of section 3.2.7.3 in chapter 3

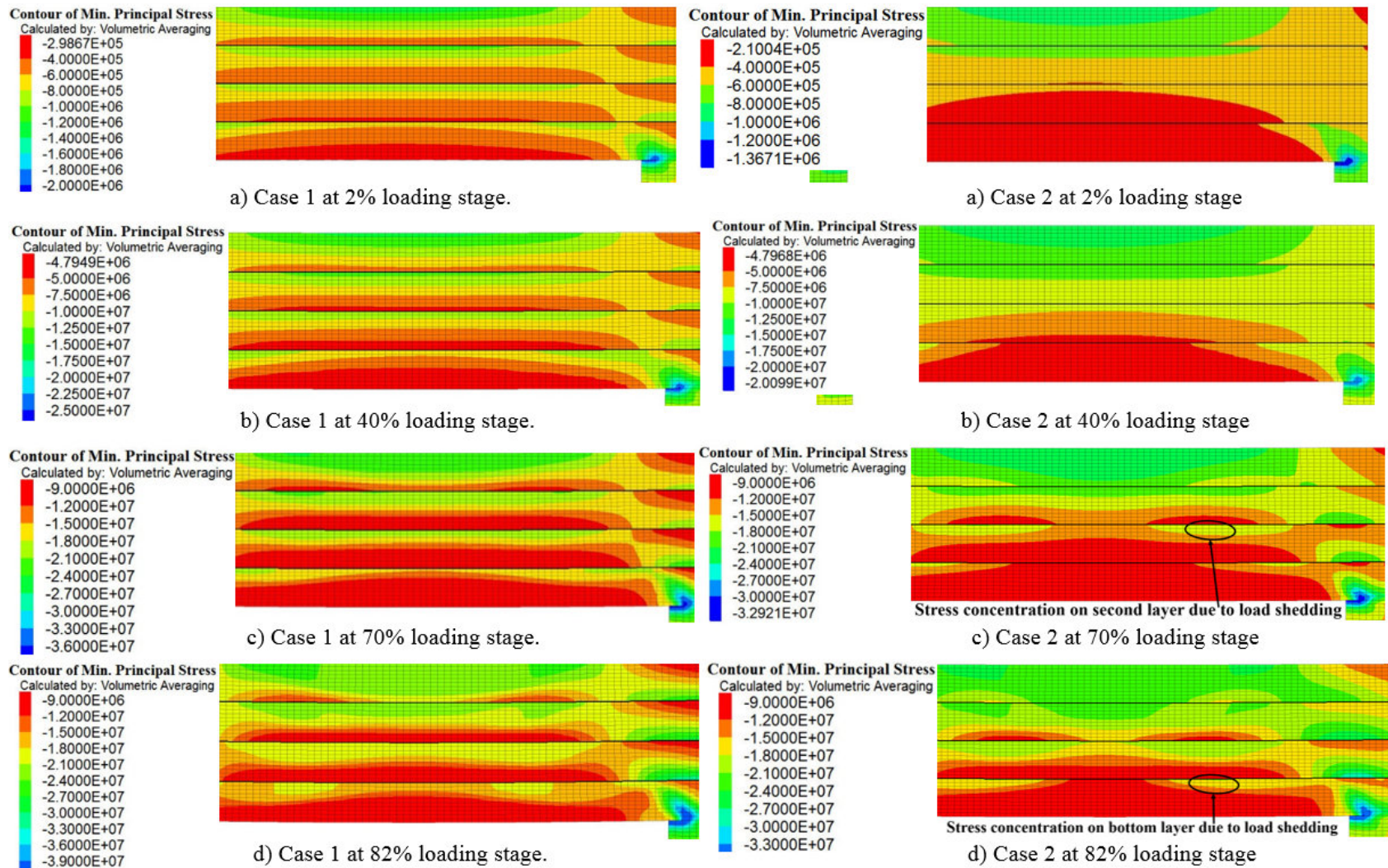


Figure 5.21 (a-d) Minimum principal stress distribution for different interface stiffness cases



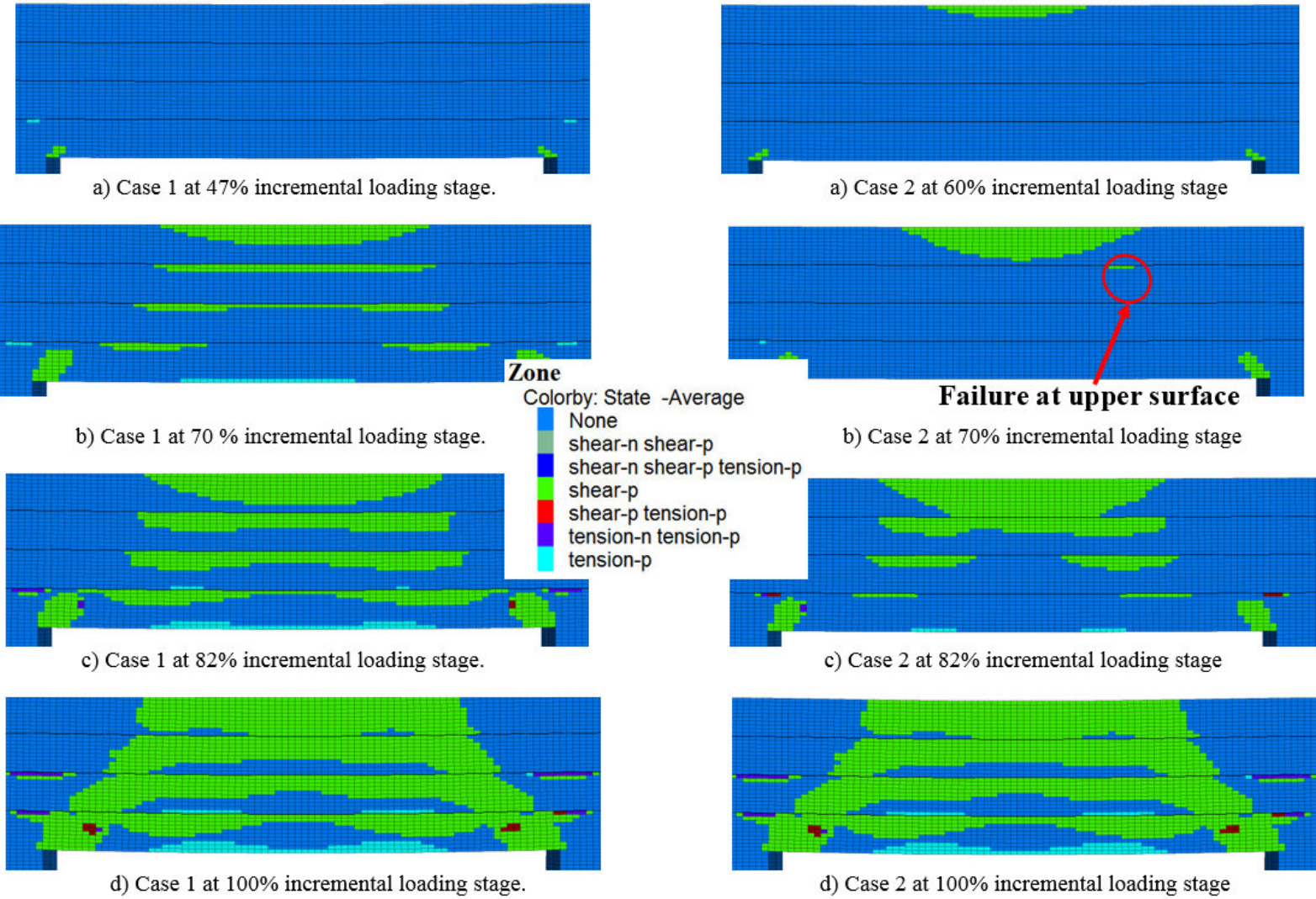


Figure 5.22 (a-d) Failure propagation for different interface stiffness cases

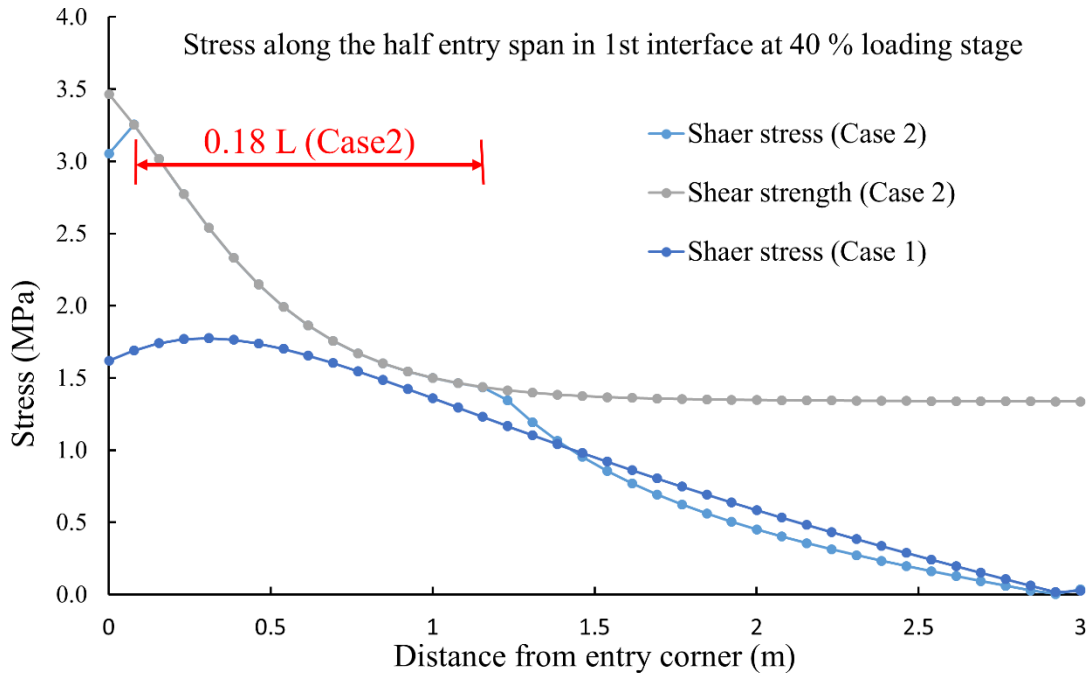


Figure 5.23 Inter-bed slipping at 40 % loading stage for different interface stiffness case

### 5.5 Limitation of Solid beam on elastic abutment model

The beam analysis in plastic state provided a detailed insight into layer interaction and its influence on failure propagation within the laminated shale roof. However, there are some limitations based on model assumptions, which are as follows:

- Boundary effect
- Simplified bending profile of shale roof.
- No clear influence of horizontal stress magnitude on failure propagation.
- Bending profile of bolted shale roof was not studied.

Due to the vertical load on the top of the shale roof, high stress boundary in the beam model, high stress concentration occurred in the top layer, which resulted in failure initiation at its upper surface along with the propagation of failure towards the entry. This behavior is not observed in underground coal mines with a laminated roof. The *in-situ* vertical load on shale roof will depend on its interaction with overburden strata, and any high-stress concentration is compensated by deformation of overlying strata.

The vertical load profile is based on an analytical solution that excludes bending of overlying strata, and therefore, the magnitude was assumed constant for all loading stages. This results in a simplified bending profile of the shale roof, which is unlikely to be observed in underground mines. As mentioned earlier, shale roof, due to its interaction with overburden strata, will have more complex bending profile as compared to the beam model. The load profile was applied in 100-increment stage by assuming a single stress path. Due to this reason, the beam model underestimated the influence of horizontal stress as it produced similar failure propagation irrespective of the magnitude of horizontal stress.

The roof bolting process was not included in the current research, which is used to provide beam building and suspension effect to a laminated roof (Panek, 1962; Peng, 2005). In the current study, the beam building effect was incorporated indirectly by assuming higher interface cohesion value (1.3 MPa). The model with high cohesion value showed significant layer interaction as failure initiated and propagated from entry corners. However, the models only gave a simplified effect of bolting as the increase in laminar plane's shear resistance was uniform along the entire span, which is not observed in mines. In addition, the approach does not simulate the suspension effect of the roof bolt.

## **5.6 Summary**

In this chapter, plastic beam analysis was performed on to understand layer (laminar) interaction in a laminated shale roof. Solid Beam on Elastic Abutment beam was simulated under the elasto-plastic state in FLAC3D. The advantage of this approach is simplified bending profile of immediate roof as compared to the anisotropic mine model in chapter 3. This analysis provided a detailed understanding of into layer interaction and its influence on failure propagation within the laminated shale roof. The critical findings are as follows:

- The compression arch is formed in each layer of the laminated roof due to the presence of weak/ laminar plane, which resulted in high-stress concentration at the upper surface of these layers.
- The exact location of high-stress concentration at the upper surface is dependent on bending profile of shale roof and interface (laminar plane) shear strength.

- The parametric study showed no significant influence of high horizontal stress on failure progression into shale roof, which was due to incremental loading in each case.
- With the decrease in the lamination thickness, the bending stiffness of individual layers decreased resulting in the higher extent of failure at a given loading stage. Due to the same reason, the thinly laminated roof after significant bending underwent layer separation, which results in the formation of thin beams and subsequent collapse of the entire roof.
- If high interface cohesion (1.3 MPa) used in the study is considered as a representation of the beam building effect of roof bolting. It can be concluded that even with bolting, a thinly laminated roof can easily undergo delamination if it is allowed to bend significantly.
- Laminar interaction is highly dependent on interface cohesion as it dictates location and degree of delamination. For instance, low interface cohesion allowed the formation of individual beams; as a result, failure is concentrated around mid-span.
- For interface with high cohesion, significant layer interaction occurred that resulted in the failure being more concentrated towards entry corners.
- The interface stiffness significantly affected the layer interaction within the shale roof. A multi-layer roof with stiffer laminar planes will create a composite beam. However, the interface stiffness did not significantly affect the final failure profile of shale roof.



## 6. PLATEN DESIGN

### 6.1. Experimental Design and Set-Up

Layer interaction in laminated shale roof is not limited to plane strain conditions as seen in various cutter roof cases discussed in section 2.2.1.4 of chapter 2. The cutter roof failure progressively moves through bolt planes indicating the failure is accurately represented by plate type failure instead of beam. In the preceding chapters, the layer interaction was investigated assuming plane strain conditions where beam or mine models were used with joint/interface elements that represented weak planes between two laminated rock layers. However, similar analysis in three-dimension is difficult to validate, as it would involve complex bending of thin plates of finite dimension. Additionally, this analysis is not very useful without accurate representation of lamination in numerical models. Furthermore, most studies (Ray, 2009; Gadde and Peng, 2005) suggested that using interfaces in a three-dimensional analysis would limit the propagation of cutter failure in shale roof.

For understanding the underlying mechanism of failure propagation from one lamina to another, experiments are needed that involved three-dimensional bending of laminated rocks. A true-triaxial setup would have been ideal for this research effort. However, such equipment is limited in availability and beyond the financial scope of the current research. In addition, the stress state on the boundary and vicinity of excavation are in a biaxial stress state where  $\sigma_1$ ,  $\sigma_2 \neq 0$  and  $\sigma_3$  is either zero or very low compared to the two other principal stresses. Therefore, initial attempt was to use the biaxial platen designed by Arora and Mishra, 2015. However, numerical analysis of the platen design showed that it was not accurately applying true biaxial loads during the test. A detailed discussion on the design is presented in section 6.2. Furthermore, various studies (Mogi 1967; Yun, 2008; Bobet, 2001; Amadei et al., 1986) suggested problems such as friction effect, misalignment of applied load and stiffness of loading system should be considered while designing any poly-axial loading device. Therefore, the platen design was modified and validated by comparing failure modes and peak strength of Berea sandstone with other biaxial devices. In addition to these platens, a confining device was used to apply true-triaxial load on a 50.8 mm cubical specimen. After validating the device, the next step was to test on shale samples. However,

correctly sized specimens of shale could not be obtained in the stipulated time and therefore no test was performed on shale specimens. However, the setup was included in this thesis to represent a device that can accurately test rock specimens with biaxial and true-triaxial loading conditions.

## 6.2. The Biaxial Platen

The design of the biaxial frame was based on the device by Arora and Mishra, 2015 (Figure 6.1). The frame consists of two platens with arms (extended section of the platen) mounted on a 50.8 mm cubical rock specimen. The arms have four surface area that (“e”, “f”, “g” and “h”) apply load on to four faces of the cubical specimen. Figure 6.1 shows the dimensions of the mild hardened steel platens. Two arms (one for each platen) (“g” and “h”) are 50.8 mm (2 in.) in length and completely cover two faces of the specimen. The remaining arms, “e” and “f” are slightly shorter in length, i.e., 45.7 mm (1.8 in.) to prevent contact between the two platens during loading. The adjacent arms of each platen assumed to apply an equal load to the specimen, replicating the biaxial stress conditions with  $\sigma_1 = \sigma_2$  and  $\sigma_3 = 0$ . In relation to field conditions, the Figure 6.2 (a) is referred that shows the possible stresses that act on a roof when an entry is created in the coal seam. “ $\sigma_{h1}$ ” & “ $\sigma_{h2}$ ” are the in – situ principal horizontal stresses and “V” is the overburden stress. The case where,  $\sigma_{h1} = \sigma_{h2}$ , was replicated inside the platen as shown in Figure 6.2b. “P” is the load provided by the uniaxial compression testing machine from the bottom moving platen, “R” is the reactionary force applied by the top fixed platen. These forces are split by the biaxial platens to apply the stress component “N” acting normal to the laminations.

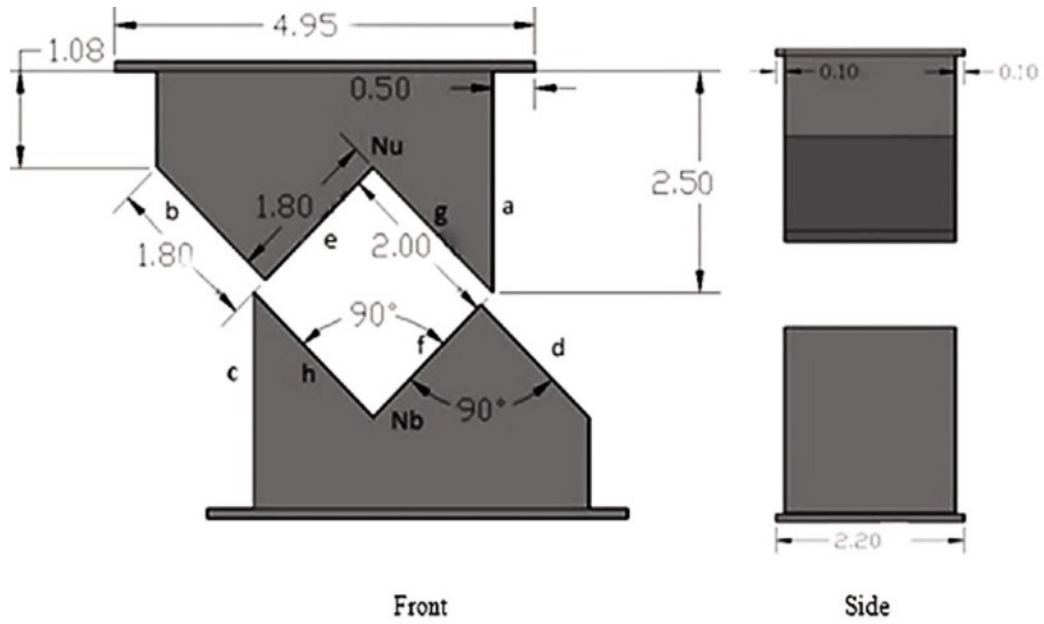


Figure 6.1 Platen designed by Arora and Mishra 2015. (Unit: inch)

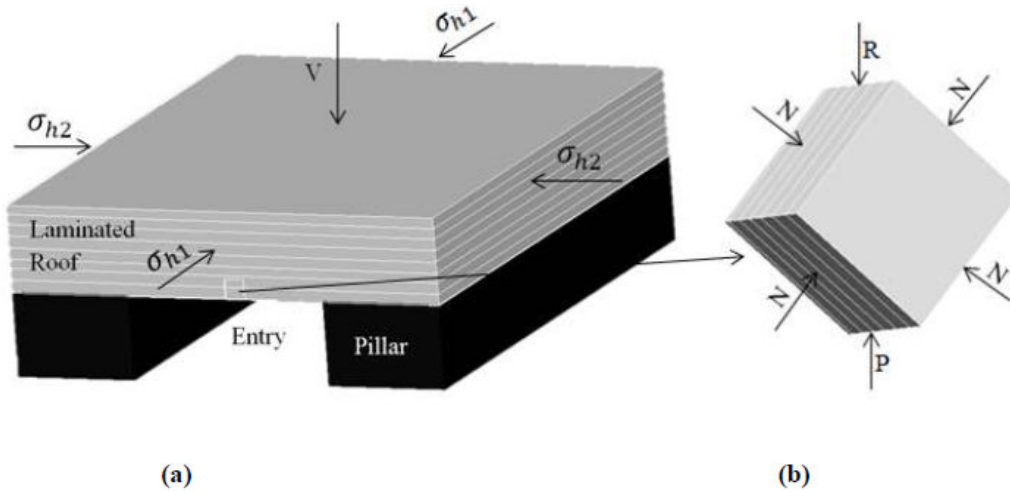


Figure 6.2 (a) Stress acting on the roof of an entry (b) Stress distribution on specimen inside UCS testing machine (Arora and Mishra 2015).

Numerical analysis of the design was performed in 3DEC to assess the exact loading conditions of the design. The results showed unsymmetrical displacement profile that produced rotation at one side of the specimen (Figure 6.3a). Therefore, platen was redesigned to make symmetrical arms (Figure 6.4a-b) to overcome these limitations. The improved design, when simulated in 3DEC, showed symmetric vertical displacement contour without any rotation (Figure 6.3b). The inner surfaces of the platen were machine-smoothened to remove any undulated surface that may create additional stress concentrations.

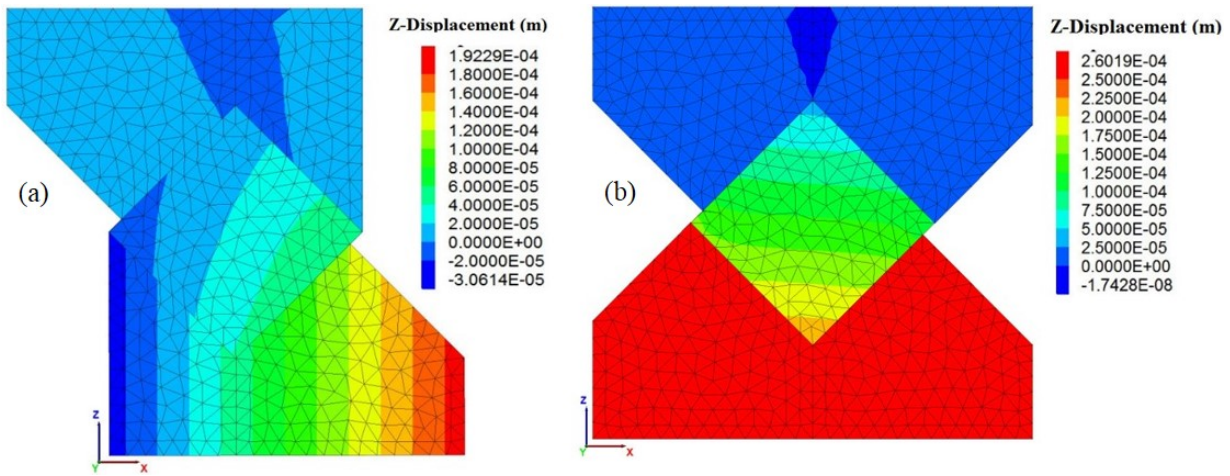


Figure 6.3 Vertical displacement contours: (a) biaxial device by Arora and Mishra, 2015, (b) modified biaxial design used in this study.

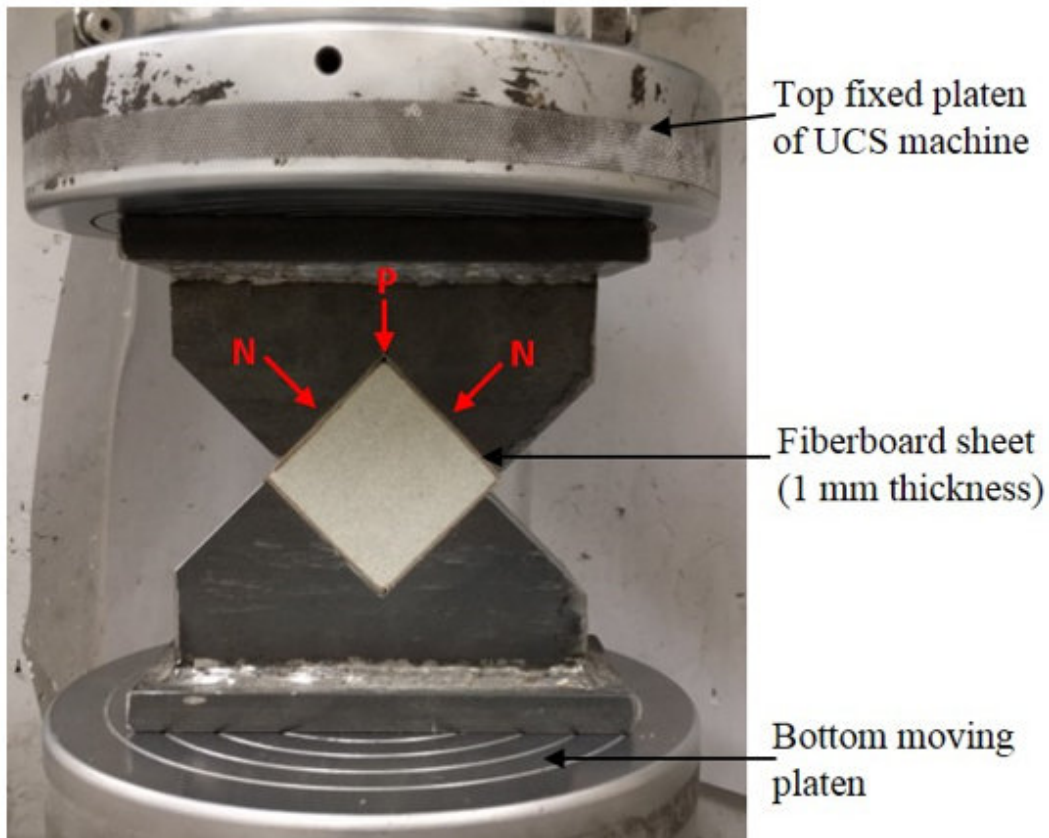
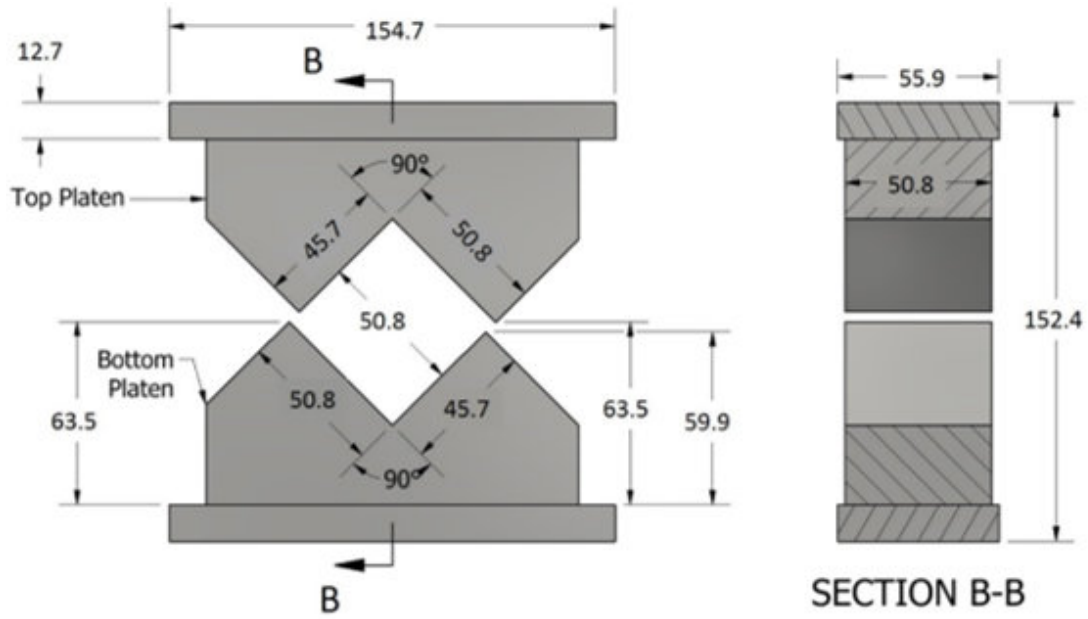


Figure 6.4 (a) Schematic view of experimental set-up of biaxial test with confining device (Units: mm) (top); (b) Test setup with biaxial platens ( $\sigma_1 = \sigma_2$ ).

The biaxial frame (Figure 6.4a-b) can apply only one set of biaxial stress ( $\sigma_1 = \sigma_2$ ). Therefore, biaxial tests with constant intermediate principal stress  $\sigma_2$  were conducted using a confining device (controlled with hydraulic jack) along with two steel cubic spacers (Figure 6.5). The confining device consists of two square plates with the dimension of 49.53 (length)  $\times$  49.53 (breadth)  $\times$  6.35 (height) mm. The square plates are attached to the two hollow beams that are interconnected through tension rods. The beams are suspended through the mounting plate that is attached to the upper platen of the load frame using ball joint rods. The setup is connected to the plunger of a hydraulic jack, attached to the hollow beam on the left side. The hydraulic jack controlled the confinement stress on the specimen during the biaxial test. Two cubic steel spacers (dimensions of 50.8  $\times$  50.8  $\times$  49.53 mm) are placed on the top and bottom of the specimen. They were used to transfer the axial load from the platens of the uniaxial loading frame to the specimen, whereas the square plates of confining device applied constant intermediate stress. It is to be noted that as square plates are interconnected through tension rods, there is a limit to the amount of load that can be applied which depends on the tensile strength of tension rods.

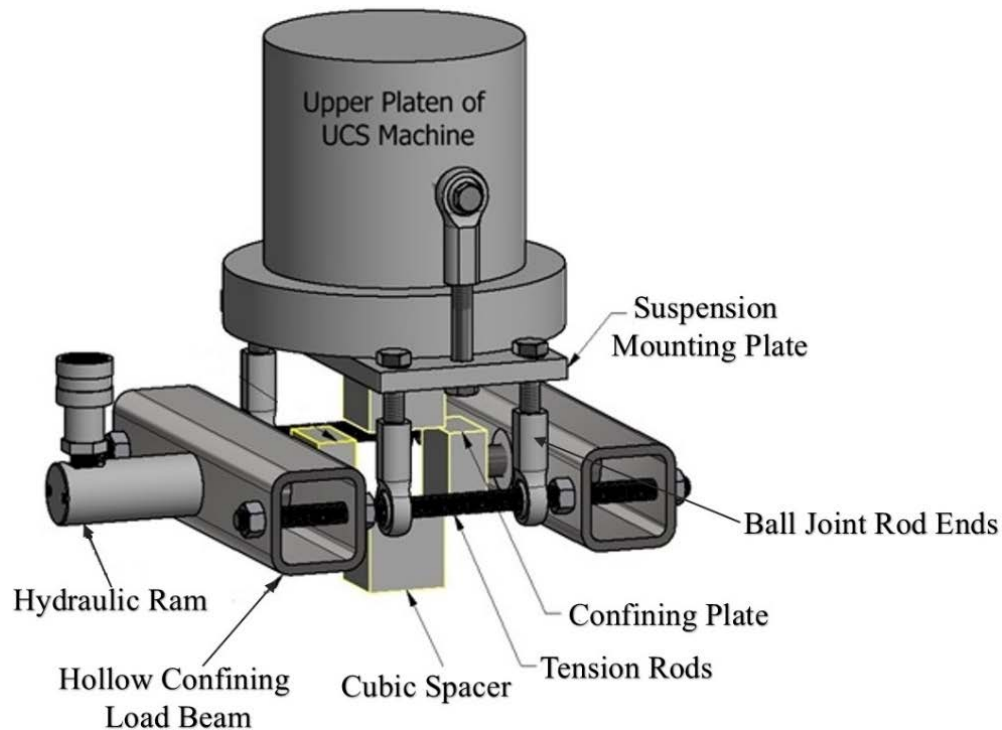


Figure 6.5 Schematic view of experimental set-up of biaxial test with confining device ( $\sigma_2 = \text{constant}$ ).

### 6.3. Modification of biaxial platens for true triaxial test

The objective of this test was to analyze the effect of confinement on the movement of the rock and the failure response of the specimen in a triaxial stress state. Various researchers have comprehensively investigated failure and strength envelope of different rock types (Handin et al., (1967); Colmenares and Zoback, 2002; Al-Ajmi and Zimmerman, 2005). However, these studies used true triaxial and biaxial devices that required time-consuming efforts (Haimson and Chang, 2000; Walsri et al., (2009), Amadei et al., 1984; Yun et al., (2010); Kulatilake et al., (2006). A simple and cost-effective true-triaxial setup was designed to be used with a uniaxial loading device. The apparatus consists of consist of confining device in conjunction with biaxial frame mentioned earlier. The entire setup is placed in the compression-testing machine (Figure 6.6) to replicate two conditions,  $\sigma_1 = \sigma_2 > \sigma_3$  and  $\sigma_3 = \text{constant}$  load condition. As mentioned in section 6.2, there is a limit to the amount of load that can be applied by square plates.

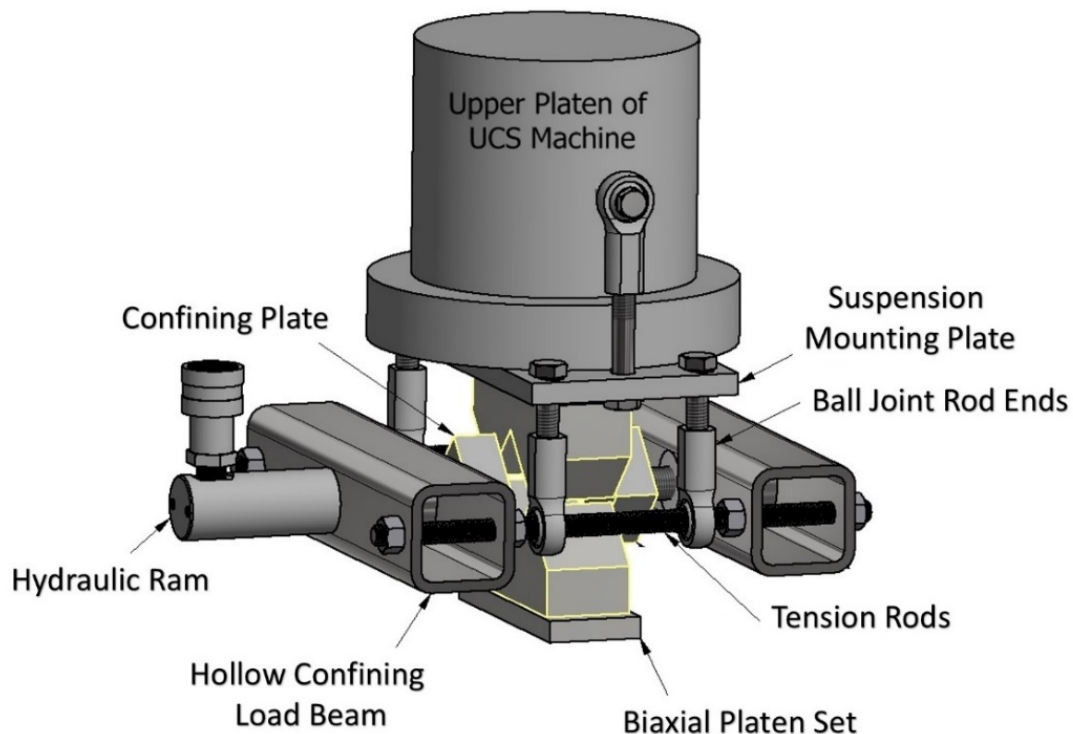


Figure 6.6 Schematic view of experimental set-up of true-triaxial test (biaxial frame with confining device) replicating  $\sigma_1 = \sigma_2 > \sigma_3$  and  $\sigma_3 = \text{constant}$



## 6.4. Uniaxial Compression Testing Machine

The specimens were tested in a servo-hydraulic compression-testing machine (Material Test System). Load is applied by controlling the movement of the lower movable platen, which is controlled in two ways, namely: force and stroke (displacement) control. The user sets a pre-defined value for force or displacement rate, which the load frames, apply on the specimen (figure 6.7). It also consists of a data acquisition system and standalone software called MPT (Multi-purpose Test software) that is used for designing and running a suite of tests. The MPT (Multi-purpose Test software) allows the user to program various load paths and constraints for completion of the test. A linear variable differential transformer (LVDT) is mounted below the lower platen that measures the displacement. Therefore, it is also used to measure the axial deformation of the specimen.



Figure 6.7 MTS servo controlled compression testing machine and its component 1) Machine Load (2) Glass Shield (3) Hydraulic Actuator (4) Manual Control System (5) Strain Gauge Control Panel (6) Computer (7) MTS Data Acquisition System (8) Upper steel platen with circular grooves (9) Specimen (10) Lower steel platen with circular grooves

## 6.5. Friction Effect

A fundamental assumption in the testing of rock specimens under uniaxial or biaxial loading is that the axial stress is uniformly distributed at the loading surfaces, which are typically the principal planes. However, this assumption becomes untenable upon consideration that a frictional constraint develops at the interface between the loaded faces of specimen and loading platens of test machine during the compressive loading process (Labuz and Bridell, 1993). For this purpose, numerical simulations of biaxial test design were performed in 3DEC (discussed in section 6.2). The analysis indicated that by minimizing the friction coefficient of the material between the rock-platen interfaces, true biaxial loading conditions could be achieved.

The first attempt to reduce the frictional shear was by using soft packing and lubricants between the sample and loading platen (Föppl, 1900). However, the packing created lateral tensile stresses and non-uniform stress distribution in the sample, which reduced its apparent strength (Föppl, 1900). Other subsequent attempts to eliminate the end effects included the use of Araldite platens, lubricants on the  $\sigma_2$  face (Mogi, 1967), cardboard sheets (Parrott, 1970), aluminum foil and a thin film of silicone bearing grease (Obermeier, 1971), steel brush platens (made of closely spaced 3.2 mm square steel pins) (Brown, 1974). Most recently, Labuz and Brindell, 1993, reported of various friction reducers like graphite, molybdenum disulfide, stearic acid and Teflon sheets of 0.05 mm thick used in uniaxial tests. They found stearic acid followed by Teflon sheets to be highly effective in removing the end effect.

In this research, tests were conducted in uniaxial, biaxial and triaxial stress states on cubical sandstone specimens. First, steric acid, a mixture of equal proportion of stearic acid crystals and Vaseline heated in an oven at around 70°C was used. However, analysis of the failure mode of cubical specimens from uniaxial to true triaxial stress conditions reveals dominant axial splitting failure mode in all tests (Figure 6.8a-c.). Additionally, the average peak strength under uniaxial stress state was around 22 MPa which increased to 27.39 MPa in a biaxial stress state ( $\sigma_1 = \sigma_2$  loading condition) and to 28.36 MPa for true-triaxial state ( $\sigma_1 = \sigma_2$  and  $\sigma_3 = 6.2 \text{ MPa}$ ). The increased peak strength was only 3.54% from biaxial to triaxial stress state at confinement around 0.28 times the UCS value of cubical specimen. This slight increase along with same dominant failure mode regardless of loading conditions suggested that steric acid was unsuitable for the

biaxial frame. Other lubricants such as Teflon sheets, Molybdenum Disulphide, and corrugated fiberboard sheets were tried and finally, corrugated fiberboard sheets as suggested by Lundborg, 1967 were found to be the best fit for this biaxial platen apparatus. The fiberboard served two purposes – to compensate for the lack of flatness on the sample ends and to reduce the friction angle.

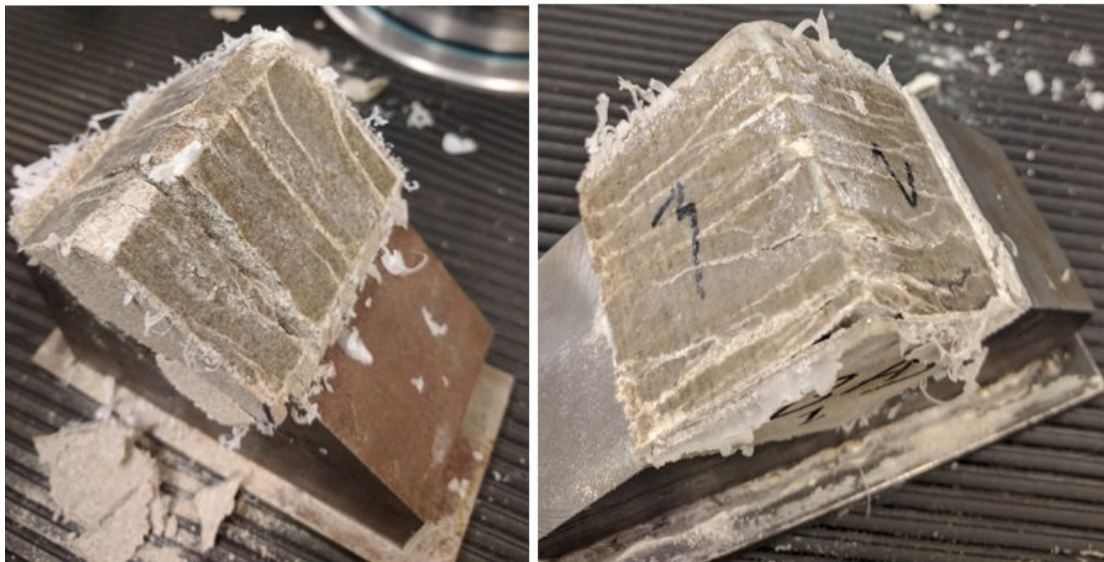
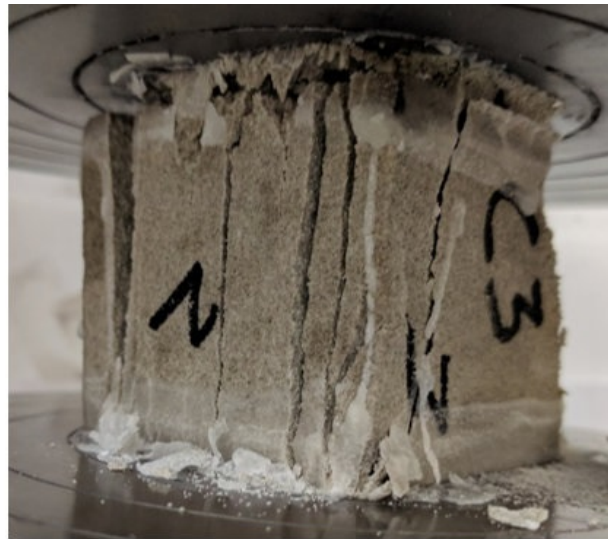


Figure 6.8 Axial splitting in 50.8 mm cubical sandstone specimen (a) uniaxial stress state; (b)biaxial stress state( $\sigma_1 = \sigma_2$ ); (c) triaxial stress state ( $\sigma_1 = \sigma_2$  and  $\sigma_3 = 6.2$  MPa)

## **6.6. Laboratory Investigation**

### **6.6.1. Validation of biaxial device**

To validate the biaxial frame and confining device design, a study involving influence of poly-axial stress state on failure response of Berea sandstone was conducted. The failure mode and peak strength values obtained in the biaxial stress conditions were compared then with existing biaxial devices. Additionally, the influence of specimen size in uniaxial stress conditions on failure modes was also studied so as to have a complete understanding of failure mode transition from standard UCS test to triaxial test on cubical specimen.

### **6.6.2. Rock types and specimen geometry**

Berea sandstone was selected for investigation with specimens of cylindrical, cuboidal and cubical geometry. Cylindrical specimens were used for standard uniaxial compression test. The cuboidal and cubical specimens were used to study the size effect under uniaxial compression test. Additionally, cubical samples were used for biaxial and true triaxial tests.

### **6.6.3. Lithologic description**

Large blocks of Berea sandstone (600 mm x 400 mm x 154 mm) were procured from Cleveland Quarries. The lithologic description was based on X-Ray Diffraction analysis and information from Cleveland Quarries. Berea sandstone used in this study is called “Liver Rocks”. It is homogenous rock with no visible lamination. Ambient Porosity was around 18-20 %.

### **6.6.4. Specimen Preparation**

Five group of specimens were prepared from the large Berea sandstone blocks (Figure 6.9). The specimens were cut using a machine-operated rock saw with a circular cutting blade. All the surfaces of the specimen were grounded using a combination of a handheld grinding machine and sandpaper to achieve the desired dimension with tolerance to +0.20 mm and smoothness with tolerance of  $\Delta/d$  0.0043 mm in accordance with ASTM standards (ASTM,1998). The angle between the adjacent face was kept at  $90^0$  with a tolerance of  $0.25^0$ . Specimens were oven-dried and weighed repeatedly until they were dry, and no weight loss was recorded. The average dry density of Berea sandstone was  $2,450 \text{ kg/m}^3$ .

- Group A: cylindrical specimens, 50.8 mm in diameter and 101.6 mm in length, with a height/width ratio (H/D) of 2.
- Group B: cuboidal specimens, 50.8 mm x 50.8 mm x 101.6 mm, with a height/width (H/W) ratio of 2.
- Group C: cubical specimens, 50.8 mm x 50.8 mm x 50.8 mm, with a height/width (H/W) ratio of 1.0.
- Group D: cuboidal specimens, 50.8 mm x 50.8 mm x 25.4 mm, with a height/width (H/W) ratio of 0.5.

Groups A was used to determine standard Uniaxial Compressive Strength (UCS) of Berea sandstone. All specimens except of Group A had square cross-section (50.8 mm x 50.8 mm). Groups B, C and D were used to study the size effect in the uniaxial compressive test. Additionally, Group B was used in biaxial and true triaxial tests to validate platen design and understand the transition in peak strength and failure mode form uniaxial to triaxial stress state.

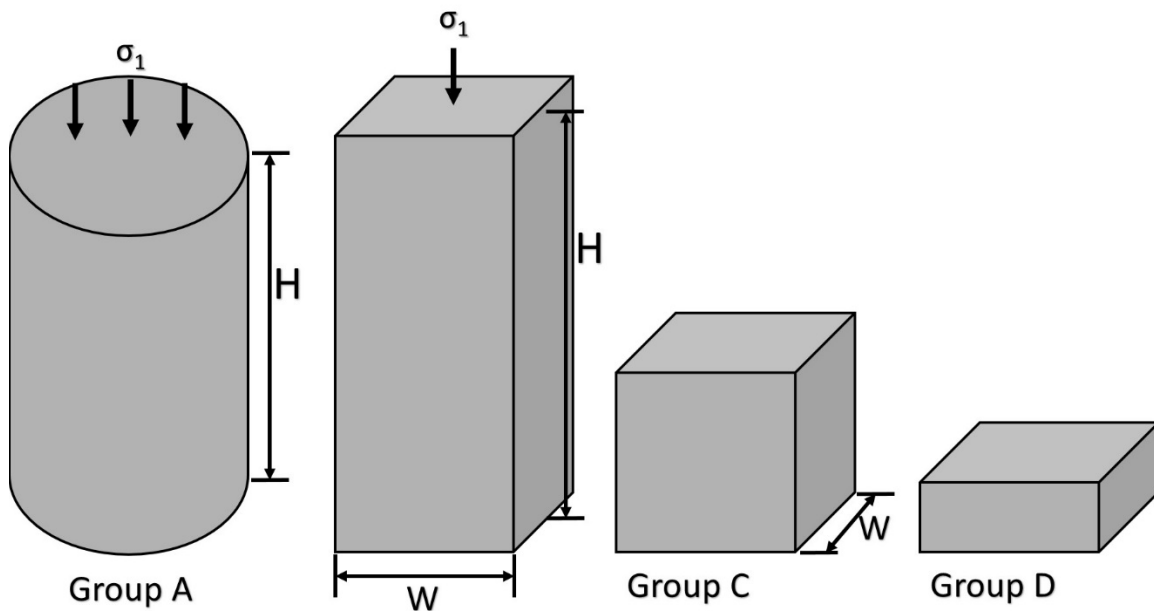


Figure 6.9 The geometric shapes of the four groups of Berea sandstone specimens (H, W represent height, width and of the prism specimen, respectively)

### **6.6.5. Uniaxial compression test**

The uniaxial compression tests are performed to determine the failure mode and peak strength in uniaxial stress state. Four group of specimens as mentioned in section 6.6.4 were used to investigate the influence of specimen size on failure mode and peak strength of Berea sandstone. The number of tests performed in each group is shown in Table 6.1. For specimens with square shaped cross-section (Group B, C and D), cubic spacers of dimension:  $50.8 \times 50.8 \times 49.53$  mm were placed on the top and bottom of the specimen. These spacers ensured uniform loading on the specimen's end surfaces by removing the effect of circular grooves in the platens of the uniaxial loading device. Additionally, cardboard was used between the rock-plate interface in all tests to maintain uniformity and reduce end effects in all these tests. For these tests, stroke control mode was used to apply load on the rock specimen with a rate of 0.00254 mm/s. Stroke control mode assists in minimizing sudden failure of a specimen and in observing its complete behavior including post-failure characteristics. The entire set-up (specimens along with cubic spacers) was placed on the machine's platen and a small load of 100lbs was applied to raise the platen and ensure proper contact between the platens of the uniaxial device and cubic spacers. The test was initiated by lowering the machine platen that applied load on the cubic spacers. As the test progressed, failure in the specimen was carefully recorded. On the completion of the test, the specimen failure was analyzed and photographed to capture the post-test state of the specimen. The uniaxial device's load cell measured the ultimate load for each test. The peak strength was then calculated from the ultimate load for each specimen.

Table 6.1 List of test parameters used in uniaxial test

Group	Specimen Shape	Specimen Slenderness (H/W) ratio	Number of tests
A	Cylindrical	2	5
B	Cuboidal	2	5
C	Cubical	1	5
D	Cuboidal	0.5	5

#### 6.6.6. Biaxial compression test

Biaxial tests were carried out on 50.8 mm cubic specimens from group C either using the biaxial frame (Figure 6.4b) or the confining device (Figure 6.5) depending on loading conditions.

##### 6.6.6.1 Loading path

Two load paths were used in the experimental investigation under biaxial stress state (Figure 6.10). The load path 1 was performed using the biaxial frame (Figure 6.4b) which represents high intermediate stress ( $\sigma_1 = \sigma_2$ ) where both principal stresses were increased until failure. In loading path 2, square plates of confining device applied the constant intermediate stress ( $\sigma_2 = \text{constant}$ ), and uniaxial frame increased the maximum principal stress  $\sigma_1$  until failure (Figure 6.5). Additionally, in tests under loading path 2, three intermediate stress levels, i.e.,  $\sigma_2 = 6.89, 13.789$  and 27.58 MPa stress were used. The test parameters used in biaxial tests are provided in Table 6.2



Table 6.2 List of test parameters used in biaxial test

Number of tests	Loading Path	Specimen shape	$\sigma_1/\sigma_2$ stress ratio	Intermediate principal stress $\sigma_2$ (MPa)
5	1	Cubical	$\sigma_1 = \sigma_2$	Peak strength
5	2	Cubical	$\sigma_2 = 0.12\sigma_c$ ( <i>constant</i> )	6.89
5	2	Cubical	$\sigma_2 = 0.233\sigma_c$ ( <i>constant</i> )	13.789
5	2	Cubical	$\sigma_2 = 0.46\sigma_c$ ( <i>constant</i> )	27.58

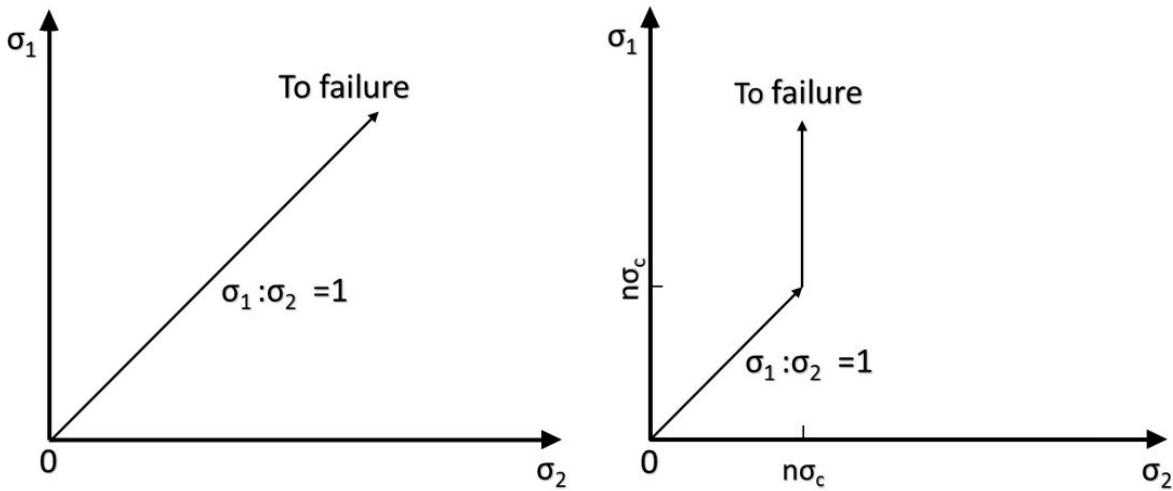


Figure 6.10 Biaxial test (a) Loading path 1, (b) Loading path 2 ( $n\sigma_c$  represent magnitude of constant intermediate stress in terms of average UCS of cubical sandstone)

### 6.6.6.2 Test Procedure

In biaxial tests, the procedure used was similar to the uniaxial compression tests. In all biaxial tests, stroke control mode used to apply load on the rock specimen with a rate of 0.00254 mm/s to maintain uniformity with uniaxial tests.

For loading path 1, biaxial frame along with cubical specimen was kept inside the uniaxial loading device. Test procedure is similar to uniaxial compressive tests in section 6.6.5. After the completion of the test, the specimen failure was analyzed and photographed to capture the post-test state of the specimen. In each test, ultimate load was recorded from uniaxial load cell. The peak strength ( $\sigma_1 = \sigma_2$ ) was then calculated using approximate stress acting on the faces of the specimen in contact with the biaxial platen. As shown in Figure 6.4b, if P is the force applied by the machine platen of the compression test rig, N is the force component acting normal to the face of the specimen, as given by:

$$N = P \cos 45^\circ \quad \text{Equation 6.1}$$

$A_{\text{avg}}$  is the approximate area of the face of the cubic specimen in contact with the biaxial platen, calculated by

$$A_{\text{avg}} = (A_1 + A_2)/2 \quad \text{Equation 6.2}$$

Where,  $A_1$  and  $A_2$  are specimen area in contact with adjacent arms of the biaxial platen.

$$\text{Peak strength } \sigma_1 = N / A_{\text{avg}} \quad \text{Equation 6.3}$$

Similar test procedure was adopted for loading path 2, where the confining device applied the constant intermediate stress,  $\sigma_2$ . The confining device was mounted on uniaxial loading device and specimen along with cubic spacer were kept inside of the uniaxial device (Figure 6.5). In these tests, peak strength,  $\sigma_1$  was calculated from ultimate load and corresponding intermediate principal,  $\sigma_2$  was recorded from assigned preset value in hydraulic jack.

### 6.6.7 True-triaxial test

True-triaxial tests were performed on 50.8 mm cubic specimens from group C using biaxial frame in conjunction with the confining device (Figure 6.6). This test follows a novel loading path (Figure 6.11), i.e.,  $\sigma_3 = \text{constant}$  (by confining device) and  $\sigma_1 = \sigma_2$  (by biaxial frame) was increased till failure. The stress state replicated in this test also corresponds to axisymmetric extension (Ma et al., 2017). These tests were conducted under three levels of minor principal stress, i.e.,  $\sigma_3 = 0, 6.2$  and  $20.68$  MPa. Higher confinement tests cannot be performed due to limited load capacity of confining device, as mentioned in section 6.3. The list of test parameters used in true-triaxial tests were given Table 6.3. The test procedure is similar to the biaxial test with loading path 2.

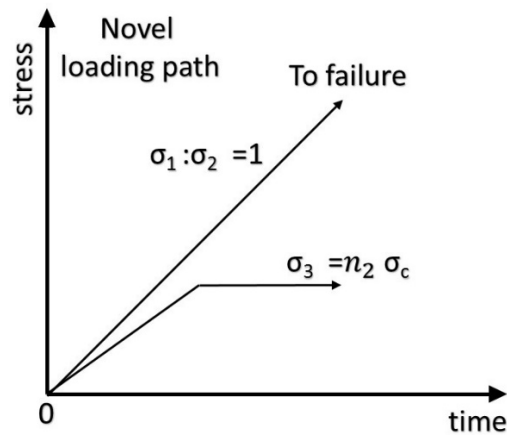


Figure 6.11 Novel loading path (Ma and Haimson 2017) used in true triaxial testing,  $n_2 \sigma_c$  represent magnitude of constant minor principal stress in terms of average UCS.

Table 6.3 List of test parameters used in true-triaxial test

Number of tests	Specimen shape	$\sigma_3/\sigma_c$ stress ratio	Minor principal stress $\sigma_3$ (MPa)
5	Cubical	$\sigma_3 = 0$	0
5	Cubical	$\sigma_3 = 0.11\sigma_c$	6.2
5	Cubical	$\sigma_3 = 0.35\sigma_c$	20.68

## **6.7 Test Limitations**

Although the design of biaxial platen and confinement apparatus is simple and cost-effective, there are few limitations, which are as follows:

1. The specimens that can be tested in biaxial and true-triaxial test were limited to 50.8 mm cubes.
2. The specimens were not instrumented to obtain strain measurements.
3. Effect of friction between the platens of the load frame and the biaxial platens was not investigated.
4. The friction at rock-platen interface could not be completely eliminated.
5. True-triaxial test under high confinement cannot be performed due to limited load capacity of confining device.

## **6.8 Test Results**

In this section, results of all tests from uniaxial to true-triaxial stress state were presented. For each test type, first peak strength data was analyzed followed by failure mechanism. Additionally, suitable failure envelopes for biaxial and triaxial stress states were also determined in section 6.8.4.2 and 6.8.5.1 respectively.

### **6.8.1 Uniaxial compressive test**

Five specimens for each of the four groups of sandstone mentioned in section 6.6.4 were tested in a uniaxial stress state. The main objective of these tests were to understand the influence of specimen size on failure mechanism and strength of uniaxial loaded rocks. The test results of uniaxial compressive tests for each group, .i.e., A, B, C and D are provided in Table 6.4 to 6.7.

Table 6.4 Results of uniaxial compressive tests for group A.

Specimen No.	Specimen Shape	Specimen Slenderness (H/W) ratio	UCS (MPa)	Average Peak Strength, $\sigma_1 \pm$ Standard Deviation (MPa)
A-01	Cylindrical	2	61.72	$50.53 \pm 7.46$
A-02	Cylindrical	2	41.72	
A-03	Cylindrical	2	53.03	
A-04	Cylindrical	2	47.21	
A-05	Cylindrical	2	48.98	

Table 6.5 Results of uniaxial compressive tests for group B.

Specimen No.	Specimen Shape	Specimen Slenderness (H/W) ratio	UCS (MPa)	Average Peak Strength, $\sigma_1 \pm$ Standard Deviation (MPa)
B-01	Cuboidal	2	50.94	$53.6 \pm 3.56$
B-02	Cuboidal	2	58.49	
B-03	Cuboidal	2	55.43	
B-04	Cuboidal	2	53.58	
B-05	Cuboidal	2	49.56	

Table 6.6 Results of uniaxial compressive tests for group C.

Specimen No.	Specimen Shape	Specimen Slenderness (H/W) ratio	UCS (MPa)	Average Peak Strength, $\sigma_1 \pm$ Standard Deviation (MPa)
C-01	Cubical	1	55.84	58.72 $\pm$ 6.03
C-02	Cubical	1	52.72	
C-03	Cubical	1	65.84	
C-04	Cubical	1	64.56	
C-05	Cubical	1	54.63	

Table 6.7 Results of uniaxial compressive tests for group D.

Specimen No.	Specimen Shape	Slenderness (H/W) ratio	UCS (MPa)	Average Peak Strength, $\sigma_1 \pm$ Standard Deviation (MPa)
D-01	Cuboidal	0.5	61.72	69.47 $\pm$ 4.83
D-02	Cuboidal	0.5	70.50	
D-03	Cuboidal	0.5	74.85	
D-04	Cuboidal	0.5	69.03	
D-05	Cuboidal	0.5	71.27	

### 6.8.1.1 Influence of specimen size on UCS of sandstone

The uniaxial compressive strengths of the tested sandstone specimens with different slenderness ( $H/W$ , where  $H$  is height of specimen,  $W$  is width of specimen) ratio is plotted in Figure 6.12a. All the specimens except Group A, which include standard cylindrical, had square cross-section (50.8 mm x 50.8 mm). The average uniaxial compressive strength ( $\sigma_c$ ) showed an increase by 29.6%, i.e., 53.6 MPa to 69.47 MPa as the specimen height was decreased from 101.6 mm ( $H/W = 2$ ) to 25.4 mm ( $H/W = 0.5$ ) (Table 6.5-6.7). This trend is often attributed to end effect that activates confined zone near the specimen ends (Xu and Cai, 2017). Therefore, as specimen slenderness decreased (or specimen height in this study), area of the specimen under confinement increased resulting in a higher peak strength (Figure 6.12b). The average UCS value was around 50.5 MPa (Table 6.4) in standard cylindrical specimen lower by 6% as compared to cuboidal specimens of same height (around 53.6 MPa). This small increase in peak strength from circular to square shaped cross-section suggested limited influence of cross-sectional shape on the UCS of sandstone.



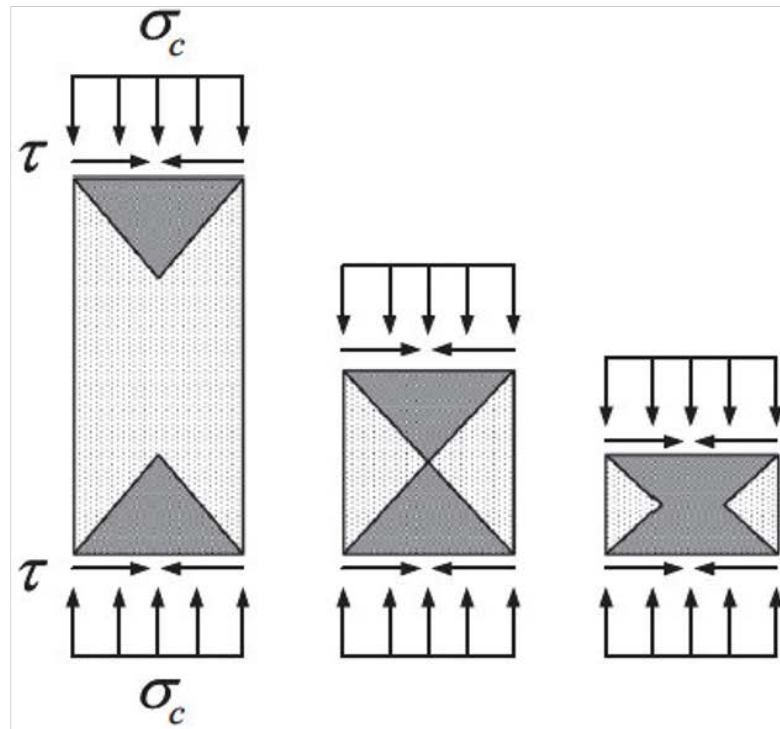
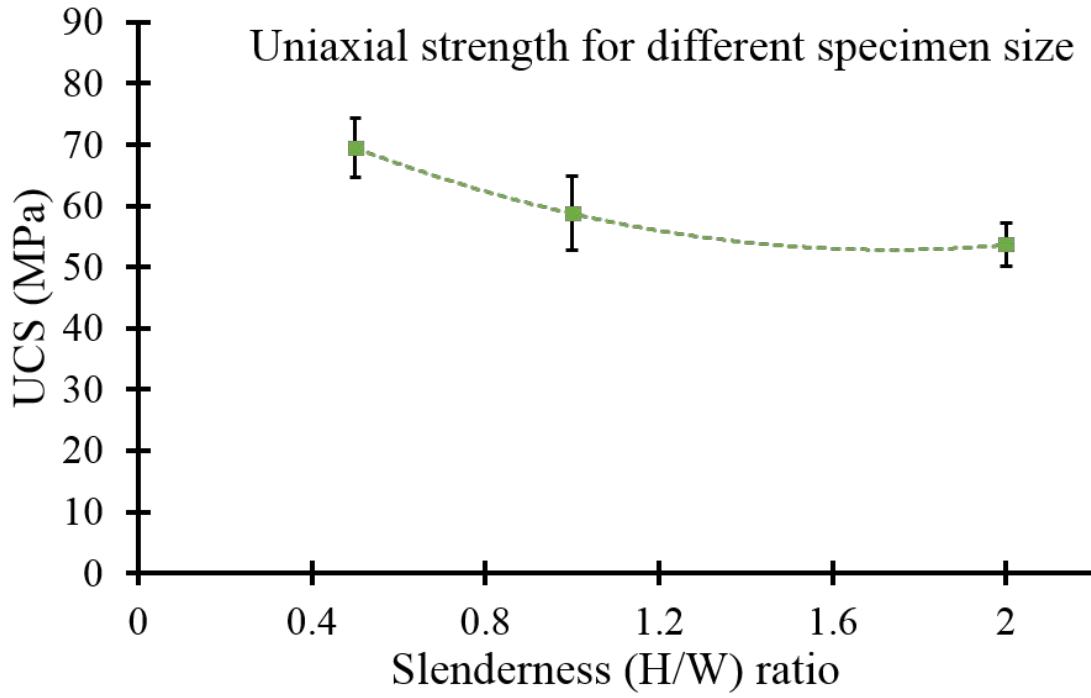


Figure 6.12 (a) UCS of square shaped cross-section specimens with different slenderness obtained from uniaxial compression test (top); (b) Illustration of end effect in specimens with different slenderness in rock uniaxial compression tests (redraw based on Xu and Cai, 2017).

### 6.8.1.2 Influence of specimen size on failure mechanism of sandstone

Figure 6.13a-c shows the transition of failure mode as slenderness ( $H/W$ ) ratio of sandstone specimen decreased from 2 to 0.5. In all specimen sizes, spalling occurred at free faces followed by violent failure of central portion. The degree of spalling varied depending on the specimen size. For instance, minute spalling at outer surface of the specimen with  $H/W$  ratio of 2.0 increased to larger region extending up to the central portion of specimen for cases with  $H/W = 0.5$ . In specimen with  $H/D$  ratio equal to 2, dominant single plane shear failure occurred in the central region as shown in Figure 6.13a. Whereas, cross-shear failure occurred in the inner-core resulting in the conical/pyramidal shape in specimen along in case of  $H/D$  ratio is 1 (Figure 6.13b). In specimens with  $H/D$  ratio is 0.5, huge spalling occurred in V-shaped region extending from outer surface to central portion in leaving behind hourglass type failure (Figure 6.13c).

The change in failure mode with specimen size is attributed to end effect as shown in Figure 6.12b. Feng et al 2017, investigated the failure mechanism for different specimen size using XFEM based numerical code. They analyzed crack evolution at different stage of loading which represents transition from intact rock to fractured rock to understand the friction effect caused by end constraint. They found that in specimen with  $H/D$  ratio equal to 2, end constraint created only a small region of confinement near the specimen ends (similar to Figure 6.12b) thereby allowing the meso-cracks to initiate around the center of the specimen. These cracks propagate towards outer surface in diagonal direction, which is a region of low confinement. Similarly, localized shear band (due to gradual coalesce of cracks) are formed resulting in development of shear failure plane across specimen height similar to seen in Figure 6.13a. Whereas, in case of  $H/D=1$ , confined region is much larger but with no overlapping, which provides unconfined zone around the center of the specimen (Figure 6.12b) thereby allowing some meso-cracks to initiate around the specimen center. However, majority of cracks will form in the low confined region near outer surface resulting in significant spalling in that region. These cracks at outer region may propagate towards the center of the specimen resulting in formation of shear plane similar to figure 6.13b. In case of  $H/D=0.5$ , confined region from specimen ends overlap (Figure 6.12b), which cause meso-cracks to form at the outer surface. These cracks propagate and coalesce towards the center forming opposite vertex cone areas resulting in hourglass failure (Feng et al 2017) as seen in Figure 6.13c

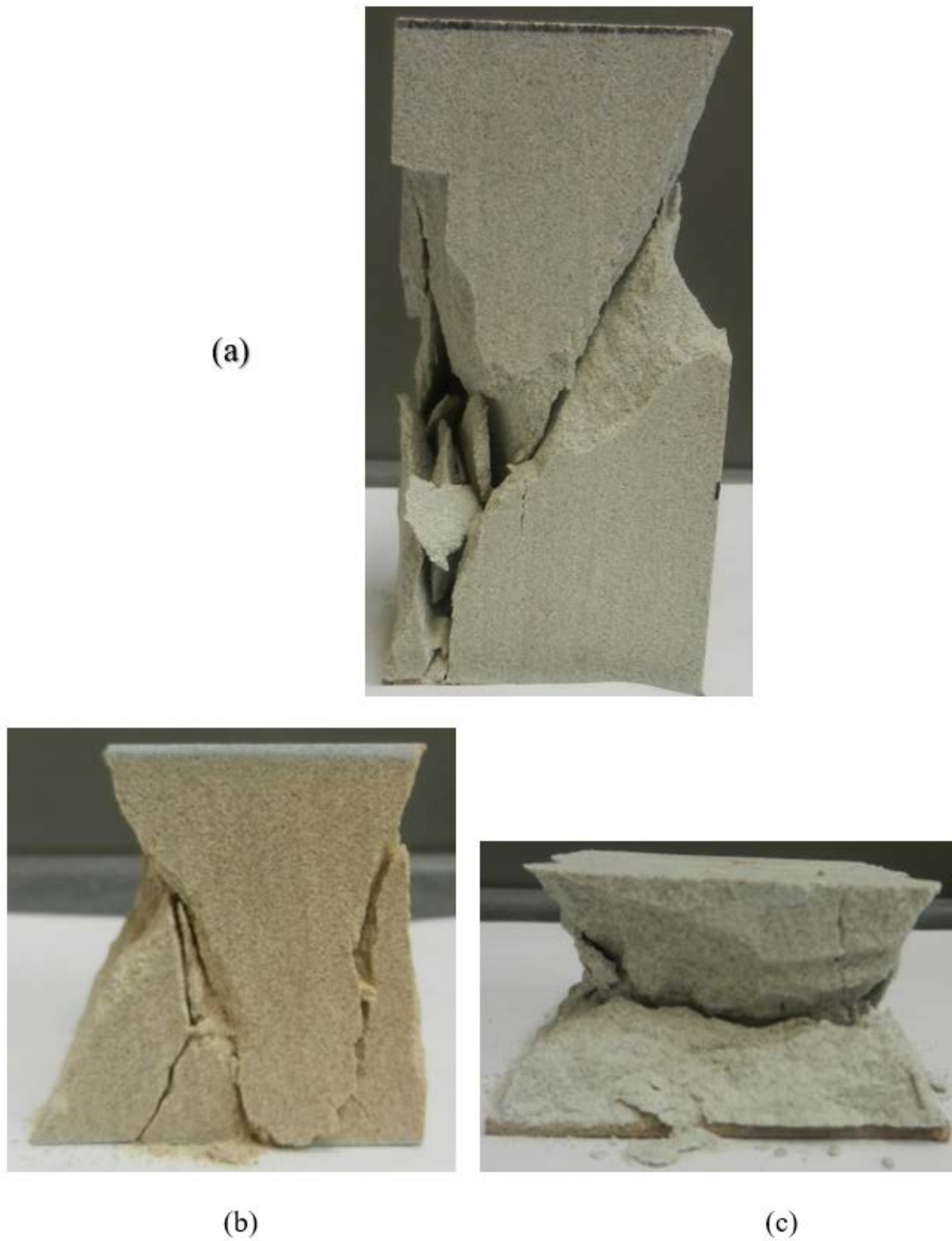


Figure 6.13 (a) Dominant shear failure with spalling at outer surface in cuboidal specimen of 101.16 mm height ( $H/D=2$ ); (b) cross-shear failure of inner-core along with spalling at outer surface in cubical Specimen of 50.8 mm height ( $H/D=1$ ); (c) Hourglass type failure cuboidal specimen of 25.4 mm height Specimen ( $H/D=1/2$ ).

### 6.8.2 Biaxial compressive test

Biaxial tests were performed on 50.8 mm cubical specimen for two loading paths as shown in Figure 6.10. For loading path 2, i.e. constant intermediate stress,  $\sigma_2$ , the test was performed on three stress level (i.e.,  $\sigma_2 = 6.89, 13.79$  and  $27.58$  MPa). Five specimens were tested for each intermediate stress,  $\sigma_2$ . The peak strength data and corresponding principal stresses of each test are presented in Table 6.8-6.11.

Table 6.8 Results of biaxial tests for loading path 2, constant  $\sigma_2$  of 6.89 MPa

Specimen No.	$\sigma_3/\sigma_c$ stress ratio	$\sigma_1$ (MPa)	$\sigma_2$ (MPa)	Average stress (MPa)		$\sigma_1 : \sigma_2$ at failure
				$\sigma_1$	$\sigma_2$	
C-Bx-01	0.12	61.99	6.89	67.95	6.89	9.86
C-Bx-02	0.12	71.49	6.89			
C-Bx-03	0.12	66.52	6.89			
C-Bx-04	0.12	64.62	6.89			
C-Bx-05	0.12	75.15	6.89			

Table 6.9 Results of biaxial tests for loading path 2, constant  $\sigma_2$  of 13.79 MPa

Specimen No.	$\sigma_3/\sigma_c$ stress ratio	$\sigma_1$ (MPa)	$\sigma_2$ (MPa)	Average stress (MPa)		$\sigma_1 : \sigma_2$ at failure
				$\sigma_1$	$\sigma_2$	
C-Bx-06	0.233	74.66	13.79	73.73	13.79	5.34
C-Bx-07	0.233	75.14	13.79			
C-Bx-08	0.233	71.97	13.79			
C-Bx-09	0.233	66.72	13.79			
C-Bx-10	0.233	80.18	13.79			

Table 6.10 Results of biaxial tests for loading path 2, constant  $\sigma_2$  of 27.58 MPa

Specimen No.	$\sigma_3/\sigma_c$ stress ratio	$\sigma_1$ (MPa)	$\sigma_2$ (MPa)	Average stress (MPa)		$\sigma_1 : \sigma_2$ at failure
				$\sigma_1$	$\sigma_2$	
C-Bx-11	0.46	84.16	27.58	87.17	27.58	3.17
C-Bx-12	0.46	83.30	27.58			
C-Bx-13	0.46	90.03	27.58			
C-Bx-14	0.46	86.68	27.58			
C-Bx-15	0.46	88.68	27.58			

Table 6.11 Results of biaxial tests for loading path 1,  $\sigma_1 = \sigma_2$

Specimen No.	$\sigma_1$ (MPa)	$\sigma_2$ (MPa)	Average stress (MPa)		$\sigma_1 : \sigma_2$ at failure
			$\sigma_1$	$\sigma_2$	
C-Bx-16	78.99	78.99	77.29	77.29	1
C-Bx-17	72.66	72.66			
C-Bx-18	76.55	76.55			
C-Bx-19	73.38	73.38			
C-Bx-20	84.85	84.85			

### 6.8.2.1 Influence of loading path on peak strength of cubic sandstone

The results from biaxial tests plotted as peak strength,  $\sigma_1$  (major principal stress) against corresponding intermediate principal stress,  $\sigma_2$  as shown in Figure 6.14. It is observed that for loading path 2, the peak strength  $\sigma_1$  increased with increase in the intermediate principal stress,  $\sigma_2$ . The average peak strength,  $\sigma_{1avg}$  increased from 67.95 MPa to 73.73 MPa as  $\sigma_2$  increased from 6.89 to 13.79 MPa (Table 6.8-6.10). The percentage increase in peak strength was around 15.71 % and 25.56 % from its UCS value (58.72 MPa) for constant  $\sigma_2 = 6.2$  and 13.79 MPa respectively. The average peak strength further increased to 87.17 MPa (Table 6.10) as  $\sigma_2$  increased to  $0.46\sigma_c$  (27.58 MPa). However, for loading path 1, which represents high intermediate stress ( $\sigma_1 = \sigma_2$ ), the peak strength decreased to 77.29 MPa. Although, peak strength for load path 1 was lower as compared to tests when  $\sigma_2 = 0.45\sigma_c$  under loading path 2 (Figure 6.14). It is still 1.31 times the UCS value. It is concluded that the biaxial strength of sandstone is higher than its uniaxial equivalent at any level of intermediate principal stress. Yun, 2008 showed similar observation for granite and coalmine sandstone rocks that the peak strength,  $\sigma_1$  was highest for  $\sigma_2 \sim 0.5\sigma_c$  and decreased under high intermediate principal stress, i.e.,  $\sigma_1 = \sigma_2$ .

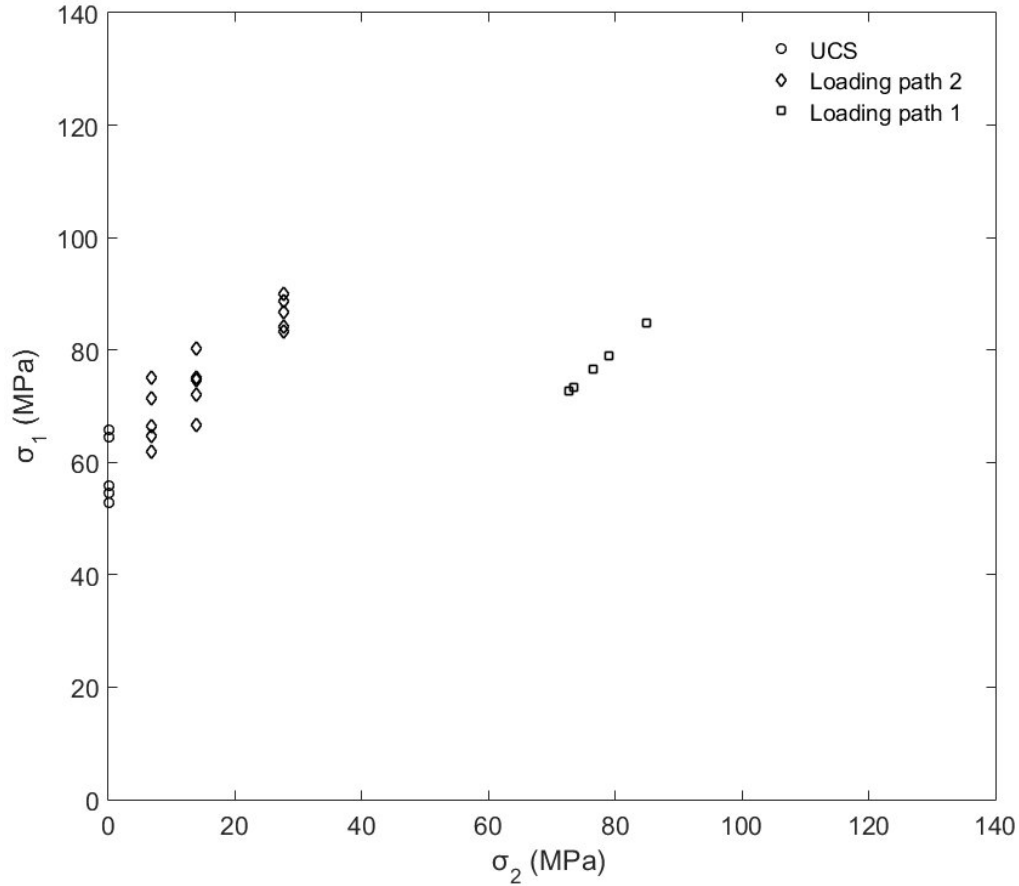


Figure 6.14 Experimental results obtained from biaxial tests for different loading paths

### 6.8.2.2 Influence of loading path on failure mechanism of cubic sandstone

The transition of failure mode from uniaxial to biaxial stress conditions was analyzed to understand the failure mechanism of sandstone specimens under biaxial stress state. In the uniaxial stress state, specimens exhibited spalling on all free faces of the cube followed by violent failure of the mid-section. The mid-section of the specimen mostly failed in shear with multiple planes intersecting each other (Figure 6.15a). These failure planes oriented in the  $\sigma_1 - \sigma_2/\sigma_3$  plane leaving conical or pyramid-like shaped central portion. Figure 6.15b shows splitting in the  $\sigma_2 - \sigma_3$  plane.

When specimens were tested biaxially, the failure mechanism was characterized by varying the degree of spalling at free faces along with the shear failure of the mid-section. The intensity of spalling depended upon the magnitude of confinement by the intermediate stress. Figure 6.16-

6.18 shows, the typical failure mechanism in specimens subjected to the biaxial test under load path 2 (i.e.,  $\sigma_2 = \text{constant}$ ). At  $\sigma_2 = 6.89$  MPa, failure was characterized by splitting at the outer ends of  $\sigma_2$  faces along with dominant shear failure plane (Figure 6.16). The failure plane oriented in the  $\sigma_2 - \sigma_3$  plane and the strike in the  $\sigma_1$  direction. However, when confinement is increased to 13.79 MPa, no splitting was observed at outer ends of  $\sigma_2$  faces (Figure 6.17b). Though dominant failure planes (conjugate shear planes) still oriented in the  $\sigma_2 - \sigma_3$  plane Figure 6.17a, shearing also occurred in  $\sigma_1 - \sigma_3$  plane (Figure 6.17b). When intermediate stress is further increased to 27.58 MPa ( $\sigma_2 = 0.45\sigma_c$ ), the dominant shear failure occurred in the  $\sigma_1 - \sigma_3$  plane whose strike was in the  $\sigma_2$  direction (Figure 6.17a), and no shearing was observed in the  $\sigma_2 - \sigma_3$  plane (Figure 6.18b). Yun et al., 2008, showed similar observation that under high intermediate stress, shearing occurred in the central section of a coalmine sandstone whose strike was in the  $\sigma_2$  direction. It can be concluded in biaxial tests on sandstone samples under loading path 2, shear failure plane rotated with increase in intermediate principal stress,  $\sigma_2$ .

For specimens subjected to load path 1 ( $\sigma_1 = \sigma_2$ ), spalling occurred at free faces followed by splitting which occupied a large portion of specimen volume (Figure 6.19a). Further, splitting planes are nearly perpendicular to the unconfined direction ( $\sigma_3 = 0$ ) with dip and strike direction in the  $\sigma_1 - \sigma_2$  plane. The remaining central portion of specimen failed under shear whose strike is a combination of both  $\sigma_1$  and  $\sigma_2$  axis (Figure 6.19a-c). Therefore, the dominant shear plane has rotated as compared to the test with load path 1 ( $\sigma_2 = 27.58$  MPa) where its strike was along the  $\sigma_2$  axis.



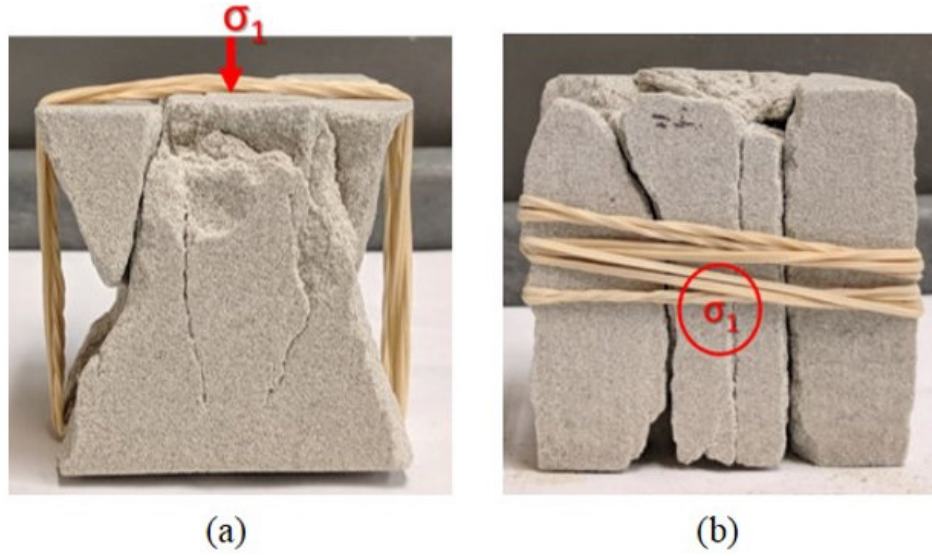


Figure 6.15 Failure mode of sandstone samples in uniaxial test: (a)  $\sigma_1 - \sigma_2$  plane, (b)  $\sigma_2 - \sigma_3$  plane.

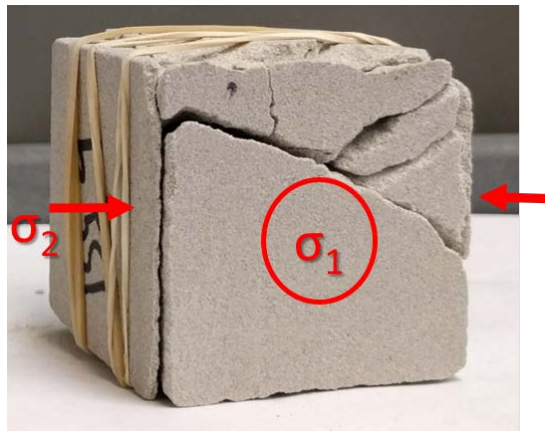


Figure 6.16 Failure mode of sandstone samples in biaxial test with loading path 2, under  $\sigma_2$  of 6.89 MPa.

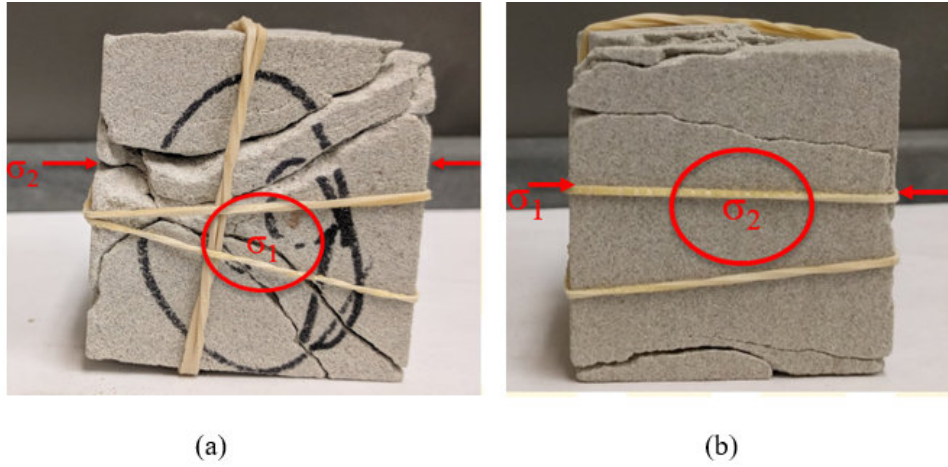


Figure 6.17 Failure mode of sandstone samples in biaxial test with loading path 2, under  $\sigma_2$  of 13.79 MPa: (a)  $\sigma_2 - \sigma_3$  plane, (b)  $\sigma_1 - \sigma_3$  plane.

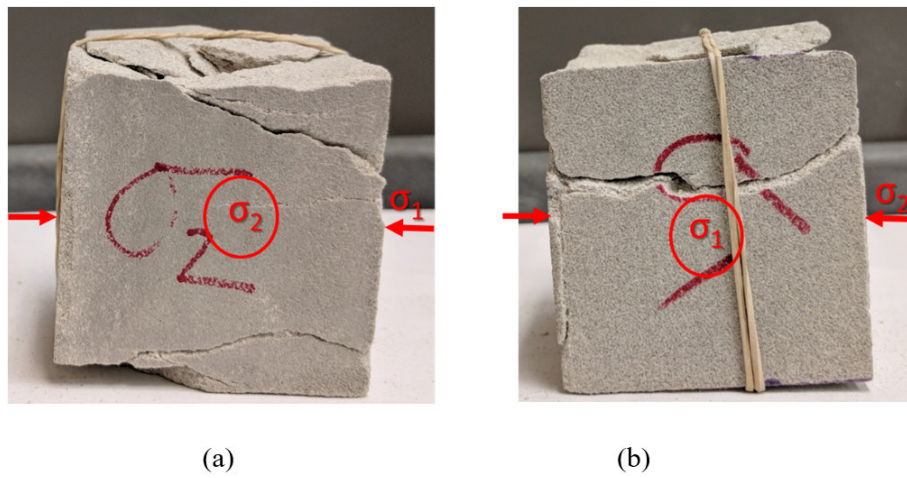


Figure 6.18 Failure mode of sandstone samples in biaxial test with loading path 2 under  $\sigma_2$  of 27.58 MPa: (a)  $\sigma_2 - \sigma_3$  plane, (b)  $\sigma_1 - \sigma_3$  plane

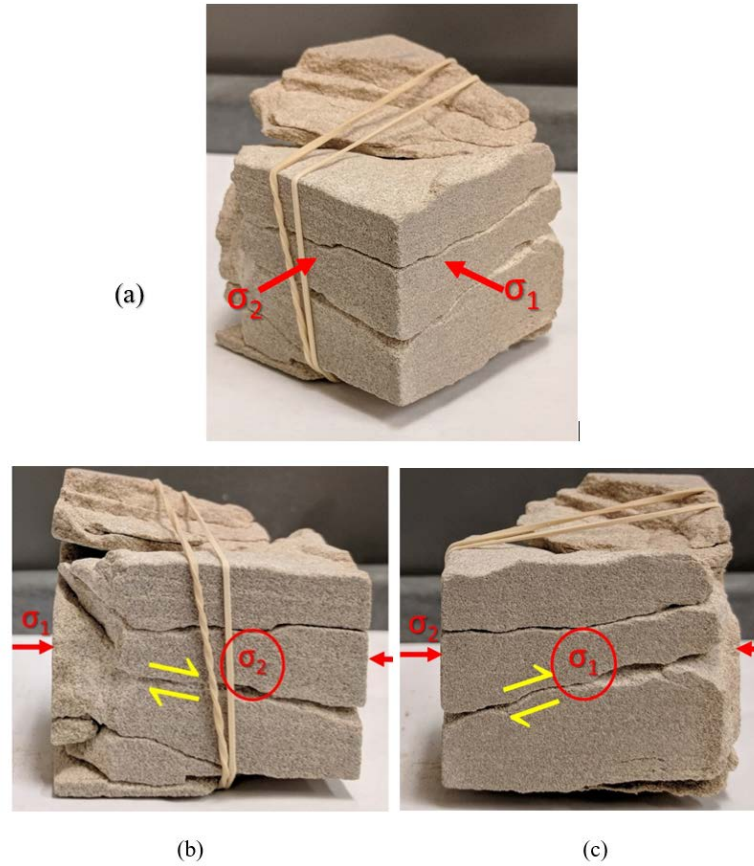


Figure 6.19 Failure mode of sandstone samples in biaxial test with loading path 1: (a) Diagonal view, (b)  $\sigma_1 - \sigma_3$  plane, (c)  $\sigma_2 - \sigma_3$  plane.

### 6.8.3 True-triaxial test

True-triaxial tests were performed on 50.8 mm cubical specimen using biaxial frame in conjunction with confining device (Figure 6.6), representing novel loading path,  $\sigma_1 = \sigma_2$  and  $\sigma_3 =$  constant (Figure 6.11). This novel loading path corresponds to triaxial extension (Ma et al.,2017) instead of compression test due to high intermediate stress,  $\sigma_2$ . The tests were performed at two stress levels (i.e.,  $\sigma_3 = 6.2$  and 20.68 MPa). Five specimens were tested for each minor principal stress,  $\sigma_2$ . The peak strength data along with corresponding principal stresses of each test are presented in Table 6.12-6.13.

Table 6.12 Results of true triaxial tests for constant  $\sigma_3$  of 6.2 MPa

Specimen No.	$\sigma_3/\sigma_c$ stress ratio	$\sigma_3$ (MPa)	$\sigma_1$ (MPa)	$\sigma_2$ (MPa)	Average stress (MPa)	
					$\sigma_1$	$\sigma_2$
C-Tx-01	0.11	6.2	101.43	101.43	136.73	136.73
C-Tx-02	0.11	6.2	107.44	107.44		
C-Tx-03	0.11	6.2	92.37	92.37		
C-Tx-04	0.11	6.2	98.22	98.22		
C-Tx-05	0.11	6.2	95.07	95.07		

Table 6.13 Results of true-triaxial tests for constant  $\sigma_3$  of 20.68 MPa

Specimen No.	$\sigma_3/\sigma_c$ stress ratio	$\sigma_3$ (MPa)	$\sigma_1$ (MPa)	$\sigma_2$ (MPa)	Average stress (MPa)	
					$\sigma_1$	$\sigma_2$
C-Tx-06	0.35	20.68	151.44	151.44	136.73	136.73
C-Tx-07	0.35	20.68	142.40	142.40		
C-Tx-08	0.35	20.68	122.29	122.29		
C-Tx-09	0.35	20.68	138.56	138.56		
C-Tx-10	0.35	20.68	128.94	128.94		

### 6.8.3.1 Influence of confinement on peak strength under triaxial stress state

The failure data points from true-triaxial tests were plotted as peak strength,  $\sigma_1$  against corresponding minor principal stress,  $\sigma_3$  in Figure 6.20. As confinement  $\sigma_3$  increases, peak strength,  $\sigma_1$  also increased. However, this plot does not clearly reflect the effect of intermediate principal stress as the influence of load path was ignored (Ma and Haimson, 2016). Therefore, failure results were represented by two principal stress invariants (Figure 6.21), the octahedral shear stress at failure ( $\tau_{oct,f}$ ), and the octahedral normal stress at failure ( $\sigma_{oct,f}$ ).

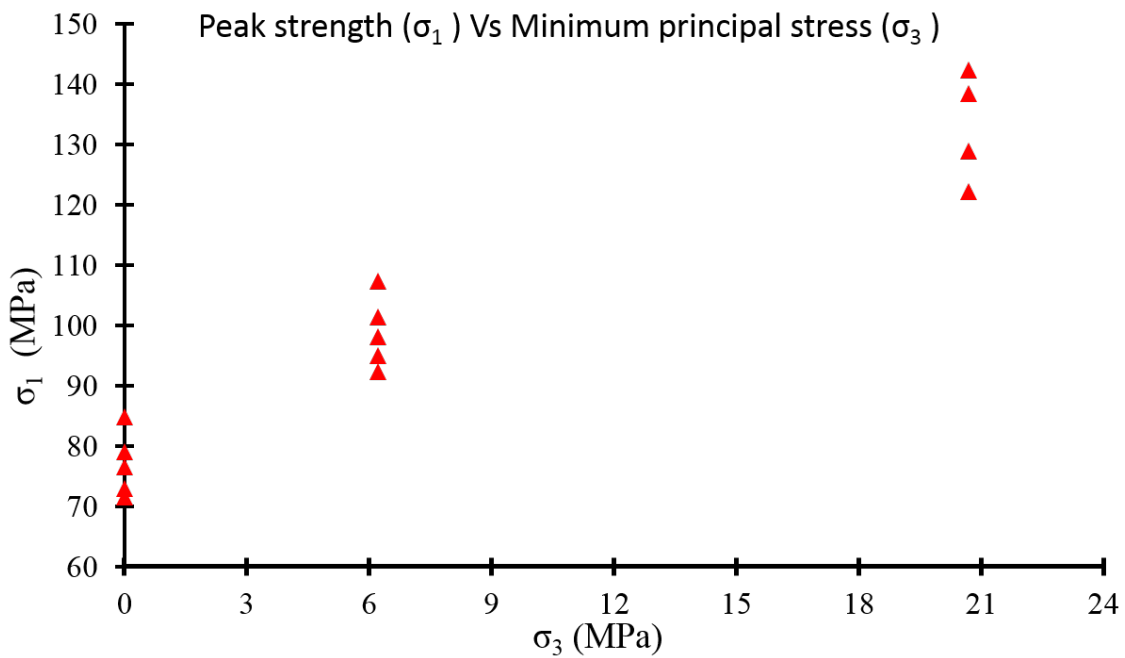


Figure 6.20 Variation of  $\sigma_1$  (peak strength) with  $\sigma_3$  in Berea sandstone for axisymmetric loading conditions ( $\sigma_1 = \sigma_2$  and  $\sigma_3 = \text{constant}$ )

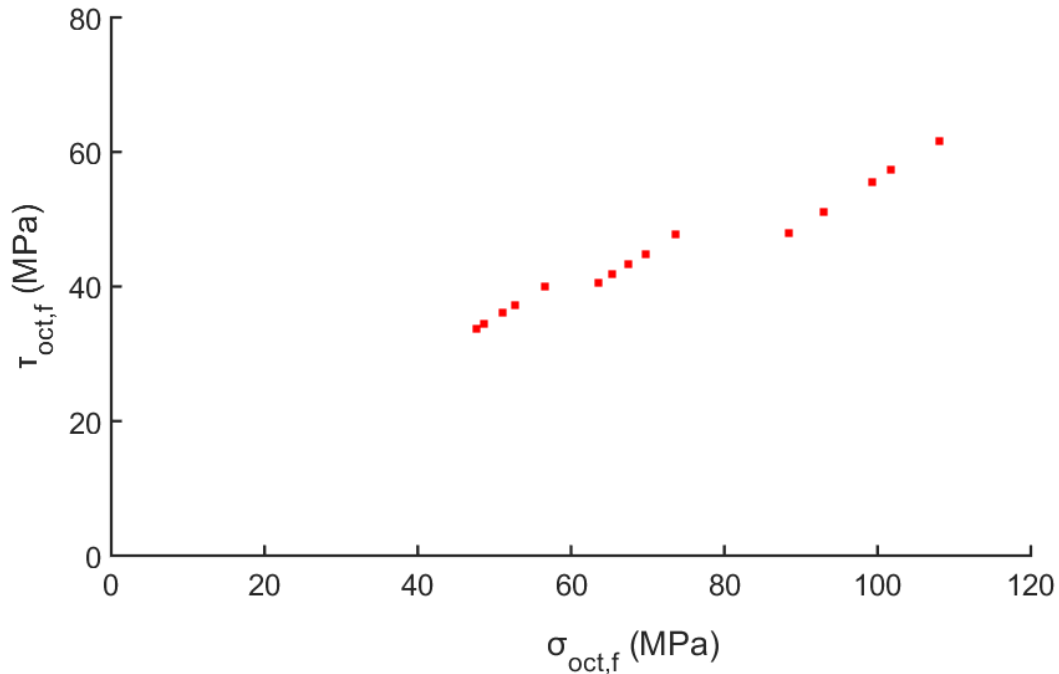


Figure 6.21 Variation of the octahedral shear at failure ( $\tau_{\text{oct,f}}$ ) with the octahedral normal stress ( $\sigma_{\text{oct,f}}$ ) in Berea sandstones for axisymmetric loading conditions ( $\sigma_1 = \sigma_2$  and  $\sigma_3 = \text{constant}$ ).

### 6.8.3.2 Influence of confinement on failure mechanism under triaxial stress state

The transition of failure mode from biaxial to triaxial stress conditions was analyzed to understand the failure mechanism of sandstone specimens under poly-axial stress state. Figure 6.22-6.24 showed typical failure mechanism for novel loading path, i.e.,  $\sigma_1 = \sigma_2$  and  $\sigma_3 = 0-20.68$  MPa. For specimens tested biaxially, spalling occurred at free faces followed by splitting which occupied a large portion of specimen volume as suggested by planes are nearly perpendicular to the unconfined direction ( $\sigma_3 = 0$ ) (Figure 6.22a-c). The remaining central portion of specimen failed under shear whose strike is a combination of both  $\sigma_1$  and  $\sigma_2$  axis.

However, when confinement was applied at free surfaces in true-triaxial tests, no spalling occurred at these outer surfaces (Figure 6.23a, Figure 6.24a). In case of triaxial test with  $\sigma_3 = 6.2$  MPa, splitting still occurred in large portion of specimen (Figure 6.23a). But these splitting planes were more inclined as compared to biaxial test (Figure 6.22a) Additionally, central portion of specimen failed under multiple shear which formed sharp angles with  $\sigma_3$  direction (Figure 6.23b-

c). For triaxial tests with higher confinement ( $\sigma_3 = 20.68$  MPa), only single shear plane was formed with no spalling at outer surface (Figure 6.24a). Further, angle this failure very steep (Figure 6.24b-c) as compared to triaxial tests under  $\sigma_3 = 20.68$  MPa (Figure 6.23b-c).

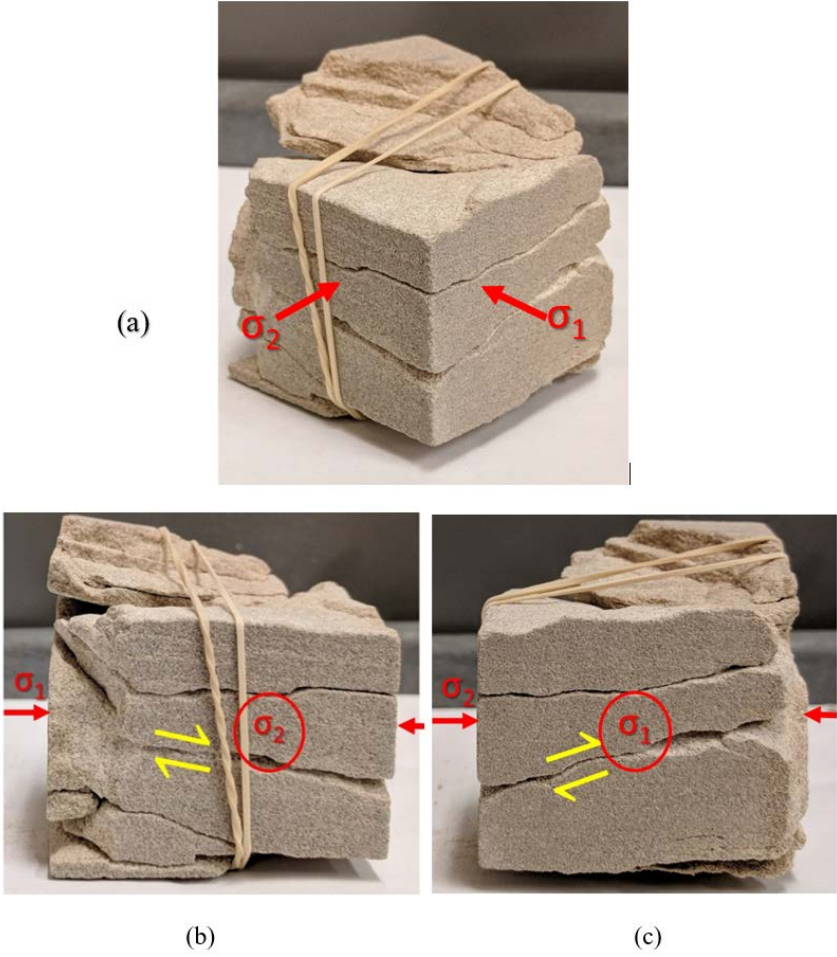


Figure 6.22 Failure mode of sandstone samples in biaxial test with loading path 1: (a) Diagonal view, (b)  $\sigma_1 - \sigma_3$  plane, (c)  $\sigma_2 - \sigma_3$  plane.



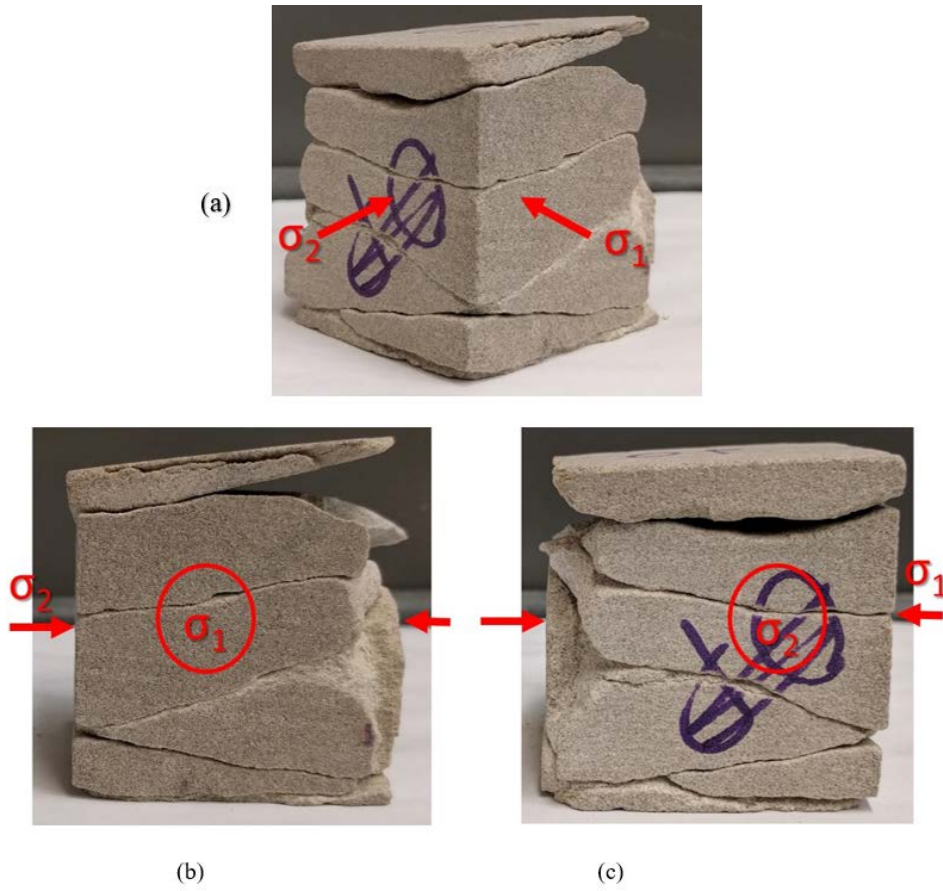


Figure 6.23 Failure mode of sandstone samples in true triaxial test under  $\sigma_3$  of 6.2 MPa: (a) Diagonal view, (b)  $\sigma_2 - \sigma_3$  plane, (c)  $\sigma_1 - \sigma_3$



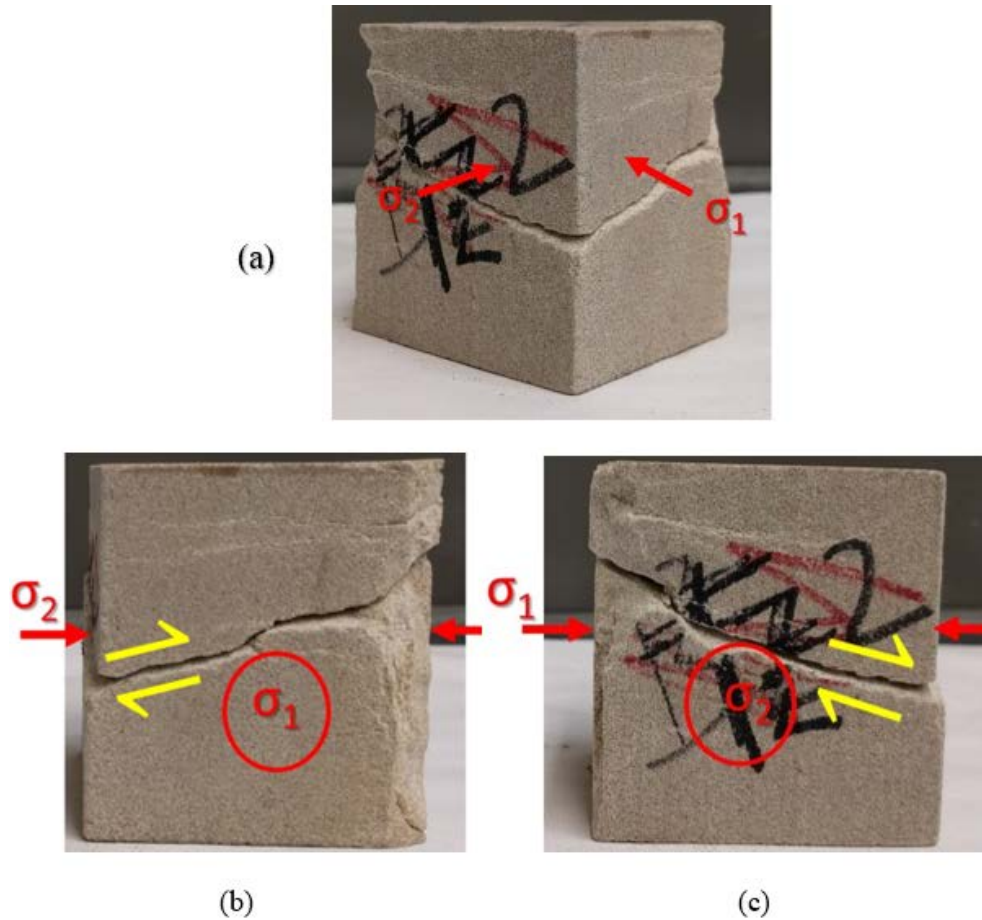


Figure 6.24 Failure mode of sandstone samples in true triaxial test under  $\sigma_3$  of 20.68 MPa:  
 (a) Diagonal view, (b)  $\sigma_1 - \sigma_3$  plane, (c)  $\sigma_2 - \sigma_3$  plane.

#### 6.8.4 Failure criterion for biaxially loaded intact rocks

As mentioned in section 6.8.2.1, the intermediate principal stress affects the failure strength of sandstone specimen. Thus, the conventional failure criteria that ignores the influence of intermediate principal stress  $\sigma_2$  cannot be used to predict the strength of Berea sandstone under biaxial compression conditions. The Mohr-Coulomb theory, which was the most widely applied theoretical criterion, and some other nonlinear criteria, which are similar to the Hoek-Brown criterion, only considered  $\sigma_1$ , and  $\sigma_3$ . In theory the intermediate principal stress does not contribute to the strength of the rock specimen; consequently, the uniaxial and biaxial compressive strengths should coincide. However, this was not the case for the Berea sandstone as seen in Figure 6.14 (section 6.8.2.1).

In this study, Drucker-Prager failure criterion that includes the intermediate principal stress was assessed by fitting the criterion with the failure data of Berea sandstone. Additionally, an empirical failure criterion based on regression analysis was derived that provided the best fit envelop for the failure data of Berea sandstone under biaxial stress condition.

#### 6.8.4.1 Drucker-Prager criterion

The Drucker-Prager criterion (Drucker and Prager, 1952) accounts for the effects of all principal stresses. It is regularly applied to brittle materials such as concrete and rock. The generalized form is expressed by using the invariants of the stress tensor, written as

$$F = \alpha I_1 + J_2^2 - k = 0 \quad \text{Equation 6.4}$$

Where  $\alpha$  and  $k$  are material constants and can be expressed in terms of friction angle,  $\phi$ , and cohesion,  $c$ , of the material.  $I_1$  and  $J_2$  stress invariants.

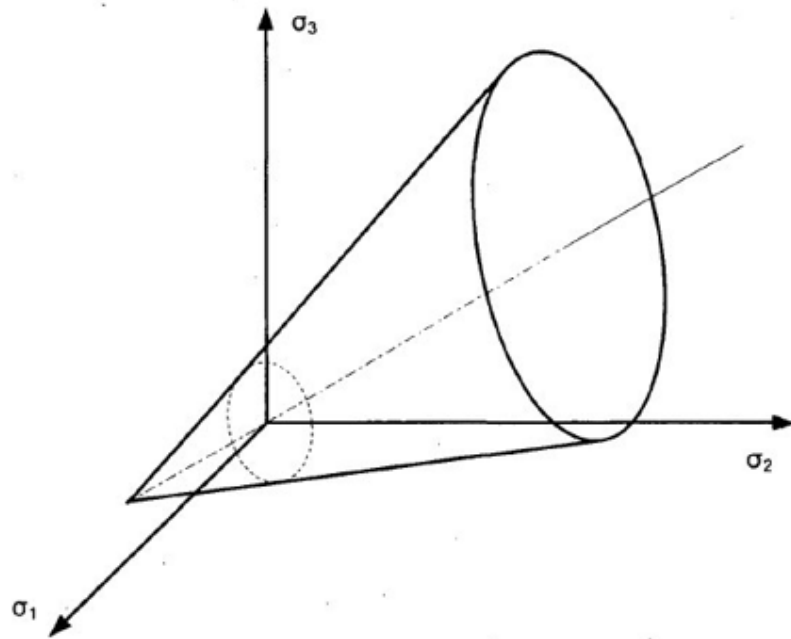
$$I_1 = \sigma_1 + \sigma_2 + \sigma_3 \quad \text{Equation 6.5}$$

$$J_2 = [(\sigma_1 - \sigma_2)^2 + (\sigma_2 - \sigma_3)^2 + (\sigma_3 - \sigma_1)^2]/6 \quad \text{Equation 6.6}$$

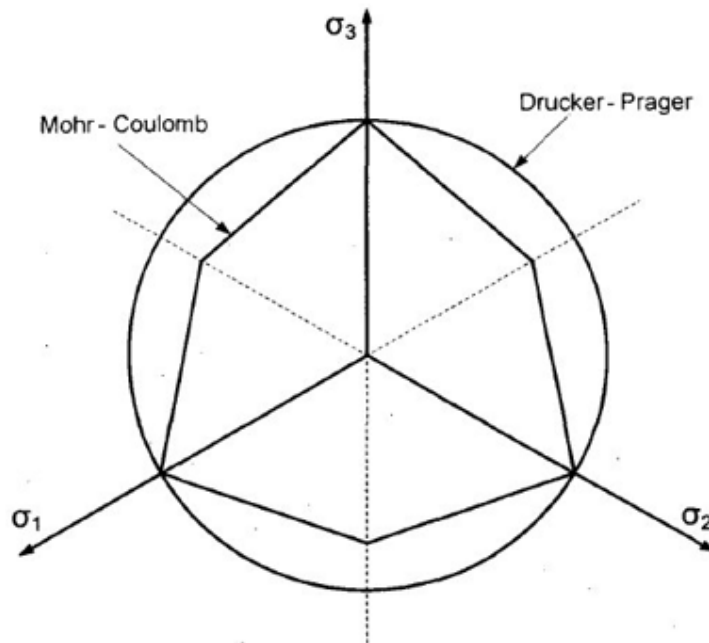
For conventional triaxial test:

$$\alpha = \frac{2 \sin \phi}{\sqrt{3}(3 - \sin \phi)} \quad \text{Equation 6.7}$$

$$k = \frac{6c \cos \phi}{\sqrt{3}(3 - \sin \phi)} \quad \text{Equation 6.8}$$



(a) Principal stress space



(b) Deviatoric plane

Figure 6.25 Drucker–Prager yield surface (a) on the principal stress space (Pariseau, 1992); (b) on the deviatoric plane (Desai and Siriwardane, 1984)

In case of biaxial stress state,  $\sigma_3 = 0$  equation 6.4 can be rewritten as

$$\alpha(\sigma_1 + \sigma_2) + \sqrt{\frac{(\sigma_1^2 - \sigma_1\sigma_2 + \sigma_2^2)}{3}} = k \quad \text{Equation 6.9}$$

Based on the average value of  $\sigma_c$  for investigated cubic rock specimen, the cohesion  $c$  of the rock for different internal frictional angles,  $\phi$ , can be calculated.

$$c = \frac{\sigma_c}{2} \left( \frac{1 - \sin \phi}{\cos \phi} \right) \quad \text{Equation 6.10}$$

In turn, a series of Drucker-Prager failure envelopes can be plotted in  $\sigma_1 - \sigma_2$  coordinates combined with experimental failure points, by which the fitted degree between the Drucker-Prager criterion and investigated failure points can be conveniently examined.

#### 6.8.4.2 Regression curve for biaxial failure points

Based on the rock failure data, the above approach was used to compare Mohr-Coulomb, Hoek-Brown, and Drucker-Prager failure envelopes within  $\sigma_1 - \sigma_2$  coordinates, as shown in Figures 6.26. For Drucker-Prager criterion, series of envelopes for different friction angles,  $\phi$  ( $\phi = 0^\circ - 25^\circ$ ) were generated for a given  $\sigma_c$  (from test results). The specific friction angle was selected by “goodness of fit” to the experimental results. Though data points at constant confinement ( $\sigma_2 = 0, 6.89, 13.78$  and  $27.58$  MPa) are scattered,  $\phi = 20^\circ - 25^\circ$  provides the best “fit” with failure points at confining stress less than 28 MPa ( $\sigma_2 < \sigma_c/2$ ). However, for the  $\sigma_1 = \sigma_2$  condition, the friction angle of  $15^\circ$  was the best “fit” with corresponding failure points (Figure 6.23a). The analysis demonstrated that while Drucker-Prager criterion accounts for the influence of intermediate stress, it provides poor correlation with biaxial test results of Berea sandstone. This conclusion was in good agreement with the study by Al-Ajmi and Zimmerman, 2005, which showed that Drucker Prager is usually not appropriate for most rocks. Furthermore, both Mohr-

Coulomb, Hoek-Brown criteria were found to substantially underestimate the biaxial strength of cubical sandstone specimen (Figures 6.26) under the condition of  $\sigma_3 = 0$ .

As no standard criteria fitted the failure data points of Berea sandstone, a regression analysis was performed to determine the best-fit polynomial curve (Figures 6.26b). A quadratic polynomial with  $R^2$  of 0.7507 was found to be the best fit for the biaxial tests data points of cubical sandstone specimens;

$$\sigma_1 = -0.0133\sigma_2^2 + 1.2797\sigma_2 + 58.969 \quad \text{Equation 6.11}$$

Figures 6.27, showed failure stress data plotted against both Mohr-Coulomb and Hoek-Brown criteria, as well as best fitted polynomial curve for the experimental results of sandstone specimen. It can be inferred that the specimen exhibits maximum strength of around 89.75 MPa at intermediate principal stress ( $\sigma_2$ ) of 48.09 MPa, which is nearly 1.528 times of the average uniaxial strength of 50.8 mm cubic specimens.

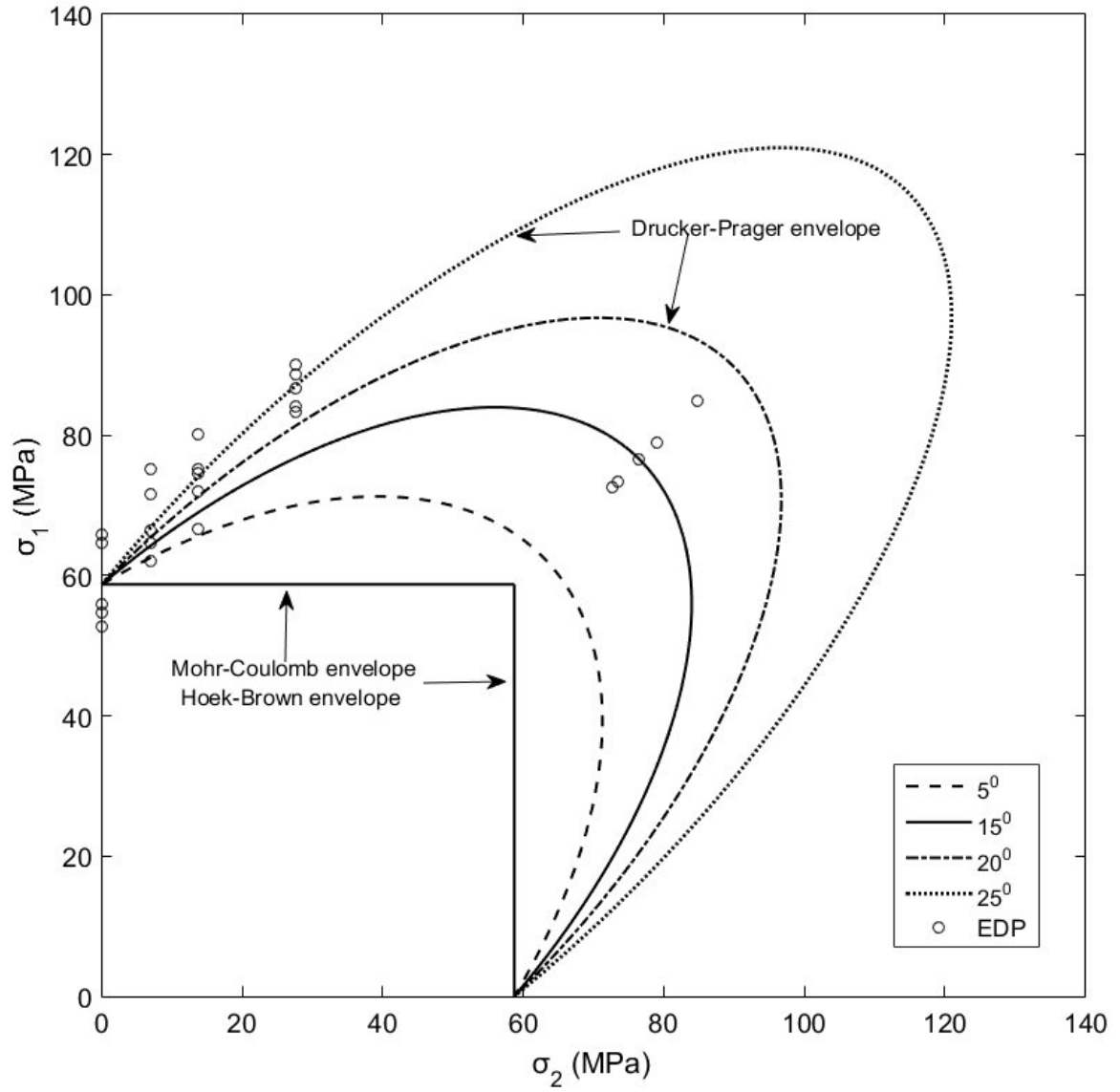


Figure 6.26 Drucker-Prager criteria with experimental data points (EDP) at failure

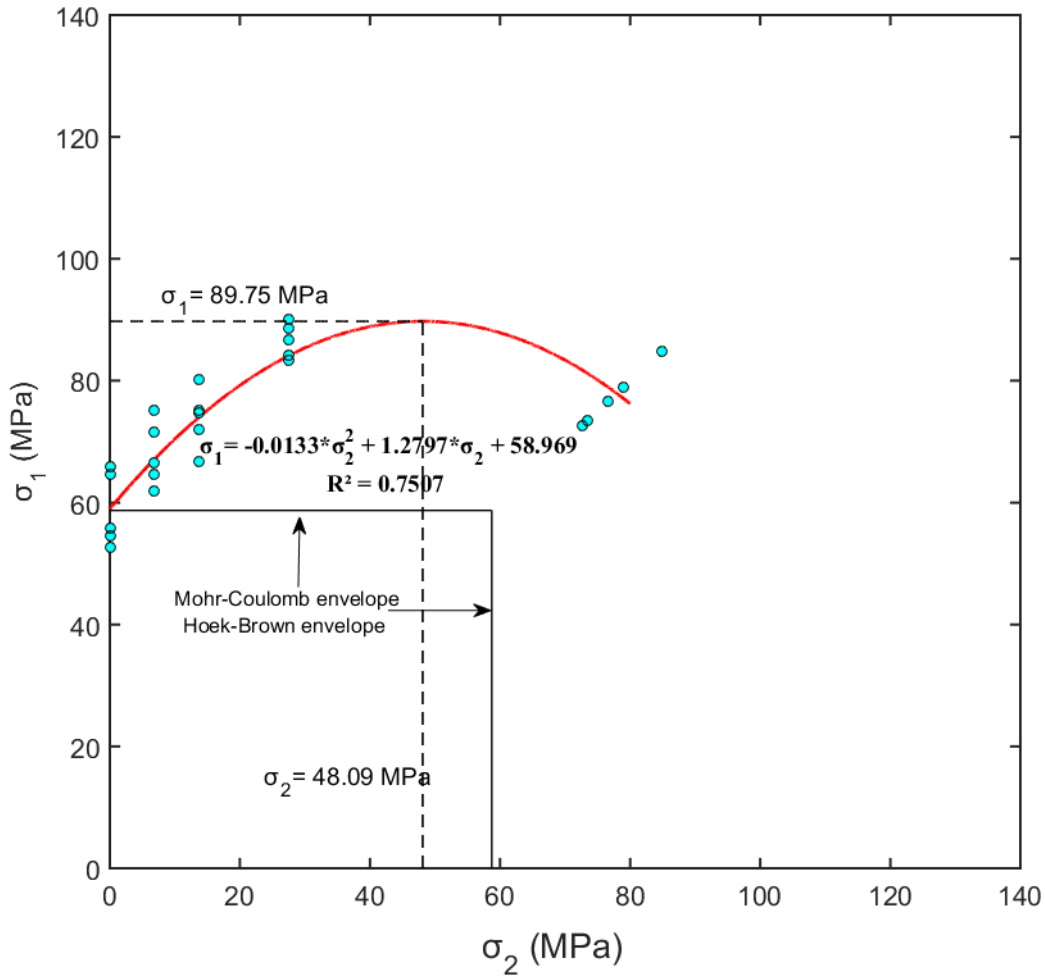


Figure 6.27 Polynomial regression curve with experimental data points (EDP) at failure.

### 6.8.5 True-triaxial failure criterion

As mentioned in earlier sections, there is significant influence of intermediate principal stress on failure strength of sandstone under biaxial and triaxial stress state. Various researchers have comprehensively investigated the influence of intermediate principal stress on rock strengths (Handin et al., (1967); Colmenares and Zoback, 2002; Al-Ajmi and Zimmerman, 2005). Several failure criteria have included the intermediate principal stress to describe rock strength under true triaxial stress states, e.g., modified Wiebols and Cook criterion (Wiebols and Cook, 1968) Mogi criterion (Mogi, 1971). However, no single criterion was found to be valid for most types of rock.

For instance, Colmenares and Zoback, 2002 found that out of seven different failure criteria, only modified Lade criterion fitted the failure data of Dunham dolomite and Solenhofen limestone.

For porous sandstone rocks, most of above failure criteria does not fit with experimental results due to the formation of compaction band under high *in-situ* stresses (Ma, 2014). The failure in porous sandstone rocks is exhibited by the development of localized tabular zones called failure planes. The planes form shear bands or faults at a steep angle  $\theta$  (where  $\theta$  is the angle between the normal to the plane and the  $\sigma_1$  direction) under lower in situ stresses. The planes also form compaction bands (perpendicular to the  $\sigma_1$  direction, i.e.,  $\theta = 0^\circ$ ) at higher stress regimes (Holcomb and Olsson, 2003; Sternlof et al., 2004; Sun et al., 2011). There are some failure criteria such as Nadai criteria (Nadai, 1950), 1950 Lade and Duncan criterion (Lade and Duncan 1975), Matsuoka and Nakai criterion (Matsuoka and Nakai, 1974), Modified Matsuoka-Nakai-Lade-Duncan criterion (Rudnicki, 2013) that are applicable to sandstones. However, most of these criteria require extensive experimental data to get “best-fit” criterion for particular sandstone.

In the current research, true-triaxial tests were performed only for three confinement levels (i.e.,  $\sigma_3 = 0, 6.2$  and  $20.68$  MPa) due to the limitation of confining device. Hence, Nadai criterion (Nadai, 1950) provided the “best-fit” for the experimental data.

#### **6.8.5.1 Nadai criterion**

Nadai (1950) had propounded as early as 1950 a three-dimensional failure criterion for brittle materials. He suggested that failure envelop can be represented by a single relationship in terms of the two principal stress invariants. The failure will occur when distortional strain energy reaches the critical value and is function of octahedral normal stress given by

$$\tau_{\text{oct},f} = f(\sigma_{\text{oct},f}) \quad \text{Equation 6.12}$$

Where,  $\tau_{\text{oct},f}$  and  $\sigma_{\text{oct},f}$  are octahedral shear stress at failure and the octahedral normal stress at failure respectively and are defined in terms of principal stresses as follows



$$\tau_{\text{oct},f} = \frac{1}{3} \sqrt{(\sigma_1 - \sigma_2)^2 + (\sigma_2 - \sigma_3)^2 + (\sigma_3 - \sigma_1)^2} \quad \text{Equation 6.13}$$

$$\sigma_{\text{oct},f} = (\sigma_1 + \sigma_2 + \sigma_3)/3 \quad \text{Equation 6.14}$$

The function “f” is determined from the best fitting curves for particular rock and generally can either be second order polynomial or power law. For porous sandstone rocks, the best-fit function is preferred to be quadratic equation (Olsson, 1999; Ma, 2014). Figure 6.28 showed failure data points of Berea sandstone for loading path  $\sigma_1 = \sigma_2$  and  $\sigma_3$  to be constant are fitted by quadratic equation with  $R^2$  of 0.964 as shown;

$$\tau_{\text{oct},f} = -0.0011\sigma_{\text{oct},f}^2 + 0.553\sigma_{\text{oct},f} + 10.73 \quad \text{Equation 6.15}$$

Although data points are scattered, it was observed that the average  $\tau_{\text{oct},f}$  increased with increase in  $\sigma_{\text{oct},f}$ . Ma and Haimson, 2016 showed similar observation for Bentheim and Coconino sandstones. Additionally, for Bentheim sandstone a ‘cap’ value of  $\sigma_{\text{oct},f}$  was found, at which  $\tau_{\text{oct},f}$  would be maximum and then gradually decline. The cap value is generally observed at very high level of confinement. However, this cap value was not found for Berea sandstone as the level of confinement under true-triaxial test was limited to 20.68 MPa.

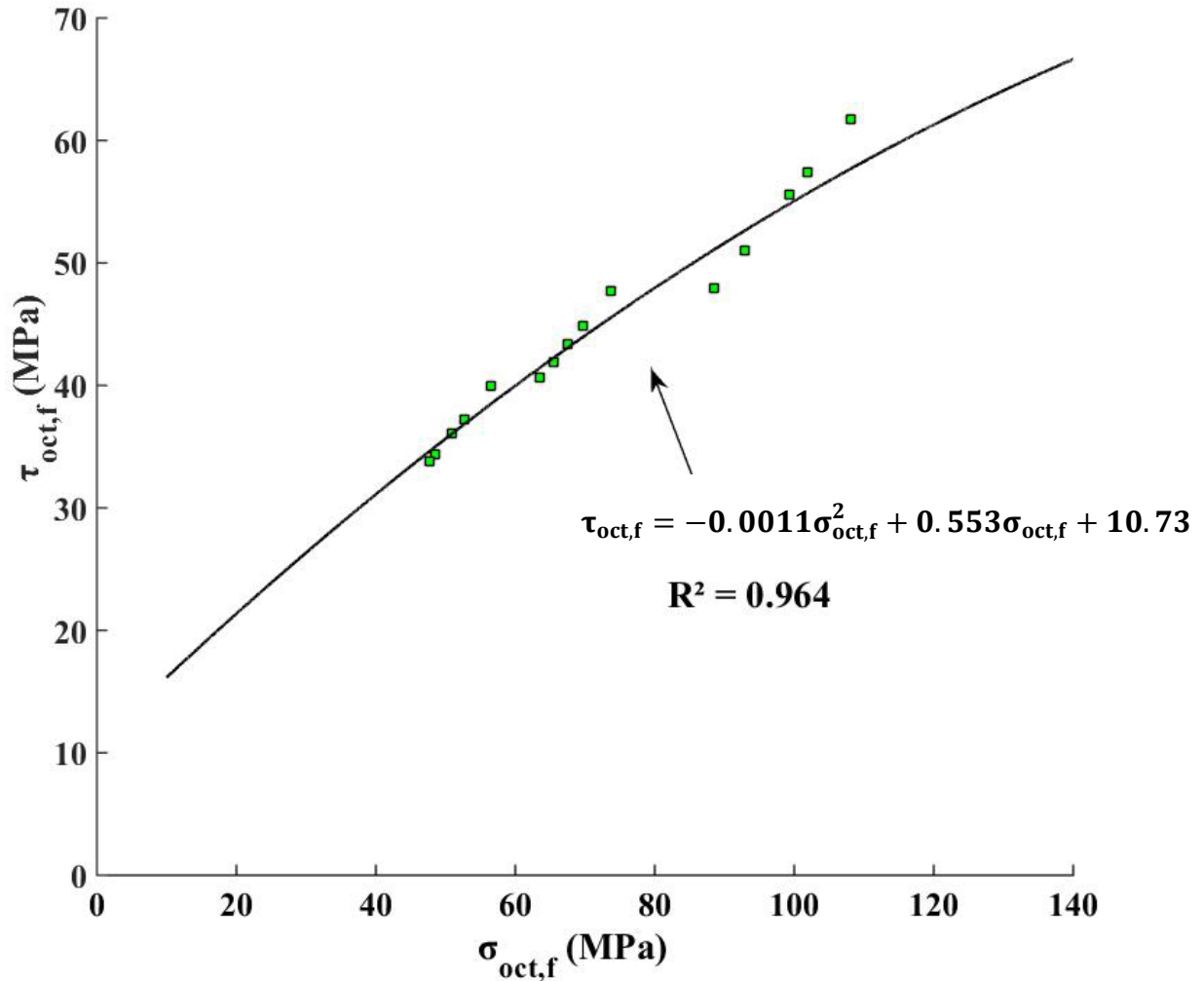


Figure 6.28 Triaxial strength envelop based on Nadai criterion fitted with experimental data points at failure for axisymmetric loading conditions ( $\sigma_1 = \sigma_2$  and  $\sigma_3 = \text{constant}$ ).

## 6.9 Summary and Conclusion

Arora and Mishra, 2015 investigated the layer interaction within laminated rock under the effect of biaxial and triaxial stresses using a biaxial device. In this research, a new biaxial frame was built based on the modified design of the original biaxial device. The tests were performed on 50.8 mm cubical specimen using the biaxial device to replicate the 3D bending of lamination rock under high horizontal loading. In addition to these platens, a confining device was used to conduct tests under limited true-triaxial loading conditions. To validate the biaxial frame and confining

device design, study involving influence of poly-axial stress state on failure response of Berea sandstone was conducted. Furthermore, confining device was also used to determine the influence of loading path on its peak strength and failure mode under biaxial stress state. Based on the laboratory investigation, the following conclusions are made:-

- The average uniaxial compressive strength ( $\sigma_c$ ) showed an increase by 29.6%, as the specimen height was decreased from 101.6 mm (H/W =2) to 25.4 mm (H/W =0.5) for square shaped cross-section Berea sandstone.
- The biaxial failure strength of 50.8 mm cubical specimen is 15.71 ~48.4 % higher than its uniaxial compressive strength. Therefore, both Mohr–Coulomb and Hoek–Brown failure criteria underestimate the biaxial strength of sandstone samples, as they ignore the effect of the intermediate principal stress.
- Generally, the biaxial strength of cubical specimen increased with increase in intermediate principal stress ( $\sigma_2$ ) under loading path 2. However, the peak strength dropped by 12.78% when  $\sigma_2$  was kept equal to  $\sigma_1$  under loading path 1, which represents high intermediate stress ( $\sigma_1 = \sigma_2$ ).
- The peak strength under true-triaxial loading condition was analyzed form of two principal stress invariants; the octahedral shear stress at failure ( $\tau_{oct,f}$ ), and the octahedral normal stress at failure ( $\sigma_{oct,f}$ ) to consider novel loading path, i.e.,  $\sigma_1 = \sigma_2$  and  $\sigma_3 = \text{constant}$  used in the current study.
- The transition of failure mode from uniaxial to triaxial stress conditions was analyzed to understand the failure mechanism of sandstone specimens under ploy-axial stress state.
- In uniaxial stress state, specimens exhibited spalling on all free faces of the cube followed by violent failure of mid-section. The mid-section of the specimen mostly failed in shear with multiple planes intersecting each other.

- When specimens were tested biaxially, the failure mechanism was characterized by varying the degree of spalling at free faces along with the shear failure of the mid-section. The intensity of spalling depended upon the magnitude of confinement by the intermediate stress.
- The shear failure plane rotated with increase in intermediate principal stress,  $\sigma_2$  from plane with strike in the  $\sigma_1$  direction for  $\sigma_2 = 6.89$  MPa to plane with strike in the  $\sigma_2$  direction for  $\sigma_2 = 27.58$  MPa ( $\sigma_2 = 0.45\sigma_c$ ). Finally, under  $\sigma_1 = \sigma_2$  shear plane orientation was a combination of both  $\sigma_1$  and  $\sigma_2$  axis.
- In true-triaxial tests, failure was similar to biaxial tests under loading path 1 ( $\sigma_1 = \sigma_2$ ) with splitting towards outer surface (faces perpendicular minimum principal stress,  $\sigma_3$ ) and shear failure occurred in central portion of specimen.
- The volume of specimen under splitting decreased with increase in confinement or minimum principal stress ( $\sigma_3$ ) from occupying a large portion of specimen at  $\sigma_3 = 0$  to no splitting at  $\sigma_3 = 20.68$  MPa.
- To account for influence of intermediate principal stress ( $\sigma_2$ ) in observed biaxial tests, Drucker-Prager failure was tried initially. However, no specific friction angle was usable for failure strength at different confining stress.
- An empirical failure criterion was derived using regressions analysis of data points at failure. The criterion is a quadratic polynomial with  $R^2$  of 0.7507.
- For true-triaxial strength envelope, 3D failure criterion by Nadai (1950) was found to be good fit with  $R^2$  of 0.9

## 7. CONCLUSION AND RECOMMENDATION

### 7.1 Conclusion

The objective this research was to understand the influence of lamination on behavior of shale roof under high horizontal stress. High horizontal *in-situ* stresses and laminated immediate roof have been a detrimental combination for underground coal mines in the eastern United States. In addition, these conditions pose challenging ground control problems to researchers. The field observation suggested that the failure in laminated roof is highly dependent on the layer interaction (inter-laminar interaction), i.e., location and degree of delamination determined whether failure is dome-shaped, shear of stiff beds or cutter roof. Most of current studies on field scale numerical simulation either assumed laminated roof to be “equivalent isotropic” and ignored the layer-interaction or assumed laminar planes similar to the infilled joints with low shear and tensile strength. However, laboratory scale studies showed significant strength of laminar plane and their influence on failure progression in a shale rock. Therefore, it is imperative to investigate the inter-laminar interaction and its influence on failure progression in shale roof to bring forth underlying mechanism behind various failure modes like cutter roof.

In this research, an anisotropic model was used in FLAC3D which modelled shale rock as the isotropic rock along with (representing the matrix material within the laminates) along with discontinuities (representing the weak plane between laminates). Instead of including whole network of lamination (thickness ~ 1-10 mm), an approach involving a representative number of laminations sufficient to include the underlying mechanism was adopted. In this approach, the influence of lamination thickness on behavior of shale roof was analyzed. In addition, the anisotropic model was compared with equivalent isotropic model to have detailed understanding of the basic difference between two models. This research showed that the inclusion of laminations in numerical models modifies the shape of the plastic yield zone and increases the vertical roof deflection as compared to the prediction using isotropic material modelling approach.

The anisotropic model identified three behavioral responses of shale roof namely: stress channeling, multi-beam coupling, and self-stabilizing beams based on lamination thickness that are not present in isotropic model. In addition, these behavior types were also found to be highly

dependent on laminar plane properties and horizontal stress. The laminar plane's tensile strength controlled the behavior of the thinly laminated roof. For instance, in case of zero tensile strength of interface, layers separated to form individual beams and undergo buckling at mid-span for small lamination thickness ( $< 150$  mm). While in the case of high tensile strength (0.3 MPa). The delamination and failure are more concentrated towards the entry corner, which indicated that lamination properties have a significant influence on the layer interaction and failure progression within the shale roof. Although this model provided a detailed insight into behavior of laminated roof, underlying mechanism behind the failure progression from one layer remained ambiguous. This limitation was due to the complex layer interaction in shale roof, which is result of its interaction with overburden strata. Therefore, beam analysis was used to develop a simplified layer-interaction model and then investigate its influence on the behavior of the laminated roof under elastic and plastic state.

The elastic beam analysis was conducted using three beam models namely: Solid beam model, Voussoir beam model, Solid Beam on Elastic Abutment in UDEC to understand the layer interaction in a laminated shale roof under uniform loading. The advantage this approach was simplified bending profile of immediate roof as compared to the anisotropic mine model which allowed detailed understanding of layer-interaction within laminated roof. These models provide insight into the influence of horizontal stress and lamination parameters on layer interaction and bending profile of shale roof however, within elastic limit. Of all these beam models, solid beam on elastic abutment model is the most appropriate model to simulate the laminated roof under high horizontal stress as it suggests shear failure initiation at entry corners. In addition, results showed that buckling was the probable failure in thinly laminated roof especially under high horizontal stress. Layer interaction was found to be highly dependent on joint (laminar plane) shear strength with multi-layered roof acting as composite beam under high joint cohesion. However, elastic analysis only predicted the initiation of failure. The influence of layer interaction on failure progression in shale roof could not be investigated. In addition, beam models were analyzed only for low *in-situ* stresses as uniform loading was applied on shale roof.

The plastic beam analysis was conducted using solid beam on elastic abutment model in FLAC3D. The model also simulated high *in-situ* stress condition by accounting the formation of pressure arch on the vertical load profile on top of shale roof from overburden strata. The vertical load profile was calculated based on the analytical solution that estimated stress distribution within the roof after the excavation of a single mine entry. Layer interaction and failure propagation was found to be highly dependent on interface (laminar plane) cohesion as it dictates location and degree of delamination. The thinly laminated roof can delaminate very easily if it is allowed to bend significantly irrespective lamination strength. This behavior can also occur in bolted roof if tensioned bolt is used.

Layer interaction in laminated shale roof was not limited to plane strain condition as seen in various cutter roof cases. The cutter roof failure progressively moves through bolt planes indicating the failure is more accurately represented by plate type failure instead of beam. For better understanding of the underlying mechanism of failure propagation from one lamina to another, experiments are required that involved three-dimensional bending of shale rocks. For this purpose, a biaxial platen was used based on design by Arora and Mishra, 2015. In addition to these platens, a confining device was used to apply true-triaxial load on a 50.8 mm cubical specimen. To validate the biaxial frame and confining device design, study involving influence of poly-axial stress state on failure response of Berea sandstone was conducted. The failure mode and peak strength values obtained in biaxial stress conditions were compared with existing biaxial devices. Furthermore, influence of the specimen size in uniaxial stress conditions on failure modes was also studied to have complete understanding of failure mode transition from standard UCS test to triaxial test on cubical specimen.

After validating the device, the next step involved testing on shale samples. However, correct sized specimens of shale could not be obtained in the stipulated time and therefore no test was performed on shale specimens. The setup was included in this thesis to represent a device that can accurately test rock specimens with biaxial and true-triaxial loading conditions.

## **7.2 Future recommendation**

This research is a preliminary investigation into influence of lamination on the behavior of shale roof under high horizontal stress. Although much research has been conducted on strength

anisotropy on laboratory scale due to presence of lamination, the field scale simulation has been limited due to high computational requirements. Based on the investigation carried on this research, the following work is identified for any future studies:

- A rigorous testing of lamination properties, as well as residual strength and dilation parameters is necessary to more accurately represent laminar plane in a numerical model and determine its influence on the anisotropic behavior.
- The peak strength parameters of the laminar planes can be estimated from direct-shear tests on cubical sample and Brazilian tests on circular disk specimens at different lamination orientation.
- Rock support is necessary to maintain stability and safety in underground excavations. The next step would be to simulate bolted shale roof and assess the change in failure initiation and progression within shale roof using these simplified beam model.
- Although strain-softening behavior has significant limitation in its application, it has been successful in simulating cutter failure in isotropic rock. Therefore, its use with roof bolting can be used in beam models to identify more accurate layer-interaction during failure progression in shale roof.
- For three-dimensional analysis, experiments on cubical shale sample in biaxial and triaxial devices used in this study can provide a realistic understanding of layer-interaction at laboratory scale. The biaxial frame can be used to investigate actual delamination process at different loading condition especially like high horizontal stress condition that exist as biaxial stress state in vicinity of mine entry.



## REFERENCES

- Adhikary, D. P. (2010) *Shortcomings in the standard continuum based Implicit Joint model of layered rocks*, Journal of Geology and Mining Research Vol 2, pp. 23–28.
- Aggson, J. R., and Curran, J. (1978) *Coal Mine Control Problems Associated with a High Horizontal Stress Field*, SME annual meeting 1978, Denver, CO, USA.
- Ahola, M. P., Donato, D.A., and Kripakov, N.P. (1991) *Application of Numerical Modeling techniques to Analysis of Cutter Roof Failure*, USBM IC 9287.
- Al-Ajmi, A.M., and Zimmerman, R.W. (2005) *Relation between the Mogi and the Coulomb failure criteria*. International Journal of Rock Mechanics and Mining Sciences. Vol.42, pp. 3,431–3,439.
- Amadei, B., and Robinson, M. J. (1986) *Strength of rock in multiaxial loading conditions*. Proceedings of the 27th U.S. Rock Mechanics Symposium, Tuscaloosa.
- Amadei, B., Janoo, V., and Robison, M.J. (1984) *Strength of Indiana limestone in true biaxial loading conditions*. Proceedings of the 25th US symposium on rock mechanics. Northwestern University.
- Ambrose, J. (2014) *Failure of Anisotropic Shales under Triaxial Stress Conditions*, PhD thesis, Imperial College, 265 pp.
- Arora S., and Mishra, B. (2015) *Investigation of the failure mode of shale rocks in biaxial and triaxial compression tests*, International Journal of Rock Mechanics and Mining Sciences; Vol.79, pp. 109-123.
- ASTM.(1998) *Preparing rock core specimens and determining dimensional and shape tolerances*, Annual book of ASTM standards, pp. 687–690.

- Badr, S., Mendoza, R., Kieffer, S., Salamon, M.D.G., and Ozbay, U. (2003). *Numerical Modeling of Longwalls in Deep Coal Mines*, Proceedings of the 22nd International Conference on Ground Control in Mining, West Virginia University, Morgantown, West Virginia, pp. 37-43.
- Bajpayee, T. S., Pappas, D. M., and Ellenberger, J. L. (2014) *Roof Instability: What Reportable Non-Injury Roof Falls in Underground Coal Mines Can Tell Us*, Professional Safety, Vol. 59, No. 3, pp. 57-62.
- Bandis, S. C., Lumsden, A. C., and Barton, N. R. (1983) *Fundamentals of rock joint deformation*, International journal of Rock Mechanics and Mining sciences, Vol. 20, pp. 249-268
- Bandis, S.C. (1990) *Mechanical properties of rock joints*, Proceedings of the International symposium on Rock joints, Norway, Balkema, Rotterdam, pp. 125-140.
- Barton, N. R., and Choubey, V. (1977) *The shear strength of rock joints in theory and practice*. Rock Mechanics. Vol 10 pp. 1-54.
- Bobet, A. (2001) *Influence of the loading apparatus on the stresses within biaxial samples*, Geotechnical Testing Journal—the American Society for Testing and Materials. Vol 24 pp. 256–272.
- Bona, P., Min, K. B. (2015). *Bonded-particle discrete element modeling of mechanical behavior of transversely isotropic rock*, International Journal of Rock Mechanics and Mining Sciences; Vol 76, pp. 243-255,
- Beer G, Meek J. L, Cowling R (1981) *Prediction of behaviour of shale hanging walls in deep underground excavations*, Proceedings of the 5th I.S.R.M. Symposium. Melbourne. pp. 45-51.
- Boggs, S. J. (1987). *Principles of Sedimentology and Stratigraphy*. Merrill Publishing Company, Westerville.

- Brady, B. H. G., and Brown, E. T. (2006) *Rock Mechanics for underground mining*, Third Edition. Springer, Dordrecht, the Netherlands.
- Brown, E. T. (1974) *Fracture of rock under uniform biaxial compression*. Proceedings of the 3rd International Society for Rock Mechanics Congress, Denver, USA, pp. 111-117
- Bauer, E. R. (1990) *Cutter Roof Failure: Six Case Studies in the Northern Appalachian Coal Basin,* USBM IC, IC 9266.
- Cai, M., Kaiser, P. K., Uno, H., Tasaka, Y., Minami, M. (2004). *Estimation of rock mass strength and deformation modulus of jointed hard rock masses using the GSI system*”. International Journal of Rock Mechanics and Mining Sciences; Vol 41 pp. 3–19.
- Cai, M. (2008) *Influence of intermediate principal stress on rock fracturing and strength near excavation boundaries—insight from numerical modeling*. International Journal of Rock Mechanics and Mining Sciences; Vol 45, pp. 5,763–5,772.
- Chen, H. J. (1999) *Stress Analysis in Longwall Entry Roof under High Horizontal Stress*, Ph.D. dissertation, West Virginia University, pp. 278.
- Cho, J.W., Kim, H., Jeon, S., Min, K.B. (2012). *Deformation and strength anisotropy of Asan gneiss, Boryeong shale, and Yeoncheon schist*, International Journal of Rock Mechanics and Mining Sciences; Vol 50 pp. 158–69.
- Chong, Z., Li, X., Hou, P., Wu, Y., Zhang, J., Chen, T., Liang, S. (2017) *Numerical Investigation of Bedding Plane Parameters of Transversely Isotropic Shale*, Rock Mechanics and Rock Engineering; Vol 50, pp.1183-1204.
- Colmenares, L.B., and Zoback, M. D. (2002) *A statistical evaluation of intact rock failure criteria constrained by polyaxial test data for five different rocks*, International Journal of Rock Mechanics and Mining Sciences. Vol 39 pp. 6,695–6,729.

- Colwell, M. (2004). *Analysis and design of rib support (ADRS). A rib support design methodology for Australian Collieries*. ACARP end of project report C11027 (p. 325). Brisbane: Australian Coal Association Research Program (ACARP).
- Colwell, M., R. Frith., and G., Reed. (2008) *Tailgate 802 - Grasstree Mine: A Case Study in Pragmatic Roof Support Design in Aziz*, Proceedings of the Coal Operators' Conference, University of Wollongong & the Australasian Institute of Mining and Metallurgy, pp. 75-91.
- Colwell, M., and Frith, R. (2012). *Analysis and design of faceroad roof support (ADFRS). A roof support design methodology for longwall installation roadways*. ACARP end of project report C19008 (p. 214). Brisbane: Australian Coal Association Research Program (ACARP).
- Desai, C. S., and Siriwardane, H. S. (1984) *Constitutive Laws for Engineering Materials with Emphasis on Geologic Materials*, Prentice-Hall, Inc., Englewood Cliffs, New Jersey, U.S.A.
- Dinsdale, J. R. (1935) *Ground Pressures and Pressure Pro-files Around Mining Excavations*, Colliery Eng., Vol. 12, pp. 406-409.
- Diederichs, M.S., and Kaiser, P.K. (1999) *Stability of large excavations in laminated hard rock masses: the voussoir analogue revisited*, International Journal of Rock Mechanics and Mining Sciences; Vol 36, pp. 97-117.
- Dolinar, D.R., (2003) *Variation of horizontal stresses and strains in mines in bedded deposits in the eastern and mid-western United States*, Proceeding of the 22<sup>nd</sup> International Conference on Ground Control in Mining, West Virginia University, Morgantown, West Virginia, pp. 178-185.
- Drucker, D. C., and Prager, W. (1952) *Soil mechanics and plastic analysis in limit design*, Quarterly Applied Mathematics; Vol 10, pp. 157-165.
- Duan, K., Kwok, C.Y. (2015) *Discrete element modeling of anisotropic rock under Brazilian test conditions*, International Journal of Rock Mechanics and Mining Sciences; Vol 78, pp. 46–56

- Duvall, W. I. (1935) *Stress Analysis Applied to Underground Mining Problems, Part I -Stress Analysis Applied to Single Openings*, USBM IC 4192.
- Esterhuizen, G. S., and Bajpayee, T. S. (2012) *Horizontal Stress Related Failure In Bedded Mine Roofs-insight From Field Observations And Numerical Models*, Proceedings of the 46th US Rock Mechanics/Geomechanics Symposium, Chicago, IL, pp. 68-77.
- Esterhuizen, G. S., Bajpayee, T. S., Ellenberger, J. L., & Murphy, M. M. (2013) *Practical Estimation of Rock Properties for Modeling Bedded Coal Mine Strata Using the Coal Mine Roof Rating*. Proceedings of the 47th US Rock Mechanics/Geomechanics Symposium, San Francisco, California.
- Evans, W. H. (1941) *The strength of undermined strata*, Trans Inst Min Metall; Vol 50, pp. 475–500.
- Feng, F., Li, X., and Li, D. (2017) *Modeling of failure characteristics of rectangular hard rock influenced by sample height-to-width ratios: A finite/discrete element approach*, Comptes Rendus Mécanique, Vol345, pp. 317-328,
- Föppl, A. (1900) *Die Abhängigkeit der Bruchgefahr von der Art des Spannungszustandes. Mitteilungen aus dem Mechanischen Laboratorium, Technische Hochschule, München Vol 27.*
- Frith, R. (2000). *The use of cribless tailgates in longwall extraction*, Proceeding of the 19<sup>th</sup> International Conference on Ground Control in Mining, West Virginia University, Morgantown, West Virginia, pp. 84–92.
- Gadde, M. M., and Peng, S. S. (2005), *Numerical simulation of cutter roof failures under weak roof conditions*, SME annual meeting 2005, Salt Lake City, Utah, pp. 459-469.

- Gadde, M., Rusnak, J., Honse, J., and Peng, S.S. (2007) *On rock failure criteria for coal measure rocks*. Proceedings of the 26th International Conference on Ground Control in Mining, West Virginia University, Morgantown, West Virginia, pp. 361-369.
- Gale, W.J., Mark, C., Oyler, D.C., and Chen, J. (2004) *Computer simulation of Ground control behavior and Rock Bolt Interaction at Emerald Mine*, Proceedings of the 23rd International Conference on Ground Control in Mining, West Virginia University, Morgantown, West Virginia, pp. 27-34.
- Glamheden, R., Hökmark, H., and Christiansson, R. (2004). *Modeling creep in jointed rock masses*, Proceedings of the 1st International UDEC/3DEC Symposium: Numerical Modeling of Discrete Materials in Geotechnical Engineering, Civil Engineering and Earth Science, Bochum, Germany.
- Hajiabdolmajid, V., Kaiser, P.K., and Martin, C.D. (2002) *Modelling brittle failure of rock*, International Journal of Rock Mechanics and Mining Sciences; Vol 39, pp. 731-741.
- Handin, J., Heard, H.C., and Magouirk, J.N. (1967) *Effect of the intermediate principal stress on the failure of limestone, dolomite, and glass at different temperature and strain rate*, J Geophys Res. Vol 72, pp. 2,611–2,640.
- Hebblewhite, B. (2009) *25 Years of Ground Control Developments, Practices, and Issues in Australia. PROC*, Proceedings of the 25th International Conference on Ground Control in Mining, West Virginia University, Morgantown.
- He, J., Afolagboye, L.O. (2018) *Influence of layer orientation and interlayer bonding force on the mechanical behavior of shale under Brazilian test conditions*, Acta Mechanica Sinica; Vol 34, pp. 349-358.
- Hoek, E., and Brown, E.T. (1980) *Underground excavations in rock*, The Institute of Mining and Metallurgy, London, England

- Hill III, J. L. (1986) *Cutter Roof Failure: An Overview of the Causes and Methods for Control*, USBM IC 9094.
- Hill, J. L., III, and Bauer, E. R. (1984) *An Investigation of the Causes of Cutter Roof Failure in a Central Pennsylvania Coal Mine: A Case Study*, Proceedings of the 25<sup>th</sup> Symposium on Rock Mechanics, Evanston, IL, USA, pp. 603-614.
- Holcomb, D. J. and Olsson, W. A. (2003) *Compaction localization and fluid flow*, J. Geophys. Res. Vol 108.
- Iannacchione, A. T., Popp J. T., and Rulli J. A., (1984) *The Occurrence and Characterization of Geologic Anomalies and Cutler Roof Failure: Their Effect on Gate road Stability*, Proceedings of 2nd International Conference on Stability in Underground Mining, Soc. Min. Eng. AIME, pp. 428-445.
- Itasca (2008a) *PFC2D (Particle Flow Code in 2 Dimensions), Version 4.0*, Minneapolis, Minnesota.
- Itasca (2011a) *UDEC (Universal Distinct Element Code), Version 5.0*, Minneapolis, Minnesota.
- Itasca (2012) *Fast Lagrangian Analysis of Continua in 3 Dimensions, Version 5.0, User's guide*, Minneapolis, USA.
- Jeremic, M. L. (1981) *Coal Mine Roadway Stability in Relation to Lateral Tectonic Stress-Western Canada*, Mining Engineering, pp. 704-709.
- Kent, F.L., Coggan, J.S., and Altounyan, P.F.R. (1999) *Investigation into factors affecting roadway deformation in the Selby coalfield*, Geotechnical and Geological Engineering, pp 273–289.
- Kulatilake, P.H., Park, J., and Malama, B. (2006) *A new rock mass failure criterion for biaxial loading conditions*, Geotechnical and Geological Engineering; Vol 24, pp. 4,871-4,888.

- Labuz, J.F., Bridell, J.M (1993) *Reducing frictional constraint in compression testing through lubrication*, International Journal of Rock Mechanics and Mining Sciences and Geomechanics, Vol 30, pp. 451-455.
- Lade, P. V., and Duncan, J. M. (1975) *Elastoplastic stress-strain theory for cohesionless soil*, J. Geotech. Eng. Div., ASCE Vol 101, pp. 1037-1053.
- Lendel, U. (2004) *Rock bolting and rock support and their combination in hard coal mining - a comparative study made with UDEC*, Proceedings of the 1st International UDEC/3DEC Symposium: Numerical Modeling of Discrete Materials in Geotechnical Engineering, Civil Engineering and Earth Science, Bochum, Germany.
- Ma, X. (2014) *Failure characteristics of compactive, porous sandstones subjected to true triaxial stresses*, PhD thesis, 308 pp., Univ. of Wisconsin-Madison.
- Ma, X., Rudnicki, J. W., and Haimson, B. C. (2017) *Failure characteristics of two porous sandstones subjected to true triaxial stresses: Applied through a novel loading path*, J. Geophys. Res. Solid Earth, Vol 122, pp. 2525–2540.
- Ma, X., and B. C. Haimson (2016) *Failure characteristics of two porous sandstones subjected to true triaxial stresses*, J. Geophys. Res. Solid Earth, Vol 121, pp. 6477–6498.
- Maleki, H. N., Owens, J. K., and Endicott, M. (2001) *Evaluation of Mobile Roof Support Technologies*, Proceedings of the 20th International Conference on Ground Control in Mining, West Virginia University, Morgantown, West Virginia, pp 67-77.
- Maleki, H., Stewart, C., Stone, R., Abshire, J., (2009) *Practical application of numerical modeling for the study of sudden floor heave failure mechanisms*, Proceedings of the International Workshop on Numerical Modeling for Underground Mine Excavation Design. Asheville, NC, pp. 89–100.



- Mark, C., and Mucho, T.P. (1994) *Longwall mine design for control of horizontal stress*, Proceedings, new technology for longwall ground control. US Bureau of Mines Technology Transfer Seminar, USBM SP 94-01.
- Mark, C. (1991) *Horizontal Stress and Its Effects Longwall Ground Control*, Mining Engineering, pp. 1356-1360.
- Matsuoka, H., and T. Nakai. (1974) *Stress-deformation and strength characteristics of soil under three different principal stresses*, Proceedings of the Japan Soc. Civil Engn, pp. 59-70.
- Mine Safety & Health Administration. Web page: <http://www.msha.gov/stats/statinfo.htm>. 2010.
- Mindlin, R. D. (1939) *Stress Distribution Around Tunnel*, Proceedings of Am. Soc. Civil Eng., pp. 619-642.
- Mogi, K. (1967) *Effect of the intermediate principal stress on rock failure*. *Journal of Geophysical Research* Vol 72, pp. 5117-5131.
- Mogi, K. (1971) *Fracture and flow of rocks under high triaxial compression*, J. Geophys. Res., Vol 76, pp. 1255-1269.
- Molinda, G.M. (2003). *Geologic hazards and roof stability in coal mines*, USBM; IC 9466, p. 33.
- Molinda, G., and Mark, C. (2010) *Ground failure in coal mines with weak rocks*, The Electronic Journal of Geotechnical Engineering; Vol. 15, pp. 547-588.
- Molinda, G.M., Mark, C. (1996). *Rating the strength of coal mine roof rocks*, Pittsburgh, PA: USBM, IC 9444; p. 36.
- Morsy, K., and Peng, S. S. (2001) *Typical Complete Stress-Strain Curves of Coal*, Proceedings of the 20th International Conference on Ground Control in Mining, Morgantown, West Virginia University, pp 210-217.

- Morsy, K., and Peng, S. S. (2005). *Detailed Stress Analysis of Longwall Panels*, Proceedings of the 24th International Conference on Ground Control in Mining, West Virginia University, Morgantown, West Virginia, pp 18-32.
- Murphy, M. M. (2016) *Shale Failure Mechanics and Intervention Measures in Underground Coal Mines: Results From 50 Years of Ground Control Safety Research*, Rock Mechanics and Rock Engineering; Vol 49, pp. 661-671
- Murphy, M. M., Esterhuizen, G. S., and Tulu, I. B. (2014) *Lateral Reinforcement of Fully Grouted Roof Bolts in a FLAC3D Simulated Coal Mine Entry*, Proceedings of the 48th U.S. Rock Mechanics/Geomechanics Symposium, Minneapolis, Minnesota.
- Nadai, A. (1950) *Theory of flow and fracture of solids*. McGraw-Hill, Vol. 1, pp. 572.
- Niandou, H. S., Henry, J.F., Henry J.P., Fourmaintraux, D. (1997) Laboratory investigation of the mechanical behavior of Tournemire shale. *International Journal of Rock Mechanics and Mining Sciences* Vol 34, pp.3–16.
- Ndlovu, X., and Stacy, T. R. (2007). *Observations and analyses of roof guttering in a coal mine*, The Journal of the Southern African Institute of Mining and Metallurgy, pp 477-491.
- Obermeier, S. F. (1971) *Influence of imposed stress histories and plane stress-plane strain on the mechanical properties of two limestones*. West Lafayette, Indiana, USA, Perdue University. Ph.D.: 300.
- Olsson, W. A. (1999) *Theoretical and experimental investigation of compaction bands in porous rock*, *J. Geophys. Res*; Vol 104, pp. 7219–7228.
- Pande, G. N., Beer, G. and Williams, J.R. (1990). *Numerical Methods in Rock Mechanics*, John Wiley and Sons Ltd., Chichester, England.
- Panek, L. A. (1951), *Stresses About Mine Openings in a Homogeneous Rock Body*, Edwards Brothers, Inc., New York.

- Panek, L. A. (1956). *Principles of reinforcing bedded mine roof with bolts*, USBM, IC 5156.
- Panek, L. A. (1962). *The Effect of Suspension in Bolting Bedded Mine Roof*'. USBM, IC 6183.
- Perras, M. A. (2009) *Tunneling in horizontally laminated ground: the influence of lamination thickness on anisotropic behavior and practical observations from the Niagara Tunnel Project*. M.Sc. Eng. thesis, Queen's University, Kingston.
- Perras, M.A., and Diederichs, M.S. (2007). *Engineering geology, glacial preconditioning and rock mass response to large scale underground excavations in the Niagara Region*. Proceeding from the 1<sup>st</sup> Canada-US Rock Mechanics Symposium, Vancouver, BC, Canada.
- Perras, M. A., and Diederichs, M. S. (2009b). *Modelling circular excavations in horizontally laminated ground. The role of rock and lamination strength properties*. Poster presentation at the 3rd Canada-US Rock Mechanics Symposium, Toronto, ON, Canada.
- Pariseau, W. G. (1992) *Applications of Finite Element Analysis to Mining Engineering*, Comprehensive Rock Engineering, 491-522.
- Peng, S. S. (2007). *Ground Control failures- a Pictorial view of case studies*, S.S. Peng publisher.
- Parrott, L. J. (1970) *Improved apparatus for biaxial loading of concrete specimens*, The Journal of Strain Analysis for Engineering Design Vol 5, pp. 169–76.
- Ray, A. K. (2009), *Influence of cutting sequence and time effects on cutters and roof falls in underground coal mine – numerical approach*, Ph.D. Dissertation, West Virginia University, Morgantown, USA.
- Rudnicki, J. W. (2013), *Failure of Rocks in the Laboratory and in the Earth*, Proceedings of 22nd International Congress on Theoretical and Applied Mechanics Adelaide, pp. 199-215, Springer.

- Sainsbury, B.N., and Sainsbury, D. P. (2017) *Practical Use of the Ubiquitous-Joint Constitutive Model for the Simulation of Anisotropic Rock Masses*, Rock Mechanics and Rock Engineering; Vol 2017, pp.1507-1528.
- Savin, G. N. (1961) *Stress concentration around holes*. International Series of Monographs in Aeronautics and Astronautics. Pergamon Press.
- Shabanimashcool, Mahdi., and Charlie Li. C. (2015) *Analytical approaches for studying the stability of laminated roof strata*, International Journal of Rock Mechanics and Mining Sciences; Vol 79, pp. 99-108.
- Sheorey, P. R. (1976) *An investigation of the rock mechanics aspects of a system of short face in-seam development for subsequent longwall retreat extraction*, PhD thesis, Newcastle University, 367 pp.
- Sofianos A. I. (1996). *Analysis and design of underground hard rock voussoir beam roof*. International Journal of Rock Mechanics and Mining Sciences; Vol 33, pp. 153–166.
- Sofianos, A. I., Nomikos, P.P., Tsoutrelis, C.E. (2000). *Effect of joint frequency and compliance on the response of an underground roof rock beam*. GeoEng. 2000, Melbourne, Australia.
- Sternlof, K. R., Chapin, J. R., Pollard, D. D and Durlofsky L. J. (2004), *Permeability effects of deformation band arrays in sandstone*, Am. Assoc. Petroleum Geologists. Bull. 88: 1315-1329.
- Sterling, R.L. (1980). *The ultimate load behavior of laterally con strained rock beams*, Proceedings of the 21<sup>st</sup> US Symposium on Rock Mechanics. University of Missouri-Rolla.
- Stimpson. B, Ahmed. M. (1992). *Failure of a linear Voussoir arch: a laboratory and numerical study*. Can. Geotech. J, Vol 29, pp. 188±94.
- Stephansson O. (1971), *Stability of single openings in horizontally bedded rock*, Engineering Geology, Vol 5, pp. 5-71,

- Su, W. H., and Peng, S. S. (1987), "Cutter Roof and its Causes," *Mining Science and Technology*, Vol.4, No. 2, pp. 113-32.
- Terzagi, K., Peck, R.B., Gholamreza, M. (1996) *Soil Mechanics in Engineering Practice*, Wiley, New York.
- Timoshenko, S. (1959) *Theory of Elasticity*, McGraw-HillBook Co., Inc., New York.
- Unrug, K., and Padgett, P. (2003). *RQD from the Barrel to the Box: Weatherability May be a Better Indicator for Roof Support Design*, Proceedings, 22nd International Conference on Ground Control in Mining, West Virginia University, Morgantown, West Virginia, pp. 162-167.
- Wiebols, G. A., and Cook N. G. W. (1968) *An energy criterion for the strength of rock in polyaxial compression*, *International Journal of Rock Mechanics and Mining Sciences*; Vol 5, pp. 529-549.
- Wright, F.D. (1974) *Design of Roof Bolt Patterns for Jointed Rock*, USBM
- Yun, X.Y., Yang, X.L., and Mitri, H.S. (2008) *Mechanical behavior of biaxially loaded coalmine sandstone*, *In: Boundaries of rock mechanics—recent advances and challenges for the 21st century*, Proceedings of the international young scholar symposium on rock mechanics. Beijing, China, pp. 233-237.
- Zhang, Y., Han, J., Peng, S.S., and Padgett, P. (2004). *Geo-Mechanical Property and Failures of Weak Roof Shales in Coal Mine*, Proceedings of the 23rd International Conference on Ground Control in Mining, West Virginia University, Morgantown, West Virginia, pp. 228-234.
- Zipf, R. K. (2005). *Failure Mechanics of Multiple seam Mining Interactions*, Proceedings of the 24th International Conference on Ground Control in Mining, West Virginia University, Morgantown, West Virginia, pp. 93-106.

